

NOTE TO USERS

This reproduction is the best copy available.

UMI[®]

Experiments on the dynamics of cantilevered pipes subjected to internal and/or external axial flow

by

Stephanie Rinaldi

**Department of Mechanical Engineering
McGill University
Montréal, Québec, Canada**

**Under the supervision of
Professor Michael P. Païdoussis
Dr. Christian Semler**

February 2009

**A thesis submitted to McGill University in partial fulfillment of the
requirements of the degree of Master of Engineering**

Copyright © Stephanie Rinaldi 2009



Library and Archives
Canada

Published Heritage
Branch

395 Wellington Street
Ottawa ON K1A 0N4
Canada

Bibliothèque et
Archives Canada

Direction du
Patrimoine de l'édition

395, rue Wellington
Ottawa ON K1A 0N4
Canada

Your file Votre référence
ISBN: 978-0-494-66919-8
Our file Notre référence
ISBN: 978-0-494-66919-8

NOTICE:

The author has granted a non-exclusive license allowing Library and Archives Canada to reproduce, publish, archive, preserve, conserve, communicate to the public by telecommunication or on the Internet, loan, distribute and sell theses worldwide, for commercial or non-commercial purposes, in microform, paper, electronic and/or any other formats.

The author retains copyright ownership and moral rights in this thesis. Neither the thesis nor substantial extracts from it may be printed or otherwise reproduced without the author's permission.

AVIS:

L'auteur a accordé une licence non exclusive permettant à la Bibliothèque et Archives Canada de reproduire, publier, archiver, sauvegarder, conserver, transmettre au public par télécommunication ou par l'Internet, prêter, distribuer et vendre des thèses partout dans le monde, à des fins commerciales ou autres, sur support microforme, papier, électronique et/ou autres formats.

L'auteur conserve la propriété du droit d'auteur et des droits moraux qui protègent cette thèse. Ni la thèse ni des extraits substantiels de celle-ci ne doivent être imprimés ou autrement reproduits sans son autorisation.

In compliance with the Canadian Privacy Act some supporting forms may have been removed from this thesis.

While these forms may be included in the document page count, their removal does not represent any loss of content from the thesis.

Conformément à la loi canadienne sur la protection de la vie privée, quelques formulaires secondaires ont été enlevés de cette thèse.

Bien que ces formulaires aient inclus dans la pagination, il n'y aura aucun contenu manquant.


Canada

Abstract

The main objective of this thesis is to study and investigate the dynamics and stability of cantilevered structures subjected to internal, external, or simultaneous internal and external axial flows. This was accomplished, in some cases, by deriving the linear equations of motion using a Newtonian approach and, in other cases, by making the necessary modifications to existing theoretical models. The continuous cantilevered systems were then discretized using the Galerkin method in order to determine their complex eigenfrequencies. Moreover, numerous experiments were performed to compare and validate, or otherwise, the theoretical models proposed. More specifically, the four cantilevered systems studied were the following: (i) a pipe conveying fluid that is fitted with a stabilizing end-piece, which suppresses flutter by blocking the straight-through exit of flow at the downstream end; (ii) a pipe aspirating fluid, which flutters at low flow velocities in its first mode; (iii) a free-clamped cylinder (i.e. with the upstream end free and the downstream end clamped) in confined axial flow, which also flutters at low flow velocities in its first mode and eventually develops a buckling instability; and (iv) a pipe subjected to internal flow, which after exiting the pipe is transformed to a confined counter-current annular flow, that becomes unstable by flutter too.

Sommaire

L'objectif principal de cette thèse est d'étudier la dynamique et la stabilité de structures encastrées-libres soumises à des écoulements axiaux internes, externes, ou mixtes. D'un point de vue théorique ceci a été accompli, dans certains cas, en dérivant les équations linéaires du système en utilisant une approche newtonienne et, dans d'autres cas, en faisant les modifications nécessaires à des modèles déjà existants. Les équations différentielles partielles ont par la suite été discrétisées en utilisant la méthode de Galerkin afin de déterminer les fréquences propres complexes des systèmes continus encastrés-libres. De plus, de nombreuses expériences en laboratoire ont été effectuées pour comparer et valider (ou invalider) les modèles théoriques proposés. Plus précisément, quatre systèmes encastrés-libres ont été étudiés : (i) un tuyau parcouru par un fluide interne et équipé d'un bout en plastique stabilisant, qui supprime le flottement en bloquant la sortie directe de l'écoulement à l'extrémité aval; (ii) un tuyau aspirant un fluide, qui flotte dans son premier mode propre à de faibles vitesses de débit; (iii) un cylindre encastré en aval et libre en amont soumis à un écoulement externe confiné par un canal rigide, qui flotte également dans son premier mode propre à de faibles vitesses de débit, et qui développe par la suite une instabilité statique (c'est-à-dire par flambage); et (iv) un tuyau parcouru par un fluide interne qui se déverse dans un espace confiné autour du tuyau se transformant en un écoulement annulaire en direction inverse, et qui devient lui aussi instable par flottement.

Acknowledgements

First and foremost, I would like to thank my supervisor, Professor Michael P. Païdoussis, for his continual guidance and support throughout my graduate studies. I am grateful to him for sharing his wisdom and knowledge of fluid-structure interactions with me, in addition to providing me with invaluable suggestions regarding my research. I feel privileged to have had the opportunity to work with Professor Païdoussis. His professional, yet friendly nature, and his genuine commitment to both his research and his students is a true inspiration. I would also like to thank Dr. Christian Semler for the co-supervision of a part of this work, and for his help and insight during our meetings.

I would like to extend my appreciation to my colleagues, past and present, in the fluid-structure interactions group at McGill University for their company, assistance, and friendly discussions: Prof. Zenon del Prado, Konstantinos Karagiozis, Yahya Modarres-Sadeghi, Liaosha Tang, James Wang, Frédérick Gosselin, Matthew Wadham-Gagnon, Dana Blake Giacobbi, Pierre-David Létourneau, Julien Segala, and Eugene Grinevich. In particular, I would like to thank Dana for being a great friend from the very beginning, and for providing the laboratory with some musical entertainment every now and again.

Special thanks go out to Mary Fiorilli-St-Germain for her helpfulness, and for our frequent, albeit short, “girl talks” whenever I pass by her office. I am further indebted to Benedict Besner of École Polytechnique, Tony Micozzi, Nick De Palma, Sam Minter, Roy Westgate, Andy Hofmann, Georges Tewfik, François Di Quinzio, and Mario Iacobaccio of McGill University for their technical assistance during the course of my graduate studies, and without whom my experiments would never have been completed.

I am also grateful to the Natural Sciences and Engineering Research Council of Canada (NSERC) and le Fonds Québécois de la Recherche sur la Nature et les Technologies (FQRNT) for their generous funding.

Finally, I would like to express my gratitude to my family and friends, in particular my wonderful parents, Berenice Di Re Rinaldi and Giuseppe Rinaldi, for their unconditional love, understanding, and encouragement throughout the course of my life, especially during my university years. The completion of this thesis would never have been possible without their constant support, and so I dedicate this work to them.

Nomenclature

The symbols that are presented here are those which appear most frequently throughout this thesis; thus, the following list is not, in any way, exhaustive but rather limited. It should also be mentioned that, whenever the need arises, additional symbols that do not appear in the following list will be defined in the text. Moreover, the dimensionless counterparts of dimensional quantities are not generally stated here.

Alphabetic Symbols:

	cross-sectional flow area of the pipe, $\pi D_i^2/4$
A	cross-sectional area of the cylinder, $\pi D^2/4$
A_e	external cross-sectional area of the pipe, $\pi D_o^2/4$
A_i	internal cross-sectional area of the pipe, $\pi D_i^2/4$
c	viscous damping due to the surrounding fluid
C_b	base drag coefficient
C_D	form drag coefficient
C_f	friction drag coefficient
C_N	normal friction drag coefficient
C_T	tangential friction drag coefficient
D	diameter of the cylinder
D_{ch}	diameter of the rigid channel confinement
D_h	hydraulic diameter
D_i	inner diameter of the pipe
D_o	outer diameter of the pipe
E	Young's modulus of the pipe or cylinder
E^*	viscoelastic damping of the pipe or cylinder
EI	flexural rigidity of the pipe or cylinder
f	shape parameter for the tapered end
f	frequency of oscillation of the pipe or cylinder in Hertz

f_n	natural frequency of the pipe or cylinder in its n th mode in Hertz
g	gravitational acceleration
I	area moment of inertia of the pipe or cylinder
ℓ	length of the tapered end
L	length of the pipe or cylinder
m	mass per unit length of the pipe or cylinder
m_e	mass of the end-piece
M	mass per unit length of the internal fluid
M_a	added mass per unit length due to the surrounding fluid
p	mean axial pressure
\bar{p}	externally applied pressure
p_e	external mean axial pressure
p_i	internal mean axial pressure
t	temporal variable
T	period of an oscillatory cycle
T	axial tension
\bar{T}	externally applied tension
u	dimensionless axial velocity of the fluid
u_e	dimensionless external axial velocity of the fluid
u_i	dimensionless internal axial velocity of the fluid
U	axial velocity of the fluid
U_e	external axial velocity of the fluid
U_i	internal axial velocity of the fluid
w	lateral deflection of the pipe or cylinder
ΔW	work done by the fluid on the pipe or cylinder in an oscillatory cycle
x, y	spatial variables
x_e	parameter equal to $\frac{1}{A} \int_L^{L+\ell} A(x) dx$ for the tapered end attached to the cylinder
$()_{cr}$	critical value

Greek Symbols:

α	ratio of the flow velocities v and U for aspirating pipe
$\bar{\alpha}$	viscoelastic damping of the pipe or cylinder
$\bar{\gamma}$	depressurization parameter for aspirating pipe
δ	downstream parameter ($\delta = 0$: axially unconstrained; $\delta = 1$: axially constrained)
δ_n	logarithmic decrement of the pipe or cylinder in its n th mode
δ_s	entry parameter for aspirating pipe ($\delta_s = 0$: vertical entry; $\delta_s = 1$: tangential entry)
κ	shear force factor for aspirating pipe
$\bar{\mu}^*$	hysteretic damping of the pipe or cylinder
μ_e	dynamic viscosity of the fluid
ν	Poisson ratio of the pipe or cylinder
ρ	density of the pipe or cylinder
ρ_e	density of the external fluid
ρ_f	density of the fluid
ρ_i	density of the internal fluid
$\bar{\tau}_a$	axial time delay for aspirating pipe
$\bar{\tau}_\ell$	lateral time delay for aspirating pipe
χ	confinement parameter
ψ	ratio of the angles ϑ and χ for aspirating pipe
ω	dimensionless complex frequency of the pipe or cylinder
Ω	frequency of oscillation of the pipe or cylinder in rad/s

Table of Contents

Abstract.....	i
Sommaire	ii
Acknowledgements	iii
Nomenclature	iv
 Chapter 1: Introduction	 1
1.1 Motivation and General Remarks	1
1.2 Literature Review.....	2
1.2.1 The cantilevered pipe conveying fluid.....	2
1.2.2 The cantilevered pipe aspirating fluid.....	7
1.2.3 The cantilevered cylinder in axial flow	11
1.2.4 The cantilevered tubular beam subjected to internal and external flow	17
1.3 Outline of the Thesis	21
 Chapter 2: Dynamics of a Cantilevered Pipe Conveying Fluid Fitted with a Stabilizing End-Piece	 23
2.1 Introduction.....	23
2.2 Theoretical Investigation	26
2.2.1 Theoretical model	26
2.2.2 Theoretical results.....	29
2.3 Experimental Investigation	33
2.3.1 Experimental apparatus.....	33
2.3.2 Experimental procedure	36
2.3.3 Experimental results.....	37
2.4 Summary	41
 Chapter 3: Dynamics of a Cantilevered Pipe Aspirating Fluid	 42
3.1 Introduction.....	42
3.2 Theoretical Investigation	43

3.2.1 Païdoussis, Semler & Wadham-Gagnon (2005) model with non-negligible gravity	43
3.2.2 Delay and non-purely-tangential entry model I	54
3.2.3 Delay and non-purely-tangential entry model II	58
3.2.4 Delay and non-purely-tangential entry model III	60
3.2.5 Theoretical results	63
3.3 Experimental Investigation	73
3.3.1 Experimental apparatus	73
3.3.2 Experimental procedure	76
3.3.3 Experimental results	79
3.4 Summary	91
Chapter 4: Dynamics of a Free-Clamped Cylinder in Confined Axial Flow	94
4.1 Introduction	94
4.2 Theoretical Investigation	97
4.2.1 Theoretical model	97
4.2.2 Theoretical results	106
4.3 Experimental Investigation	109
4.3.1 Experimental apparatus	109
4.3.2 Experimental procedure	111
4.3.3 Experimental results	111
4.4 Summary	121
Chapter 5: Dynamics of a Cantilevered Pipe Subjected Simultaneously to Counter-current Internal and Confined External Axial Flows	123
5.1 Introduction	123
5.2 Theoretical Investigation	126
5.2.1 Païdoussis, Luu & Prabhakar (2008) model	126
5.2.2 Theoretical results	137
5.3 Experimental Investigation	140
5.3.1 Experimental apparatus	140

5.3.2 Experimental procedure	142
5.3.3 Experimental results.....	143
5.4 Summary	160
Chapter 6: Conclusion	162
6.1 Concluding Remarks.....	162
6.1.1 Dynamics of a cantilevered pipe conveying fluid fitted with a stabilizing end-piece	162
6.1.2 Dynamics of a cantilevered pipe aspirating fluid	163
6.1.3 Dynamics of a free-clamped cylinder in confined axial flow.....	164
6.1.4 Dynamics of a cantilevered pipe subjected simultaneously to counter-current internal and confined external axial flows	165
6.2 Future Work	167
Bibliography	169
Appendix A: Pipe Casting Process	176
Appendix B: Determination of Flexural Rigidity and Damping	178
Appendix C: Optron Displacement Calibration	183
Appendix D: Experimental Measurement of Flow Velocity	185
Appendix E: Experimental Measurement of Frequency.....	190
Appendix F: Technical Drawings	192
Appendix G: Shear Boundary Condition for a Free-Clamped Cylinder in Confined Axial Flow	200
Appendix H: Improvements to the Model for a Free-Clamped Cylinder in Confined Axial Flow	203

CHAPTER 1

Introduction

1.1 Motivation and General Remarks

Systems involving flow-induced vibrations will never cease to exist, whether they arise in nature or in engineering systems. Consequently, knowledge of fluid-structure interactions is an important tool that every engineer should possess in his toolbox. Although some flow-induced vibrations are desirable, such as for making music using woodwind instruments, many are undesirable and even dangerous, especially in engineering systems where large-amplitude vibrations may be detrimental not only to equipment, but also to human life.

It has become steadily recognized over the past years that the pipe conveying fluid is a model dynamical problem, or a paradigm in dynamics [see Païdoussis & Li (1993) and Païdoussis (1998, 2004)]. Païdoussis & Li (1993) noted that the pipe conveying fluid is a physically simple system that is governed by relatively simple equations. Furthermore, experiments are fairly easy to perform, and experimental results can be easily compared with theoretical ones. In addition, the system is more general than other paradigms, such as the column subjected to a compressive load or the rotating shaft. Most importantly, however, the pipe conveying fluid is the simplest fluid-structure interactions problem from which more complex variants may be derived and studied, as we shall soon discover in this and upcoming chapters.

This thesis deals with slender flexible cylindrical structures subjected to either internal and/or external axial flow, which are systems that are readily found in engineering. Some examples of engineering applications include Coriolis mass-flow

meters, hydroelastic ichthyoid propulsion systems, deep-water risers, towed flexible barges, towed seismic arrays, nuclear reactor internals, and other power-generating systems [see Païdoussis (1998, 2004)]. In general, however, research in this field has usually been curiosity-driven [see Païdoussis (1993)] with engineering applications arising some years after the dynamics of a particular system have been understood and established. It suffices to say that the study of fluid-structure interactions is not a dying engineering field, given the multitude of research papers that are continually being added to the literature. In what follows, a selective rather than exhaustive literature review of cantilevered cylindrical structures subjected to either internal and/or external axial flow is presented. The interested reader can find a much fuller review in Païdoussis (1998, 2004).

1.2 Literature Review

1.2.1 *The cantilevered pipe conveying fluid*

The dynamics of pipes conveying fluid was first studied almost 70 years ago by Bourrières (1939), who derived the correct nonlinear equations of motion by modelling the pipe conveying fluid by two infinitely flexible and inextensible strings located one within the other. He also obtained remarkably accurate information regarding the stability of the cantilevered system, but he was unable to predict the critical flow velocity at the onset of oscillatory instability because of the unavailability of computers. Ashley & Haviland (1950) revisited the problem to elucidate the vibration of the Trans-Arabian pipe line, yet they arrived at an incorrect equation of motion. The correct linear equations of motion were then derived by Feodos'ev (1951), Housner (1952), and Niordson (1953) using three different approaches, but their focus was mainly on the stability characteristics of the simply-supported system rather than the cantilevered one.

Benjamin (1961a,b) was the first to tackle the problem of articulated cantilevered pipes conveying fluid from both a theoretical and experimental perspective. He modelled the articulated cantilevered system, which possesses n degrees of freedom, as a series of n rigid pipes interconnected by n flexible joints, whereby the upstream end is clamped and the downstream end is free, and he also considered the continuous cantilevered system to

be a limiting case of the articulated one when n tends to infinity. He adapted the Lagrangian method to deal with systems having infinite energy, that is, where momentum constantly flows in and out, and arrived at the correct equation for the energy gained by the chain of pipes from the fluid over a period of oscillation, T ,

$$\Delta W = \int_0^T -MU(\dot{\mathbf{R}}^2 + U\boldsymbol{\tau} \cdot \dot{\mathbf{R}})dt, \quad (1.1)$$

where \mathbf{R} denotes the position vector at the free end of the last pipe, and $\boldsymbol{\tau}$ denotes the unit vector in the tangential direction at the free end of the last pipe. He then used Hamilton's principle to derive the linear equation of motion, valid for infinitesimal motions, for a continuously flexible pipe conveying fluid,

$$EI \frac{\partial^4 w}{\partial x^4} + MU^2 \frac{\partial^2 w}{\partial x^2} + 2MU \frac{\partial^2 w}{\partial x \partial t} + (M + m) \frac{\partial^2 w}{\partial t^2} = 0. \quad (1.2)$$

He was also the first to observe, at sufficiently high flow velocities, the oscillatory instability in articulated pipes conveying fluid – the discrete equivalent of the continuously flexible pipe. Furthermore, if the fluid was water, he sometimes observed buckling when the pipes were suspended vertically, that is, when the effect of gravity was significant. However, if the fluid was air, static instabilities were never observed.

Gregory & Païdoussis (1966a,b) further studied, both theoretically and experimentally, the dynamics of a continuous cantilevered pipe conveying fluid confined to move in a horizontal plane. They derived the linear equation of motion using the Newtonian approach, also arriving at Eqn. (1.2), and constructed stability curves for the dimensionless critical frequency of oscillation, ω_{cr} , and dimensionless critical flow velocity, u_{cr} , as a function of the mass parameter, β , by solving the equation of motion using exact and approximate methods. It is noteworthy to mention that the more general case where the free end of the pipe is fitted with a convergent nozzle was also considered. Experiments by Gregory & Païdoussis (1966b) confirmed the oscillatory instability that was observed by Benjamin (1961b). They also found that damping can be unpredictably destabilizing in some circumstances.

Later, Païdoussis (1970a) studied, both theoretically and experimentally, the dynamics of a vertically hung, continuous cantilevered pipe conveying fluid, and concluded that buckling does not occur for this type of system after all, regardless of the fluid being conveyed. This paradox was later clarified in a paper by Païdoussis & Deksnis (1970). On the other hand, he found that standing cantilevers, whereby the free end is located above the clamped one, of long or intermediate length buckled under their own weight at zero flow velocity, regained stability (became straightened) with increasing flow, and then developed flutter; while those of short length exhibited the same dynamical behaviour as regular hanging cantilevers. Païdoussis (1970a) derived essentially the same expression as Benjamin (1961a) for the work done by the fluid on the pipe over a period of oscillation, T , namely

$$\Delta W = -MU \int_0^T \left[\left(\frac{\partial w}{\partial t} \right)^2 + U \left(\frac{\partial w}{\partial t} \right) \left(\frac{\partial w}{\partial x} \right) \right] dt. \quad (1.3)$$

Consequently, if both ends of the pipe are supported, then $(\partial w / \partial t) = 0$ at both ends, and $\Delta W = 0$ always; thus, the system is conservative, and oscillatory instabilities are not possible. For cantilevered pipes, however, $\Delta W \neq 0$ generally. Since $w(0, t) = 0$, Eqn. (1.3) may be rewritten as

$$\Delta W = -MU \int_0^T \left[\left(\frac{\partial w}{\partial t} \right)_L^2 + U \left(\frac{\partial w}{\partial t} \right)_L \left(\frac{\partial w}{\partial x} \right)_L \right] dt \neq 0. \quad (1.4)$$

Therefore, if U is positive and sufficiently small, then $\Delta W < 0$, and free motions of the cantilevered pipe are damped since the energy gained by the pipe from the fluid is negative. Alternatively, if U is positive and sufficiently large, and $(\partial w / \partial x)_L$ and $(\partial w / \partial t)_L$ have opposite signs over most of the cycle, then $\Delta W > 0$, and free motions of the cantilevered pipe are amplified since the pipe gains energy from the fluid. This suggests a dragging, lagging motion which has, in fact, been observed by all of the researchers mentioned thus far.

Païdoussis & Issid (1974) later derived a more general linear equation of motion for a pipe conveying fluid in which gravity, dissipation in the material of the pipe,

dissipation to the surrounding fluid, external tensioning, and external pressurization effects were included, and U was no longer assumed to be constant, namely

$$\begin{aligned} & \left(E^* \frac{\partial}{\partial t} + E \right) I \frac{\partial^4 w}{\partial x^4} + [MU^2 - \bar{T} + \bar{p}A(1 - 2\nu\delta)] \frac{\partial^2 w}{\partial x^2} \\ & - \left[(M + m)g - M \frac{dU}{dt} \right] (L - x) \frac{\partial^2 w}{\partial x^2} + 2MU \frac{\partial^2 w}{\partial x \partial t} \\ & + (M + m)g \frac{\partial w}{\partial x} + c \frac{\partial w}{\partial t} + (M + m) \frac{\partial^2 w}{\partial t^2} = 0. \end{aligned} \quad (1.5)$$

In addition, Semler *et al.* (1994) derived the nonlinear equation of motion for a cantilevered, as well as for a simply-supported pipe conveying fluid, using energy and Newtonian methods. These equations were validated and compared to existing equations, and it was concluded that the equations of Semler *et al.* (1994) were not only the most correct, but also the most complete.

Hill & Swanson (1970) extended the work of Gregory & Païdoussis (1966a,b) to include the effect of additional lumped masses on the dynamics of a cantilevered pipe conveying fluid. It is interesting to note that the only difference in the linear equation of motion, given by Eqn. (1.2), is that the mass of the pipe per unit length, m , is replaced with $m(x)$, which is given by

$$m(x) = m + \sum_{k=1}^N m_k \delta(x - x_k), \quad (1.6)$$

where m_k are the N lumped masses located at a distance x_k from the clamped end, and $\delta(x - x_k)$ is a Dirac delta function. Hill & Swanson (1970) solved the equation of motion using the Galerkin method for a number of different cases, and then constructed stability curves for the dimensionless critical flow velocity, u_{cr} , and dimensionless frequency of oscillation, ω_{cr} , as a function of the mass parameter, β . In most cases, the effect of additional lumped masses was destabilizing when compared to the plain system, and was dependent both on the location of the lumped masses, as well as on the parameters of the system. Further studies on this topic have been carried out by Jendrzejczyk & Chen (1985), and Chen & Jendrzejczyk (1985), to name only two, from an experimental perspective.

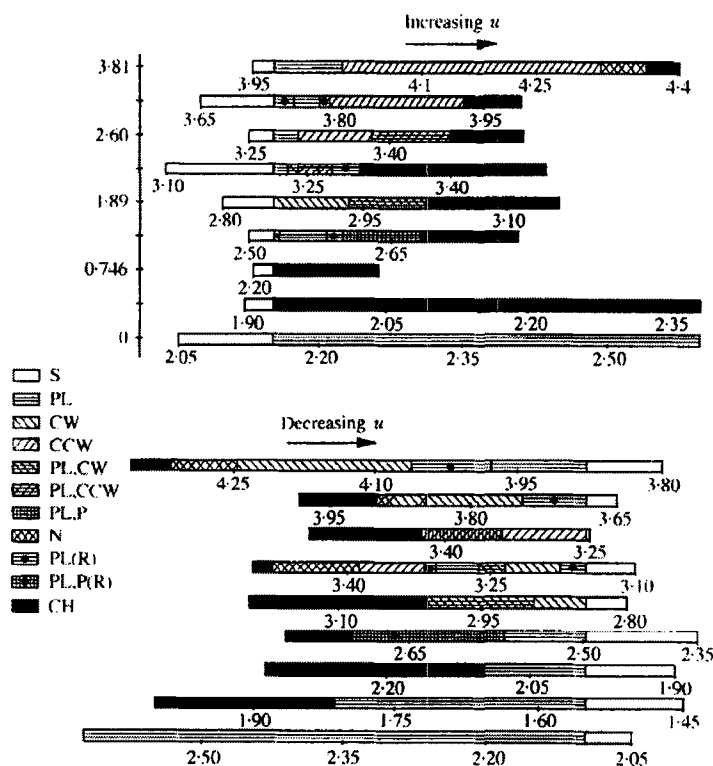


Figure 1.1. Transition from equilibrium to chaos; a plot of u versus Γ_e : S: stationary pipe; PL: planar oscillation; CW: clockwise rotating motion; CCW: counter-clockwise rotating motion; PL,CW: clockwise rotating planar oscillation; PL,CCW: counter-clockwise rotating planar oscillation; PL(R): planar oscillation rotating through a finite angle; PL,P: coupled planar and pendular oscillation; PL,P(R): coupled planar and pendular oscillation rotating through a finite angle; N: nutation; CH: chaos [Copeland & Moon (1992)].

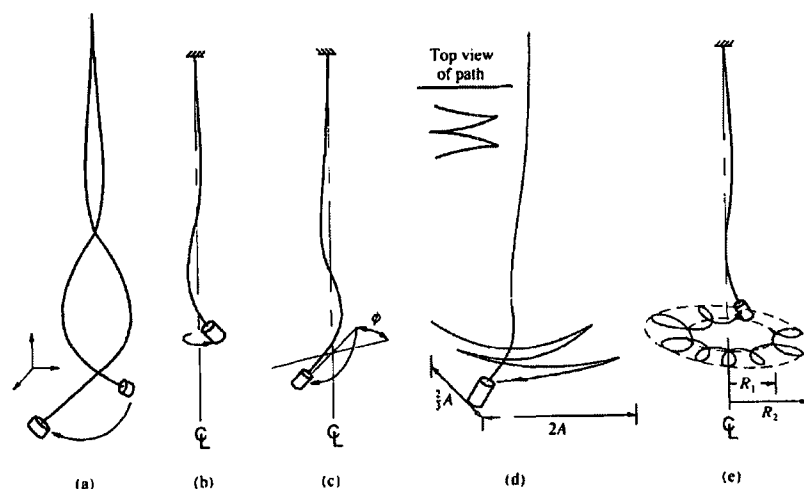


Figure 1.2. Sketches of the various periodic motions: (a) PL; (b) CCW; (c) PL(R); (d) PL,P; (e) N [Copeland & Moon (1992)].

Copeland & Moon (1992) studied the three-dimensional nonlinear dynamics of a cantilevered pipe conveying fluid with an end-mass attached at the free end, and demonstrated that this system possessed an extremely rich dynamical behaviour during its transition from equilibrium to chaos, as shown in Figs. 1.1 and 1.2. Païdoussis & Semler (1998) studied the same system, both theoretically and experimentally, yet they considered only planar motion, and they modelled the pipe as a beam with flexural rigidity. In an earlier study, Semler & Païdoussis (1995) showed that the route to chaos for the two-dimensional system with a mass defect, that is, with a negative end-mass rather than a positive one, is via type I intermittency. More recently, Wadham-Gagnon *et al.* (2007) derived the complete three-dimensional nonlinear equations of motion for a cantilevered pipe conveying fluid with an end-mass attached at the free end, and Modarres-Sadeghi *et al.* (2007) studied the dynamics of the system, and compared the results to the experiments conducted by Païdoussis & Semler (1998).

1.2.2 *The cantilevered pipe aspirating fluid*

The first experiments involving a cantilevered pipe aspirating fluid, whereby the fluid is aspirated from the free end to the clamped one, were carried out in the mid-1960s by Professor Michael P. Païdoussis of McGill University while he was working at the Chalk River Nuclear Laboratories in Chalk River, Ontario. Unfortunately, flutter was never observed, and the experiments were eventually abandoned because of a large transmural pressure that caused a shell-type buckling collapse near the clamped end, even after reinforcement of the pipe at that location [see Païdoussis (1998)]. In 1986, Païdoussis built a new experimental set-up at McGill University to revisit the problem, but a rather unfortunate event involving the bursting of a rubber hose in his set-up brought about the abandonment of this experiment in disgust [see Païdoussis (1998)].

A year earlier, Païdoussis & Luu (1985) had studied the dynamics of a cantilevered pipe aspirating fluid, its main application being the deep ocean mining of minerals, such as manganese nodules, on the sea floor. The effects of marine currents and other perturbations were neglected in an effort to isolate the effects of the internal flow on the stability of the system. In their analysis, $+U$ was essentially replaced with $-U$ in the

equation of motion for the cantilevered pipe conveying fluid, which also included the effects of gravity, buoyancy, added mass, viscous damping, and an end-mass. Consequently, it was concluded that the cantilevered pipe aspirating fluid loses stability by flutter at very low flow velocities; in the absence of damping, the pipe is inherently unstable, thereby losing stability at practically zero flow velocity. Nevertheless, these conclusions were not convincing, given that experiments up to that point had suggested that the cantilevered pipe was actually stable at low flow velocities.

Païdoussis (1998, 1999) re-evaluated the problem of a cantilevered pipe aspirating fluid to illustrate that the system is actually stable at infinitesimally small flow velocities. The latter was attributed to the fact that the flow entering the free end of the pipe is not a jet, as is the case for a pipe discharging fluid, but rather a sink-like flow. Thus, the gauge pressure at the free end and throughout the pipe is not zero; rather, a depressurization arises, equal to

$$\bar{p} = -\rho U^2 \equiv -MU^2/A. \quad (1.7)$$

Hence, a term equal to $\bar{p}A(\partial^2 w/\partial x^2)$ was added to the equation of motion, given by Eqn. (1.2), as follows:

$$EI \frac{\partial^4 w}{\partial x^4} + (\bar{p}A + MU^2) \frac{\partial^2 w}{\partial x^2} + 2MU \frac{\partial^2 w}{\partial x \partial t} + (M + m) \frac{\partial^2 w}{\partial t^2} = 0. \quad (1.8)$$

Therefore, for the aspirating case, $U < 0$, and Eqn. (1.7) was used for \bar{p} , which led to the conclusion that the system cannot flutter because of the absence of the centrifugal force. New experimental evidence involving two flexible elastomer pipes fitted with plastic elbows at their free ends, and interconnected by a pump at their clamped ends also suggested that the system remains stable because a centrifugal force did not arise in the pipe aspirating flow.

Later, Kuiper & Metrikine (2005) argued that the conclusion reached by Païdoussis (1998, 1999) was incorrect since the depressurization at the free end of the pipe influences the dynamics of the system only slightly. Furthermore, they reasoned that, even in the absence of the centrifugal force, the Coriolis force generates negative damping in the case of an aspirating pipe, and thus the system may lose stability after all.

They also suggested that the depressurization at the inlet should be equal to a value between $-\rho U^2$ and $-\frac{1}{2}\rho U^2$, the latter found using Bernoulli's equation; as a result, the centrifugal force may not cancel out. Moreover, Kuiper & Metrikine (2005) attributed the contradiction between existing theory and experiments to the drag caused by the non-negligible viscosity of the surrounding fluid [see also Kuiper *et al.* (2007a)].

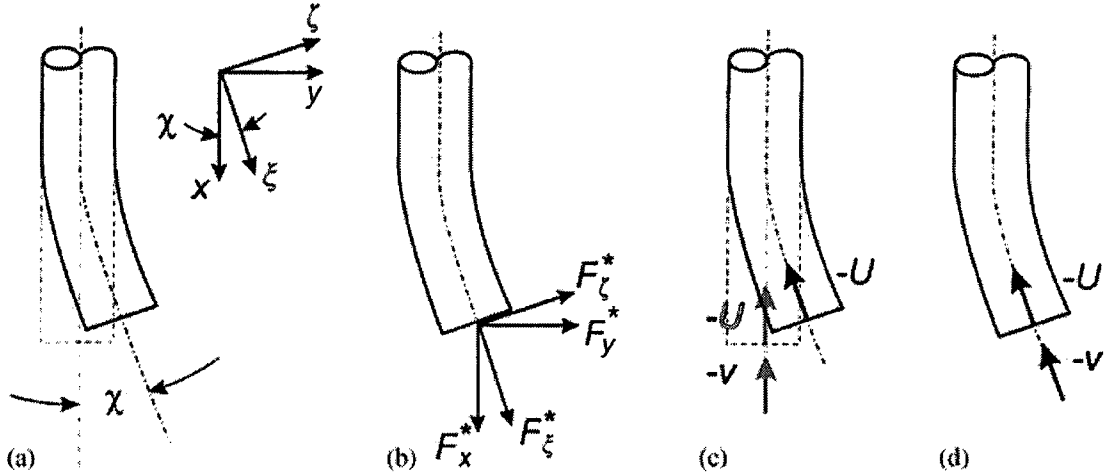


Figure 1.3. (a) The free end of the pipe, definition of the coordinate systems used, and the angle χ ; (b) definition of the forces exerted by the fluid on the pipe; (c) the inlet flow assumed in the basic model, with v always in the vertical direction; (d) the inlet flow assumed in the variant model, with v always tangential to the free end of the pipe [Païdoussis *et al.* (2005)].

This led to a reappraisal of the problem by Païdoussis *et al.* (2005), whereby two new theoretical models, as illustrated in Fig. 1.3, were proposed [see also Païdoussis (2005, 2008a)]. The basic model assumed that a small mean flow velocity facing the inlet, v , remained tangential to the undeflected pipe, i.e. it remained in the vertical direction, during the motion of the system. The linear equation of motion was determined using Newtonian methods, as well as Hamilton's principle, giving

$$\begin{aligned} & \left(E^* \frac{\partial}{\partial t} + E \right) I \frac{\partial^4 w}{\partial x^4} + \alpha M U^2 \frac{\partial^2 w}{\partial x^2} - 2 M U \frac{\partial^2 w}{\partial x \partial t} + c \frac{\partial w}{\partial t} \\ & + (M + m + M_a) \frac{\partial^2 w}{\partial t^2} + M U \left(\frac{\partial w}{\partial t} - \alpha U \frac{\partial w}{\partial x} \right) \delta(x - L) = 0, \end{aligned} \quad (1.9)$$

where $\alpha = v/U$, and $\delta(x - L)$ is a Dirac delta function. A two-mode Galerkin analysis of this model demonstrated that the system is unconditionally stable, regardless of the value of α . On the other hand, the variant model assumed that v remained tangential to the free end of the pipe; it also considered $\bar{\gamma}$, a dimensionless parameter that is related to the tensioning induced on the pipe by the depressurization at the inlet. The linear equation of motion was determined using both Newtonian methods and Hamilton's principle, giving

$$\begin{aligned} \left(E^* \frac{\partial}{\partial t} + E \right) I \frac{\partial^4 w}{\partial x^4} + [1 - (1 - \alpha)(1 + \bar{\gamma})] MU^2 \frac{\partial^2 w}{\partial x^2} - 2MU \frac{\partial^2 w}{\partial x \partial t} \\ + c \frac{\partial w}{\partial t} + (M + m + M_a) \frac{\partial^2 w}{\partial t^2} + MU \frac{\partial w}{\partial t} \delta(x - L) = 0, \end{aligned} \quad (1.10)$$

where $\alpha = v/U$, $\bar{\gamma} = \bar{T}/[(1 - \alpha)MU^2]$, and $\delta(x - L)$ is a Dirac delta function. A two-mode Galerkin analysis of this model demonstrated that the stability of the system depends on the value of the factor $[1 - (1 - \alpha)(1 + \bar{\gamma})]$, and whether or not dissipation is included. Consequently, if α and $\bar{\gamma}$ are chosen such that $[1 - (1 - \alpha)(1 + \bar{\gamma})] = 0$, then the system is unconditionally stable. However, if α and $\bar{\gamma}$ are chosen such that $[1 - (1 - \alpha)(1 + \bar{\gamma})] > 0$, and dissipation is excluded, then the system loses stability by flutter in its first mode. Also, if α and $\bar{\gamma}$ are chosen such that $[1 - (1 - \alpha)(1 + \bar{\gamma})] < 0$, and dissipation is excluded, then the system loses stability by flutter in its second mode. When dissipation is included, the system is stable for the range of flow velocities that are of practical interest. It was concluded that the flow field in the neighbourhood of the intake was the key to determining whether the centrifugal forces vanish either partially or totally; thus, a computational fluid dynamics study was initiated, and is discussed later.

Kuiper *et al.* (2007b), Kuiper & Metrikine (2008), and Kuiper (2008) investigated the dynamics of a cantilevered pipe aspirating fluid even further, to determine whether the instability predicted by theory can be captured in experiments. Their experimental set-up consisted of an approximately five meter long plastic pipe partly submerged in a large six meter diameter tank filled with water. The pipe's motion was measured using two non-contact displacement transducers positioned in two perpendicular locations. Moreover, the motion of the tip of the cantilevered pipe was recorded with an underwater camera. Their experiments showed that a partly submerged cantilevered pipe aspirating fluid does

lose stability at a specific critical flow velocity. Above this critical point, the motion of the pipe is an unpredictable and complicated combination of (i) nearly periodic orbital motions, and (ii) noise-like vibrations of small amplitude. These experimental observations were compared with existing theories, and although the correct frequencies of oscillation were predicted, the critical flow velocities for the onset of flutter, as well as the behaviour of the cantilevered pipe in the unstable region, were not. As a result, it was concluded, once more, that further study regarding the flow field near the inlet of the pipe would need to be carried out in order to improve the theoretical model of the system.

More recently, Giacobbi (2007), Giacobbi *et al.* (2008b), and Païdoussis (2008b) performed an extensive numerical investigation of a cantilevered pipe aspirating fluid using a computational fluid dynamics and finite element analysis model in *ANSYS*. The purpose of this numerical investigation was two-fold. Firstly, the flow field near the inlet of the pipe was investigated to establish estimates for the parameters α , $\bar{\gamma}$, and δ_s in the linear equation of motion for the system, given by

$$\begin{aligned} \left(E^* \frac{\partial}{\partial t} + E \right) I \frac{\partial^4 w}{\partial x^4} + [1 - (1 - \alpha)(1 + \bar{\gamma})] MU^2 \frac{\partial^2 w}{\partial x^2} - 2MU \frac{\partial^2 w}{\partial x \partial t} + c \frac{\partial w}{\partial t} \\ + (M + m + M_a) \frac{\partial^2 w}{\partial t^2} + MU \left[\frac{\partial w}{\partial t} - (1 - \delta_s) \alpha U \frac{\partial w}{\partial x} \right] \delta(x - L) = 0, \end{aligned} \quad (1.11)$$

where $\alpha = v/U$, $\bar{\gamma} = \bar{T}/[(1 - \alpha)MU^2]$, $\delta_s = 0$ or 1 for vertical or tangential entry, respectively, and $\delta(x - L)$ is a Dirac delta function. Secondly, and perhaps most importantly, the possibility of self-excited oscillations was examined. In general, the main conclusion drawn from this study was that flutter does indeed occur at critical flow velocities in the range of those observed experimentally. Another conclusion was that δ_s is very close to unity; thus, the fluid enters the pipe nearly tangentially at the inlet.

1.2.3 The cantilevered cylinder in axial flow

One of the earliest studies on the topic of long flexible cylinders in axial flow was carried out by Hawthorne (1961). He was concerned with the directional stability, or “snaking”, of the Dracone barge, which is a long flexible container with tapered ends that

is towed and designed to carry liquids that are less dense than seawater, including petrol, diesel, kerosene, and freshwater. Most importantly, he demonstrated that buckling is possible for the Dracone barge system.

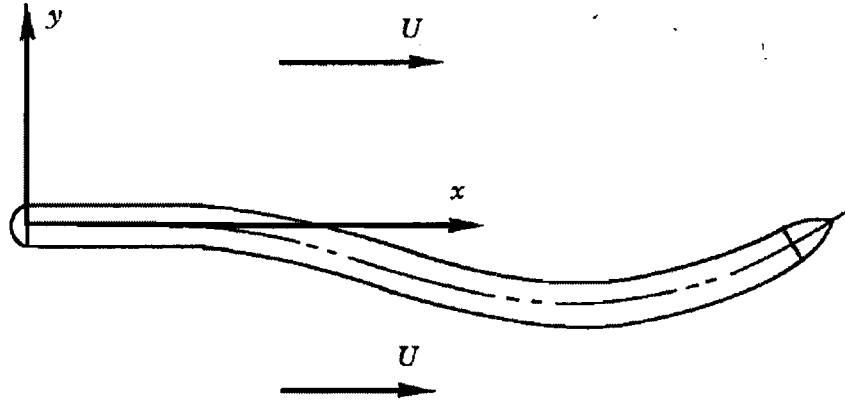


Figure 1.4. A cantilevered cylinder with a well-streamlined free end in axial flow [Païdoussis (1966a)].

Following Hawthorne's (1961) formulation for the Dracone barge, Païdoussis (1966a,b) studied, both theoretically and experimentally, the dynamics of a slender flexible cylindrical structure in axial flow, where the fluid velocity is directed parallel to the x -axis of the system. The reader is referred to Fig. 1.4 for a diagram of the cantilevered cylinder in axial flow. Païdoussis (1966a) derived the linear equation of motion for the system using Newtonian methods. Note that gravity was neglected since the motion of the cylinder was confined to a horizontal plane, and internal dissipation was not accounted for either. Therefore, for small, free, lateral motions of the cylinder, Païdoussis (1966a) obtained the following equation:

$$EI \frac{\partial^4 w}{\partial x^4} + \rho_f A \left(\frac{\partial}{\partial t} + U \frac{\partial}{\partial x} \right)^2 w - \frac{\partial}{\partial x} \left\{ \frac{1}{2} \rho_f D U^2 C_T \left[\left(1 - \frac{1}{2} \delta \right) L - x \right] \frac{\partial w}{\partial x} \right\} - \left[\delta \bar{T} + \frac{1}{2} \rho_f D^2 U^2 (1 - \delta) C_b \right] \frac{\partial^2 w}{\partial x^2} + \frac{1}{2} \rho_f D U C_N \left(\frac{\partial w}{\partial t} + U \frac{\partial w}{\partial x} \right) + m \frac{\partial^2 w}{\partial t^2} = 0, \quad (1.12)$$

written in a slightly different manner here, where $\delta = 0$ if the downstream end is not supported, and $\delta = 1$ if it is. If the two ends of the cylinder are supported, then the standard boundary conditions apply. However, if the cylinder is cantilevered, then the following boundary conditions apply at $x = L$:

$$EI \frac{\partial^2 w}{\partial x^2} = 0, \quad EI \frac{\partial^3 w}{\partial x^3} + f \rho_f A U \left(\frac{\partial w}{\partial t} + U \frac{\partial w}{\partial x} \right) - (m + f \rho_f A) x_e \frac{\partial^2 w}{\partial t^2} = 0, \quad (1.13)$$

where f is a shape parameter first introduced by Hawthorne (1961) that is related to the tapering of the free end of the cylinder, and is equal to unity for a perfectly streamlined end. Moreover,

$$x_e = \frac{1}{A} \int_L^{L+\ell} A(x) dx, \quad (1.14)$$

where ℓ is the length of the tapered end. For a cantilevered cylinder with a sufficiently streamlined end, Païdoussis (1966a) found that the system initially becomes unstable in its first mode by divergence, regains stability, and then becomes unstable in its second and third modes by flutter. He also reasoned that f plays a key role in predicting the stability of the cantilevered system. If the free end is sufficiently blunt, that is, for small enough f , then the cantilevered system is stabilized, and if $f = 0$, no buckling occurs at all. The effect of other system parameters on the stability of the system was also investigated, but is not discussed here for brevity. Moreover, in his experiments, Païdoussis (1966b) observed first-mode divergence, followed by second-mode flutter, and then third-mode flutter, as expected and predicted by theory.

Unfortunately, the equation of motion in Païdoussis (1966a) – Eqn. (1.12) here – is incorrect because, in the derivation, $F_L(\partial w / \partial x)$ was omitted in the y -direction force balance equation. This error was not detected from the beginning, and regrettably found its way into other researchers' work, including Pao (1970), and Chen & Wambsganss (1972), to name but two. The correct, and also more general, linear equation of motion, which includes internal dissipation, gravity, pressurization, and confinement effects, was derived by Païdoussis (1973) [see also Païdoussis (1974, 2004)], and is given by

$$\begin{aligned} & \left(E^* \frac{\partial}{\partial t} + E \right) I \frac{\partial^4 w}{\partial x^4} + \rho_f A \left(\frac{\partial}{\partial t} + U \frac{\partial}{\partial x} \right)^2 w - \{ \delta [\bar{T} + (1 - 2\nu)(\bar{p}A)] \\ & + [\tfrac{1}{2} \rho_f D U^2 C_T + (m - \rho_f A)g] [(1 - \tfrac{1}{2} \delta)L - x] + \tfrac{1}{2} \rho_f D^2 U^2 (1 - \delta) C_b \} \frac{\partial^2 w}{\partial x^2} \\ & + \tfrac{1}{2} \rho_f D U C_N \left(\frac{\partial w}{\partial t} + U \frac{\partial w}{\partial x} \right) + \tfrac{1}{2} \rho_f D C_D \frac{\partial w}{\partial t} + (m - \rho_f A)g \frac{\partial w}{\partial x} + m \frac{\partial^2 w}{\partial t^2} = 0, \end{aligned} \quad (1.15)$$

for a cylindrical structure in unconfined axial flow; for laterally confined flow the equation of motion is given by

$$\begin{aligned}
 & \left(E^* \frac{\partial}{\partial t} + E \right) I \frac{\partial^4 w}{\partial x^4} + \chi \rho_f A \left(\frac{\partial}{\partial t} + U \frac{\partial}{\partial x} \right)^2 w - \left\{ \delta [\bar{T} + (1 - 2\nu)(\bar{p}A)] \right. \\
 & \quad + \left[\frac{1}{2} \rho_f D U^2 C_f \left(1 + \frac{D}{D_h} \right) + (m - \rho_f A) g \right] \left[(1 - \frac{1}{2} \delta) L - x \right] \\
 & \quad + \frac{1}{2} \rho_f D^2 U^2 (1 - \delta) C_b \left. \right\} \frac{\partial^2 w}{\partial x^2} + \frac{1}{2} \rho_f D U C_f \left(\frac{\partial w}{\partial t} + U \frac{\partial w}{\partial x} \right) + \frac{1}{2} \rho_f D C_D \frac{\partial w}{\partial t} \\
 & \quad + \left[(m - \rho_f A) g + \frac{1}{2} \rho_f D U^2 C_f \left(\frac{D}{D_h} \right) \right] \frac{\partial w}{\partial x} + m \frac{\partial^2 w}{\partial t^2} = 0.
 \end{aligned} \tag{1.16}$$

Therefore, when $\chi = 1$, $D/D_h = 0$, and $C_N = C_T \equiv C_f$, then Eqn. (1.16) reduces to Eqn. (1.15), as expected. It is worth mentioning that Païdoussis (1973) reported that the correction of the frictional terms in the equation of motion did not drastically alter the dynamical behaviour of the cantilevered system, although its effect on the system with both ends supported was more pronounced. As before, at small flow velocities, free motions of the cylinder are damped, and at sufficiently high flow velocities, the cantilevered cylinder undergoes first-mode buckling, followed by second-mode and third-mode flutter at even higher flow velocities.

A fascinating comparison between cylinders subjected to external axial flow and pipes subjected to internal axial flow was made by Païdoussis (1987). If internal dissipation, gravity, tensioning, and pressurization effects are neglected, Eqn. (1.15) becomes the following:

$$EI \frac{\partial^4 w}{\partial x^4} + MU^2 \frac{\partial^2 w}{\partial x^2} + 2MU \frac{\partial^2 w}{\partial x \partial t} + F_v + (M + m) \frac{\partial^2 w}{\partial t^2} = 0, \tag{1.17}$$

where $M = \rho_f A$ is the virtual, or added, or hydrodynamic, mass of the fluid per unit length, and F_v are the viscous forces due to surface traction. Note the similarities between Eqn. (1.2) for a pipe conveying fluid and Eqn. (1.17) for a cylinder in axial flow. Païdoussis (1987) points out that the viscous forces make the system a nonconservative one, even if the ends of the cylinder are supported, and do not cancel the pressure loss forces, as is the case for a pipe conveying fluid. However, the viscous forces do not drastically alter the

dynamical behaviour of the system when both ends are supported; the system initially loses stability by buckling, and then at higher flow velocities, the system loses stability by coupled-mode flutter. This post-divergence behaviour, which does not occur experimentally for a pipe conveying fluid but does for a cylinder in axial flow, is obviously related to the viscous forces. On the other hand, the cantilevered cylinder in external axial flow behaves rather differently *vis-à-vis* that with internal flow because of the real flow effects about the free end of the cylinder. In this case, if the free end is sufficiently streamlined, the cylinder initially loses stability by divergence, and then at higher flow velocities, the system develops single-mode flutter. However, for a cantilevered pipe conveying fluid, the system loses stability only by single-mode flutter in experiments.

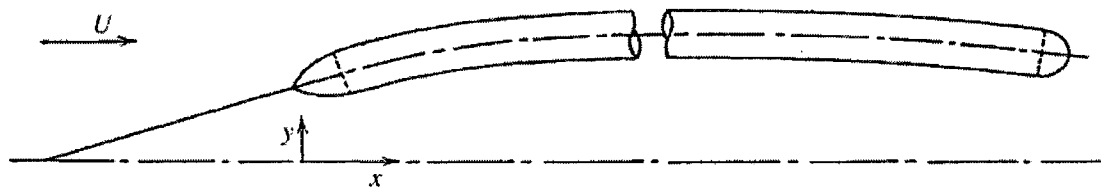


Figure 1.5. A towed cylinder in axial flow with nose and tail sections
[Païdoussis (1968)].

To date, nonlinear studies on cylindrical structures subjected to external axial flow have been rather limited. However, a great deal of work was done by Lopes *et al.* (1999a,b) to set the stage for a more rigorous look at the nonlinear dynamics of the system. Possibly the first most complete nonlinear study for cantilevered cylinders was presented in a three-part paper by Païdoussis *et al.* (2002), Lopes *et al.* (2002), and Semler *et al.* (2002), where the physical dynamics of the system were discussed, including experimental observations and the mechanisms of instability, the nonlinear equations of motion were derived, and finally, the theoretical results, both linear and nonlinear, were presented and compared with experimental ones.

A lot of work has been done on the dynamics of towed flexible cylinders in axial flow beginning with Hawthorne's (1961) work on the Dracone barge. Some years later, the original work by Païdoussis (1966a,b) on the dynamics of slender flexible cylinders in axial flow was extended to the next system under consideration, namely that of a cylinder

totally submerged in fluid, and towed at a steady speed U , by Païdoussis (1968, 1970b). The system is illustrated in Fig. 1.5. The linear equation of motion for the system, as derived by Païdoussis (1970b), is

$$EI \frac{\partial^4 w}{\partial x^4} + \rho_f A \left(\frac{\partial}{\partial t} + U \frac{\partial}{\partial x} \right)^2 w + \frac{1}{2} \rho_f DUC_N \left(\frac{\partial w}{\partial t} + U \frac{\partial w}{\partial x} \right) - \left[\frac{1}{2} \rho_f D^2 U^2 C_2 + \frac{1}{2} \rho_f DU^2 C_T (L - x) \right] \frac{\partial^2 w}{\partial x^2} + m \frac{\partial^2 w}{\partial t^2} = 0, \quad (1.18)$$

and the boundary conditions are

$$\begin{aligned} & \left[EI \frac{\partial^3 w}{\partial x^3} + f_1 \rho_f AU \left(\frac{\partial w}{\partial t} + U \frac{\partial w}{\partial x} \right) + \frac{1}{2} \rho_f D^2 U^2 \left(C_T \frac{L}{D} + C_1 + C_2 \right) \frac{w}{s} + (m + f_1 \rho_f A) x_1 \frac{\partial^2 w}{\partial t^2} \right]_{x=0} = 0, \\ & \left[-EI \frac{\partial^3 w}{\partial x^3} - f_2 \rho_f AU \left(\frac{\partial w}{\partial t} + U \frac{\partial w}{\partial x} \right) + (m + f_2 \rho_f A) x_2 \frac{\partial^2 w}{\partial t^2} \right]_{x=L} = 0, \\ & \left(EI \frac{\partial^2 w}{\partial x^2} \right)_{x=0} = \left(EI \frac{\partial^2 w}{\partial x^2} \right)_{x=L} = 0, \end{aligned} \quad (1.19)$$

where f_1 and f_2 are the shape parameters for the nose and tail, respectively, C_1 and C_2 are the coefficients of form drag for the nose and tail, respectively, and s is the length of the tow-rope. Furthermore, x_1 and x_2 in Eqn. (1.19) are given by

$$x_1 = \frac{1}{A} \int_{-\ell_1}^0 A(x) dx, \quad x_2 = \frac{1}{A} \int_L^{L+\ell_2} A(x) dx, \quad (1.20)$$

where ℓ_1 and ℓ_2 are the lengths of the nose and tail, respectively. In general, it was found that the stability of the towed system can be optimized if the nose is well-streamlined, the tail is blunt, and the length of the tow-rope is short. However, if the tail is well-streamlined, and the length of the tow-rope is not too short, then a criss-crossing or yawing motion associated with the zeroth mode of the system develops at low towing speeds. A first-mode oscillatory motion is also predicted at low towing speeds but is not discernible in experiments. It is noteworthy to mention that both the zeroth- and first-mode instabilities are essentially quasi-rigid body motions, whereas higher-mode

instabilities are flexural oscillatory motions. Thus, at higher towing speeds, the system loses stability in its second and third flexural modes. The latter was predicted by theory and confirmed by experiments.

Additional work on towed flexible cylinders has been performed by Pao (1970), Païdoussis & Yu (1976), Triantafyllou & Chryssostomidis (1984, 1985, 1989), and Dowling (1988a,b). Of particular interest is the work of Dowling (1988a), who found that very long and slender towed cylinders do not flutter. Triantafyllou & Chryssostomidis (1985) had also arrived at this conclusion by modelling the system as a string, or in other words, as a beam with negligible bending stiffness, which is pinned at the upstream end and free at the downstream end; yet, past experiments had suggested otherwise. Fortunately, an interesting paper by de Langre *et al.* (2007) concluded that very long and slender flexible cylinders in axial flow are in fact subject to flutter if their free end is well-streamlined; however, this is a coupled-mode flutter, as opposed to the presumed single-mode type that arises via a Hopf bifurcation.

1.2.4 *The cantilevered tubular beam subjected to internal and external flow*

The study of cylindrical tubular beams subjected to internal and external axial flow has a rather limited history. Perhaps the first study on the topic was by Cesari & Curioni (1971), who investigated the buckling instability of the system for various boundary conditions, namely clamped-free, clamped-clamped, pinned-supported, clamped-supported, clamped-pinned, and pinned-pinned. For the case of a clamped-free or cantilevered cylindrical structure, it was determined that buckling does not occur if the external fluid effects are ignored, as was concluded by many in the past. Furthermore, it was found that an increase in the dimensionless external mass parameter has a stabilizing effect on the system, as does an increase in the frictional force parameters. However, a broader and more extensive treatment of the subject was made by Hannoyer & Païdoussis (1978), and will be discussed in more detail shortly. In addition, specific studies involving variants of the plain system were carried out by Païdoussis & Besançon (1981), who investigated the dynamics of clustered cylindrical structures subjected to concurrent internal and external axial flow as a simplified model for a shell-and-tube heat exchanger,

and by Wang & Bloom (1999), who investigated the dynamics of submerged and inclined concentric pipes with different lengths to gain insight concerning the vibration issues of a silo water-mixing unit used in the pulp and paper industry.

Hannoyer & Païdoussis (1978) studied the dynamics of cylindrical tubular beams subjected simultaneously to internal and external axial flow, and derived the linear equation of motion in which gravity, internal dissipation, and external boundary layer growth were accounted for. Therefore, for small, free, lateral motions of the cylindrical structure, it was found that

$$\begin{aligned}
 & \left(E^* \frac{\partial}{\partial t} + E \right) I \frac{\partial^4 w}{\partial x^4} + \rho_i A_i \left(\frac{\partial}{\partial t} + U_i \frac{\partial}{\partial x} \right)^2 w \\
 & + \rho_e A_e \left(\frac{\partial}{\partial t} + U_e^* \frac{\partial}{\partial x} \right) \left(\frac{\partial w}{\partial t} + U_e \frac{\partial w}{\partial x} \right) - (\rho_e A_e - \rho_i A_i - m) g \frac{\partial w}{\partial x} \\
 & - \left\{ (T + A_e p_e - A_i p_i)_L + [(\rho_e A_e - \rho_i A_i - m) g - \frac{1}{2} C_{f\beta} \rho_e D_o U_e^2] (L - x) \right\} \frac{\partial^2 w}{\partial x^2} \\
 & + \frac{1}{2} C_{f\beta} \rho_e D_o U_e \left(\frac{\partial w}{\partial t} + U_e \frac{\partial w}{\partial x} \right) + \frac{1}{2} \mu_e C_D \frac{\partial w}{\partial t} + m \frac{\partial^2 w}{\partial t^2} = 0,
 \end{aligned} \tag{1.21}$$

where U_e^* is a reduced external flow velocity, and the usual boundary conditions for a cantilevered system apply, except for the one related to the shear force at the free end, that is, at $x = L$, which is given by

$$\begin{aligned}
 & [(\rho + f\rho_e) \bar{A}_e + (\rho_i - \rho) A_i] \ell \left(\frac{\partial^2 w}{\partial t^2} \right)_L - f\rho_e (A_e - A_i) U_e^* \left(\frac{\partial w}{\partial t} \right)_L \\
 & + [f\rho_e (A_i U_e^* - \bar{A}_e U_e) + 2\rho_i A_i U_i] \ell \left(\frac{\partial^2 w}{\partial x \partial t} \right)_L - \left(E^* \frac{\partial}{\partial t} + E \right) I \left(\frac{\partial^3 w}{\partial x^3} \right)_L \\
 & - \{ f\rho_e (A_e - A_i) U_e U_e^* + [(\rho_e - \rho) \bar{A}_e + (\rho - \rho_i) A_i] g \ell \} \left(\frac{\partial w}{\partial x} \right)_L = 0,
 \end{aligned} \tag{1.22}$$

where ℓ is the length of the tapered end, and \bar{A}_e is an average area given by

$$\bar{A}_e = \frac{1}{\ell} \int_L^{L+\ell} A_e(x) dx. \tag{1.23}$$

Note that f and \bar{A}_e were both calculated as though the end-piece were conical, and f was also calculated assuming that separation does not occur, so that

$$\bar{A}_e \approx \frac{1}{3} (A_e^{3/2} - A_i^{3/2}) / (A_e^{1/2} - A_i^{1/2}), \quad f \approx 4\ell^2 / [4\ell^2 + (D_o - D_i)^2]. \quad (1.24)$$

The system was investigated both theoretically and experimentally by Hannover & Païdoussis (1978) and agreement between the results was found to be relatively good. For a cylindrical tubular beam supported at both ends, increasing either the internal flow velocity or the external flow velocity, or even both, caused the system to initially lose stability by buckling, followed by a series of flutter and buckling instabilities. On the other hand, for a cantilevered cylindrical tubular beam, the behaviour of the system was more complicated, and depended on the internal and external flow velocities, as well as on the shape of the free end. If the free end was blunt, then the dynamics was dominated by the internal flow, and the system lost stability only by flutter. If the free end was well-streamlined, both buckling and flutter instabilities could arise, depending on the parameters of the system.

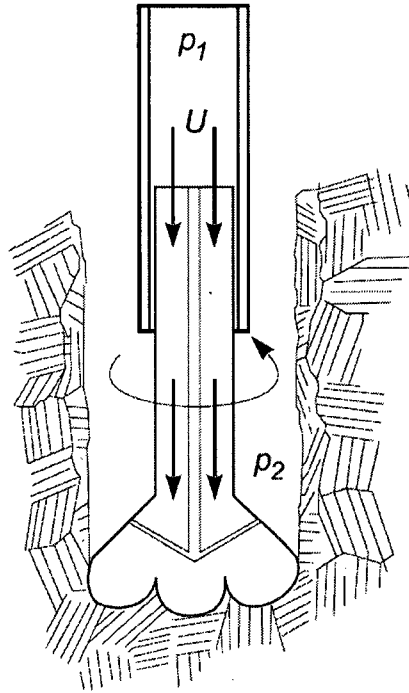


Figure 1.6. Diagram of the fallacious drill-string patent related by Den Hartog
[Den Hartog (1969)].

An interesting application of a cylindrical structure subjected simultaneously to internal and external axial flows that are counter-current and dependent on one another, in contrast to what has been discussed until now, is the patented drill-string that was described by Den Hartog (1969) in a lecture, and is shown in Fig. 1.6. In this system, slurry is pumped down a hollow drill-rod in order to rotate a floating drill-bit as a turbine, and thereby drill into underlying rock. The slurry and debris flow up around the drill-rod in an annular region formed by the drill-rod and an outer jacket, which is in contact with the ground, and the by-products of drilling are then carried away to the surface. The inventor of this patent claimed that the system would not buckle during normal operation, as is the case with traditional drill-strings, since the drill-rod is not subject to any compressive stresses, yet experiments proved otherwise. The latter has been discussed by Païdoussis (1998), who stated that the system buckles just the same, and perhaps even earlier, because of the effect of internal pressurization. This was also realized by Den Hartog (1969), who considered this to be a fallacious patent. Additional studies regarding the drill-string problem have also been made by Grigoriev (1978), Luu (1983), and Zhang & Miska (2005).

Païdoussis *et al.* (2008) also studied the linear dynamics of the idealized hollow drill-rod and floating fluid-powered drill-bit problem discussed above. They derived the linear equation of motion, the final expression being

$$\begin{aligned}
& EI \frac{\partial^4 w}{\partial x^4} + m \frac{\partial^2 w}{\partial t^2} + \rho_i A_i \left(\frac{\partial^2 w}{\partial t^2} + 2U_i \frac{\partial^2 w}{\partial x \partial t} + U_i^2 \frac{\partial^2 w}{\partial x^2} \right) \\
& + \chi \rho_e A_e \left(\frac{\partial^2 w}{\partial t^2} - 2U_e \frac{\partial^2 w}{\partial x \partial t} + U_e^2 \frac{\partial^2 w}{\partial x^2} \right) - \{(T - A_i p_i + A_e p_e)_L \\
& + [(m + \rho_i A_i - \rho_e A_e)g - \tfrac{1}{2} C_f \rho_e D_o U_e^2 (1 + D_o/D_h)](L - x)\} \frac{\partial^2 w}{\partial x^2} \\
& + [(m + \rho_i A_i - \rho_e A_e)g - \tfrac{1}{2} C_f \rho_e D_o U_e^2 (1 + D_o/D_h)] \frac{\partial w}{\partial x} \\
& + \tfrac{1}{2} C_f \rho_e D_o U_e \frac{\partial w}{\partial t} + c \frac{\partial w}{\partial t} = 0,
\end{aligned} \tag{1.25}$$

where $\rho_i = \rho_e \equiv \rho_f$, and

$$p_{iL} = p_{eL} + \rho_f U_e (U_e - U_i), \quad p_{eL} = [\rho_f g + (\tfrac{1}{2} C_f \rho_f D_o U_e^2 / A_e) (D_o/D_h)] L. \tag{1.26}$$

Furthermore, the internal and external fluid velocities are related through continuity,

$$U_i A_i = U_e A_{ch}, \quad (1.27)$$

and the usual boundary conditions for a cantilevered system apply. The main conclusions drawn from this work is that for relatively wide annular flow regions, the dynamics of the system is dominated by the internal flow. Consequently, the system is damped for small flow velocities, but loses stability by flutter at higher flow velocities. On the other hand, for relatively narrow annular flow regions, the dynamics of the system is dominated by the external flow. Thus, the system loses stability by flutter at low flow velocities since the external annular flow tends to destabilize the system. It should be noted that these critical flow velocities are just large enough to overcome the effect of dissipative forces.

Another application of this research is the design of MEMS devices, such as microcantilevers and microchannels, exhibiting very low damping, or high Q factors, for atomic force microscopy (AFM) in viscous liquids and biomolecular detection, as related by Putman *et al.* (1994), Burg & Manalis (2003), Fukuma *et al.* (2005), and Basak *et al.* (2006). Therefore, by understanding the dynamics of a cylindrical structure subjected simultaneously to internal and external axial flows, the damping of these MEMS devices could possibly be reduced drastically by subjecting the microcantilevers and microchannels to flow velocities that are close to, but inferior to the critical velocities for the onset of flutter.

1.3 Outline of the Thesis

The main objective of this thesis is to study the dynamics and stability of slender flexible cantilevered cylindrical structures, or tubular beams, subjected to either internal flow, external flow, or both flows simultaneously, using an experimental approach. The experiments were methodically designed and performed, and the results are compared with existing linear theories. Furthermore, appropriate modifications are made to the equations of motion if more effective models of the systems are sought.

This thesis encompasses six chapters. Chapter 1 provides a selective rather than exhaustive literature review of four distinct, yet closely-related, systems in fluid-structure

interactions: (i) the cantilevered pipe conveying fluid, (ii) the cantilevered pipe aspirating fluid, (iii) the cantilevered cylinder in axial flow, and (iv) the cantilevered tubular beam subjected to internal and external flow. The main objective of the thesis is stated, and an outline is also provided. Chapter 2 deals with the dynamics of a cantilevered pipe conveying fluid that is fitted with a stabilizing end-piece, which is an end-piece that effectively removes the compressive force that is necessary for flutter to develop. Chapter 3 presents the dynamics of a cantilevered pipe aspirating fluid, and attempts to answer a question that has perplexed researchers for over twenty years, that is, *do pipes aspirating fluid lose stability at infinitesimally small flow velocities?* Chapter 4 considers the dynamics of a cantilevered cylinder in axial flow, where the fluid is directed from the free end to the clamped end. Chapter 5 treats the dynamics of the infamous drill-string problem of a cantilevered pipe conveying fluid downwards which then flows upwards around the pipe in a confined annular region. Lastly, Chapter 6 contains some general conclusions and remarks concerning the theoretical and experimental results presented in this thesis, and recommendations for future work are made.

CHAPTER 2

Dynamics of a Cantilevered Pipe Conveying Fluid Fitted with a Stabilizing End-Piece

The work presented in this chapter was presented at the 21st Canadian Congress of Applied Mechanics by Rinaldi & Païdoussis (2007); however, the theoretical and experimental results have been updated, and new ones have also been computed.

2.1 Introduction

It is known, both theoretically and experimentally, that a cantilevered pipe conveying fluid is a nonconservative system that loses stability by flutter via a Hopf bifurcation. The latter can be explained by examining the expression for the work done by the fluid on the pipe over a period of oscillation, T , given by Eqn. (1.4), and repeated here,

$$\Delta W = -MU \int_0^T \left[\left(\frac{\partial w}{\partial t} \right)_L^2 + U \left(\frac{\partial w}{\partial t} \right)_L \left(\frac{\partial w}{\partial x} \right)_L \right] dt \neq 0. \quad (1.4)$$

For values of U that are positive and sufficiently small, it is clear that ΔW is negative. Therefore, the cantilevered pipe remains stable because free motions of the system are damped. However, for values of U that are positive and sufficiently large, it is clear that ΔW can be positive if the slope and velocity of the free end of the pipe have opposite signs over most of the cycle of oscillation. This dragging, lagging motion is actually observed during experiments once the critical flow velocity for flutter has been reached.

Thus, the cantilevered pipe flutters because free motions are amplified. The reader is referred to Païdoussis (1998) for an in-depth treatment of the subject, as well as for additional explanations.

A typical Argand diagram for a cantilevered pipe conveying fluid is shown in Fig. 2.1. Note that the vertical axis is the imaginary component of the dimensionless complex frequency, $\text{Im}(\omega)$, which is related to the damping of the system, while the horizontal axis is the real component of the dimensionless complex frequency, $\text{Re}(\omega)$, which represents the frequency of oscillation of the system. Furthermore, a positive value of $\text{Im}(\omega)$ gives rise to damped oscillations, while a negative value of $\text{Im}(\omega)$ gives rise to amplified oscillations. Only the four lowest modes of the cantilevered system as a function of the dimensionless flow velocity, u , are plotted. At this point, it is worth mentioning that the most general form of the linear equation of motion for a pipe conveying fluid, given by Eqn. (1.5), and repeated here,

$$\begin{aligned} & \left(E^* \frac{\partial}{\partial t} + E \right) I \frac{\partial^4 w}{\partial x^4} + [MU^2 - \bar{T} + \bar{p}A(1 - 2\nu\delta)] \frac{\partial^2 w}{\partial x^2} \\ & - \left[(M + m)g - M \frac{dU}{dt} \right] (L - x) \frac{\partial^2 w}{\partial x^2} + 2MU \frac{\partial^2 w}{\partial x \partial t} \\ & + (M + m)g \frac{\partial w}{\partial x} + c \frac{\partial w}{\partial t} + (M + m) \frac{\partial^2 w}{\partial t^2} = 0, \end{aligned} \quad (1.5)$$

may be rendered dimensionless through the use of the following dimensionless parameters:

$$\xi = \frac{x}{L}, \quad \eta = \frac{w}{L}, \quad \tau = \left(\frac{EI}{M + m} \right)^{\frac{1}{2}} \frac{t}{L^2}, \quad (2.1)$$

to yield

$$\begin{aligned} & \bar{\alpha}^* \frac{\partial^5 \eta}{\partial \xi^4 \partial \tau} + \frac{\partial^4 \eta}{\partial \xi^4} + \left[u^2 - \Gamma + \Pi(1 - 2\nu\delta) + \left(\beta^{\frac{1}{2}} \frac{du}{d\tau} - \gamma \right) (1 - \xi) \right] \frac{\partial^2 \eta}{\partial \xi^2} \\ & + 2\beta^{\frac{1}{2}} u \frac{\partial^2 \eta}{\partial \xi \partial \tau} + \gamma \frac{\partial \eta}{\partial \xi} + \sigma \frac{\partial \eta}{\partial \tau} + \frac{\partial^2 \eta}{\partial \tau^2} = 0, \end{aligned} \quad (2.2)$$

where

$$\begin{aligned}
 u &= \left(\frac{M}{EI} \right)^{1/2} UL, \quad \beta = \frac{M}{M+m}, \quad \gamma = \frac{(M+m)gL^3}{EI}, \quad \Gamma = \frac{\bar{T}L^2}{EI}, \quad \Pi = \frac{\bar{p}AL^2}{EI}, \\
 \bar{\alpha}^* &= \left[\frac{I}{E(M+m)} \right]^{1/2} \frac{E^*}{L^2}, \quad \sigma = \frac{cL^2}{[EI(M+m)]^{1/2}}, \quad \omega = \left(\frac{M+m}{EI} \right)^{1/2} \Omega L^2.
 \end{aligned} \tag{2.3}$$

From Fig. 2.1, it can be seen that, for small values of u , the flow induces damping in all four modes. However, at $u = 5.6$, the system becomes unstable by flutter in its second mode via a Hopf bifurcation. Furthermore, at $u \approx 13$, the system becomes unstable by flutter via another Hopf bifurcation in its fourth mode.

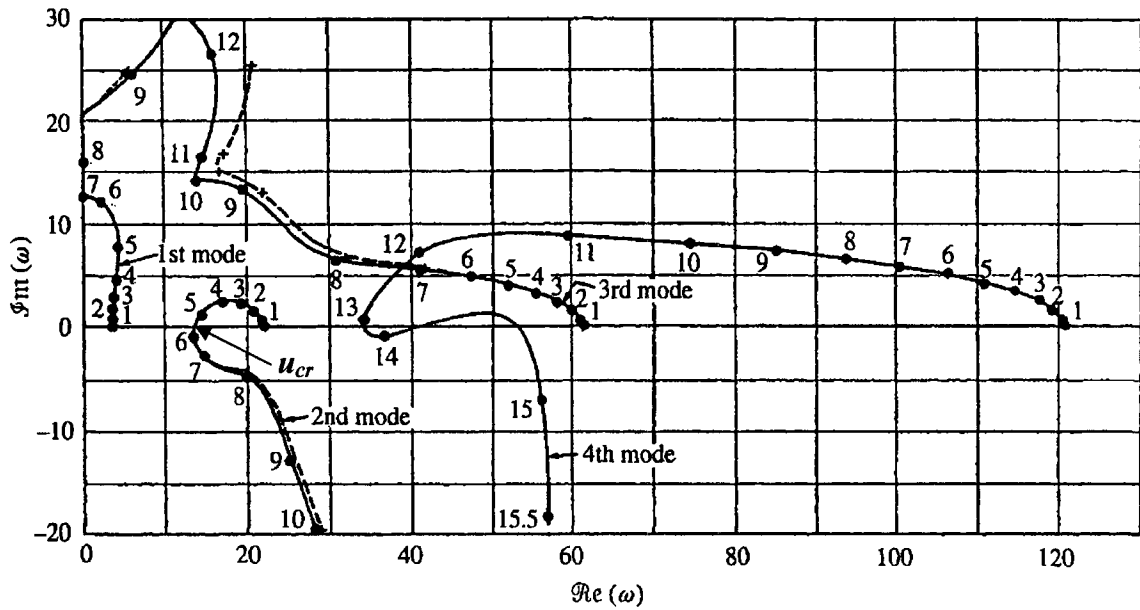


Figure 2.1. Argand diagram as a function of u for a cantilevered pipe with $\beta = 0.20$ and $\dot{u} = \gamma = \Gamma = \Pi = \bar{\alpha}^* = \sigma = 0$: — exact analysis; --- four-mode Galerkin approximation [Gregory & Paidoussis (1966a)].

But what happens when an end-mass is attached to the free end of the pipe? Although a cantilevered pipe with an end-mass flutters also, the dynamical behaviour of this system is more complex than that of the plain system. In general, the system is destabilized (loses stability at lower u), post-Hopf bifurcations are encountered, and three-dimensional chaotic motions are observed. Copeland & Moon (1992), who studied the nonlinear dynamics of pipes with added end-masses, recorded the various motions that arise during the transition from equilibrium to chaos as a function of the

dimensionless flow velocity, u , for various end-masses. In addition to the usual planar and rotational motions, rotating planar, coupled planar and pendular, and nutating oscillations were also recorded. The reader is referred to Chapter 1 for more information.

The present study was motivated by the dynamics of a flexible cantilevered pipe conveying fluid that is fitted with an end-piece or, in other words, a hollowed end-mass, which allows the fluid to either pass straight through, or to be diverted by 90° at the downstream end. In general, the present study is curiosity-driven and academic in nature rather than applications-oriented. The scope of this chapter is to present experimental and theoretical results showing that a cantilevered pipe equipped with an end-piece that diverts flow by 90° at the free end exhibits an entirely different behaviour from that when it is discharging normally.

2.2 Theoretical Investigation

2.2.1 Theoretical model

The general linear equation of motion for a cantilevered pipe conveying fluid without an end-mass at the free end has been derived by Païdoussis & Issid (1974). Furthermore, Semler & Païdoussis (1995) have shown that the presence of the end-mass may be accounted for in the equation of motion by replacing the term $(m + M)$ by the term $[m + M + m_e \delta(x - L)]$, where $\delta(x - L)$ is a Dirac delta function. Therefore, neglecting dissipation to the surrounding fluid, external pressurization effects, and assuming that the internal flow velocity remains constant, the linear equation of motion for the system becomes the following:

$$EI \left[1 + \left(\bar{\alpha} + \frac{\bar{\mu}^*}{\Omega} \right) \frac{\partial}{\partial t} \right] \frac{\partial^4 w}{\partial x^4} + (MU^2 - \bar{T}) \frac{\partial^2 w}{\partial x^2} - \left\{ \int_x^L [M + m + m_e \delta(x - L)] g dx \right\} \frac{\partial^2 w}{\partial x^2} \quad (2.4)$$

$$+ 2MU \frac{\partial^2 w}{\partial x \partial t} + [M + m + m_e \delta(x - L)] g \frac{\partial w}{\partial x} + [M + m + m_e \delta(x - L)] \frac{\partial^2 w}{\partial t^2} = 0,$$

where the internal dissipation is a combination of hysteretic and viscoelastic damping, in which a two-parameter Kelvin-Voigt model is employed for the latter [see Païdoussis &

des Trois Maisons (1971)]. Eqn. (2.4) may be rendered dimensionless through the use of the dimensionless parameters found in Eqn. (2.1) to give

$$\begin{aligned} & \left[1 + \left(\bar{\alpha}^* + \frac{\bar{\mu}^*}{\omega} \right) \frac{\partial}{\partial \tau} \right] \frac{\partial^4 \eta}{\partial \xi^4} + (u^2 - \Gamma) \frac{\partial^2 \eta}{\partial \xi^2} - \gamma \left\{ \int_{\xi}^1 [1 + \Gamma_e \delta(\xi - 1)] d\xi \right\} \frac{\partial^2 \eta}{\partial \xi^2} \\ & + 2\beta^{1/2} u \frac{\partial^2 \eta}{\partial \xi \partial \tau} + \gamma [1 + \Gamma_e \delta(x - L)] \frac{\partial \eta}{\partial \xi} + [1 + \Gamma_e \delta(x - L)] \frac{\partial^2 \eta}{\partial \tau^2} = 0, \end{aligned} \quad (2.5)$$

where u, β, γ, Γ , and ω have been defined in Eqn. (2.3), and

$$\Gamma_e = \frac{m_e}{(m + M)L}, \quad \bar{\alpha}^* = \left(\frac{EI}{M + m} \right)^{1/2} \frac{\bar{\alpha}}{L^2}. \quad (2.6)$$

The system is discretized following the Galerkin procedure and assuming a solution of the form

$$\eta(\xi, \tau) = \sum_{r=1}^N \phi_r(\xi) q_r(\tau), \quad (2.7)$$

where $\phi_r(\xi)$ are the comparison functions, taken here to be the cantilever beam eigenfunctions, and $q_r(\tau)$ are the generalized coordinates, which eventually leads to an expression of the form

$$[M]\ddot{\mathbf{q}} + [C]\dot{\mathbf{q}} + [K]\mathbf{q} = \mathbf{0}, \quad (2.8)$$

where $\mathbf{q} = \{q_1, q_2, \dots, q_N\}^T$. Specifically, Eqn. (2.7) is substituted into Eqn. (2.5) to give

$$\begin{aligned} & \sum_{r=1}^N \left\{ \lambda_r^4 \phi_r q_r + \left(\bar{\alpha}^* + \bar{\mu}^* / \omega \right) \lambda_r^4 \phi_r \dot{q}_r + (u^2 - \Gamma) \phi_r'' q_r - \gamma [(1 - \xi) + \Gamma_e] \phi_r'' q_r \right. \\ & \left. + 2\beta^{1/2} u \phi_r' \dot{q}_r + \gamma [1 + \Gamma_e \delta(x - L)] \phi_r' q_r + [1 + \Gamma_e \delta(x - L)] \phi_r \ddot{q}_r \right\} = 0. \end{aligned} \quad (2.9)$$

Thereafter, Eqn. (2.9) is multiplied by $\phi_s(\xi)$ and integrated over the domain $[0, 1]$, giving

$$\begin{aligned} & \lambda_r^4 \delta_{sr} q_r + \left(\bar{\alpha}^* + \bar{\mu}^* / \omega \right) \lambda_r^4 \delta_{sr} \dot{q}_r + (u^2 - \Gamma) c_{sr} q_r - \gamma (1 + \Gamma_e) c_{sr} q_r + \gamma d_{sr} q_r \\ & + 2\beta^{1/2} u b_{sr} \dot{q}_r + \gamma b_{sr} q_r + \gamma \Gamma_e \phi_s(1) \phi_r'(1) q_r + \delta_{sr} \ddot{q}_r + \Gamma_e \phi_s(1) \phi_r(1) \ddot{q}_r = 0, \end{aligned} \quad (2.10)$$

where

$$b_{sr} = \frac{4}{(\lambda_s/\lambda_r)^2 + (-1)^{r+s}}, \quad b_{rr} = 2, \quad (2.11)$$

$$c_{sr} = \frac{4(\lambda_r\sigma_r - \lambda_s\sigma_s)}{(-1)^{r+s} - (\lambda_s/\lambda_r)^2}, \quad c_{rr} = \lambda_r\sigma_r(2 - \lambda_r\sigma_r), \quad (2.12)$$

$$d_{sr} = \frac{4(\lambda_r\sigma_r - \lambda_s\sigma_s + 2)}{1 - (\lambda_s/\lambda_r)^4}(-1)^{r+s} - \frac{3 + (\lambda_s/\lambda_r)^4}{1 - (\lambda_s/\lambda_r)^4}b_{sr}, \quad d_{rr} = \frac{1}{2}c_{rr}, \quad (2.13)$$

for a cantilevered pipe [see Païdoussis (1998, p. 87)]. The elements of the mass $[M]$, damping $[C]$, and stiffness $[K]$ matrices in Eqn. (2.8) are found from Eqn. (2.10) to be

$$M_{sr} = \delta_{sr} + \Gamma_e \phi_s(1) \phi_r(1), \quad (2.14)$$

$$C_{sr} = (\bar{\alpha}^* + \bar{\mu}^*/\omega) \lambda_r^4 \delta_{sr} + 2\beta^{1/2} u b_{sr}, \quad (2.15)$$

$$K_{sr} = \lambda_r^4 \delta_{sr} + \gamma b_{sr} + [u^2 - \Gamma - \gamma(1 + \Gamma_e)] c_{sr} + \gamma d_{sr} + \gamma \Gamma_e \phi_s(1) \phi_r'(1). \quad (2.16)$$

Now, the mechanism for the suppression of flutter by blockage of the straight-through exit of the flow may be explained by considering the simplified linear equation of motion, in which gravity has been neglected,

$$EI \frac{\partial^4 w}{\partial x^4} + (MU^2 - \bar{T}) \frac{\partial^2 w}{\partial x^2} + 2MU \frac{\partial^2 w}{\partial x \partial t} + (M + m) \frac{\partial^2 w}{\partial t^2} = 0. \quad (2.17)$$

In this case, an axial force balance at the free end of the cantilevered pipe gives $\bar{T} = MU^2$, and so clearly the centrifugal or compressive term essential in generating flutter vanishes [see Païdoussis (1998)]. In this regard, it is often difficult to visualize how the axial flow could generate an effective compressive load, $MU^2(\partial^2 w/\partial x^2)$, but the experiments presented in Section 2.3.3 neatly demonstrate its existence.

2.2.2 Theoretical results

The system studied is a pipe with $\bar{\alpha}^* = 0.00017$, $\bar{\mu}^* = 0.03927$, $\beta = 0.142$, and $\gamma = 27.6$. Figs. 2.2 and 2.3 present the Argand diagrams using a five-mode Galerkin approximation for the first three modes as a function of the dimensionless flow velocity, u , for the unblocked cantilevered pipe that is mounted with the four-holed, i.e. $\Gamma_e = 0.196$, and the eight-holed, i.e. $\Gamma_e = 0.200$, end-piece, respectively. In both cases, the Argand diagrams are similar to the one shown in Fig. 2.1, and the system generally becomes unstable in its second mode by flutter. For $\Gamma_e = 0.196$, the critical flow velocity is $u_1 = 5.05$, and the critical frequency of oscillation is $\text{Re}(\omega_1) = 17.9$. Similarly, for $\Gamma_e = 0.200$, the critical flow velocity is $u_1 = 5.03$, and the critical frequency of oscillation is $\text{Re}(\omega_1) = 17.9$. The corresponding experimental values for the first bifurcation, which will be discussed in Section 2.3.3 and are presented in Table 2.3, are $u_1 = 5.46$ and $\text{Re}(\omega_1) = 16.3$ for both $\Gamma_e = 0.196$ and $\Gamma_e = 0.200$. Note that the multiplicative factor to switch from u to U in m/s is 1.06, while that to switch from ω to f in Hz is 0.142.

Unfortunately, linear theory cannot predict the second bifurcation; thus, it is necessary to resort to nonlinear theory, even though the model discussed until now is linear. The author is grateful to Dr. Yahya Modarres-Sadeghi for providing his *Fortran* code, which uses Houbolt's scheme to solve second order nonlinear ordinary differential equations with nonlinear inertial terms, in order to produce bifurcation diagrams so that an adequate comparison can be made between theory and experiment. The reader is referred to Wadham-Gagnon *et al.* (2007) and Modarres-Sadeghi *et al.* (2007) for the nonlinear equation of motion and dynamics, respectively, of a cantilevered pipe conveying fluid in the presence of an end-mass. Fig. 2.4 shows a bifurcation diagram of the dimensionless free-end displacement, η , versus dimensionless flow velocity, u , for the unblocked cantilevered pipe that is mounted with the four-holed end-piece. The system is stable for $u < u_1 = 5.0$, and loses stability by travelling-wave type flutter at $u_1 \approx 5.0$. Fixed-node type flutter of smaller amplitude then develops at $u_2 \approx 6.8$, and the motion of the system becomes more complex for $u_3 > 7.0$. The corresponding experimental values are $u_1 = 5.46$ and $u_2 = 8.53$, where u_1 is in reasonably good agreement with theory.

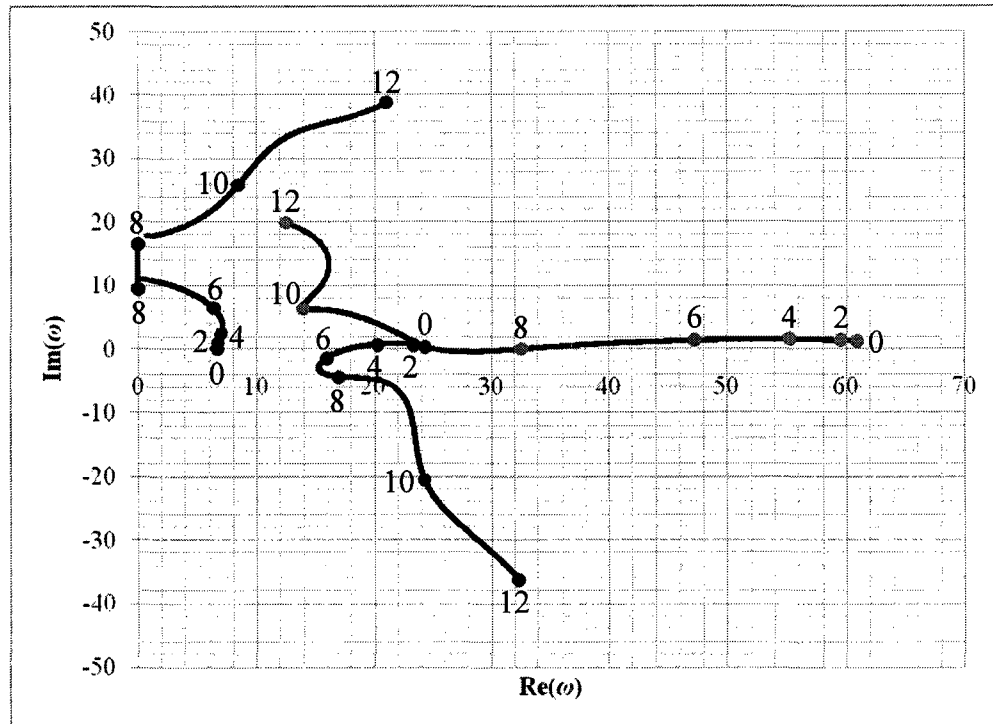


Figure 2.2. Argand diagram as a function of u for an unblocked cantilevered pipe with $\Gamma_e = 0.196$ using a five-mode Galerkin approximation.

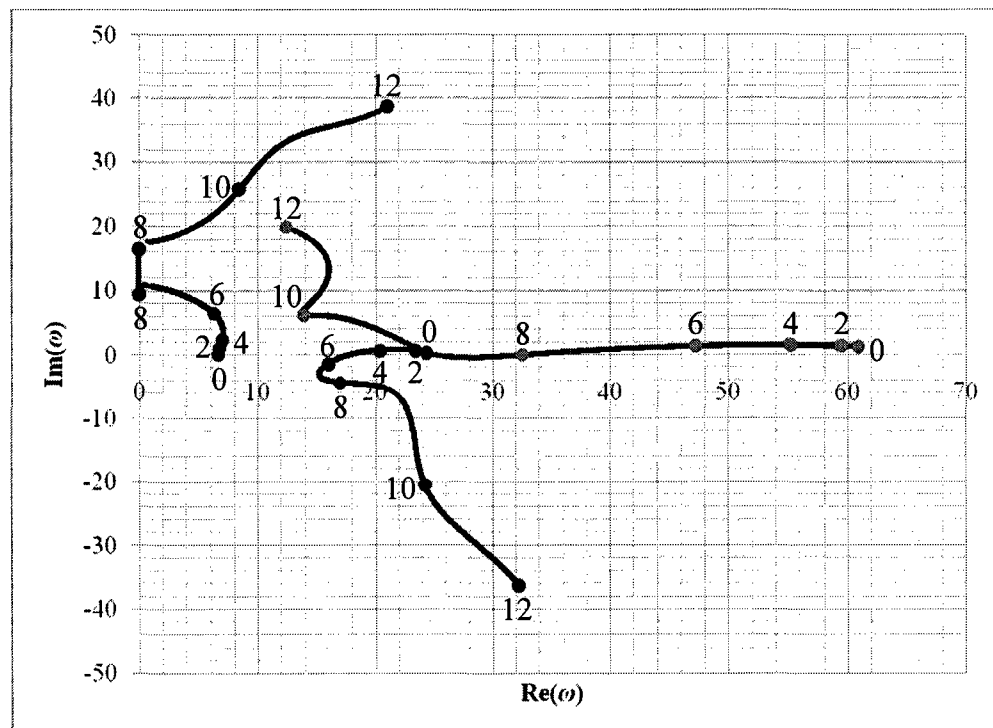


Figure 2.3. Argand diagram as a function of u for an unblocked cantilevered pipe with $\Gamma_e = 0.200$ using a five-mode Galerkin approximation.

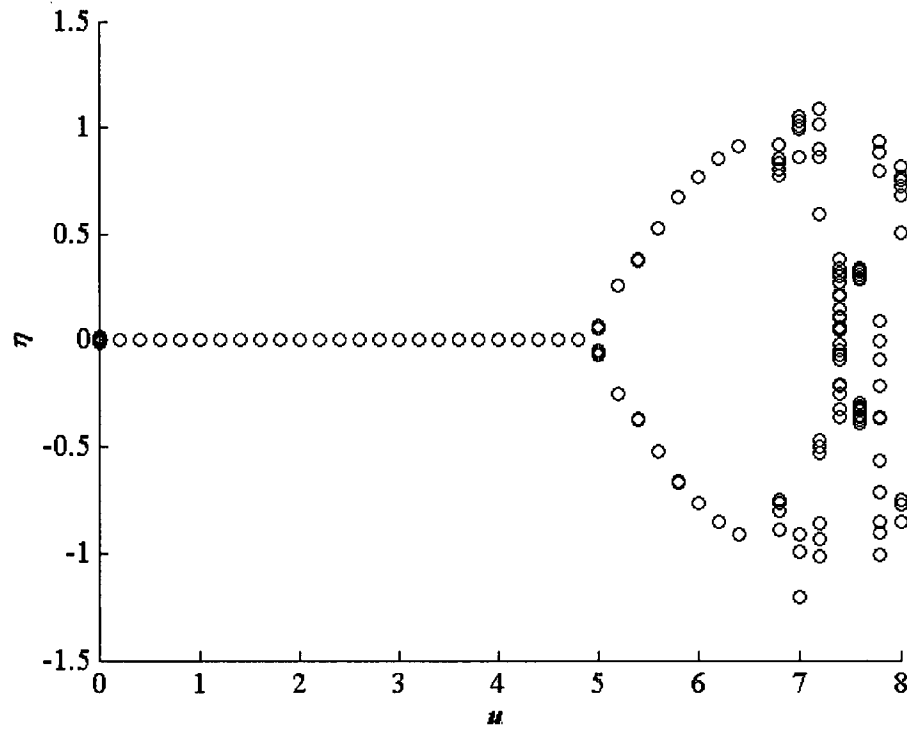


Figure 2.4. Bifurcation diagram for an unblocked cantilevered pipe with $\Gamma_e = 0.196$ using $N = 4$ modes.

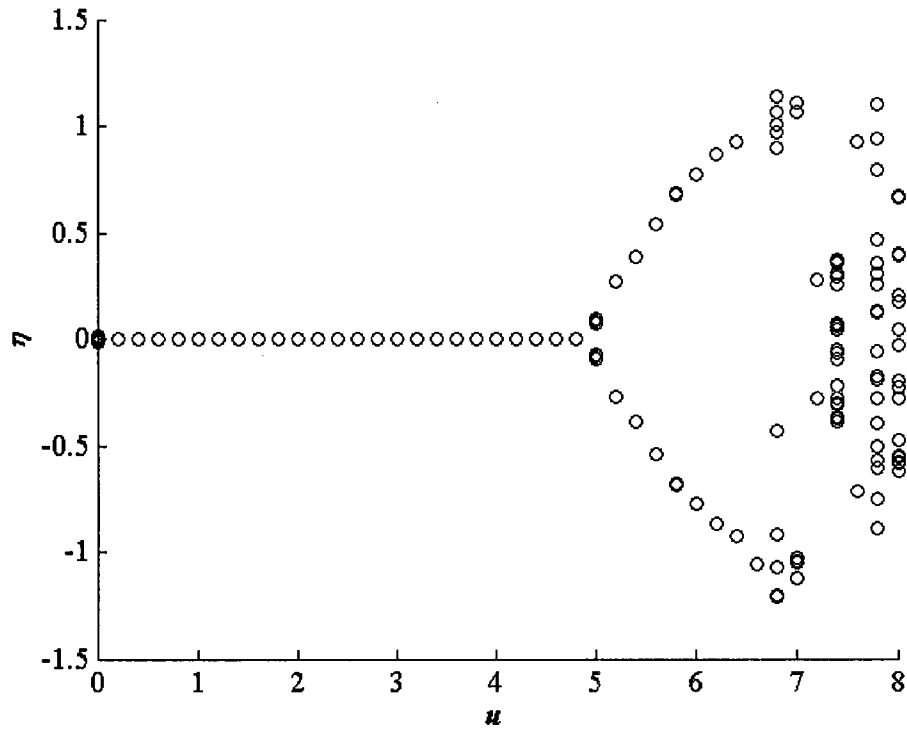


Figure 2.5. Bifurcation diagram for an unblocked cantilevered pipe with $\Gamma_e = 0.200$ using $N = 4$ modes.

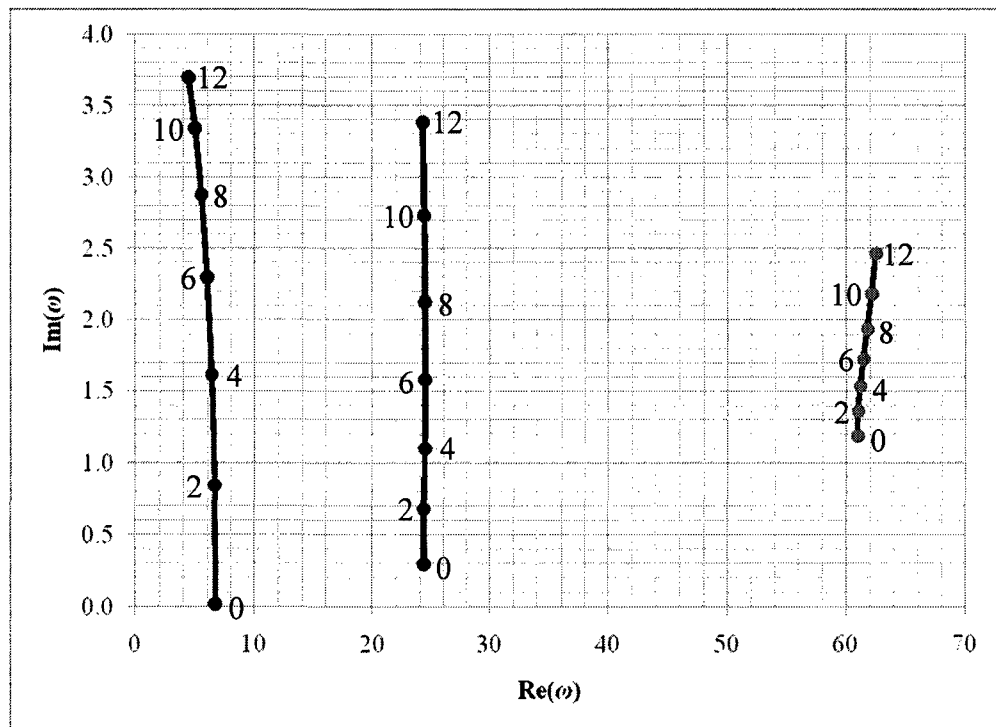


Figure 2.6. Argand diagram as a function of u for a blocked cantilevered pipe with $\Gamma_e = 0.196$ using a five-mode Galerkin approximation.

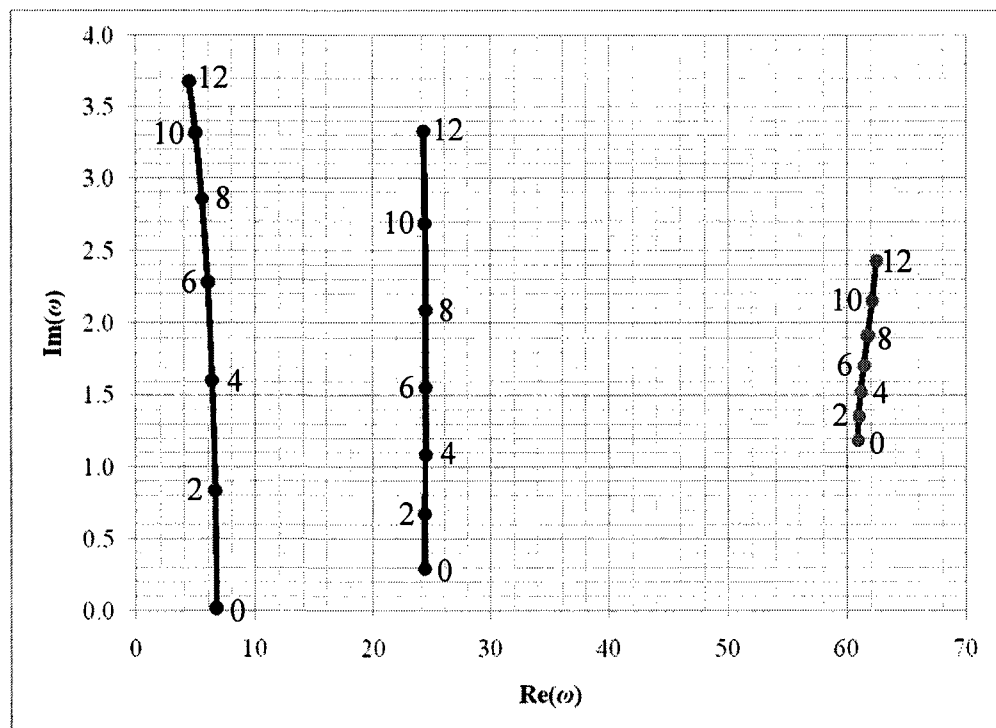


Figure 2.7. Argand diagram as a function of u for a blocked cantilevered pipe with $\Gamma_e = 0.200$ using a five-mode Galerkin approximation.

Similar results are found for the unblocked cantilevered pipe that is mounted with the eight-holed end-piece [see Fig. 2.5]. In this case, the theoretical values are also $u_1 \approx 5.0$, $u_2 \approx 6.8$, and $u_3 \approx 7.0$. The corresponding experimental values are $u_1 = 5.46$ and $u_2 = 8.54$, where u_1 is, once again, in reasonably good agreement with theory. Note that the bifurcation diagrams were obtained by a nonlinear theory correct to third order, using a finite difference method scheme with $N = 4$ modes.

Moreover, Figs. 2.6 and 2.7 present the Argand diagrams using a five-mode Galerkin approximation for the first three modes as a function of the dimensionless flow velocity, u , for the blocked cantilevered pipe that is mounted with the four-holed and the eight-holed end-piece, respectively. In both cases, the flow induces damping in all three modes. Consequently, the imaginary component of the dimensionless complex frequency, $\text{Im}(\omega)$, increases with increasing dimensionless flow velocity, u , and the system remains stable for all flow velocities investigated in the range $0 \leq u \leq 12$. This is expected since, in the equation of motion, the centrifugal term, $MU^2(\partial^2 w / \partial x^2)$, is cancelled by the blockage-induced tension on the pipe, \bar{T} .

2.3 Experimental Investigation

2.3.1 *Experimental apparatus*

The experiments were performed with a flexible elastomer pipe and two plastic end-pieces that differ solely in the number of holes machined, i.e. either four or eight holes. The fluid conveyed was water. The pipes were cast using a two-part silicone rubber kit consisting of a base and a curing agent. The reader is referred to Appendix A for a detailed procedure of the casting process. Note that a small elastomer ring was embedded at the free end of the pipe during the casting process in order to facilitate mounting the end-pieces onto the pipe during experiments. Additionally, both end-pieces were designed with a removable plug. Thus, a plugged end-piece allowed for a 90° diversion of the flow at the downstream end of the cantilevered pipe, while an unplugged end-piece allowed the straight-through passage of the flow [see Fig. 2.8].

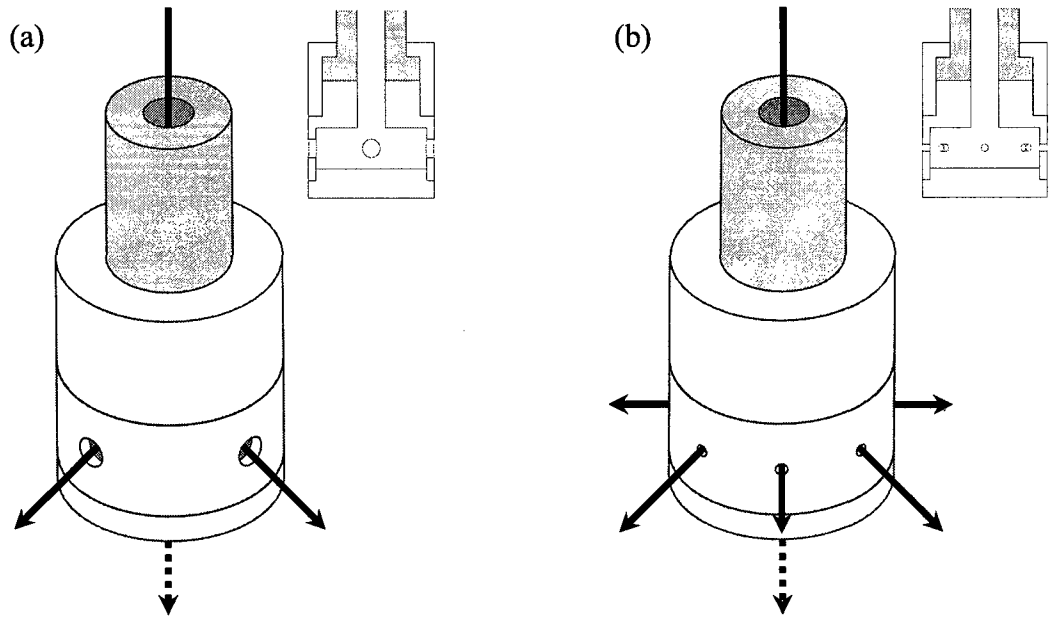


Figure 2.8. Schematic of the end-pieces with (a) four holes and (b) eight holes: — 90° diverted flow; --- straight-through flow. The inserts of (a) and (b) provide a cross-sectional view of the plugged end-piece that is mounted at the downstream end of the flexible cantilevered pipe.

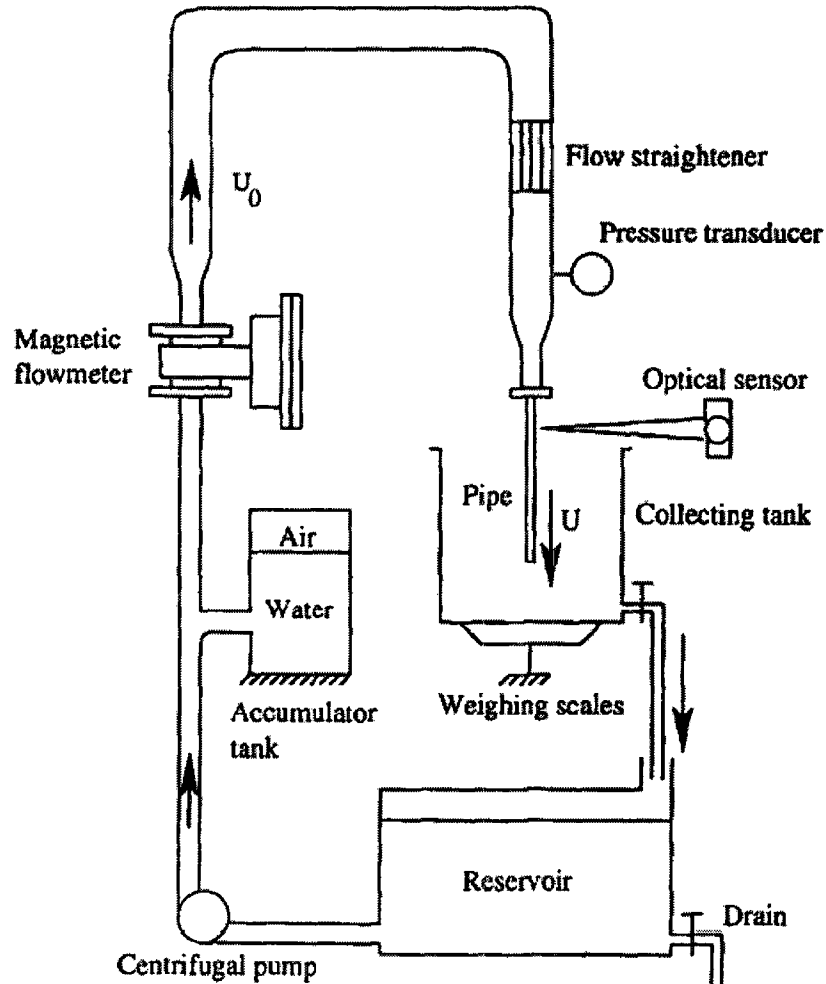
The geometrical and physical properties of the pipe and end-pieces are summarized in Tables 2.1 and 2.2. Note that f_n and δ_n are the natural frequency and log decrement of the pipe in the n th mode. For higher modes, i.e. $n \geq 4$, the log decrement of the system was approximated by $\delta_n = 0.0516n - 0.0144$, which is the linear regression line that best fits the data for the first three modes. The reader is referred to Appendix B for specific information concerning the determination of the natural frequencies, flexural rigidity, and logarithmic decrements of the cantilevered pipe system using experimental techniques.

Table 2.1. The geometrical and physical properties of the pipe

D_o [m]	D_i [m]	L [m]	EI [N·m ²]	m [kg/m]	M [kg/m]	β [-]	γ [-]
0.0159	0.00635	0.448	7.11×10^{-3}	0.191	0.0317	0.142	27.6
$\bar{\alpha}^*$ [-]	$\bar{\mu}^*$ [-]	f_1 [Hz]	f_2 [Hz]	f_3 [Hz]	δ_1 [-]	δ_2 [-]	δ_3 [-]
0.00017	0.03927	1.07	4.10	10.2	0.0346	0.0937	0.138

Table 2.2. The geometrical and physical properties of the end-pieces

End-piece	4 holes	8 holes
m_e [kg]	0.0195	0.0199
Γ_e [-]	0.196	0.200

**Figure 2.9.** Schematic of the experimental set-up [Païdoussis & Semler (1998)].

The experimental set-up consists mainly of (i) a cantilevered pipe vertically hung over (ii) a collecting tank, which rests on weighing scales, (iii) a centrifugal pump, which supplies recirculating water from a reservoir rather than from the mains, (iv) an *Omega* FMG710 magnetic flowmeter, which measures the volumetric flow rate, and (v) an *Optron* system, which is a non-contact electro-optical biaxial displacement follower system that consists of an optical head and a control unit. A schematic of the experimental set-up is shown in Fig. 2.9. The combination of a flow straightener and an accumulator tank, which attenuates pulsations from the centrifugal pump, ensures that the flow is

uniform at the inlet of the pipe. The *Optron* system is used together with *LabVIEW*, which is a graphical programming software, to acquire a time signal of the motion of the pipe at a point along its length. The acquired time signals are then analyzed using *MATLAB* to determine the frequency of oscillation of the pipe at various flow velocities. The reader is referred to Appendices D and E for a comprehensive treatment regarding the measurement of the flow velocity through the pipe, and the measurement of the frequency of oscillation of the pipe. Furthermore, additional information with regards to the experimental apparatus and set-up can be found in Païdoussis & Semler (1998).

2.3.2 *Experimental procedure*

The procedure for a water experiment involving a flexible cantilevered pipe conveying fluid that is fitted with a stabilizing end-piece is as follows:

1. Attach either a plugged or unplugged end-piece to the downstream end of the pipe depending on whether the flow is to be diverted by 90° or pass straight through.
2. Mount and clamp the upstream end of the pipe to the brass support, which is located at the water flow outlet of the piping system.
3. Connect the control unit, the low-pass filter, and the light source to power outlets with the power cords provided.
4. Connect the control unit to the optical head with the appropriate cable provided.
5. Connect the control unit to the low-pass filter with a BNC cable. Set the cut-off frequency on the low-pass filter to an appropriate value, such as 50 Hz.
6. Connect the low-pass filter to the data acquisition device with a BNC cable.
7. Connect the data acquisition device to a computer with the USB cable provided.
8. Open *LabVIEW* and load SCMEAS.VI. Set the count to an appropriate value, such as 24 000, set the rate to 400, and set the range to ± 10 V.
9. Observe the pipe through the viewer of the optical head. Position and adjust the optical head so that the desired target, which is a point that lies along the length of the pipe, is in sharp focus.
10. Set the horizontal target phase switch to either light to the right or light to the left. Set the Filter to OFF and set the Power/Mode to LIGHT LEVEL on the control unit.

11. Position the optical head so that the centre of the viewer is located within the darkest area of the target. Adjust the LOCK ON with a screwdriver until the horizontal meter reads -20% .
12. Position the optical head so that the centre of the viewer is located within the lightest area of the target. Adjust the light source, and/or the lens aperture of the optical head, and/or the high voltage on the control unit with a screwdriver until the horizontal meter reads $+40\%$.
13. Set the Power/Mode to HORIZONTAL on the control unit.
14. Position the optical head so that the horizontal meter reads 0% .
15. Turn on the pump at low flow rate by pressing the green button on the control valve. Remove any air bubbles that are trapped in the system using the release valve.
16. Slowly increase the flow rate by turning the knob of the control valve right. Release the knob at the onset of a bifurcation. At each critical flow rate, run SCMEAS.VI in *LabVIEW*, and read the volumetric flow rate from the *Omega* DPF64 ratemeter.
17. Slowly decrease the flow rate to zero by turning the knob of the control valve left. Turn off the pump by pressing the red button on the control valve.
18. Post-process the recorded time signals in *MATLAB* to obtain the frequency of oscillation of the system at each recorded step. Convert the critical volumetric flow rate readings, in litres/second, to flow velocity readings, in metres/second.

2.3.3 Experimental results

The quantitative experimental results for the first two bifurcations of a cantilevered pipe that is fitted with an unplugged end-piece are given in Table 2.3. Note that U_{cr} is the critical flow velocity measured in m/s, and f_{cr} refers to the critical frequency of oscillation of the system measured in Hz. Moreover, the time history traces and power spectral density plots for the experiments are presented in Figs. 2.10 to 2.13.

The qualitative experimental results for the two end-pieces are similar, as expected in view of their physical similarity [see Table 2.2]. At low flow velocities, the cantilevered pipe experiences an increase in damping with increasing flow, as can be

Table 2.3. Experimental critical flow velocities and frequencies of oscillations

	First bifurcation				Second bifurcation			
	U_{cr} [m/s]	u_{cr} [-]	f_{cr} [Hz]	$\text{Re}(\omega_{cr})$ [-]	U_{cr} [m/s]	u_{cr} [-]	f_{cr} [Hz]	$\text{Re}(\omega_{cr})$ [-]
4 holes	5.79	5.46	2.32	16.3	9.04	8.53	4.54	32.0
8 holes	5.79	5.46	2.32	16.3	9.05	8.54	4.54	32.0

determined by slightly perturbing the cantilevered pipe. As the flow velocity is increased, the pipe experiences a decrease in damping, eventually becoming negative and giving rise to a Hopf bifurcation. This Hopf bifurcation is characterized by two-dimensional, planar, travelling-wave type flutter involving second beam-mode shape oscillations. As the flow is increased further, a second bifurcation is encountered, which is characterized by two-dimensional, planar, fixed-node type flutter involving third beam-mode shape oscillations, and a fixed node at approximately mid-length. Furthermore, the system exhibits a higher frequency of oscillation. As the flow is increased even more, the frequency of oscillation increases further, and higher, more complex vibrational modes are observed. Eventually, the motion becomes chaotic, and impacting occurs with the walls of the collecting tank; at this point, the experiment is stopped. It should also be noted that the cantilevered pipe exhibits three-dimensional, transient behaviour just prior to the onset of the first and second bifurcations for only brief periods of time; during this time, the system searches for, and also locates, its preferred two-dimensional plane of motion for flutter to occur within.

On the other hand, the observed dynamical behaviour of a cantilevered pipe that is fitted with a plugged end-piece was entirely different. For this system, the cantilevered pipe did not display any oscillatory motion, or any other instability for that matter, as expected. Consequently, the system remained stable for all investigated flow velocities. Note that the maximum attainable flow velocity was limited by the pressure capacity of the plug. Once the pressure capacity was attained, the plug would simply break away from the end-piece without any warning, falling into the collecting tank, and the cantilevered pipe would flutter, provided that the flow velocity exceeded the critical flow velocity needed for flutter to develop.

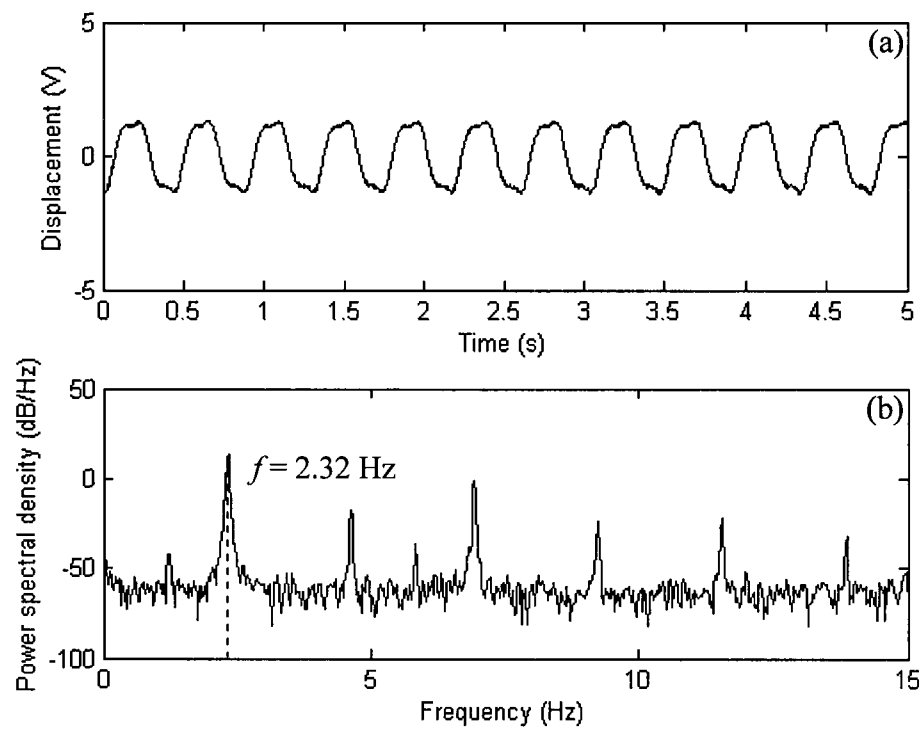


Figure 2.10. First bifurcation (a) time trace, and (b) power spectral density plot for $\Gamma_e = 0.196$.

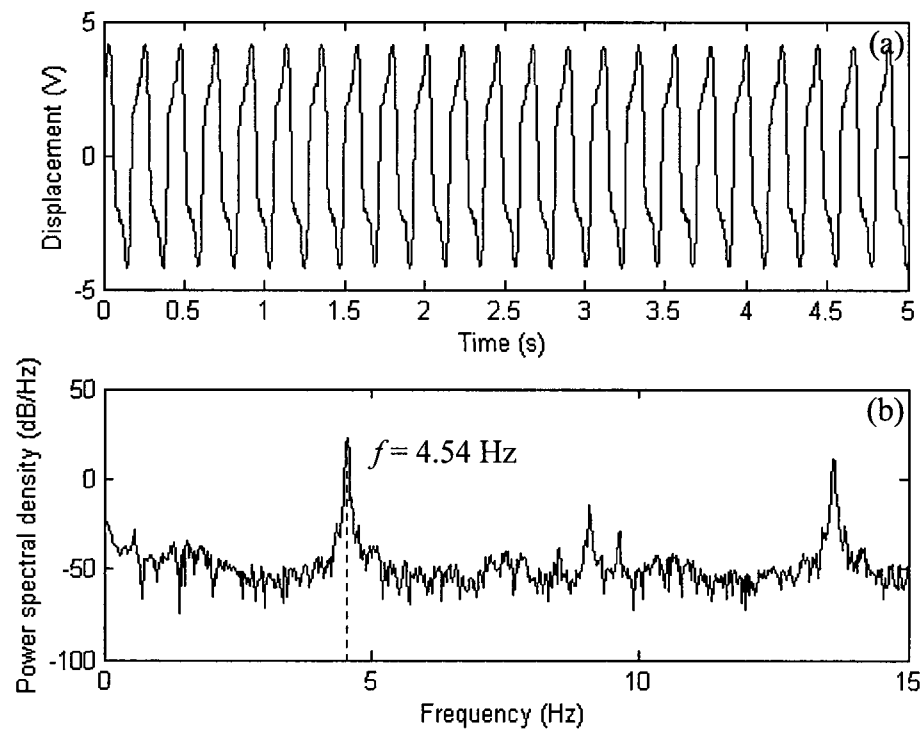


Figure 2.11. Second bifurcation (a) time trace, and (b) power spectral density plot for $\Gamma_e = 0.196$.

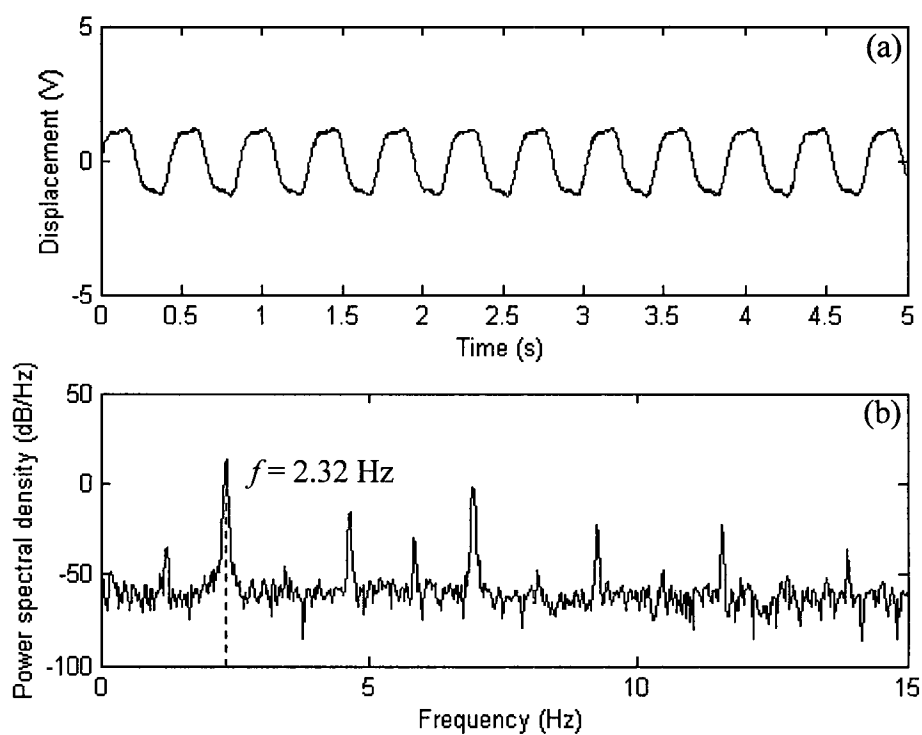


Figure 2.12. First bifurcation (a) time trace, and (b) power spectral density plot for $\Gamma_e = 0.200$.

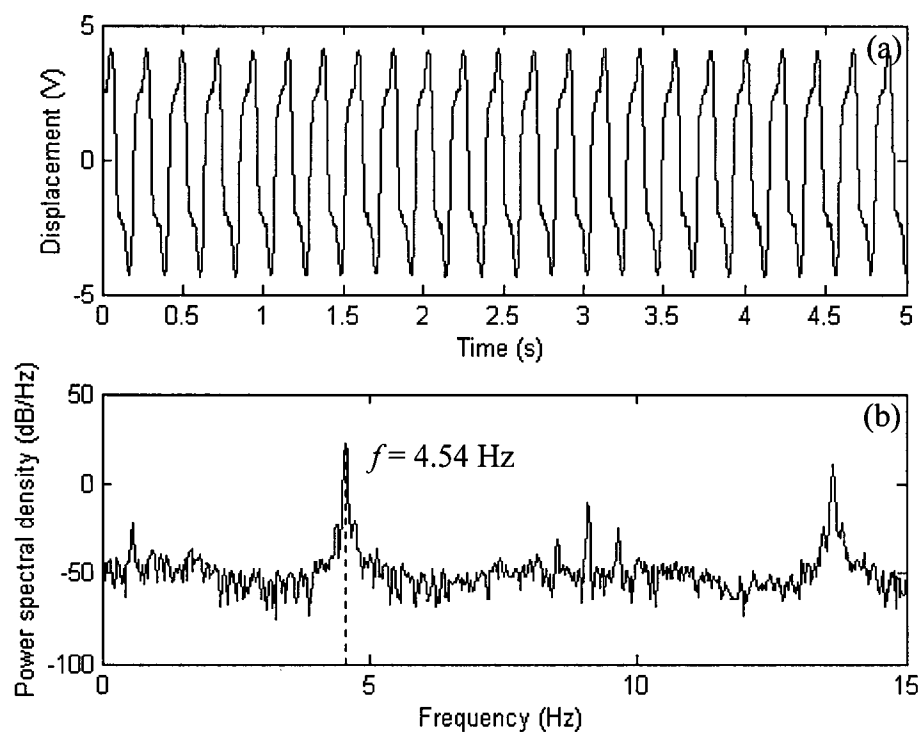


Figure 2.13. Second bifurcation (a) time trace, and (b) power spectral density plot for $\Gamma_e = 0.200$.

2.4 Summary

In this chapter, the dynamics of a flexible cantilevered pipe conveying water fitted with two different plastic end-pieces, which can either be plugged or left unplugged, was investigated. The experimental results for the first bifurcation of a cantilevered pipe fitted with an unplugged end-piece are in reasonably good agreement with both linear and nonlinear theory, and the existence of two-dimensional and chaotic behaviour, whereby the former is either a travelling-wave or a fixed-node type flutter, was successfully observed in experiments. On the other hand, the experimental results for the second bifurcation, which cannot be captured with linear theory, were nevertheless predicted by nonlinear theory; however, their quantitative agreement was not exceptionally good, resulting in errors of roughly 26% for the dimensionless critical flow velocity, u_{cr} , based on an average of the experimental and theoretical values. The reason for this latter is most probably that (i) an insufficient number of modes were used in the *Fortran* code of Modarres-Sadeghi, or (ii) the rotational inertia of the end-piece was not taken into account in the theoretical model.

Moreover, the experimental results for the cantilevered pipe fitted with a plugged end-piece are in very good agreement with the linear model presented. It has been demonstrated that the suppression of flutter is a consequence of blocking the straight-through exit, since the tension induced thereby on the pipe is equal to the effective centrifugal or compressive load that is generated by the axial flow. Hence, a plugged end-piece is, in fact, a stabilizing device; without it, the cantilevered pipe would otherwise flutter and develop more complex dynamical behaviour after the first bifurcation.

CHAPTER 3

Dynamics of a Cantilevered Pipe Aspirating Fluid

3.1 Introduction

One of the earliest models of a cantilevered pipe aspirating fluid was proposed by Païdoussis & Luu (1985), in which U was simply replaced by $-U$ in the linear equation of motion of a cantilevered pipe conveying fluid, thus leading to dynamical behaviour for the aspirating case which is the mirror-image of that for the discharging one. Thus, it was found that, in the absence of damping, the system loses stability by flutter at practically zero flow velocity, and then regains stability at a higher flow velocity. Since experiments up to that point had suggested that the system actually remains stable, Païdoussis (1998, 1999) re-evaluated the problem by examining the flow field at the inlet of the cantilevered pipe. Since the intake flow resembles a sink rather than a jet, the mean gauge pressure at the free end and throughout the pipe, \bar{p} ,[†] which was found equal to $-MU^2/A$, cancels out the centrifugal force in the linear equation of motion. Consequently, it was concluded that the cantilevered pipe aspirating fluid remains stable because of the disappearance of the centrifugal force, which is essential for flutter to develop. Kuiper & Metrikine (2005) subsequently argued that the system may flutter notwithstanding, even in the absence of the centrifugal force, because of the Coriolis force, which generates negative damping in the case of an aspirating pipe. Furthermore, they argued that the depressurization at the inlet had likely been overestimated by Païdoussis (1998, 1999), and thus the centrifugal force is not wholly cancelled out after all. This led to a reappraisal of the problem by

[†] This is the *mean* component that does not vary with axial position; on that is superimposed the axially varying component due to frictional pressure loss, the effect of which is cancelled by the axially varying tensile force on the pipe.

Païdoussis *et al.* (2005), whereby two new theoretical models were presented, and it was concluded that the flow field at the inlet of the cantilevered pipe would need to be investigated further; this time, however, using computational fluid dynamics and finite element analysis.

The present study was motivated by the dynamics of a flexible cantilevered pipe aspirating fluid, which is a dynamical problem that has perplexed researchers for many years in the field of fluid-structure interactions. In general, the present study is academic; however, applications in ocean mining, natural gas liquefaction, and gas hydrate exploitation do exist.

The scope of this chapter is three-fold. Firstly, the theoretical model proposed by Païdoussis *et al.* (2005) is re-derived with the effect of gravity included for both convenience and clarity. Secondly, the model is modified by applying axial and lateral time delays to the forces exerted on the pipe at the inlet. Note that the parameters α , $\bar{\gamma}$, and δ_s , which appear in the linear equation of motion for the system [see Section 3.2.1], are fixed based on the numerical results obtained by Dana Blake Giacobbi [see Giacobbi *et al.* (2008a)], presently a M.Eng. student at McGill University in the fluid-structure interactions group, using a computational fluid dynamics and finite element analysis model in *ANSYS*. Thirdly, the theoretical and experimental results are compared to determine whether this system loses stability by flutter at small flow velocities.

3.2 Theoretical Investigation

3.2.1 Païdoussis, Semler & Wadham-Gagnon (2005) model with non-negligible gravity

The linear equation of motion for small lateral motions of a cantilevered pipe aspirating fluid is derived using the Newtonian approach, and closely following the formulation by Païdoussis & Issid (1974) for a pipe conveying fluid, in order to arrive at the theoretical model proposed by Païdoussis *et al.* (2005). The system, consisting of a uniform flexible pipe of length L , internal perimeter S , internal cross-sectional flow area A , mass per unit length m , and flexural rigidity EI , which aspirates incompressible fluid of density ρ_f , mass per unit length M , and flowing in the pipe with a uniform axial flow

velocity U , is illustrated in Fig. 3.1. Note that the pipe is considered to be inextensible, and that the undisturbed or equilibrium axis of the pipe is assumed to be coincident with the x -axis of the system. The effect of gravity is also considered to be non-negligible. Note that the curvilinear coordinate along the centreline of the pipe, s , may be used interchangeably with the vertical coordinate, x , since the lateral motions, $w(x, t)$, are assumed to be small compared to the diameter of the pipe, i.e. L/D_o is large, and the motion is assumed to be two-dimensional and confined to, say, the x - y plane. The reader is referred to Païdoussis (1998) for the derivation of the inextensibility condition, and also for useful information concerning the Eulerian and Lagrangian coordinate systems.

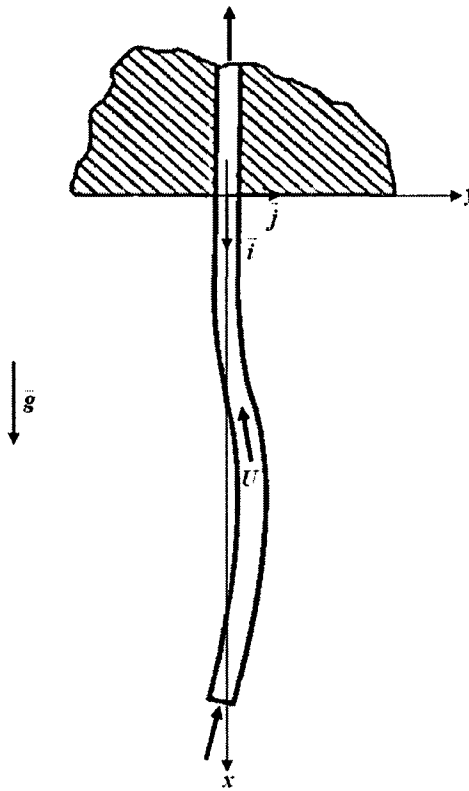


Figure 3.1. A cantilevered pipe aspirating fluid [Païdoussis & Issid (1974)].

The forces and moments acting on a small element δx of the fluid and the pipe are illustrated in Figs. 3.2 and 3.3, respectively, in which p is the fluid gauge pressure, $F\delta x$ is the reaction force of the pipe on the fluid in a direction normal to the fluid element, $qS\delta x$ is the shear force, or reaction force, of the pipe on the fluid in a direction tangential to the fluid element, $Mg\delta x$ is the weight of the fluid element, T is the axial tension, Q is the

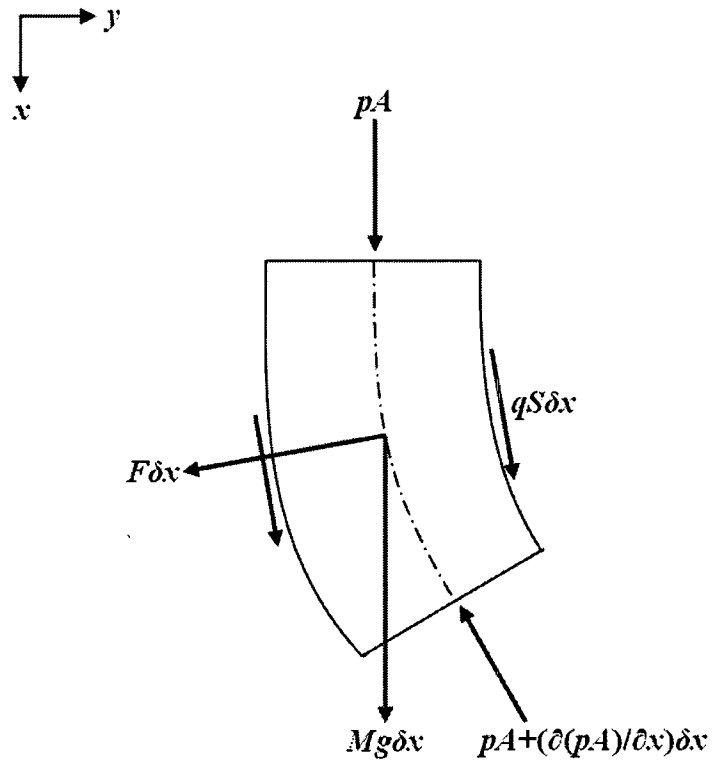


Figure 3.2. A small element δx of the fluid showing applied forces.

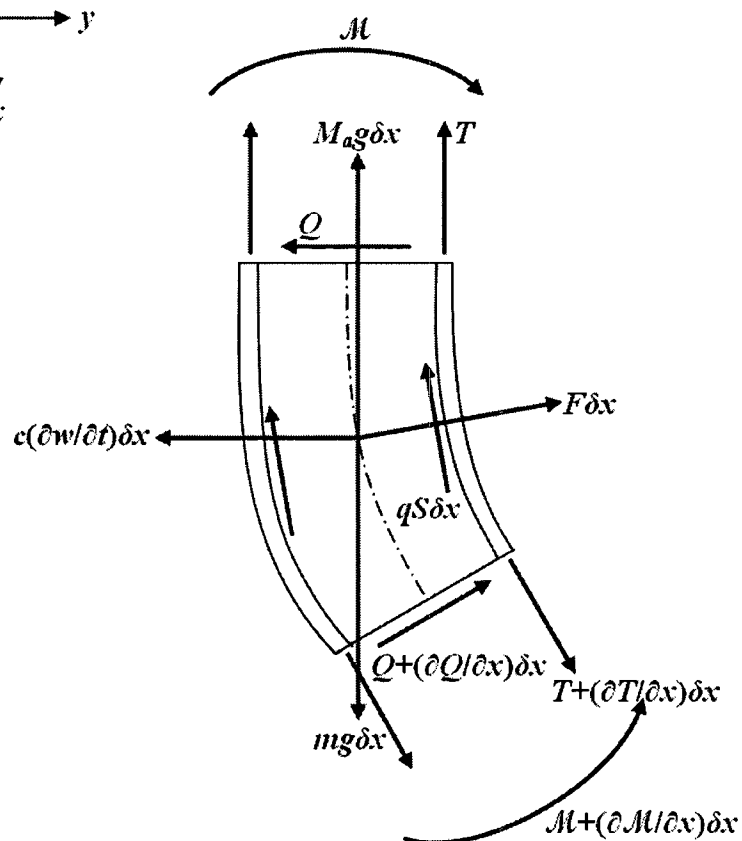


Figure 3.3. A small element δx of the pipe showing applied forces and moments.

lateral shear force, \mathcal{M} is the bending moment, $mg\delta x$ is the weight of the pipe element, $M_ag\delta x$ is the weight of the added mass, or buoyant force, due to the surrounding fluid, and $c(\partial w/\partial t)\delta x$ is the viscous damping due to the surrounding fluid. For unconfined flow, the viscous damping coefficient, c , is given by

$$c = \frac{2\sqrt{2}}{\sqrt{S}} \Omega \rho_f A_e, \quad (3.1)$$

where $S = \Omega r_o^2/\nu$, $r_o = 1/2 D_o$, D_o is the outer diameter of the pipe, Ω is the circular frequency of oscillation, and ν is the kinematic viscosity of the surrounding fluid [see Païdoussis (1998, p. 120)].

Applying Newton's second law to the fluid element shown in Fig. 3.2, the equations of motion in the x - and y -direction are

$$-A \frac{\partial p}{\partial x} + qS + Mg + F \frac{\partial w}{\partial x} = Ma_{fx}, \quad (3.2)$$

$$-F - A \frac{\partial}{\partial x} \left(p \frac{\partial w}{\partial x} \right) + qS \frac{\partial w}{\partial x} = Ma_{fy}, \quad (3.3)$$

where a_{fx} and a_{fy} are the accelerations of the fluid element in the x - and y -direction, respectively. Similarly, applying Newton's second law to the pipe element shown in Fig. 3.3, the equations of motion in the x - and y -direction are

$$\frac{\partial T}{\partial x} - qS + (m - M_a)g - F \frac{\partial w}{\partial x} = 0, \quad (3.4)$$

$$\frac{\partial Q}{\partial x} + F + \frac{\partial}{\partial x} \left(T \frac{\partial w}{\partial x} \right) - qS \frac{\partial w}{\partial x} - c \frac{\partial w}{\partial t} = (m + M_a)a_{py}, \quad (3.5)$$

where a_{py} is the acceleration of the pipe element in the y -direction. From Euler-Bernoulli beam theory, it is known that

$$Q = -\frac{\partial \mathcal{M}}{\partial x} = -EI \left[1 + \left(\bar{\alpha} + \frac{\bar{\mu}^*}{\Omega} \right) \frac{\partial}{\partial t} \right] \frac{\partial^3 w}{\partial x^3}, \quad (3.6)$$

where the internal dissipation is a combination of hysteretic and viscoelastic damping, in which a two-parameter Kelvin-Voigt model is employed for the latter [see Païdoussis & des Trois Maisons (1971)]. Note that terms of second order, such as the inertial forces in the axial direction, have been neglected from the equations of motion above, as well as the effects of angular acceleration.

Now, the velocity of the pipe element is

$$\vec{V}_p = \frac{\partial \vec{r}}{\partial t} = \frac{\partial x}{\partial t} \vec{i} + \frac{\partial y}{\partial t} \vec{j}, \quad (3.7)$$

where \vec{r} is the position vector measured from the origin to a point on the pipe. The velocity of the centre of the fluid element is

$$\vec{V}_f = \vec{V}_p - U \vec{\tau}, \quad (3.8)$$

where $\vec{\tau}$ is the unit vector tangential to the pipe, and is given by

$$\vec{\tau} = \frac{\partial x}{\partial s} \vec{i} + \frac{\partial y}{\partial s} \vec{j}. \quad (3.9)$$

Therefore,

$$\vec{V}_f = \left(\frac{\partial x}{\partial t} \vec{i} + \frac{\partial y}{\partial t} \vec{j} \right) - U \left(\frac{\partial x}{\partial s} \vec{i} + \frac{\partial y}{\partial s} \vec{j} \right) = \left(\frac{\partial}{\partial t} - U \frac{\partial}{\partial s} \right) (x \vec{i} + y \vec{j}) \equiv \frac{D \vec{r}}{Dt}, \quad (3.10)$$

where $D()/Dt$ is the material derivative. Since $y = w$, $\partial x/\partial s \approx 1$, and $\partial x/\partial t \approx 0$, the velocity of the centre of the fluid element reduces to

$$\vec{V}_f = -U \vec{i} + \left(\frac{\partial w}{\partial t} - U \frac{\partial w}{\partial x} \right) \vec{j}, \quad (3.11)$$

and the acceleration of the centre of the fluid element is

$$\vec{a}_f \equiv \frac{D^2 \vec{r}}{Dt^2} = \left(\frac{\partial}{\partial t} - U \frac{\partial}{\partial x} \right)^2 w \vec{j} = \left(\frac{\partial^2 w}{\partial t^2} - 2U \frac{\partial^2 w}{\partial x \partial t} + U^2 \frac{\partial^2 w}{\partial x^2} \right) \vec{j}. \quad (3.12)$$

Consequently,

$$a_{fx} = 0, a_{fy} = \frac{\partial^2 w}{\partial t^2} - 2U \frac{\partial^2 w}{\partial x \partial t} + U^2 \frac{\partial^2 w}{\partial x^2}, a_{py} = \frac{\partial^2 w}{\partial t^2}. \quad (3.13)$$

Eqns. (3.3), (3.5), (3.6), and (3.13) are combined to give

$$\begin{aligned} EI \left[1 + \left(\bar{\alpha} + \frac{\bar{\mu}^*}{\Omega} \right) \frac{\partial}{\partial t} \right] \frac{\partial^4 w}{\partial x^4} - \frac{\partial}{\partial x} \left[(T - pA) \frac{\partial w}{\partial x} \right] + M \left(\frac{\partial^2 w}{\partial t^2} - 2U \frac{\partial^2 w}{\partial x \partial t} + U^2 \frac{\partial^2 w}{\partial x^2} \right) \\ + c \frac{\partial w}{\partial t} + (m + M_a) \frac{\partial^2 w}{\partial t^2} = 0. \end{aligned} \quad (3.14)$$

Similarly, Eqns. (3.2), (3.4), and (3.13) are combined to give

$$\frac{\partial}{\partial x} (T - pA) = -(M + m - M_a)g. \quad (3.15)$$

Integrating Eqn. (3.15) from x to L yields

$$(T - pA)|_{x=L} - (T - pA) = -(M + m - M_a)g(L - x). \quad (3.16)$$

In general, the tension and pressure at $x = L$ is zero, unless an externally applied tension, \bar{T} , and an externally applied pressure, \bar{p} , are present. Hence, combining Eqns. (3.14) to (3.16), the equation of motion for a cantilevered pipe aspirating fluid becomes

$$\begin{aligned} EI \left[1 + \left(\bar{\alpha} + \frac{\bar{\mu}^*}{\Omega} \right) \frac{\partial}{\partial t} \right] \frac{\partial^4 w}{\partial x^4} + [MU^2 - (\bar{T} - \bar{p}A) - (M + m - M_a)g(L - x)] \frac{\partial^2 w}{\partial x^2} \\ - 2MU \frac{\partial^2 w}{\partial x \partial t} + (M + m - M_a)g \frac{\partial w}{\partial x} + c \frac{\partial w}{\partial t} + (M + m + M_a) \frac{\partial^2 w}{\partial t^2} = 0. \end{aligned} \quad (3.17)$$

The forces exerted by the fluid on the pipe at the inlet, which is inclined at an angle $\chi \equiv \tan^{-1}(\partial w / \partial x)_L \approx (\partial w / \partial x)_L$, are illustrated in Fig. 3.4 for both the (x, y) - and (ξ, ζ) -coordinate system, and a mean flow velocity, v , is also shown facing the inlet of the pipe. Thus, it is assumed that a sudden change in the flow velocity from $-v$ to $-U$ arises as the fluid enters the pipe, giving rise to the parameter $\alpha = v/U$. We consider two possibilities, differentiated by a new parameter, δ_s : (i) v is unrealistically assumed to remain in the vertical position at all times, and we identify this by $\delta_s = 0$; (ii) v remains tangential to the free end of the pipe at all times, and in this case $\delta_s = 1$. Now, the forces exerted by the

pipe on the fluid in the x - and y -direction are equal to the change in momentum, $MU(\Delta U)$.

For $\delta_s = 0$, we have

$$F_x = MU[-U \cos \chi - (-v)] \quad (3.18)$$

$$F_y = MU[(\dot{w}_L - U \sin \chi) - 0] \quad (3.19)$$

where $\dot{w}_L = (\partial w / \partial t)_L$, and for $\delta_s = 1$, we have

$$F_x = MU[-U \cos \chi - (-v \cos \chi)] \quad (3.20)$$

$$F_y = MU[(\dot{w}_L - U \sin \chi) - (-v \sin \chi)] \quad (3.21)$$

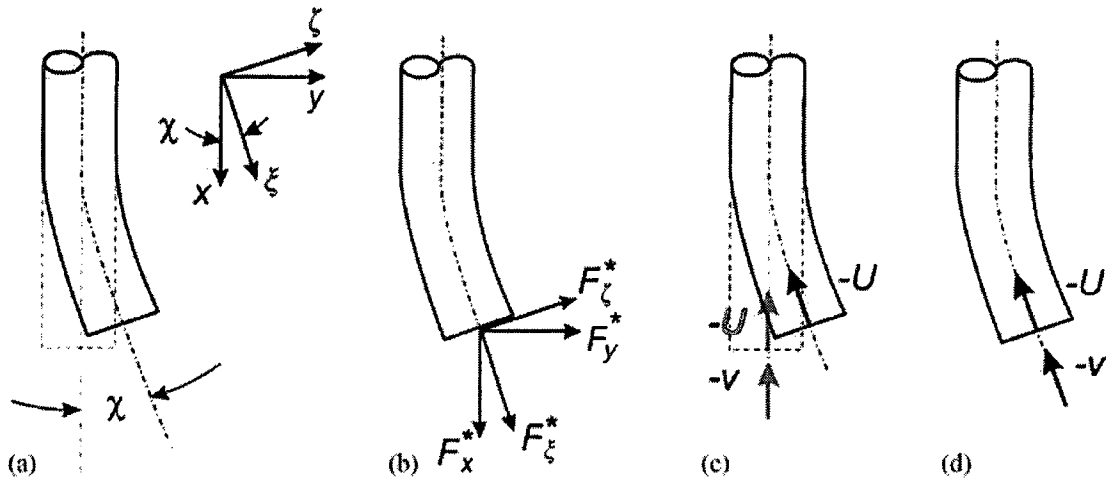


Figure 3.4. (a) The free end of the pipe, the definition of the coordinate systems used, and the angle χ ; (b) definition of the forces exerted by the fluid on the pipe; (c) the unrealistic inlet flow, with v always in the vertical direction ($\delta_s = 0$); (d) the tangential follower inlet flow, with v always tangential to the free end of the pipe ($\delta_s = 1$)

[Païdoussis *et al.* (2005)].

Since χ is presumed to be small, then

$$\cos \chi \approx 1, \quad (3.22)$$

$$\sin \chi \approx \chi \approx w'_L, \quad (3.23)$$

where $w'_L = (\partial w / \partial x)_L$. Therefore, for $\delta_s = 0$, the forces F_x and F_y can be written as

$$F_x = -MU^2(1 - \alpha), \quad (3.24)$$

$$F_y = MU(\dot{w}_L - Uw'_L), \quad (3.25)$$

and for $\delta_s = 1$,

$$F_x = -MU^2(1 - \alpha), \quad (3.26)$$

$$F_y = MU[\dot{w}_L - (1 - \alpha)Uw'_L] \quad (3.27)$$

The forces exerted by the fluid on the pipe at the inlet, F_x^* and F_y^* , are equal and opposite to those exerted by the pipe on the fluid at the inlet, F_x and F_y . Thus, for $\delta_s = 0$,

$$F_x^* = MU^2(1 - \alpha), \quad (3.28)$$

$$F_y^* = -MU(\dot{w}_L - Uw'_L), \quad (3.29)$$

and for $\delta_s = 1$,

$$F_x^* = MU^2(1 - \alpha), \quad (3.30)$$

$$F_y^* = -MU[\dot{w}_L - (1 - \alpha)Uw'_L] \quad (3.31)$$

The forces exerted by the fluid on the pipe at the inlet in the ξ - and ζ -direction, respectively, are

$$F_\xi^* \approx F_x^*, \quad (3.32)$$

$$F_\zeta^* \approx -MU[\dot{w}_L - (1 - \delta_s)\alpha Uw'_L] \quad (3.33)$$

It is now supposed that

$$-\bar{p}A = F_\xi^* = MU^2(1 - \alpha), \quad (3.34)$$

$$\bar{T} = -\bar{\gamma}\bar{p}(A_e - A) = f\gamma(1 - \alpha)MU^2 = \bar{\gamma}(1 - \alpha)MU^2, \quad (3.35)$$

where $0 < \gamma < 1$, $\bar{\gamma} = f\gamma$, $f = (A_e - A)/A$, and A_e and A are the external and internal cross-sectional areas of the pipe, respectively [see Païdoussis *et al.* (2005)]. Consequently,

$$(\bar{T} - \bar{p}A) = (1 - \alpha)(1 + \bar{\gamma})MU^2. \quad (3.36)$$

Moreover, the equation of motion for a cantilevered pipe aspirating fluid, Eqn. (3.17), is subject to the appropriate boundary conditions for a cantilevered pipe. At $x = 0$,

$$w = \frac{\partial w}{\partial x} = 0, \quad (3.37)$$

and at $x = L$,

$$EI \frac{\partial^2 w}{\partial x^2} = EI \frac{\partial^3 w}{\partial x^3} - MU \left[\frac{\partial w}{\partial t} - (1 - \delta_s) \alpha U \frac{\partial w}{\partial x} \right] = 0, \quad (3.38)$$

where the shear force boundary condition is related to F_ζ^* , and can be inserted in the equation of motion by means of a Dirac delta function, $\delta(x - L)$ [see Païdoussis (1998, p. 13)]. Eqns. (3.17), (3.36), and (3.38) are combined to give

$$\begin{aligned} EI \left[1 + \left(\bar{\alpha} + \frac{\bar{\mu}^*}{\Omega} \right) \frac{\partial}{\partial t} \right] \frac{\partial^4 w}{\partial x^4} + [1 - (1 - \alpha)(1 + \bar{\gamma})] MU^2 \frac{\partial^2 w}{\partial x^2} \\ - (M + m - M_a)g(L - x) \frac{\partial^2 w}{\partial x^2} - 2MU \frac{\partial^2 w}{\partial x \partial t} + (M + m - M_a)g \frac{\partial w}{\partial x} \\ + c \frac{\partial w}{\partial t} + (M + m + M_a) \frac{\partial^2 w}{\partial t^2} + MU \left[\frac{\partial w}{\partial t} - (1 - \delta_s) \alpha U \frac{\partial w}{\partial x} \right] \delta(x - L) = 0. \end{aligned} \quad (3.39)$$

Eqn. (3.39) is rendered dimensionless through the use of the following dimensionless parameters:

$$\xi = \frac{x}{L}, \quad \eta = \frac{w}{L}, \quad \tau = \left(\frac{EI}{M + m + M_a} \right)^{1/2} \frac{t}{L^2}, \quad (3.40)$$

to yield

$$\begin{aligned}
& \left[1 + \left(\bar{\alpha}^* + \frac{\bar{\mu}^*}{\omega} \right) \frac{\partial}{\partial \tau} \right] \frac{\partial^4 \eta}{\partial \xi^4} + \{ [1 - (1 - \alpha)(1 + \bar{\gamma})] \mu^2 - \gamma(1 - \xi) \} \frac{\partial^2 \eta}{\partial \xi^2} - 2\beta^{1/2} u \frac{\partial^2 \eta}{\partial \xi \partial \tau} \\
& + \gamma \frac{\partial \eta}{\partial \xi} + \sigma \frac{\partial \eta}{\partial \tau} + \frac{\partial^2 \eta}{\partial \tau^2} + \left[\beta^{1/2} u \frac{\partial \eta}{\partial \tau} - (1 - \delta_s) \alpha u^2 \frac{\partial \eta}{\partial \xi} \right] \delta(\xi - 1) = 0,
\end{aligned} \tag{3.41}$$

where

$$\begin{aligned}
u &= \left(\frac{M}{EI} \right)^{1/2} UL, \quad \beta = \frac{M}{M + m + M_a}, \quad \gamma = \frac{(M + m - M_a)gL^3}{EI}, \\
\bar{\alpha}^* &= \left(\frac{EI}{M + m + M_a} \right)^{1/2} \frac{\bar{\alpha}}{L^2}, \quad \sigma = \frac{cL^2}{[EI(M + m + M_a)]^{1/2}}, \\
\omega &= \left(\frac{M + m + M_a}{EI} \right)^{1/2} \Omega L^2.
\end{aligned} \tag{3.42}$$

The system is discretized following the Galerkin procedure and assuming a solution of the form

$$\eta(\xi, \tau) = \sum_{r=1}^N \phi_r(\xi) q_r(\tau), \tag{3.43}$$

where $\phi_r(\xi)$ are the comparison functions, taken here to be the cantilever beam eigenfunctions, and $q_r(\tau)$ are the generalized coordinates, which eventually leads to an expression of the form

$$[M]\ddot{\mathbf{q}} + [C]\dot{\mathbf{q}} + [K]\mathbf{q} = \mathbf{0}, \tag{3.44}$$

where $\mathbf{q} = \{q_1, q_2, \dots, q_N\}^T$. Specifically, Eqn. (3.43) is substituted into Eqn. (3.41) to give

$$\begin{aligned}
& \sum_{r=1}^N \left\{ \lambda_r^4 \phi_r q_r + \left(\bar{\alpha}^* + \bar{\mu}^* / \omega \right) \lambda_r^4 \phi_r \dot{q}_r + \{ [1 - (1 - \alpha)(1 + \bar{\gamma})] \mu^2 - \gamma(1 - \xi) \} \phi_r'' q_r \right. \\
& - 2\beta^{1/2} u \phi_r' \dot{q}_r + \gamma \phi_r' q_r + \sigma \phi_r \dot{q}_r + \phi_r \ddot{q}_r + \beta^{1/2} u \delta(\xi - 1) \phi_r \dot{q}_r \\
& \left. - (1 - \delta_s) \alpha u^2 \delta(\xi - 1) \phi_r' q_r \right\} = 0.
\end{aligned} \tag{3.45}$$

Thereafter, Eqn. (3.45) is multiplied by $\phi_s(\xi)$ and integrated over the domain $[0, 1]$ to give

$$\begin{aligned}
& \lambda_r^4 \delta_{sr} q_r + (\bar{\alpha}^* + \bar{\mu}^* / \omega) \lambda_r^4 \delta_{sr} \dot{q}_r + \{[1 - (1 - \alpha)(1 + \bar{\gamma})]u^2 - \gamma\} c_{sr} q_r + \gamma d_{sr} q_r \\
& - 2\beta^{1/2} u b_{sr} \dot{q}_r + \gamma b_{sr} q_r + \sigma \delta_{sr} \dot{q}_r + \delta_{sr} \ddot{q}_r + \beta^{1/2} u \phi_s(1) \phi_r(1) \dot{q}_r \\
& - (1 - \delta_s) \alpha u^2 \phi_s(1) \phi_r'(1) q_r = 0,
\end{aligned} \tag{3.46}$$

where

$$b_{sr} = \frac{4}{(\lambda_s / \lambda_r)^2 + (-1)^{r+s}}, \quad b_{rr} = 2, \tag{3.47}$$

$$c_{sr} = \frac{4(\lambda_r \sigma_r - \lambda_s \sigma_s)}{(-1)^{r+s} - (\lambda_s / \lambda_r)^2}, \quad c_{rr} = \lambda_r \sigma_r (2 - \lambda_r \sigma_r), \tag{3.48}$$

$$d_{sr} = \frac{4(\lambda_r \sigma_r - \lambda_s \sigma_s + 2)}{1 - (\lambda_s / \lambda_r)^4} (-1)^{r+s} - \frac{3 + (\lambda_s / \lambda_r)^4}{1 - (\lambda_s / \lambda_r)^4} b_{sr}, \quad d_{rr} = \frac{1}{2} c_{rr}, \tag{3.49}$$

for a cantilevered pipe [see Païdoussis (1998, p. 87)]. The elements of the mass $[M]$, damping $[C]$, and stiffness $[K]$ matrices in Eqn. (3.44) are found from Eqn. (3.46) to be

$$M_{sr} = \delta_{sr}, \tag{3.50}$$

$$C_{sr} = [(\bar{\alpha}^* + \bar{\mu}^* / \omega) \lambda_r^4 + \sigma] \delta_{sr} - 2\beta^{1/2} u b_{sr} + \beta^{1/2} u \phi_s(1) \phi_r(1), \tag{3.51}$$

$$K_{sr} = \lambda_r^4 \delta_{sr} + \gamma b_{sr} + \{[1 - (1 - \alpha)(1 + \bar{\gamma})]u^2 - \gamma\} c_{sr} + \gamma d_{sr} - (1 - \delta_s) \alpha u^2 \phi_s(1) \phi_r'(1). \tag{3.52}$$

Now, in the upcoming three sections, the theoretical model proposed by Païdoussis *et al.* (2005) is modified to include two distinct time delays, which arise because the forces at the free end of the cantilevered pipe do not develop instantaneously, but rather take time to be fully realized. Furthermore, the mean flow velocity, v , facing the inlet of the pipe is now generally directed at an angle \mathcal{G} , as shown in Fig. 3.5, whereby $0 \leq \mathcal{G} \leq \chi$, giving rise to the parameter $\psi = \mathcal{G} / \chi$. As a result, the case of vertical entry is recovered when $\psi = 0$, and that of tangential entry is recovered when $\psi = 1$. However, ψ is not limited to either 0 or 1; it may take on any value in the range $0 \leq \psi \leq 1$. Nevertheless, as related by Giacobbi *et al.* (2008a), ψ is very close to 1, at least for air-flow, because the fluid enters the pipe almost tangentially at the inlet. Note that the

primary difference between the three models to be presented in what follows is the sequence of application of the time delays.

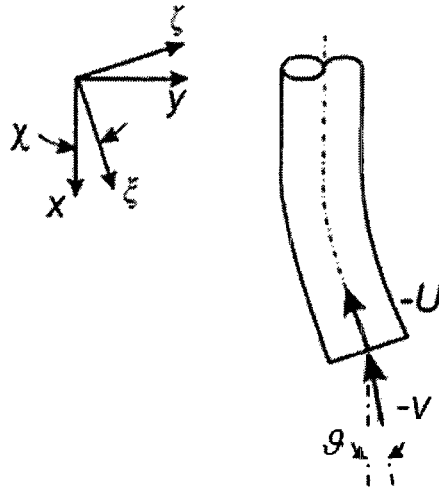


Figure 3.5. The free end of the pipe and the definition of the angle ϑ
[Païdoussis *et al.* (2005)].

3.2.2 Delay and non-purely-tangential entry model I

The forces exerted by the pipe on the fluid at the inlet in the x - and y -direction are equal to the change of momentum, $MU(\Delta U)$, and may be written as follows:

$$F_x = MU[-U \cos \chi - (-v \cos \vartheta)] \quad (3.53)$$

$$F_y = MU[(\dot{w}_L - U \sin \chi) - (-v \sin \vartheta)] \quad (3.54)$$

Since χ and ϑ are presumed to be small, then Eqns. (3.22) and (3.23) hold, in addition to

$$\cos \vartheta \approx 1, \quad (3.55)$$

$$\sin \vartheta \approx \vartheta \approx \psi \chi \approx \psi w'_L. \quad (3.56)$$

Therefore, the forces F_x and F_y can be written as

$$F_x = -MU^2(1 - \alpha), \quad (3.57)$$

$$F_y = MU[\dot{w}_L - (1 - \alpha\psi)Uw'_L] \quad (3.58)$$

The forces exerted by the fluid on the pipe at the inlet, F_x^* and F_y^* , are equal and opposite to those exerted by the pipe on the fluid at the inlet, F_x and F_y . Thus,

$$F_x^* = MU^2(1 - \alpha), \quad (3.59)$$

$$F_y^* = -MU[\dot{w}_L - (1 - \alpha\psi)Uw'_L] \quad (3.60)$$

The forces exerted by the fluid on the pipe at the inlet in the ξ - and ζ -direction, respectively, are

$$F_\xi^* \approx F_x^*, \quad (3.61)$$

$$F_\zeta^* \approx -MU[\dot{w}_L - (1 - \psi)\alpha Uw'_L] \quad (3.62)$$

Next, we apply two distinct delays to F_ξ^* and F_ζ^* : one in the axial or ξ -direction, $\bar{\tau}_a$, and another in the lateral or ζ -direction, $\bar{\tau}_\ell$. Both $\bar{\tau}_a$ and $\bar{\tau}_\ell$ are assumed to be constants, and to have the following forms:

$$\bar{\tau}_a = \frac{D_i}{U_{cr}} \text{ or } \bar{\tau}_a = \frac{\frac{1}{2}D_i}{U_{cr}}, \quad (3.63)$$

$$\bar{\tau}_\ell = \frac{D_o}{\frac{1}{2}L\Omega} \text{ or } \bar{\tau}_\ell = \frac{D_o}{\frac{1}{4}L\Omega}, \quad (3.64)$$

where $\Omega = \Omega(U = U_{cr}) = \Omega(U = 0)$ is a good approximation for Ω since the latter is not known in advance. Additionally, it is presumed that

$$w = \bar{w} \exp[i\Omega(t - \bar{\tau})] = \bar{w} \exp(i\Omega t) \exp(-i\Omega \bar{\tau}) = \bar{w} \exp(i\Omega t) \exp(-i\varphi), \quad (3.65)$$

where $\varphi = \Omega \bar{\tau}$. Furthermore,

$$\dot{w} = i\Omega \bar{w} \exp(i\Omega t) \exp(-i\varphi) = i\Omega w, \quad (3.66)$$

leading to the expression

$$i = \frac{1}{\Omega} \frac{\partial}{\partial t} () \rightarrow i\varphi = \frac{\varphi}{\Omega} \frac{\partial}{\partial t} () = \bar{\tau} \frac{\partial}{\partial t} (). \quad (3.67)$$

Note that Eqn. (3.67) is correct only if Ω is real, that is, on the boundary of neutral stability. Thus, the delayed forces exerted by the fluid on the pipe at the inlet in the ξ - and ζ -direction are

$$F_{\xi}^* \approx MU^2(1 - \alpha)\exp(-i\varphi_a), \quad (3.68)$$

$$F_{\zeta}^* \approx -MU[\dot{w}_L - (1 - \psi)\alpha U w'_L]\exp(-i\varphi_{\ell}), \quad (3.69)$$

where

$$\exp(-i\varphi_a) = \cos(-\varphi_a) + i\sin(-\varphi_a) \approx 1 - i\varphi_a = 1 - \bar{\tau}_a \frac{\partial}{\partial t} (), \quad (3.70)$$

$$\exp(-i\varphi_{\ell}) = \cos(-\varphi_{\ell}) + i\sin(-\varphi_{\ell}) \approx 1 - i\varphi_{\ell} = 1 - \bar{\tau}_{\ell} \frac{\partial}{\partial t} (). \quad (3.71)$$

Hence,

$$F_{\xi}^* \approx MU^2(1 - \alpha) \left[1 - \bar{\tau}_a \frac{\partial}{\partial t} () \right], \quad (3.72)$$

$$F_{\zeta}^* \approx -MU[\dot{w}_L - (1 - \psi)\alpha U w'_L] \left[1 - \bar{\tau}_{\ell} \frac{\partial}{\partial t} () \right]. \quad (3.73)$$

It is now supposed that

$$-\bar{p}A = F_{\xi}^* = MU^2(1 - \alpha) \left[1 - \bar{\tau}_a \frac{\partial}{\partial t} () \right], \quad (3.74)$$

$$\bar{T} = -\bar{\gamma}\bar{p}(A_e - A) = f\gamma(1 - \alpha)MU^2 \left[1 - \bar{\tau}_a \frac{\partial}{\partial t} () \right] = \bar{\gamma}(1 - \alpha)MU^2 \left[1 - \bar{\tau}_a \frac{\partial}{\partial t} () \right]. \quad (3.75)$$

Consequently,

$$(\bar{T} - \bar{p}A) = (1 - \alpha)(1 + \bar{\gamma})MU^2 \left[1 - \bar{\tau}_a \frac{\partial}{\partial t} () \right]. \quad (3.76)$$

Furthermore, the equation of motion for a cantilevered pipe aspirating fluid, Eqn. (3.17), is subject to the appropriate boundary conditions for a cantilevered pipe. At $x = 0$, Eqn. (3.37) applies, and at $x = L$,

$$EI \frac{\partial^2 w}{\partial x^2} = EI \frac{\partial^3 w}{\partial x^3} - MU \left[1 - \bar{\tau}_\ell \frac{\partial}{\partial t} \right] \left[\frac{\partial w}{\partial t} - (1 - \psi) \alpha U \frac{\partial w}{\partial x} \right] = 0, \quad (3.77)$$

where the shear force boundary condition is related to F_ζ^* , and can be inserted in the equation of motion by means of a Dirac delta function, $\delta(x - L)$. Eqns. (3.17), (3.76), and (3.77) are combined to give

$$\begin{aligned} EI \left[1 + \left(\bar{\alpha} + \frac{\bar{\mu}^*}{\Omega} \right) \frac{\partial}{\partial t} \right] \frac{\partial^4 w}{\partial x^4} + [1 - (1 - \alpha)(1 + \bar{\gamma})] MU^2 \frac{\partial^2 w}{\partial x^2} \\ - (M + m - M_a) g (L - x) \frac{\partial^2 w}{\partial x^2} + (1 - \alpha)(1 + \bar{\gamma}) MU^2 \bar{\tau}_a \frac{\partial^3 w}{\partial x^2 \partial t} \\ - 2MU \frac{\partial^2 w}{\partial x \partial t} + (M + m - M_a) g \frac{\partial w}{\partial x} + c \frac{\partial w}{\partial t} \\ + (M + m + M_a) \frac{\partial^2 w}{\partial t^2} + MU \left[\frac{\partial w}{\partial t} - (1 - \psi) \alpha U \frac{\partial w}{\partial x} \right] \delta(x - L) \\ - MU \bar{\tau}_\ell \left[\frac{\partial^2 w}{\partial t^2} - (1 - \psi) \alpha U \frac{\partial^2 w}{\partial x \partial t} \right] \delta(x - L) = 0. \end{aligned} \quad (3.78)$$

Eqn. (3.78) may be rendered dimensionless through the use of the dimensionless parameters given in Eqn. (3.40) to yield

$$\begin{aligned} \left[1 + \left(\bar{\alpha}^* + \frac{\bar{\mu}^*}{\omega} \right) \frac{\partial}{\partial \tau} \right] \frac{\partial^4 \eta}{\partial \xi^4} + \{ [1 - (1 - \alpha)(1 + \bar{\gamma})] \mu^2 - \gamma(1 - \xi) \} \frac{\partial^2 \eta}{\partial \xi^2} \\ + (1 - \alpha)(1 + \bar{\gamma}) \mu^2 \bar{\tau}_a^* \frac{\partial^3 \eta}{\partial \xi^2 \partial \tau} - 2\beta^{1/2} u \frac{\partial^2 \eta}{\partial \xi \partial \tau} + \gamma \frac{\partial \eta}{\partial \xi} + \sigma \frac{\partial \eta}{\partial \tau} + \frac{\partial^2 \eta}{\partial \tau^2} \\ + \left[\beta^{1/2} u \left(\frac{\partial \eta}{\partial \tau} - \bar{\tau}_\ell^* \frac{\partial^2 \eta}{\partial \tau^2} \right) - (1 - \psi) \alpha u^2 \left(\frac{\partial \eta}{\partial \xi} - \bar{\tau}_\ell^* \frac{\partial^2 \eta}{\partial \xi \partial \tau} \right) \right] \delta(\xi - 1) = 0, \end{aligned} \quad (3.79)$$

where Eqn. (3.42) holds, in addition to

$$\bar{\tau}_a^* = \left(\frac{EI}{M + m + M_a} \right)^{1/2} \frac{\bar{\tau}_a}{L^2}, \quad \bar{\tau}_\ell^* = \left(\frac{EI}{M + m + M_a} \right)^{1/2} \frac{\bar{\tau}_\ell}{L^2}. \quad (3.80)$$

The system is discretized following the Galerkin method described in Section 3.2.1, giving

$$M_{sr} = \delta_{sr} - \beta^{1/2} u \bar{\tau}_\ell^* \phi_s(1) \phi_r(1), \quad (3.81)$$

$$C_{sr} = \left[(\bar{\alpha}^* + \bar{\mu}^*/\omega) \lambda_r^4 + \sigma \right] \delta_{sr} - 2\beta^{1/2} u b_{sr} + (1-\alpha)(1+\bar{\gamma}) u^2 \bar{\tau}_a^* c_{sr} \\ + \beta^{1/2} u \phi_s(1) \phi_r(1) + (1-\psi) \alpha u^2 \bar{\tau}_\ell^* \phi_s(1) \phi_r'(1), \quad (3.82)$$

$$K_{sr} = \lambda_r^4 \delta_{sr} + \gamma b_{sr} + \left\{ [1 - (1-\alpha)(1+\bar{\gamma})] u^2 - \gamma \right\} c_{sr} + \gamma d_{sr} - (1-\psi) \alpha u^2 \phi_s(1) \phi_r'(1). \quad (3.83)$$

3.2.3 Delay and non-purely-tangential entry model II

Once again, the forces exerted by the fluid on the pipe at the inlet in the x - and y -direction are given by Eqns. (3.59) and (3.60), while those in the ξ - and ζ -direction are given by Eqns. (3.61) and (3.62). An axial delay, $\bar{\tau}_a$, given by Eqn. (3.63), is then applied to F_ξ^* to yield Eqn. (3.72). Proceeding with the ζ -direction, we obtain

$$F_\zeta^* \approx -MU [\dot{w}_L - (1-\psi) \alpha U w_L' - (1-\alpha) U \bar{\tau}_a \dot{w}_L'] \quad (3.84)$$

Next, a lateral delay, $\bar{\tau}_\ell$, given by Eqn. (3.64), is applied to Eqn. (3.84) to give

$$F_\zeta^* \approx -MU [\dot{w}_L - (1-\psi) \alpha U w_L' - (1-\alpha) U \bar{\tau}_a \dot{w}_L'] \left[1 - \bar{\tau}_\ell \frac{\partial}{\partial t} \left(\cdot \right) \right]. \quad (3.85)$$

Thus, in this model (model II), the delay in the ζ -direction is applied sequentially to that in the ξ -direction, instead of the two being applied in parallel (as in model I).

The equation of motion for a cantilevered pipe aspirating fluid, Eqn. (3.17), is subject to the appropriate boundary conditions for a cantilevered pipe. At $x = 0$, Eqn. (3.37) applies, and at $x = L$,

$$EI \frac{\partial^2 w}{\partial x^2} = 0, \quad (3.86)$$

$$EI \frac{\partial^3 w}{\partial x^3} - MU \left[1 - \bar{\tau}_\ell \frac{\partial}{\partial t} \right] \left[\frac{\partial w}{\partial t} - (1 - \psi) \alpha U \frac{\partial w}{\partial x} - (1 - \alpha) U \bar{\tau}_a \frac{\partial^2 w}{\partial x \partial t} \right] = 0,$$

where the shear force boundary condition is related to F_ζ^* , and can be inserted in the equation of motion by means of a Dirac delta function, $\delta(x - L)$. Eqns. (3.17), (3.76), and (3.86) are combined to give

$$\begin{aligned} EI \left[1 + \left(\bar{\alpha} + \frac{\bar{\mu}^*}{\Omega} \right) \frac{\partial}{\partial t} \right] \frac{\partial^4 w}{\partial x^4} + [1 - (1 - \alpha)(1 + \bar{\gamma})] MU^2 \frac{\partial^2 w}{\partial x^2} \\ - (M + m - M_a) g(L - x) \frac{\partial^2 w}{\partial x^2} + (1 - \alpha)(1 + \bar{\gamma}) MU^2 \bar{\tau}_a \frac{\partial^3 w}{\partial x^2 \partial t} \\ - 2MU \frac{\partial^2 w}{\partial x \partial t} + (M + m - M_a) g \frac{\partial w}{\partial x} + c \frac{\partial w}{\partial t} \\ + (M + m + M_a) \frac{\partial^2 w}{\partial t^2} + MU \left[\frac{\partial w}{\partial t} - (1 - \psi) \alpha U \frac{\partial w}{\partial x} - (1 - \alpha) U \bar{\tau}_a \frac{\partial^2 w}{\partial x \partial t} \right] \delta(x - L) \\ - MU \bar{\tau}_\ell \left[\frac{\partial^2 w}{\partial t^2} - (1 - \psi) \alpha U \frac{\partial^2 w}{\partial x \partial t} - (1 - \alpha) U \bar{\tau}_a \frac{\partial^3 w}{\partial x \partial t^2} \right] \delta(x - L) = 0. \end{aligned} \quad (3.87)$$

The dimensionless form of Eqn. (3.87), via Eqn. (3.40), is

$$\begin{aligned} \left[1 + \left(\bar{\alpha}^* + \frac{\bar{\mu}^*}{\omega} \right) \frac{\partial}{\partial \tau} \right] \frac{\partial^4 \eta}{\partial \xi^4} + \{ [1 - (1 - \alpha)(1 + \bar{\gamma})] u^2 - \gamma(1 - \xi) \} \frac{\partial^2 \eta}{\partial \xi^2} \\ + (1 - \alpha)(1 + \bar{\gamma}) u^2 \bar{\tau}_a^* \frac{\partial^3 \eta}{\partial \xi^2 \partial \tau} - 2\beta^{1/2} u \frac{\partial^2 \eta}{\partial \xi \partial \tau} + \gamma \frac{\partial \eta}{\partial \xi} + \sigma \frac{\partial \eta}{\partial \tau} + \frac{\partial^2 \eta}{\partial \tau^2} \\ + \left[\beta^{1/2} u \frac{\partial \eta}{\partial \tau} - (1 - \psi) \alpha u^2 \frac{\partial \eta}{\partial \xi} - (1 - \alpha) u^2 \bar{\tau}_a^* \frac{\partial^2 \eta}{\partial \xi \partial \tau} \right] \delta(\xi - 1) \\ - \left[\beta^{1/2} u \bar{\tau}_\ell^* \frac{\partial^2 \eta}{\partial \tau^2} - (1 - \psi) \alpha u^2 \bar{\tau}_\ell^* \frac{\partial^2 \eta}{\partial \xi \partial \tau} - (1 - \alpha) u^2 \bar{\tau}_a^* \bar{\tau}_\ell^* \frac{\partial^3 \eta}{\partial \xi \partial \tau^2} \right] \delta(\xi - 1) = 0, \end{aligned} \quad (3.88)$$

where Eqns. (3.42) and (3.80) still hold. Galerkin discretization follows, as in Section 3.2.1, yielding

$$M_{sr} = \delta_{sr} - \beta^{1/2} u \bar{\tau}_\ell^* \phi_s(1) \phi_r(1) + (1 - \alpha) u^2 \bar{\tau}_a^* \bar{\tau}_\ell^* \phi_s(1) \phi_r'(1), \quad (3.89)$$

$$C_{sr} = \left[(\bar{\alpha}^* + \bar{\mu}^* / \omega) \lambda_r^4 + \sigma \right] \delta_{sr} - 2\beta^{1/2} u b_{sr} + (1 - \alpha)(1 + \bar{\gamma}) u^2 \bar{\tau}_a^* c_{sr} \\ + \beta^{1/2} u \phi_s(1) \phi_r(1) - (1 - \alpha) u^2 \bar{\tau}_a^* \phi_s(1) \phi_r'(1) + (1 - \psi) \alpha u^2 \bar{\tau}_\ell^* \phi_s(1) \phi_r'(1), \quad (3.90)$$

$$K_{sr} = \lambda_r^4 \delta_{sr} + \gamma b_{sr} + \left\{ [1 - (1 - \alpha)(1 + \bar{\gamma})] u^2 - \gamma \right\} c_{sr} + \gamma d_{sr} - (1 - \psi) \alpha u^2 \phi_s(1) \phi_r'(1). \quad (3.91)$$

3.2.4 Delay and non-purely-tangential entry model III

Here, the forces exerted by the pipe on the fluid at the inlet in the x - and y -direction are given by Eqns. (3.53) and (3.54), i.e. as in model I. Next, we apply a delay $\bar{\tau}_a$ as in Eqn. (3.63) to F_x , and a delay $\bar{\tau}_\ell$ as in Eqn. (3.64) to F_y , but only to the terms related to the fluid velocity inside the pipe, i.e. not those involving v , to obtain

$$F_x = MU \left[-U \cos \chi \exp(-i\varphi_a) - (-v \cos \vartheta) \right], \quad (3.92)$$

$$F_y = MU \left[(\dot{w}_L - U \sin \chi) \exp(-i\varphi_\ell) - (-v \sin \vartheta) \right], \quad (3.93)$$

where $\exp(-i\varphi_a)$ and $\exp(-i\varphi_\ell)$ are given by Eqns. (3.70) and (3.71), respectively. Since χ and ϑ are presumed to be small, then Eqns. (3.22), (3.23), (3.55), and (3.56) hold. Therefore, the forces F_x and F_y can be written as

$$F_x = -MU^2 \left[(1 - \alpha) - \bar{\tau}_a \frac{\partial}{\partial t} () \right], \quad (3.94)$$

$$F_y = MU \left[\dot{w}_L - (1 - \alpha\psi) U w'_L - \bar{\tau}_\ell \frac{\partial}{\partial t} (\dot{w}_L - U w'_L) \right]. \quad (3.95)$$

The forces exerted by the fluid on the pipe at the inlet, F_x^* and F_y^* , are equal and opposite to those exerted by the pipe on the fluid at the inlet, F_x and F_y . Thus,

$$F_x^* = MU^2 \left[(1 - \alpha) - \bar{\tau}_a \frac{\partial}{\partial t} () \right], \quad (3.96)$$

$$F_y^* = -MU \left[\dot{w}_L - (1 - \alpha\psi)Uw'_L - \bar{\tau}_\ell \frac{\partial}{\partial t} (\dot{w}_L - Uw'_L) \right]. \quad (3.97)$$

The forces exerted by the fluid on the pipe at the inlet in the ξ - and ζ -direction, respectively, are

$$F_\xi^* \approx F_x^*, \quad (3.98)$$

$$F_\zeta^* \approx -MU [\dot{w}_L - (1 - \psi)\alpha Uw'_L - \bar{\tau}_\ell \dot{w}_L + (\bar{\tau}_\ell - \bar{\tau}_a)U\dot{w}'_L] \quad (3.99)$$

It is now supposed that

$$-\bar{p}A = F_\xi^* = MU^2 \left[(1 - \alpha) - \bar{\tau}_a \frac{\partial}{\partial t} () \right], \quad (3.100)$$

$$\bar{T} = -\bar{\gamma}\bar{p}(A_e - A) = f\gamma MU^2 \left[(1 - \alpha) - \bar{\tau}_a \frac{\partial}{\partial t} () \right] = \bar{\gamma}MU^2 \left[(1 - \alpha) - \bar{\tau}_a \frac{\partial}{\partial t} () \right]. \quad (3.101)$$

Consequently,

$$(\bar{T} - \bar{p}A) = (1 + \bar{\gamma})MU^2 \left[(1 - \alpha) - \bar{\tau}_a \frac{\partial}{\partial t} () \right]. \quad (3.102)$$

The equation of motion for a cantilevered pipe aspirating fluid, Eqn. (3.17), is subject to the appropriate boundary conditions for a cantilevered pipe. At $x = 0$, Eqn. (3.37) applies, and at $x = L$,

$$EI \frac{\partial^2 w}{\partial x^2} = EI \frac{\partial^3 w}{\partial x^3} - \kappa MU \left[\frac{\partial w}{\partial t} - (1 - \psi)\alpha U \frac{\partial w}{\partial x} - \bar{\tau}_\ell \frac{\partial^2 w}{\partial t^2} + (\bar{\tau}_\ell - \bar{\tau}_a)U \frac{\partial^2 w}{\partial x \partial t} \right] = 0, \quad (3.103)$$

where the shear force boundary condition is related to F_ζ^* , and can be incorporated in the equation of motion via a Dirac delta function, $\delta(x - L)$. Note that an arbitrary factor, κ , has been introduced since it is presumed that the shear force at the inlet does not fully materialize. Eqns. (3.17), (3.102), and (3.103) are combined to give

$$\begin{aligned}
& EI \left[1 + \left(\bar{\alpha} + \frac{\bar{\mu}^*}{\Omega} \right) \frac{\partial}{\partial t} \right] \frac{\partial^4 w}{\partial x^4} + [1 - (1 - \alpha)(1 + \bar{\gamma})] MU^2 \frac{\partial^2 w}{\partial x^2} \\
& - (M + m - M_a) g (L - x) \frac{\partial^2 w}{\partial x^2} + (1 + \bar{\gamma}) MU^2 \bar{\tau}_a \frac{\partial^3 w}{\partial x^2 \partial t} \\
& - 2MU \frac{\partial^2 w}{\partial x \partial t} + (M + m - M_a) g \frac{\partial w}{\partial x} + c \frac{\partial w}{\partial t} \\
& + (M + m + M_a) \frac{\partial^2 w}{\partial t^2} + \kappa MU \left[\frac{\partial w}{\partial t} - (1 - \psi) \alpha U \frac{\partial w}{\partial x} \right] \delta(x - L) \\
& - \kappa MU \left[\bar{\tau}_\ell \frac{\partial^2 w}{\partial t^2} - (\bar{\tau}_\ell - \bar{\tau}_a) U \frac{\partial^2 w}{\partial x \partial t} \right] \delta(x - L) = 0.
\end{aligned} \tag{3.104}$$

Utilizing Eqn. (3.40), the dimensionless equation of motion is

$$\begin{aligned}
& \left[1 + \left(\bar{\alpha}^* + \frac{\bar{\mu}^*}{\omega} \right) \frac{\partial}{\partial \tau} \right] \frac{\partial^4 \eta}{\partial \xi^4} + \{ [1 - (1 - \alpha)(1 + \bar{\gamma})] \mu^2 - \gamma(1 - \xi) \} \frac{\partial^2 \eta}{\partial \xi^2} \\
& + (1 + \bar{\gamma}) \mu^2 \bar{\tau}_a^* \frac{\partial^3 \eta}{\partial \xi^2 \partial \tau} - 2\beta^{1/2} u \frac{\partial^2 \eta}{\partial \xi \partial \tau} + \gamma \frac{\partial \eta}{\partial \xi} + \sigma \frac{\partial \eta}{\partial \tau} + \frac{\partial^2 \eta}{\partial \tau^2} \\
& + \kappa \left[\beta^{1/2} u \frac{\partial \eta}{\partial \tau} - (1 - \psi) \alpha u^2 \frac{\partial \eta}{\partial \xi} - \beta^{1/2} u \bar{\tau}_\ell^* \frac{\partial^2 \eta}{\partial \tau^2} \right. \\
& \left. + (\bar{\tau}_\ell^* - \bar{\tau}_a^*) \mu^2 \frac{\partial^2 \eta}{\partial \xi \partial \tau} \right] \delta(\xi - 1) = 0,
\end{aligned} \tag{3.105}$$

where Eqns. (3.42) and (3.80) hold. The system is discretized following the Galerkin procedure described in Section 3.2.1 to give

$$M_{sr} = \delta_{sr} - \kappa \beta^{1/2} u \bar{\tau}_\ell^* \phi_s(1) \phi_r(1), \tag{3.106}$$

$$\begin{aligned}
C_{sr} = & \left[(\bar{\alpha}^* + \bar{\mu}^*/\omega) \lambda_r^4 + \sigma \right] \delta_{sr} - 2\beta^{1/2} u b_{sr} + (1 + \bar{\gamma}) \mu^2 \bar{\tau}_a^* c_{sr} \\
& + \kappa \beta^{1/2} u \phi_s(1) \phi_r(1) + \kappa (\bar{\tau}_\ell^* - \bar{\tau}_a^*) \mu^2 \phi_s(1) \phi_r'(1),
\end{aligned} \tag{3.107}$$

$$K_{sr} = \lambda_r^4 \delta_{sr} + \gamma b_{sr} + \{ [1 - (1 - \alpha)(1 + \bar{\gamma})] \mu^2 - \gamma \} c_{sr} + \gamma d_{sr} - \kappa (1 - \psi) \alpha u^2 \phi_s(1) \phi_r'(1). \tag{3.108}$$

3.2.5 Theoretical results

The three delay and non-purely-tangential entry models described in Sections 3.2.2 to 3.2.4 were investigated numerically using *MATLAB*, and only the most pertinent results are presented here for brevity. The system studied is a flexible pipe with $\bar{\alpha}^* = 0.00030$, $\bar{\mu}^* = 0.03578$, $\beta = 6.10 \times 10^{-4}$, and $\gamma = 11.9$, which corresponds to a physical system with the following dimensional quantities: $D_o = 0.0159$ m, $D_i = 0.00934$ m, $L = 0.401$ m, $EI = 7.63 \times 10^{-3}$ N·m², $m = 0.144$ kg/m, $M = 8.81 \times 10^{-5}$ kg/m, and $M_a = 3.01 \times 10^{-4}$ kg/m. Tables 3.1 and 3.2 present the various models and delays, respectively, that appear throughout this section, where $U_{cr} = 61.3$ m/s and $\Omega = 1.107$ Hz were chosen based on experimental results, which will be presented in Section 3.3.3.

In addition, Tables 3.3, 3.4, and 3.5 present the nondimensional frequencies, ω , at $u = 1.00$ (for the first three modes) and at $u = u_{cr}$ for a particular system. More specifically, Table 3.3 shows the effect of the various models on the dynamics of a system with $\alpha = 0.40$, $\bar{\gamma} = 0.30$, and $\psi = 1.00$, which is the most realistic model based on the work of Giacobbi *et al.* (2008a), as a function of the various delays if gravity and damping effects are included in the equation of motion, while Tables 3.4 and 3.5 show the effect of the various delays on the dynamics of a system with specified parameters using model III-C. Note that an “F” in the “Instability” row corresponds to a loss of stability via flutter, while a “B” corresponds to a loss via buckling, and that the bracketed term following the “F” or “B” refers to the unstable mode or modes. Moreover, it should be mentioned that the multiplicative factor to switch from u to U in m/s is 23.2, while that to switch from ω to f in Hz is 0.228.

Referring to Table 3.3, when no delay is applied, models I, II, and III-A yield identical results and nondimensional critical flow velocities, i.e. $u_{cr} = 4.32$; however, models III-B and III-C result in lower critical flow velocities. Similarly, when delay III or IV is applied, models I, II, and III-A exhibit similar nondimensional frequencies and critical flow velocities, i.e. $u_{cr} \approx 4$, while models III-B and III-C yield lower critical flow velocities, i.e. $u_{cr} \approx 3$ and $u_{cr} \approx 2$, respectively. Furthermore, in all of the above cases, model III-C results in the lowest nondimensional critical flow velocities; when no delay is applied, $u_{cr} = 2.10$, when delay III is applied, $u_{cr} = 2.08$, and when delay IV is applied,

$u_{cr} = 2.06$. On the other hand, when delay I, II, V, or VI is applied, models I and II yield very similar, if not identical, dynamical results and nondimensional critical flow velocities, i.e. $u_{cr} \approx 4$; however, models III-A, III-B, and III-C result in higher critical flow velocities when compared to the latter, the largest being for model III-C. Lastly, the system always loses stability in its first mode by flutter via a Hopf bifurcation.

Table 3.1. Definition of the various models studied

	Description
Model I	The model of Section 3.2.2
Model II	The model of Section 3.2.3
Model III-A	The model of Section 3.2.4 with $\kappa = 1.00$
Model III-B	The model of Section 3.2.4 with $\kappa = 0.80$
Model III-C	The model of Section 3.2.4 with $\kappa = 0.60$

Table 3.2. Definition of the various delays studied

	$\bar{\tau}_a$ [s]	$\bar{\tau}_\ell$ [s]
No Delay	0	0
Delay I	0	$D_o / (\frac{1}{2} L\Omega)$
Delay II	0	$D_o / (\frac{1}{4} L\Omega)$
Delay III	$\frac{1}{2} D_i / U_{cr}$	0
Delay IV	D_i / U_{cr}	0
Delay V	$\frac{1}{2} D_i / U_{cr}$	$D_o / (\frac{1}{2} L\Omega)$
Delay VI	D_i / U_{cr}	$D_o / (\frac{1}{4} L\Omega)$

Referring to Table 3.4, if gravity and damping effects are excluded from model III-C when studying the dynamics of a system with specified α , $\bar{\gamma}$, and ψ parameters, the system is unstable by flutter in all three modes at practically zero flow velocity, i.e. $u_{cr} = 0.01$, which is the smallest nondimensional flow velocity step, Δu , in the *MATLAB* code. In addition, for all of the system parameters studied, the nondimensional frequencies for a specific mode are practically the same at u_{cr} , regardless of the delay that is applied, i.e. $\omega_1 \approx 3.52$, $\omega_2 \approx 22.0$, and $\omega_3 \approx 61.7$.

Referring to Table 3.5, if gravity and damping effects are included in model III-C, then the dynamics of a system with specified α , $\bar{\gamma}$, and ψ is more complex. More

specifically, a system with either $\alpha = 0.40$ and $\bar{\gamma} = 0.30$, or $\alpha = 0.20$ and $\bar{\gamma} = 0.25$, always loses stability by flutter in its first mode, and is either equally or slightly more stable for $\psi = 0.95$ than for $\psi = 1.00$, based on the critical flow velocities, regardless of the delay that is applied. On the other hand, a system with $\alpha = 0.20$, $\bar{\gamma} = 0.50$, and $\psi = 0.95$ loses stability by buckling in its second mode at very high nondimensional flow velocities, i.e. $u_{cr} \approx 16$, when delay I or V is applied, and loses stability by flutter in its first mode when either no delay or when delay II, III, IV, or VI is applied, while a system with $\alpha = 0.20$, $\bar{\gamma} = 0.50$, and $\psi = 1.00$ always loses stability by flutter in its first mode, regardless of the delay that is applied. Furthermore, a system with $\alpha = 0.20$ and $\bar{\gamma} = 0.50$ is either as much or slightly more stable for $\psi = 0.95$ than for $\psi = 1.00$, based on the critical flow velocities, when either no delay or when delay II, III, IV, or VI is applied, and is less stable for $\psi = 0.95$ than for $\psi = 1.00$ when delay I or V is applied. Lastly, delays I, II, V, and VI are always stabilizing when compared to the case of no delay, while delays III and IV are always destabilizing, based on the critical flow velocities.

In general, the system with $\alpha = 0.40$ and $\bar{\gamma} = 0.30$ exhibits the lowest critical flow velocities, is slightly more stable for $\psi = 0.95$ than for $\psi = 1.00$, and as the shear force factor, κ , is decreased from 1.00 to 0.80 to 0.60, the critical flow velocities are increased when delay I, II, V, or VI is applied, and they are decreased when either no delay or when delay III or IV is applied. Thus, it is evident that α , $\bar{\gamma}$, ψ , κ , $\bar{\tau}_a$, and $\bar{\tau}_\ell$ need to be fixed before any comparison with experiments can be done in the upcoming section.

Thus, from Tables 3.3, 3.4, and 3.5, the most realistic system (in terms of similarity with observed behaviour [see Section 3.3.3]) is given by model III with $\alpha = 0.40$ and $\bar{\gamma} = 0.30$, in which gravity and damping effects have been included, ψ is very close to 1.00, the shear force factor, κ , is less than 1.00, and either no delay or delay III or IV is applied, i.e. when the lateral delay, $\bar{\tau}_\ell$, is zero.

Moreover, the results suggest that the lateral delay, $\bar{\tau}_\ell$, was overestimated because the critical flow velocities are too high when delay I, II, V, or VI is applied. After some review, it was discovered that $\bar{\tau}_\ell$ was actually overestimated by a factor of 2π since the frequency of oscillation, Ω , was not converted from Hz to rad/s in the *MATLAB* code.

Table 3.3. Values of ω at $u = 1$ and at $u = u_{cr}$ for a system with $\alpha = 0.40$, $\bar{\gamma} = 0.30$, $\psi = 1.00$, and non-negligible gravity and damping effects

NO DELAY					
	Model I	Model II	Model III-A	Model III-B	Model III-C
$\text{Re}(\omega_1) @ u = 1$	5.583	5.583	5.583	5.583	5.583
$\text{Im}(\omega_1) @ u = 1$	0.044	0.044	0.044	0.034	0.025
$\text{Re}(\omega_2) @ u = 1$	24.192	24.192	24.192	24.192	24.192
$\text{Im}(\omega_2) @ u = 1$	0.438	0.438	0.438	0.428	0.418
$\text{Re}(\omega_3) @ u = 1$	63.955	63.955	63.955	63.955	63.955
$\text{Im}(\omega_3) @ u = 1$	1.646	1.646	1.646	1.636	1.626
Instability	F (1 st)	F (1 st)	F (1 st)	F (1 st)	F (1 st)
u_{cr}	4.32	4.32	4.32	3.12	2.10
$\text{Re}(\omega) @ u = u_{cr}$	5.915	5.915	5.915	5.738	5.642
$\text{Im}(\omega) @ u = u_{cr}$	0.000	0.000	0.000	0.000	0.000

DELAY I					
	Model I	Model II	Model III-A	Model III-B	Model III-C
$\text{Re}(\omega_1) @ u = 1$	5.611	5.611	5.611	5.605	5.600
$\text{Im}(\omega_1) @ u = 1$	0.044	0.044	0.320	0.255	0.190
$\text{Re}(\omega_2) @ u = 1$	24.321	24.321	24.289	24.272	24.254
$\text{Im}(\omega_2) @ u = 1$	0.441	0.441	1.476	1.254	1.034
$\text{Re}(\omega_3) @ u = 1$	64.287	64.287	64.205	64.161	64.114
$\text{Im}(\omega_3) @ u = 1$	1.658	1.658	3.342	2.982	2.629
Instability	F (1 st)	F (1 st)	F (1 st)	F (1 st)	F (1 st)
u_{cr}	4.31	4.31	8.44	8.55	8.66
$\text{Re}(\omega) @ u = u_{cr}$	6.026	6.026	8.804	8.702	8.580
$\text{Im}(\omega) @ u = u_{cr}$	0.000	0.000	-0.003	-0.001	0.000

DELAY II					
	Model I	Model II	Model III-A	Model III-B	Model III-C
$\text{Re}(\omega_1) @ u = 1$	5.639	5.639	5.641	5.629	5.617
$\text{Im}(\omega_1) @ u = 1$	0.044	0.044	0.604	0.480	0.357
$\text{Re}(\omega_2) @ u = 1$	24.454	24.454	24.370	24.341	24.309
$\text{Im}(\omega_2) @ u = 1$	0.444	0.444	2.575	2.115	1.668
$\text{Re}(\omega_3) @ u = 1$	64.638	64.638	64.399	64.331	64.252
$\text{Im}(\omega_3) @ u = 1$	1.670	1.670	5.178	4.412	3.675
Instability	F (1 st)	F (1 st)	F (1 st)	F (1 st)	F (1 st)
u_{cr}	4.29	4.29	7.88	8.09	8.31
$\text{Re}(\omega) @ u = u_{cr}$	6.140	6.140	9.198	9.059	8.899
$\text{Im}(\omega) @ u = u_{cr}$	0.000	0.000	-0.001	-0.001	-0.001

DELAY III					
	Model I	Model II	Model III-A	Model III-B	Model III-C
$\text{Re}(\omega_1) @ u = 1$	5.583	5.583	5.583	5.583	5.583
$\text{Im}(\omega_1) @ u = 1$	0.044	0.044	0.044	0.034	0.024
$\text{Re}(\omega_2) @ u = 1$	24.192	24.192	24.192	24.192	24.192
$\text{Im}(\omega_2) @ u = 1$	0.438	0.437	0.436	0.426	0.416
$\text{Re}(\omega_3) @ u = 1$	63.955	63.955	63.955	63.955	63.955
$\text{Im}(\omega_3) @ u = 1$	1.644	1.643	1.641	1.631	1.622
Instability	F (1 st)	F (1 st)	F (1 st)	F (1 st)	F (1 st)
u_{cr}	4.35	4.26	4.22	3.06	2.08
$\text{Re}(\omega) @ u = u_{cr}$	5.921	5.904	5.897	5.731	5.640
$\text{Im}(\omega) @ u = u_{cr}$	0.000	0.000	0.000	0.000	0.000

Table 3.3. *cont'd*

DELAY IV					
	Model I	Model II	Model III-A	Model III-B	Model III-C
$\text{Re}(\omega_1) @ u = 1$	5.583	5.583	5.583	5.583	5.583
$\text{Im}(\omega_1) @ u = 1$	0.044	0.044	0.043	0.034	0.024
$\text{Re}(\omega_2) @ u = 1$	24.192	24.192	24.192	24.192	24.192
$\text{Im}(\omega_2) @ u = 1$	0.437	0.436	0.434	0.424	0.415
$\text{Re}(\omega_3) @ u = 1$	63.955	63.955	63.955	63.955	63.955
$\text{Im}(\omega_3) @ u = 1$	1.642	1.640	1.636	1.627	1.617
Instability	F (1 st)	F (1 st)	F (1 st)	F (1 st)	F (1 st)
u_{cr}	4.38	4.20	4.12	3.00	2.06
$\text{Re}(\omega) @ u = u_{cr}$	5.926	5.894	5.880	5.724	5.639
$\text{Im}(\omega) @ u = u_{cr}$	0.000	0.000	0.000	0.000	0.000

DELAY V					
	Model I	Model II	Model III-A	Model III-B	Model III-C
$\text{Re}(\omega_1) @ u = 1$	5.611	5.611	5.611	5.605	5.600
$\text{Im}(\omega_1) @ u = 1$	0.044	0.044	0.320	0.255	0.189
$\text{Re}(\omega_2) @ u = 1$	24.321	24.319	24.289	24.272	24.254
$\text{Im}(\omega_2) @ u = 1$	0.440	0.440	1.474	1.252	1.032
$\text{Re}(\omega_3) @ u = 1$	64.287	64.280	64.206	64.161	64.114
$\text{Im}(\omega_3) @ u = 1$	1.656	1.654	3.337	2.978	2.624
Instability	F (1 st)	F (1 st)	F (1 st)	F (1 st)	F (1 st)
u_{cr}	4.33	4.25	8.39	8.51	8.63
$\text{Re}(\omega) @ u = u_{cr}$	6.030	6.012	8.839	8.733	8.606
$\text{Im}(\omega) @ u = u_{cr}$	0.000	0.000	-0.003	-0.001	-0.001

DELAY VI					
	Model I	Model II	Model III-A	Model III-B	Model III-C
$\text{Re}(\omega_1) @ u = 1$	5.639	5.639	5.641	5.629	5.617
$\text{Im}(\omega_1) @ u = 1$	0.045	0.044	0.604	0.479	0.356
$\text{Re}(\omega_2) @ u = 1$	24.454	24.447	24.370	24.341	24.309
$\text{Im}(\omega_2) @ u = 1$	0.442	0.441	2.571	2.112	1.665
$\text{Re}(\omega_3) @ u = 1$	64.638	64.609	64.400	64.331	64.253
$\text{Im}(\omega_3) @ u = 1$	1.666	1.663	5.168	4.403	3.666
Instability	F (1 st)	F (1 st)	F (1 st)	F (1 st)	F (1 st)
u_{cr}	4.35	4.18	7.73	7.96	8.20
$\text{Re}(\omega) @ u = u_{cr}$	6.154	6.109	9.287	9.140	8.973
$\text{Im}(\omega) @ u = u_{cr}$	0.000	0.000	0.000	-0.002	-0.001

Table 3.4. Values of ω at $u = 1$ and at $u = u_{cr}$ for a system with negligible gravity and damping effects computed using model III-C

$\alpha = 0.40, \bar{\gamma} = 0.30, \psi = 0.95, \gamma = 0, \bar{\alpha}^* = 0, \bar{\mu}^* = 0, \sigma = 0$							
	No Delay	Delay I	Delay II	Delay III	Delay IV	Delay V	Delay VI
Re(ω_1) @ $u = 1$	3.534	3.543	3.549	3.534	3.534	3.543	3.549
Im(ω_1) @ $u = 1$	-0.020	0.149	0.321	-0.020	-0.020	0.149	0.321
Re(ω_2) @ $u = 1$	21.963	22.024	22.074	21.963	21.963	22.024	22.075
Im(ω_2) @ $u = 1$	-0.020	0.574	1.184	-0.021	-0.023	0.572	1.181
Re(ω_3) @ $u = 1$	61.612	61.789	61.945	61.612	61.612	61.789	61.945
Im(ω_3) @ $u = 1$	-0.020	0.961	1.983	-0.024	-0.028	0.957	1.974
Instability	F (1 st - 3 rd)	F (1 st - 3 rd)	F (1 st - 3 rd)	F (1 st - 3 rd)	F (1 st - 3 rd)	F (1 st - 3 rd)	F (1 st - 3 rd)
u_{cr}	0.01	0.01	0.01	0.01	0.01	0.01	0.01
Re(ω_1) @ $u = u_{cr}$	3.516	3.516	3.516	3.516	3.516	3.516	3.516
Im(ω_1) @ $u = u_{cr}$	0.000	0.000	0.000	0.000	0.000	0.000	0.000
Re(ω_2) @ $u = u_{cr}$	22.034	22.035	22.036	22.034	22.034	22.035	22.036
Im(ω_2) @ $u = u_{cr}$	0.000	0.000	0.000	0.000	0.000	0.000	0.000
Re(ω_3) @ $u = u_{cr}$	61.697	61.699	61.701	61.697	61.697	61.699	61.701
Im(ω_3) @ $u = u_{cr}$	0.000	0.000	0.000	0.000	0.000	0.000	0.000

$\alpha = 0.40, \bar{\gamma} = 0.30, \psi = 1.00, \gamma = 0, \bar{\alpha}^* = 0, \bar{\mu}^* = 0, \sigma = 0$							
	No Delay	Delay I	Delay II	Delay III	Delay IV	Delay V	Delay VI
Re(ω_1) @ $u = 1$	3.543	3.553	3.559	3.543	3.543	3.553	3.559
Im(ω_1) @ $u = 1$	-0.020	0.149	0.320	-0.020	-0.020	0.149	0.320
Re(ω_2) @ $u = 1$	21.968	22.029	22.080	21.968	21.968	22.029	22.080
Im(ω_2) @ $u = 1$	-0.020	0.574	1.184	-0.021	-0.023	0.572	1.181
Re(ω_3) @ $u = 1$	61.615	61.792	61.948	61.615	61.615	61.792	61.948
Im(ω_3) @ $u = 1$	-0.020	0.961	1.983	-0.024	-0.028	0.957	1.974
Instability	F (1 st - 3 rd)	F (1 st - 3 rd)	F (1 st - 3 rd)	F (1 st - 3 rd)	F (1 st - 3 rd)	F (1 st - 3 rd)	F (1 st - 3 rd)
u_{cr}	0.01	0.01	0.01	0.01	0.01	0.01	0.01
Re(ω_1) @ $u = u_{cr}$	3.516	3.516	3.516	3.516	3.516	3.516	3.516
Im(ω_1) @ $u = u_{cr}$	0.000	0.000	0.000	0.000	0.000	0.000	0.000
Re(ω_2) @ $u = u_{cr}$	22.034	22.035	22.036	22.034	22.034	22.035	22.036
Im(ω_2) @ $u = u_{cr}$	0.000	0.000	0.000	0.000	0.000	0.000	0.000
Re(ω_3) @ $u = u_{cr}$	61.697	61.699	61.701	61.697	61.697	61.699	61.701
Im(ω_3) @ $u = u_{cr}$	0.000	0.000	0.000	0.000	0.000	0.000	0.000

$\alpha = 0.20, \bar{\gamma} = 0.50, \psi = 0.95, \gamma = 0, \bar{\alpha}^* = 0, \bar{\mu}^* = 0, \sigma = 0$							
	No Delay	Delay I	Delay II	Delay III	Delay IV	Delay V	Delay VI
Re(ω_1) @ $u = 1$	3.487	3.497	3.502	3.487	3.487	3.497	3.502
Im(ω_1) @ $u = 1$	-0.019	0.151	0.325	-0.019	-0.020	0.151	0.325
Re(ω_2) @ $u = 1$	22.092	22.153	22.204	22.092	22.092	22.153	22.204
Im(ω_2) @ $u = 1$	-0.020	0.574	1.185	-0.022	-0.023	0.572	1.181
Re(ω_3) @ $u = 1$	61.770	61.946	62.102	61.770	61.770	61.946	62.102
Im(ω_3) @ $u = 1$	-0.020	0.961	1.982	-0.025	-0.029	0.956	1.973
Instability	F (1 st - 3 rd)	F (1 st - 3 rd)	F (1 st - 3 rd)	F (1 st - 3 rd)	F (1 st - 3 rd)	F (1 st - 3 rd)	F (1 st - 3 rd)
u_{cr}	0.01	0.01	0.01	0.01	0.01	0.01	0.01
Re(ω_1) @ $u = u_{cr}$	3.516	3.516	3.516	3.516	3.516	3.516	3.516
Im(ω_1) @ $u = u_{cr}$	0.000	0.000	0.000	0.000	0.000	0.000	0.000
Re(ω_2) @ $u = u_{cr}$	22.034	22.035	22.036	22.034	22.034	22.035	22.036
Im(ω_2) @ $u = u_{cr}$	0.000	0.000	0.000	0.000	0.000	0.000	0.000
Re(ω_3) @ $u = u_{cr}$	61.697	61.699	61.701	61.697	61.697	61.699	61.701
Im(ω_3) @ $u = u_{cr}$	0.000	0.000	0.000	0.000	0.000	0.000	0.000

Table 3.4. *cont'd*

$\alpha = 0.20, \bar{\gamma} = 0.50, \psi = 1.00, \gamma = 0, \bar{\alpha}^* = 0, \bar{\mu}^* = 0, \sigma = 0$							
	No Delay	Delay I	Delay II	Delay III	Delay IV	Delay V	Delay VI
$\text{Re}(\omega_1) @ u = 1$	3.492	3.501	3.507	3.492	3.492	3.501	3.507
$\text{Im}(\omega_1) @ u = 1$	-0.019	0.151	0.325	-0.020	-0.020	0.151	0.325
$\text{Re}(\omega_2) @ u = 1$	22.095	22.156	22.207	22.095	22.095	22.156	22.207
$\text{Im}(\omega_2) @ u = 1$	-0.020	0.574	1.185	-0.022	-0.023	0.572	1.181
$\text{Re}(\omega_3) @ u = 1$	61.772	61.948	62.104	61.772	61.772	61.948	62.104
$\text{Im}(\omega_3) @ u = 1$	-0.020	0.961	1.982	-0.025	-0.029	0.956	1.973
Instability	F (1 st - 3 rd)	F (1 st - 3 rd)	F (1 st - 3 rd)	F (1 st - 3 rd)	F (1 st - 3 rd)	F (1 st - 3 rd)	F (1 st - 3 rd)
u_{cr}	0.01	0.01	0.01	0.01	0.01	0.01	0.01
$\text{Re}(\omega_1) @ u = u_{cr}$	3.516	3.516	3.516	3.516	3.516	3.516	3.516
$\text{Im}(\omega_1) @ u = u_{cr}$	0.000	0.000	0.000	0.000	0.000	0.000	0.000
$\text{Re}(\omega_2) @ u = u_{cr}$	22.034	22.035	22.036	22.034	22.034	22.035	22.036
$\text{Im}(\omega_2) @ u = u_{cr}$	0.000	0.000	0.000	0.000	0.000	0.000	0.000
$\text{Re}(\omega_3) @ u = u_{cr}$	61.697	61.699	61.701	61.697	61.697	61.699	61.701
$\text{Im}(\omega_3) @ u = u_{cr}$	0.000	0.000	0.000	0.000	0.000	0.000	0.000

$\alpha = 0.20, \bar{\gamma} = 0.25, \psi = 0.95, \gamma = 0, \bar{\alpha}^* = 0, \bar{\mu}^* = 0, \sigma = 0$							
	No Delay	Delay I	Delay II	Delay III	Delay IV	Delay V	Delay VI
$\text{Re}(\omega_1) @ u = 1$	3.511	3.521	3.527	3.511	3.511	3.521	3.527
$\text{Im}(\omega_1) @ u = 1$	-0.020	0.150	0.323	-0.020	-0.020	0.150	0.323
$\text{Re}(\omega_2) @ u = 1$	22.032	22.093	22.144	22.032	22.032	22.093	22.144
$\text{Im}(\omega_2) @ u = 1$	-0.020	0.574	1.185	-0.021	-0.023	0.572	1.181
$\text{Re}(\omega_3) @ u = 1$	61.696	61.872	62.028	61.696	61.696	61.872	62.028
$\text{Im}(\omega_3) @ u = 1$	-0.020	0.961	1.983	-0.024	-0.028	0.957	1.974
Instability	F (1 st - 3 rd)	F (1 st - 3 rd)	F (1 st - 3 rd)	F (1 st - 3 rd)	F (1 st - 3 rd)	F (1 st - 3 rd)	F (1 st - 3 rd)
u_{cr}	0.01	0.01	0.01	0.01	0.01	0.01	0.01
$\text{Re}(\omega_1) @ u = u_{cr}$	3.516	3.516	3.516	3.516	3.516	3.516	3.516
$\text{Im}(\omega_1) @ u = u_{cr}$	0.000	0.000	0.000	0.000	0.000	0.000	0.000
$\text{Re}(\omega_2) @ u = u_{cr}$	22.034	22.035	22.036	22.034	22.034	22.035	22.036
$\text{Im}(\omega_2) @ u = u_{cr}$	0.000	0.000	0.000	0.000	0.000	0.000	0.000
$\text{Re}(\omega_3) @ u = u_{cr}$	61.697	61.699	61.701	61.697	61.697	61.699	61.701
$\text{Im}(\omega_3) @ u = u_{cr}$	0.000	0.000	0.000	0.000	0.000	0.000	0.000

$\alpha = 0.20, \bar{\gamma} = 0.25, \psi = 1.00, \gamma = 0, \bar{\alpha}^* = 0, \bar{\mu}^* = 0, \sigma = 0$							
	No Delay	Delay I	Delay II	Delay III	Delay IV	Delay V	Delay VI
$\text{Re}(\omega_1) @ u = 1$	3.516	3.526	3.531	3.516	3.516	3.526	3.531
$\text{Im}(\omega_1) @ u = 1$	-0.020	0.150	0.323	-0.020	-0.020	0.150	0.323
$\text{Re}(\omega_2) @ u = 1$	22.035	22.096	22.146	22.035	22.035	22.096	22.147
$\text{Im}(\omega_2) @ u = 1$	-0.020	0.574	1.184	-0.021	-0.023	0.572	1.181
$\text{Re}(\omega_3) @ u = 1$	61.697	61.874	62.030	61.697	61.697	61.874	62.030
$\text{Im}(\omega_3) @ u = 1$	-0.020	0.961	1.983	-0.024	-0.028	0.957	1.974
Instability	F (1 st - 3 rd)	F (1 st - 3 rd)	F (1 st - 3 rd)	F (1 st - 3 rd)	F (1 st - 3 rd)	F (1 st - 3 rd)	F (1 st - 3 rd)
u_{cr}	0.01	0.01	0.01	0.01	0.01	0.01	0.01
$\text{Re}(\omega_1) @ u = u_{cr}$	3.516	3.516	3.516	3.516	3.516	3.516	3.516
$\text{Im}(\omega_1) @ u = u_{cr}$	0.000	0.000	0.000	0.000	0.000	0.000	0.000
$\text{Re}(\omega_2) @ u = u_{cr}$	22.034	22.035	22.036	22.034	22.034	22.035	22.036
$\text{Im}(\omega_2) @ u = u_{cr}$	0.000	0.000	0.000	0.000	0.000	0.000	0.000
$\text{Re}(\omega_3) @ u = u_{cr}$	61.697	61.699	61.701	61.697	61.697	61.699	61.701
$\text{Im}(\omega_3) @ u = u_{cr}$	0.000	0.000	0.000	0.000	0.000	0.000	0.000

Table 3.5. Values of ω at $u = 1$ and at $u = u_{cr}$ for a system with non-negligible gravity and damping effects computed using model III-C

$\alpha = 0.40, \bar{\gamma} = 0.30, \psi = 0.95, \gamma \neq 0, \bar{\alpha}^* \neq 0, \bar{\mu}^* \neq 0, \sigma \neq 0$							
	No Delay	Delay I	Delay II	Delay III	Delay IV	Delay V	Delay VI
$\text{Re}(\omega_1) @ u = 1$	5.577	5.594	5.611	5.577	5.577	5.594	5.611
$\text{Im}(\omega_1) @ u = 1$	0.025	0.190	0.357	0.025	0.024	0.190	0.357
$\text{Re}(\omega_2) @ u = 1$	24.187	24.249	24.304	24.187	24.187	24.249	24.304
$\text{Im}(\omega_2) @ u = 1$	0.418	1.034	1.668	0.416	0.415	1.032	1.665
$\text{Re}(\omega_3) @ u = 1$	63.952	64.111	64.249	63.952	63.952	64.111	64.250
$\text{Im}(\omega_3) @ u = 1$	1.626	2.629	3.675	1.622	1.618	2.624	3.666
Instability	F (1 st)	F (1 st)	F (1 st)	F (1 st)	F (1 st)	F (1 st)	F (1 st)
u_{cr}	2.11	8.67	8.32	2.09	2.07	8.64	8.20
$\text{Re}(\omega) @ u = u_{cr}$	5.618	8.577	8.895	5.617	5.616	8.604	8.975
$\text{Im}(\omega) @ u = u_{cr}$	0.000	0.000	-0.002	0.000	0.000	-0.001	0.000

$\alpha = 0.40, \bar{\gamma} = 0.30, \psi = 1.00, \gamma \neq 0, \bar{\alpha}^* \neq 0, \bar{\mu}^* \neq 0, \sigma \neq 0$							
	No Delay	Delay I	Delay II	Delay III	Delay IV	Delay V	Delay VI
$\text{Re}(\omega_1) @ u = 1$	5.583	5.600	5.617	5.583	5.583	5.600	5.617
$\text{Im}(\omega_1) @ u = 1$	0.025	0.190	0.357	0.024	0.024	0.189	0.356
$\text{Re}(\omega_2) @ u = 1$	24.192	24.254	24.309	24.192	24.192	24.254	24.309
$\text{Im}(\omega_2) @ u = 1$	0.418	1.034	1.668	0.416	0.415	1.032	1.665
$\text{Re}(\omega_3) @ u = 1$	63.955	64.114	64.252	63.955	63.955	64.114	64.253
$\text{Im}(\omega_3) @ u = 1$	1.626	2.629	3.675	1.622	1.617	2.624	3.666
Instability	F (1 st)	F (1 st)	F (1 st)	F (1 st)	F (1 st)	F (1 st)	F (1 st)
u_{cr}	2.10	8.66	8.31	2.08	2.06	8.63	8.20
$\text{Re}(\omega) @ u = u_{cr}$	5.642	8.580	8.899	5.640	5.639	8.606	8.973
$\text{Im}(\omega) @ u = u_{cr}$	0.000	0.000	-0.001	0.000	0.000	-0.001	-0.001

$\alpha = 0.20, \bar{\gamma} = 0.50, \psi = 0.95, \gamma \neq 0, \bar{\alpha}^* \neq 0, \bar{\mu}^* \neq 0, \sigma \neq 0$							
	No Delay	Delay I	Delay II	Delay III	Delay IV	Delay V	Delay VI
$\text{Re}(\omega_1) @ u = 1$	5.548	5.565	5.582	5.548	5.548	5.565	5.582
$\text{Im}(\omega_1) @ u = 1$	0.025	0.192	0.361	0.025	0.025	0.192	0.361
$\text{Re}(\omega_2) @ u = 1$	24.303	24.364	24.420	24.303	24.303	24.365	24.420
$\text{Im}(\omega_2) @ u = 1$	0.416	1.032	1.667	0.414	0.412	1.031	1.664
$\text{Re}(\omega_3) @ u = 1$	64.104	64.263	64.401	64.104	64.104	64.263	64.402
$\text{Im}(\omega_3) @ u = 1$	1.623	2.626	3.672	1.619	1.614	2.621	3.662
Instability	F (1 st)	B (2 nd)	F (1 st)	F (1 st)	F (1 st)	B (2 nd)	F (1 st)
u_{cr}	2.61	16.08	13.60	2.55	2.50	16.08	12.60
$\text{Re}(\omega) @ u = u_{cr}$	5.446	0.000	15.702	5.451	5.455	0.000	15.159
$\text{Im}(\omega) @ u = u_{cr}$	0.000	0.000	0.000	0.000	0.000	0.000	-0.001

$\alpha = 0.20, \bar{\gamma} = 0.50, \psi = 1.00, \gamma \neq 0, \bar{\alpha}^* \neq 0, \bar{\mu}^* \neq 0, \sigma \neq 0$							
	No Delay	Delay I	Delay II	Delay III	Delay IV	Delay V	Delay VI
$\text{Re}(\omega_1) @ u = 1$	5.551	5.568	5.585	5.551	5.551	5.568	5.585
$\text{Im}(\omega_1) @ u = 1$	0.025	0.192	0.361	0.025	0.025	0.192	0.361
$\text{Re}(\omega_2) @ u = 1$	24.305	24.367	24.422	24.305	24.305	24.367	24.422
$\text{Im}(\omega_2) @ u = 1$	0.416	1.032	1.667	0.414	0.412	1.030	1.664
$\text{Re}(\omega_3) @ u = 1$	64.106	64.264	64.403	64.106	64.106	64.265	64.403
$\text{Im}(\omega_3) @ u = 1$	1.623	2.626	3.672	1.619	1.614	2.621	3.662
Instability	F (1 st)	F (1 st)	F (1 st)	F (1 st)	F (1 st)	F (1 st)	F (1 st)
u_{cr}	2.59	18.86	13.60	2.53	2.48	17.70	12.60
$\text{Re}(\omega) @ u = u_{cr}$	5.468	18.888	15.701	5.472	5.476	18.157	15.158
$\text{Im}(\omega) @ u = u_{cr}$	0.000	-0.001	0.000	0.000	0.000	-0.001	-0.001

Table 3.5. *cont'd*

$\alpha = 0.20, \bar{\gamma} = 0.25, \psi = 0.95, \gamma \neq 0, \bar{\alpha}^* \neq 0, \bar{\mu}^* \neq 0, \sigma \neq 0$							
	No Delay	Delay I	Delay II	Delay III	Delay IV	Delay V	Delay VI
Re(ω_1) @ $u = 1$	5.564	5.580	5.597	5.564	5.564	5.580	5.597
Im(ω_1) @ $u = 1$	0.025	0.191	0.359	0.025	0.025	0.191	0.359
Re(ω_2) @ $u = 1$	24.249	24.311	24.366	24.249	24.249	24.311	24.366
Im(ω_2) @ $u = 1$	0.417	1.033	1.668	0.415	0.414	1.031	1.665
Re(ω_3) @ $u = 1$	64.032	64.191	64.329	64.033	64.033	64.191	64.330
Im(ω_3) @ $u = 1$	1.625	2.627	3.673	1.621	1.616	2.623	3.665
Instability	F (1 st)	F (1 st)	F (1 st)	F (1 st)	F (1 st)	F (1 st)	F (1 st)
u_{cr}	2.30	14.62	11.69	2.27	2.24	14.18	11.14
Re(ω) @ $u = u_{cr}$	5.551	11.281	11.295	5.551	5.552	11.284	11.297
Im(ω) @ $u = u_{cr}$	0.000	-0.001	0.000	0.000	0.000	-0.001	0.000

$\alpha = 0.20, \bar{\gamma} = 0.25, \psi = 1.00, \gamma \neq 0, \bar{\alpha}^* \neq 0, \bar{\mu}^* \neq 0, \sigma \neq 0$							
	No Delay	Delay I	Delay II	Delay III	Delay IV	Delay V	Delay VI
Re(ω_1) @ $u = 1$	5.566	5.583	5.600	5.566	5.566	5.583	5.600
Im(ω_1) @ $u = 1$	0.025	0.191	0.359	0.025	0.025	0.191	0.359
Re(ω_2) @ $u = 1$	24.251	24.313	24.368	24.251	24.251	24.313	24.369
Im(ω_2) @ $u = 1$	0.417	1.033	1.668	0.415	0.414	1.031	1.665
Re(ω_3) @ $u = 1$	64.034	64.193	64.331	64.034	64.034	64.193	64.332
Im(ω_3) @ $u = 1$	1.625	2.627	3.673	1.620	1.616	2.623	3.665
Instability	F (1 st)	F (1 st)	F (1 st)	F (1 st)	F (1 st)	F (1 st)	F (1 st)
u_{cr}	2.29	14.62	11.69	2.26	2.23	14.18	11.14
Re(ω) @ $u = u_{cr}$	5.566	11.277	11.293	5.566	5.566	11.280	11.296
Im(ω) @ $u = u_{cr}$	0.000	-0.001	0.000	0.000	0.000	-0.001	0.000

However, Fig. 3.6 demonstrates that this error has a small impact on the critical flow velocity results since the correct values for the lateral delay, $\bar{\tau}_\ell$, fall within the range $10^{-2} \text{ s} \leq \bar{\tau}_\ell \leq 10^{-1} \text{ s}$, where u_{cr} is found to vary only slightly. Hence, it was deemed unproductive to repeat the relevant calculations in Tables 3.3, 3.4, and 3.5. Nevertheless, a more realistic $\bar{\tau}_\ell$ would be within the range $10^{-5} \text{ s} \leq \bar{\tau}_\ell \leq 10^{-3} \text{ s}$ because this would result in lower critical flow velocities.

Fig. 3.7 presents a typical Argand diagram using model III-C, in which gravity and damping effects are included, and a five-mode Galerkin approximation for the first three modes as a function of u for an aspirating pipe with $\alpha = 0.40$, $\bar{\gamma} = 0.30$, $\psi = 1.00$, $\kappa = 0.60$, $\bar{\tau}_a = D_i/U_{cr} = 1.52 \times 10^{-4} \text{ s}$, and $\bar{\tau}_\ell = 10^{-3} \text{ s}$. Note that the lateral delay, $\bar{\tau}_\ell$, was chosen rather arbitrarily based on Fig. 3.6. From Fig. 3.7, it can be observed that the system becomes unstable by flutter via a Hopf bifurcation in its first mode at $u_{cr} = 2.63$, while the second and third modes are subject to flow-induced damping for $0 \leq u \leq 12$.

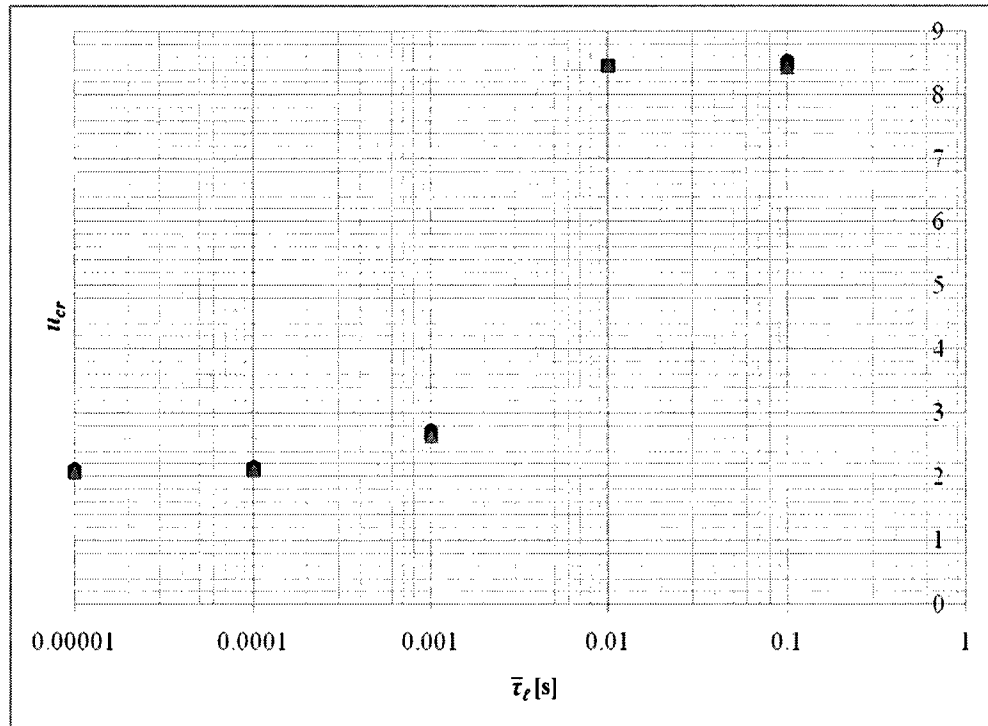


Figure 3.6. Nondimensional critical flow velocity, u_{cr} , as a function of the lateral delay,

$\bar{\tau}_\ell$, for $\bullet \bar{\tau}_a = 0$, $\blacksquare \bar{\tau}_a = \frac{1}{2} D_i / U_{cr} = 7.62 \times 10^{-5} s$, $\blacktriangle \bar{\tau}_a = D_i / U_{cr} = 1.52 \times 10^{-4} s$.

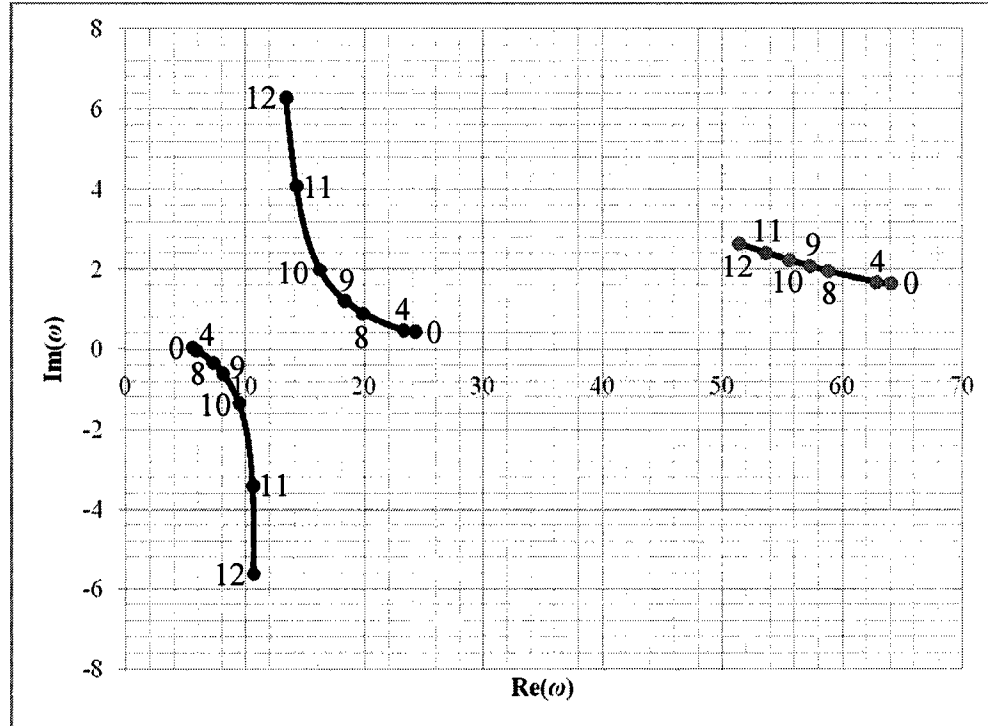


Figure 3.7. Argand diagram as a function of u for $\alpha = 0.40$, $\bar{\gamma} = 0.30$, $\psi = 1.00$, $\kappa = 0.60$,

$\bar{\tau}_a = 1.52 \times 10^{-4} s$, and $\bar{\tau}_\ell = 10^{-3} s$ using a five-mode Galerkin approximation.

3.3 Experimental Investigation

3.3.1 *Experimental apparatus*

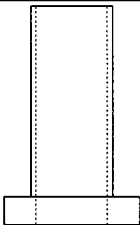
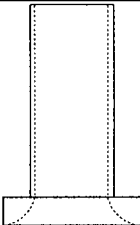
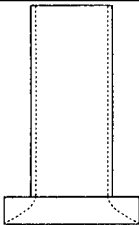
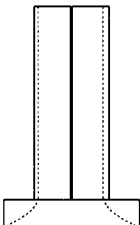
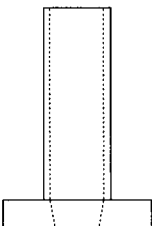
The experiments of a cantilevered pipe aspirating fluid were conducted using air, as opposed to water, the usual choice for the case of a cantilevered pipe conveying fluid. Earlier water experiments led to unconvincing results for two main reasons. Firstly, dissipation to the surrounding fluid is increased when the pipe is submerged in water, a fluid that is more viscous than air. Therefore, oscillations that are damped out in water become discernible in air. Secondly, with water flow, a shell-type buckling collapse occurs near the clamped end of the cantilevered pipe, which is due to a large transmural pressure difference as the flow velocity is increased; this may be eliminated if air is chosen as the working fluid.

The present experiments were performed with three flexible pipes: (i) an ordinary elastomer pipe, (ii) a stiffened elastomer pipe, and (iii) a denser elastomer pipe. The second pipe was stiffened by inserting a thin metal blade along the length of the pipe during the casting process in order to confine the motion of the pipe to a two-dimensional plane. Note that, if the ordinary elastomer pipe is used, the system exhibits three-dimensional behaviour. The third pipe was made denser, and thus heavier, by introducing fine copper particles within the two-part silicone rubber mixture during the casting process, and was also cut shorter in length. The reader is referred to Appendix A for a detailed procedure of the conventional casting process. Table 3.6 presents the geometrical and physical properties of each flexible elastomer pipe described above. Note that f_n and δ_n are the natural frequency and log decrement of the pipe in the n th mode. For higher modes, i.e. $n \geq 4$, the log decrement of the system is approximated by the linear regression line that best fits the data for the first three modes. The reader is referred to Appendix B for specific information concerning the determination of the natural frequencies, flexural rigidity, and logarithmic decrements of the cantilevered pipe system using experimental techniques. Additionally, the pipes were fitted with differently profiled end-pieces, which are illustrated in Table 3.7, in order to prevent what appears to

Table 3.6. The geometrical and physical properties of the pipes

Properties	Pipe 1	Pipe 2	Pipe 3
D_o [m]	0.0159	0.0159	0.0159
D_i [m]	0.00934	0.00794	0.00635
L [m]	0.401	0.412	0.346
EI [N·m ²]	7.63×10^{-3}	8.25×10^{-3}	1.10×10^{-2}
m [kg/m]	0.144	0.184	0.355
M [kg/m]	$f(\text{fluid density})$	$f(\text{fluid density})$	$f(\text{fluid density})$
M_a [kg/m]	$f(\text{fluid density})$	$f(\text{fluid density})$	$f(\text{fluid density})$
β [-]	$f(\text{fluid density})$	$f(\text{fluid density})$	$f(\text{fluid density})$
γ [-]	$f(\text{fluid density})$	$f(\text{fluid density})$	$f(\text{fluid density})$
$\bar{\alpha}^*$ [-]	0.00030	0.00030	0.00023
$\bar{\mu}^*$ [-]	0.03578	0.03914	0.04863
f_1 [Hz]	1.27	1.20	1.34
f_2 [Hz]	5.47	5.08	5.86
f_3 [Hz]	14.8	12.5	15.6
δ_1 [-]	0.0423	0.0438	0.0587
δ_2 [-]	0.119	0.101	0.141
δ_3 [-]	0.160	0.215	0.183
δ_n [-]	$0.0590n - 0.0107$	$0.0854n - 0.0511$	$0.0623n + 0.0030$

Table 3.7. The various end-pieces used during the air experiments

	End-piece A	End-piece B	End-piece C
Pipe 1			
Pipe 2			
Pipe 3			

be either a shell-type flutter or dynamic divergence instability, which produces a very loud noise, followed quickly afterwards by a shell-type buckling collapse at the free end of the pipe when the flow velocity attained $u \approx 6.59$ in an experiment with pipe 1. The various profiled end-pieces were also used for better fluid entry at the free end of the cantilevered pipe.

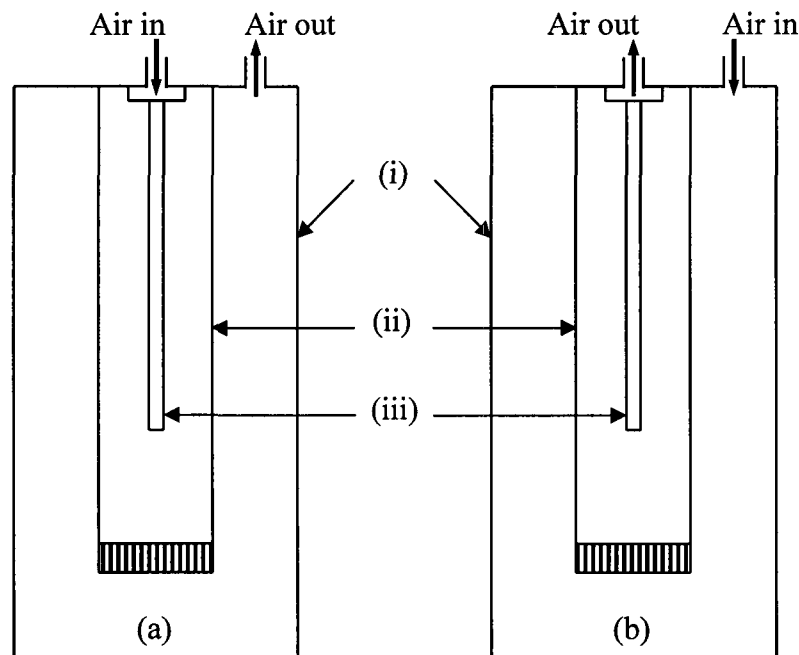


Figure 3.8. (a) Discharging configuration; (b) aspirating configuration.

(i) Large steel tank; (ii) plexiglas protective conduit; (iii) flexible elastomer pipe.

The experimental set-up consists primarily of (i) a large steel tank, (ii) an internal plexiglas flow-guiding protective conduit, (iii) an *Optron* system, which is a non-contact electro-optical biaxial displacement follower system that consists of an optical head and a control unit, and (iv) a flexible elastomer pipe. The large steel tank is the one built by Païdoussis in 1986 at McGill University to conduct experiments involving a cantilevered pipe aspirating water [see Chapter 1]. The author is indebted to Dana Blake Giacobbi for removing the rust that had formed over the years, and also painting the interior surface of the tank, so that it may be used for experiments once again. The tank, which possesses a plexiglas window for viewing and recording purposes, as well as three pressure gauges located at three different locations, can easily be switched to accommodate either a discharging or an aspirating cantilevered pipe, as shown in Fig. 3.8. The internal plexiglas

flow-guiding protective conduit (15 cm \times 15 cm in internal cross-section) is placed within the tank, and attached by eight bolts to the top cover of the tank, such that it appears suspended. The combination of a screen, a honeycomb, and an additional screen is found at the bottom end of the conduit for flow-straightening purposes. This ensures that the air entering the conduit does not disturb nor perturb the pipe during experiments.

The *Optron* system is used in combination with *LabVIEW* to acquire a time signal of the motion of the pipe at various flow velocities. The acquired time signals are then analysed using *MATLAB* to extract useful information, or more specifically, the frequency and amplitude of oscillation of the cantilevered pipe at a particular flow velocity. Note that the *Optron* system must be calibrated before each experiment so that the amplitude scale of a time signal corresponds to a displacement in millimetres rather than a voltage. The reader is referred to Appendices C, D, and E for information regarding the displacement calibration of the *Optron* system, the experimental measurement of the flow velocity, and the experimental measurement of the frequency of oscillation of the system.

3.3.2 *Experimental procedure*

The procedure for a typical air experiment involving an aspirating cantilevered pipe is outlined below. Figs. 3.9 and 3.10 should be consulted as they provide some useful information.

1. Mount and clamp a flexible elastomer pipe at one end to the brass support that is located at the air flow outlet, and attached by three bolts to the top cover of the large steel tank. Note that a pressure gauge and a muffler are also attached to the brass support.
2. Connect the control unit, the low-pass filter, and the light source to power outlets with the power cords provided.
3. Connect the control unit to the optical head with the appropriate cable provided.
4. Connect the control unit to the low-pass filter with a BNC cable. Set the cut-off frequency on the low-pass filter to an appropriate value, such as 50 Hz.
5. Connect the low-pass filter to the data acquisition device with a BNC cable.
6. Connect the data acquisition device to a computer with the USB cable provided.

7. Open *LabVIEW* and load SCMEAS.VI. Set the count to an appropriate value, such as 24 000, set the rate to 400, and set the range to ± 10 V.
8. Observe the pipe through the viewer of the optical head. Position and adjust the optical head so that the desired target, which is a point that lies along the length of the pipe and usually corresponds to the free end, is in sharp focus.
9. Set the horizontal target phase switch to either light to the right or light to the left. Set the Filter to OFF and set the Power/Mode to LIGHT LEVEL on the control unit.
10. Position the optical head so that the centre of the viewer is located within the darkest area of the target. Adjust the LOCK ON with a screwdriver until the horizontal meter reads -20% .
11. Position the optical head so that the centre of the viewer is located within the lightest area of the target. Adjust the light source, and/or the lens aperture of the optical head, and/or the high voltage on the control unit with a screwdriver until the horizontal meter reads $+40\%$.
12. Set the Power/Mode to HORIZONTAL on the control unit.
13. Calibrate the *Optron* system so that the amplitude scale of the resulting time signals corresponds to a displacement in millimetres rather than a voltage [see Appendix C].
14. Position the optical head so that the horizontal meter reads 0% .
15. Attach the braided hose, which is connected to a pressurized reservoir, to the air inlet.
16. Open the main air valve that supplies the laboratory with compressed air from a source located in the basement of the Macdonald Engineering Building of McGill University.
17. Verify that manometer valve 3 is open. Open manometer valves 1 and 2 together. Close manometer valve 3. Note that a water (or mercury) manometer is used to measure the difference between the upstream and downstream pressure of the orifice plate. Refer to Figs. 3.9 and 3.10.
18. Increase the flow velocity in incremental steps using the air control valve. At each step, run SCMEAS.VI in *LabVIEW*, record the values of P_1 , $\Delta P = P_1 - P_2$, P_3 , P_4 , P_5 , T , and estimate the frequency, f , with a chronometer and the maximum amplitude, A , with a ruler that is glued to the acrylic glass protective housing. Refer to Fig. 3.10.

19. Decrease the flow velocity to zero using the air control valve, and then close the main air valve. Close manometer valves 1 and 2 together. Open manometer valve 3.
20. Post-process the recorded time signals in *MATLAB* to obtain the frequency and the amplitude of oscillation of the system at each recorded step.

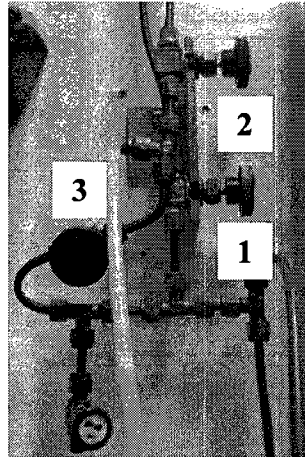


Figure 3.9. Schematic of the manometer valves.

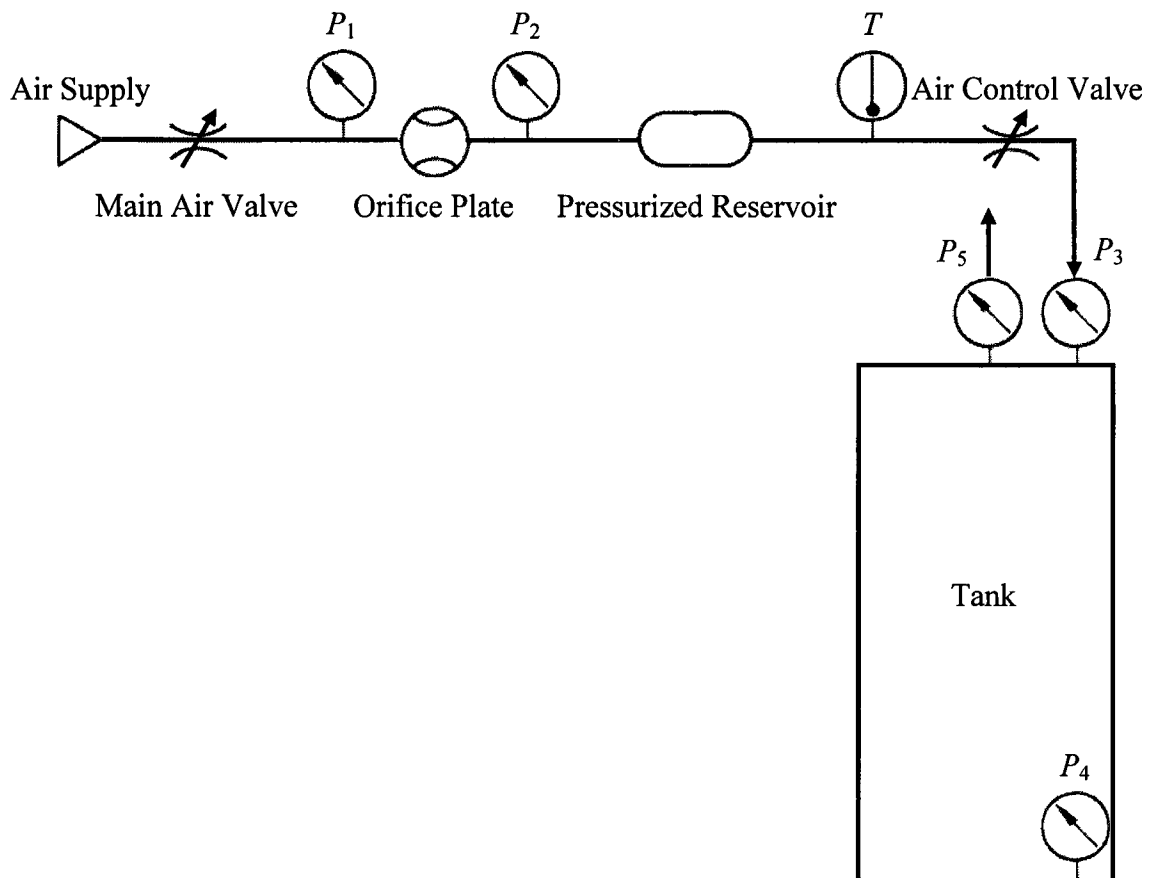


Figure 3.10. Schematic of the experimental set-up.

3.3.3 Experimental results

Table 3.8 presents the numerical values of some key theoretical and experimental results, such as the multiplicative factors to switch from u to U in m/s and ω to f in Hz, the critical flow velocities for flutter and critical frequencies of oscillation using model III-C with parameters $\alpha = 0.40$, $\bar{\gamma} = 0.30$, $\psi = 1.00$, $\kappa = 0.60$, $\bar{\tau}_a = D_i/U_{cr}$, and $\bar{\tau}_\ell = 10^{-3}$ s, and the experimental flow velocities, amplitudes, and frequencies that were recorded during the aspirating pipe experiments. Note that the multiplicative factors are approximate since they are based on the average air density in and surrounding the pipe for a particular experiment. However, the experimental results were plotted using the true multiplicative factors, which vary for each pipe and each flow velocity recorded. Note that the subscripts i and f in Table 3.8 refer to the *initial* and *final* values recorded in an experiment, respectively.

The experimental results for ten separate experiments involving a cantilevered pipe aspirating fluid are presented in Figs. 3.11 to 3.20. Typically, a bifurcation diagram of amplitude versus nondimensional flow velocity, and a diagram of frequency versus nondimensional flow velocity are presented in each figure. Note that the time history signals were generally obtained for a point located close to the free end of the pipe; the exact location is mentioned in Figs. 3.11 to 3.20. Furthermore, each experiment is labelled based on the pipe tested, as well as the end-piece used. For example, Experiment 1A refers to the use of pipe 1 and end-piece A, as identified in Table 3.7. Note, however, that the letter X in Experiment 1X refers to the use of no end-piece, which always results in shell-type flutter and buckling instabilities at the free end of the pipe. If available, visual estimates for frequency and amplitude are also included in Figs. 3.11 to 3.20.

In general, the amplitude of oscillation of the system increases as the flow velocity is increased. More specifically, at low flow velocities, the amplitude grows slowly, but at higher flow velocities, the amplitude grows much quicker. Note that pipe 1 exhibits the largest amplitudes, while pipe 3 exhibits the smallest. Thus the question remains: *Does a cantilevered pipe aspirating fluid lose stability by flutter at small flow velocities?* The answer is *yes*, if one considers a flow velocity of approximately 60 m/s to be small. Unfortunately, smaller flow velocities cannot be attained with the experimental set-up

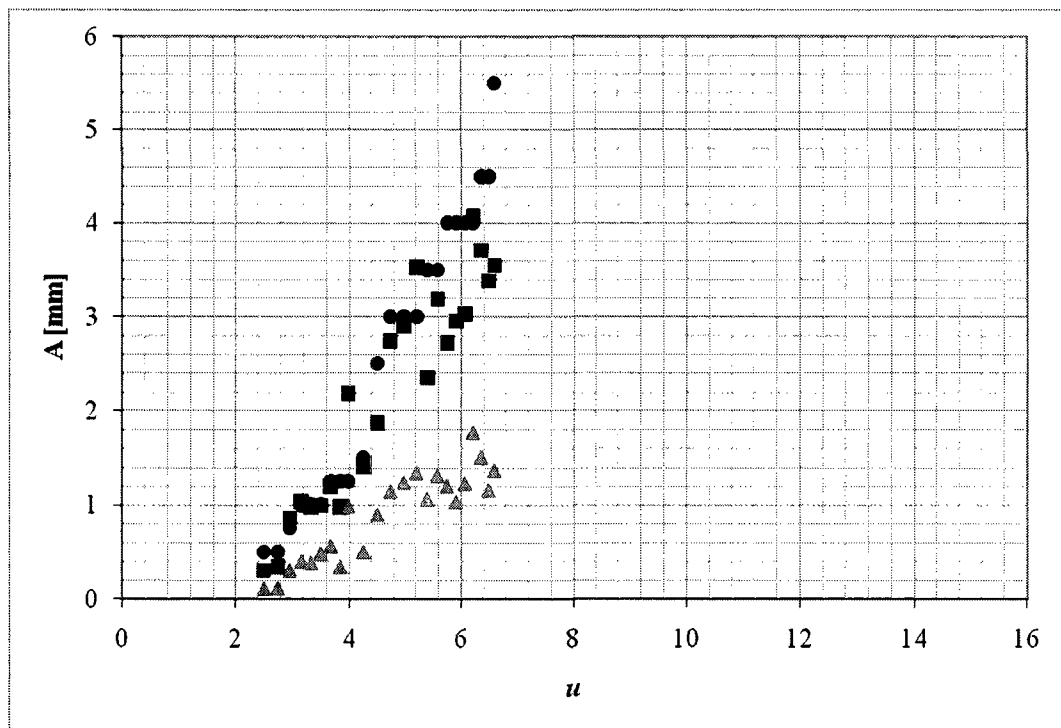
currently being used because of an unstable and inadequate air flow supply from the mains at lower flow velocities. However, it can definitely be said that the cantilevered pipe aspirating fluid does flutter for all measurable flow velocities. The numerical results of Giacobbi (2007) and Giacobbi *et al.* (2008b) also confirm this.

Furthermore, although it is tempting to explain the non-zero amplitude measurements at low flow velocities with either the presence of flow irregularities or structural imperfections, the frequency versus nondimensional flow velocity graphs do provide some additional valuable insight. In every experiment, the frequency remains

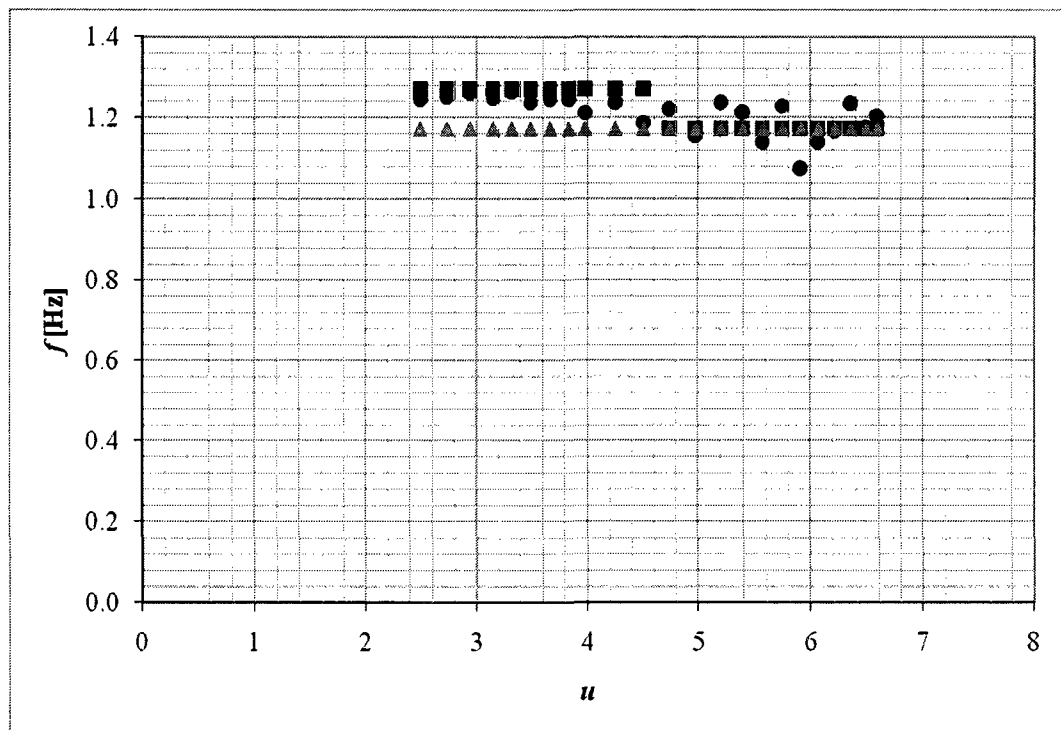
Table 3.8. Key results including multiplicative factors, vibration amplitudes, flow velocities, and vibration frequencies

Experiment	Multiplicative factors		Theoretical critical values		Experimental flow velocities		Experimental max amplitudes	
	$u \rightarrow U$	$\omega \rightarrow f$	u_{cr}	$Re(\omega_{cr})$	$u_i = u_{cr}$	u_f	A_i [mm]	A_f [mm]
1X – Run #1	23.2	0.228	2.61	5.69	2.49	6.58	0.312	3.55
1A – Run #1	22.7	0.227	2.58	5.68	2.54	10.0	0.945	18.8
1A – Run #2	21.8	0.227	2.49	5.67	2.49	10.4	0.369	13.4
1A – Run #3	21.8	0.227	2.48	5.67	2.49	10.3	N/A	N/A
1B – Run #1	21.9	0.227	2.50	5.67	2.49	11.0	0.194	15.0
1C – Run #1	22.0	0.227	2.52	5.68	2.60	11.0	0.616	11.4
2A – Run #1	21.6	0.198	2.89	6.15	2.81	9.38	0.124	2.97
2A – Run #2	24.7	0.198	3.27	6.19	2.84	7.50	0.0782	2.28
2A – Run #3	23.4	0.198	3.11	6.17	2.83	8.39	0.125	2.58
3A – Run #1	38.6	0.234	6.06	6.49	1.96	5.68	0.0627	0.445

Experiment	Experimental rms amplitudes		Experimental frequencies					
	A_i [mm]	A_f [mm]	(PSD – 8 windows) [Hz]			(PSD – 16 windows) [Hz]		
			1	2	3	1	2	3
1X – Run #1	0.107	1.38	1.27	1.17	None	1.17	None	None
1A – Run #1	0.372	6.25	1.17	1.07	0.977	1.17	0.977	None
1A – Run #2	0.151	5.97	1.17	1.07	0.977	1.17	0.977	None
1A – Run #3	N/A	N/A	1.17	1.07	0.977	1.17	0.977	None
1B – Run #1	0.0663	5.40	1.17	1.07	0.977	1.17	0.977	None
1C – Run #1	0.202	3.84	1.17	1.07	0.977	1.17	0.977	None
2A – Run #1	0.0547	1.12	1.07	None	None	1.17	0.977	None
2A – Run #2	0.0291	0.967	1.07	None	None	1.17	0.977	None
2A – Run #3	0.0563	1.11	1.07	None	None	1.17	0.977	None
3A – Run #1	0.0176	0.169	1.37	1.27	None	1.37	None	None

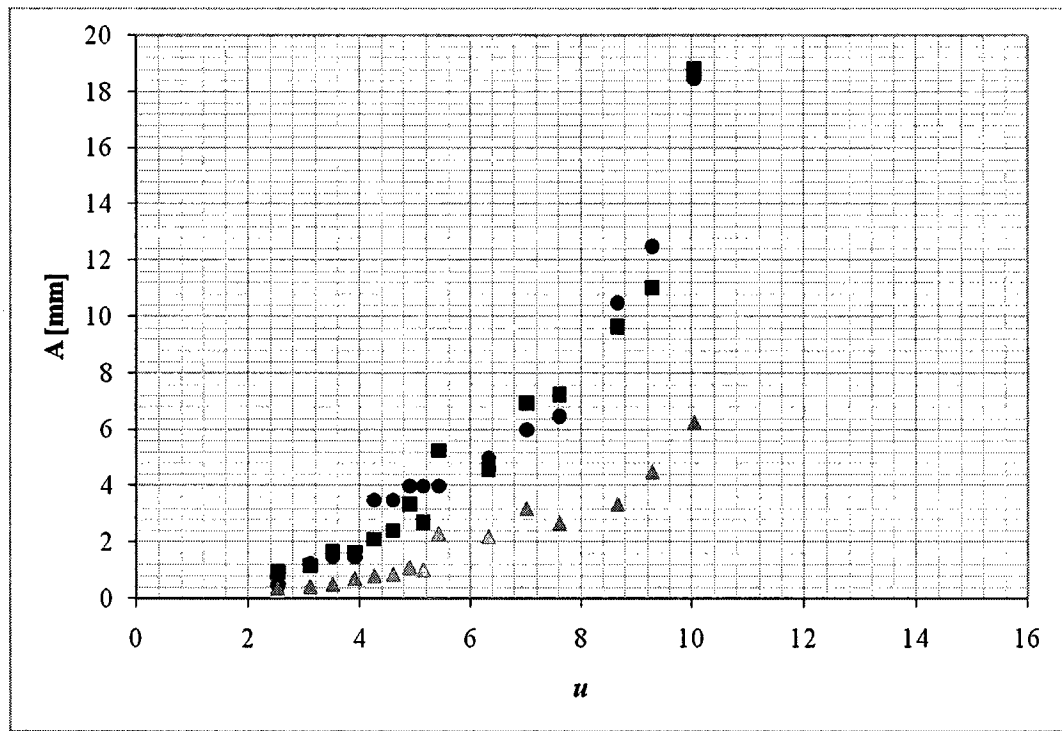


(a)

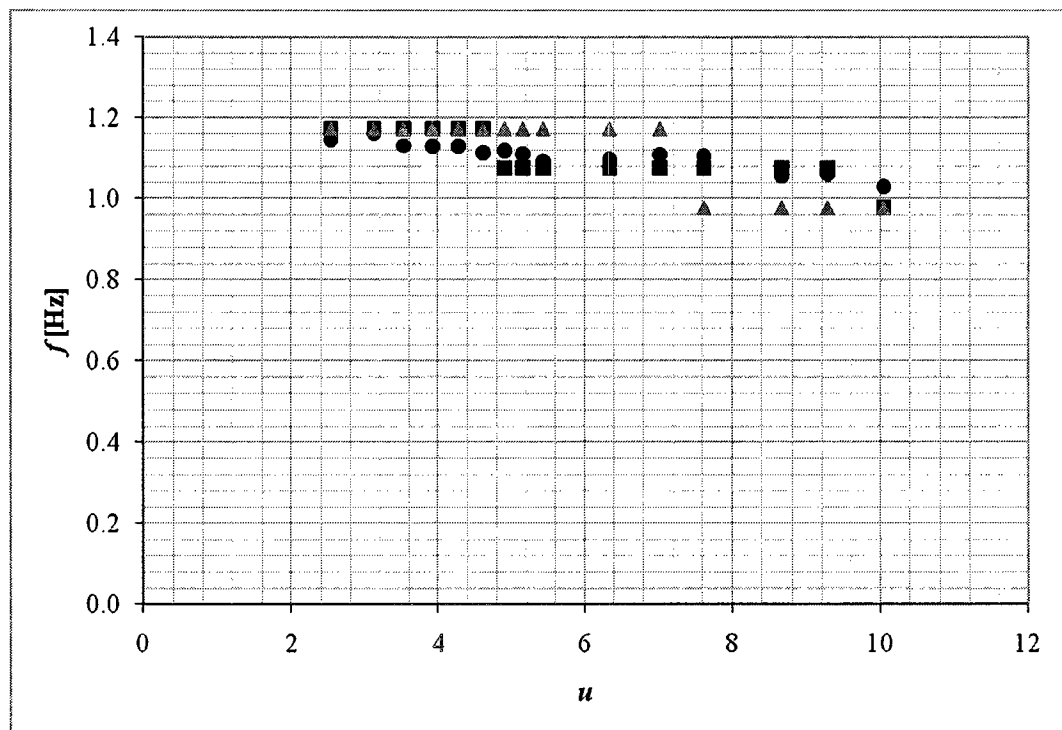


(b)

Figure 3.11. Results of Experiment 1X – Run #1 measured at the free end of the pipe.
 (a) amplitude versus u : ● ruler estimate, ■ max amplitude, ▲ rms amplitude; (b) frequency versus u : ● chronometer estimate, ■ PSD (8 windows), ▲ PSD (16 windows).

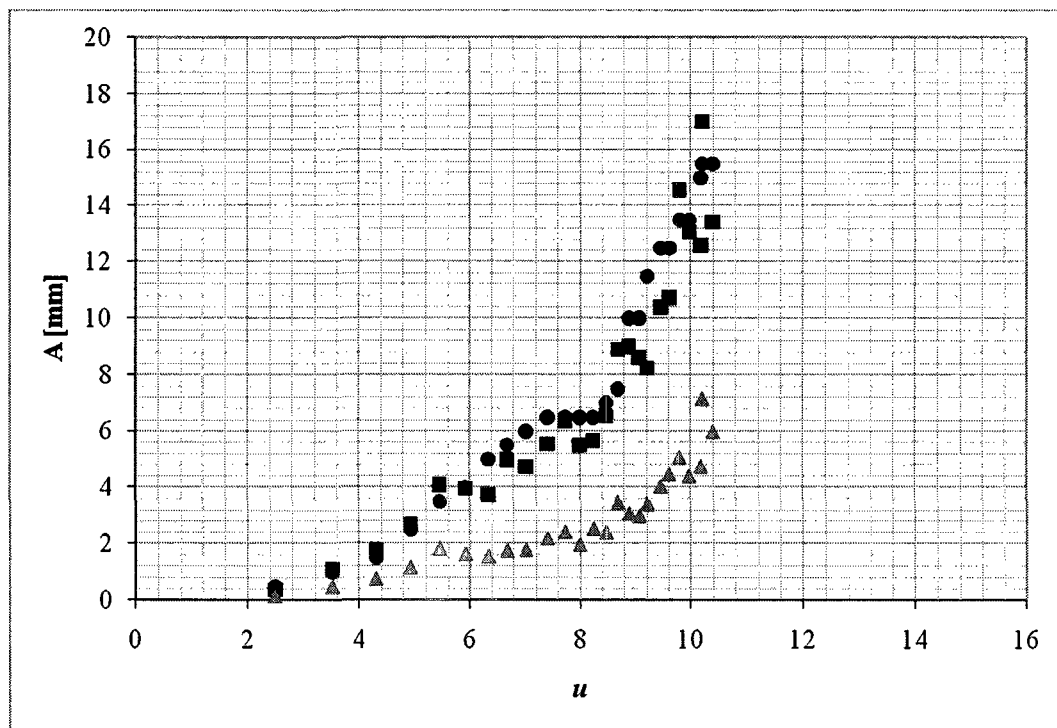


(a)

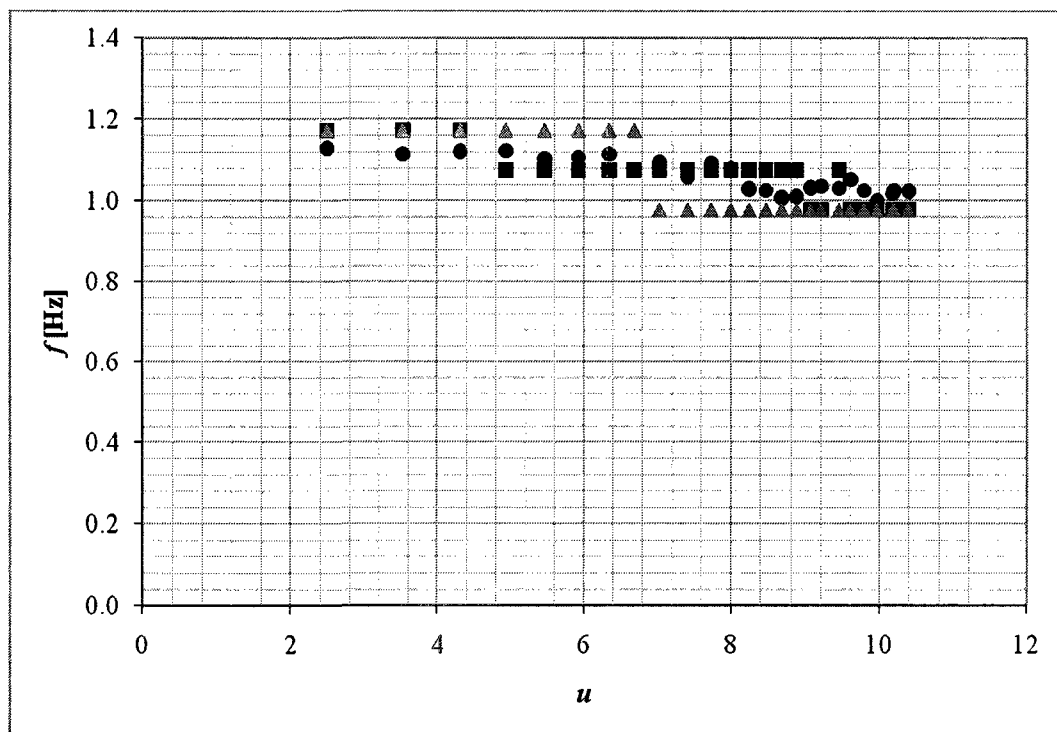


(b)

Figure 3.12. Results of Experiment 1A – Run #1 measured 5 mm above the free end of the pipe. (a) amplitude versus u : ● ruler estimate, ■ max amplitude, ▲ rms amplitude; (b) frequency versus u : ● chronometer estimate, ■ PSD (8 windows), ▲ PSD (16 windows).



(a)



(b)

Figure 3.13. Results of Experiment 1A – Run #2 measured 5 mm above the free end of the pipe. (a) amplitude versus u : ● ruler estimate, ■ max amplitude, ▲ rms amplitude; (b) frequency versus u : ● chronometer estimate, ■ PSD (8 windows), ▲ PSD (16 windows).

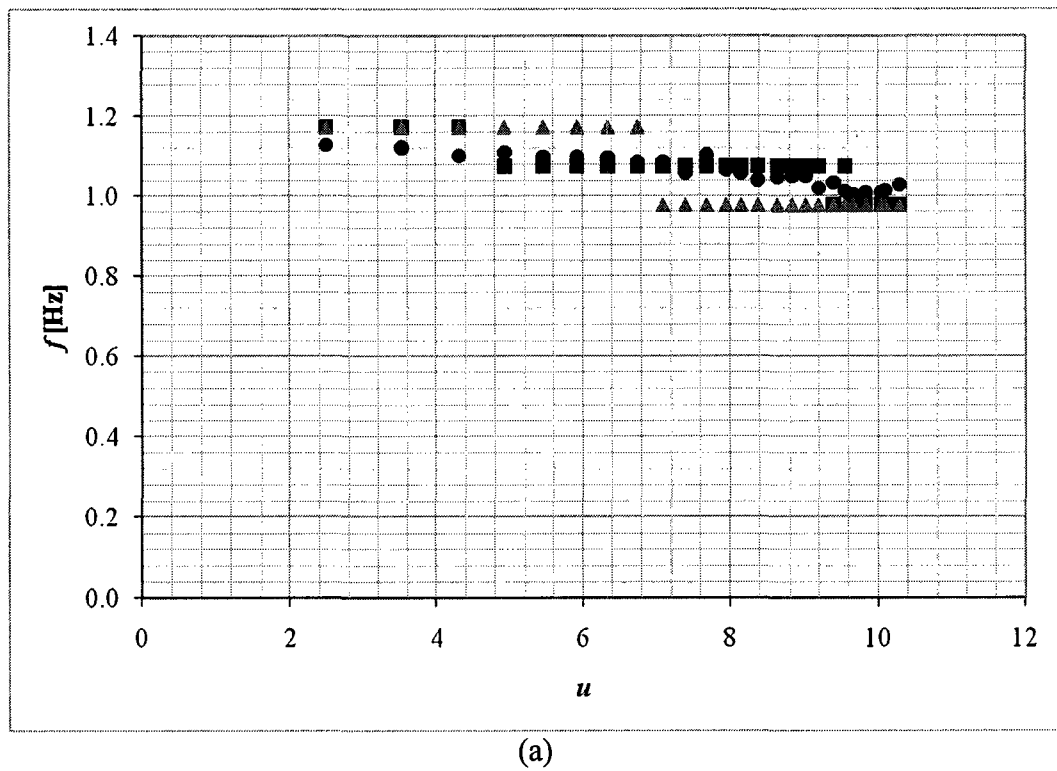
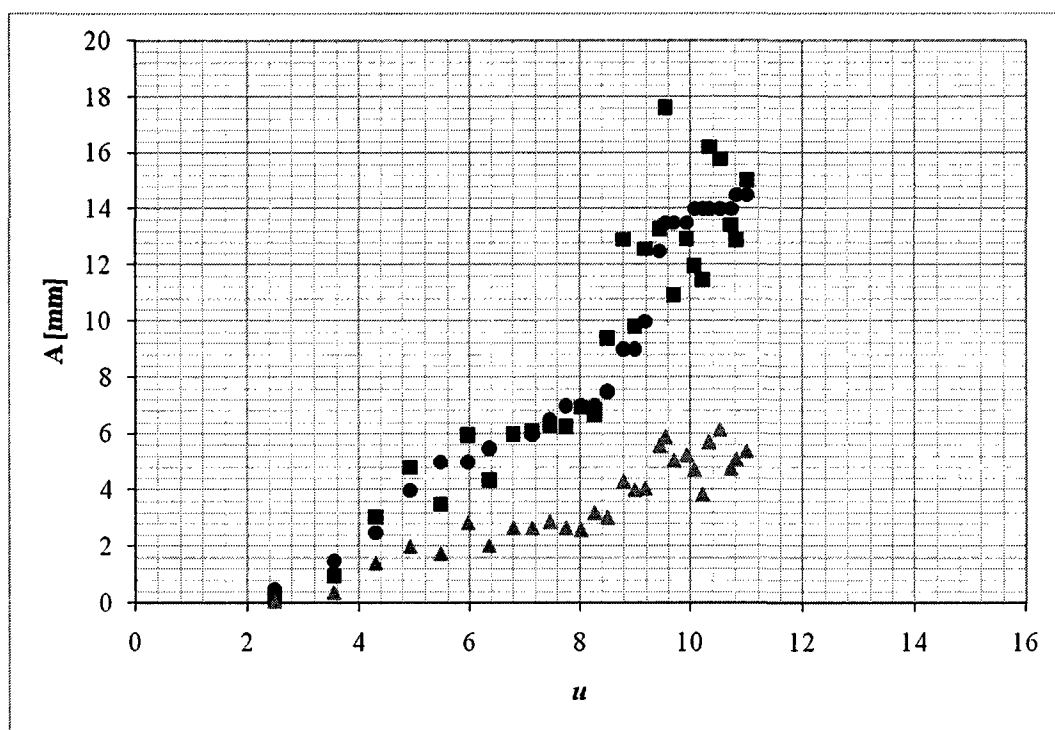
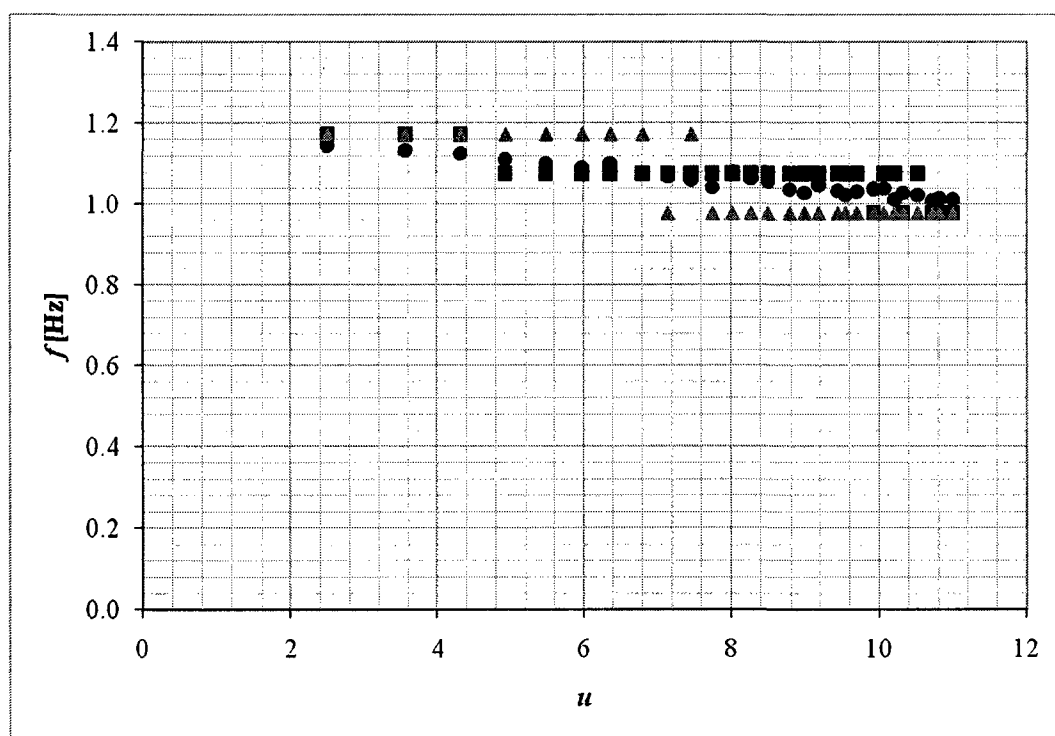


Figure 3.14. Results of Experiment 1A – Run #3 measured 76 mm above the free end of the pipe. (a) frequency versus u : ● chronometer estimate, ■ PSD (8 windows), ▲ PSD (16 windows).

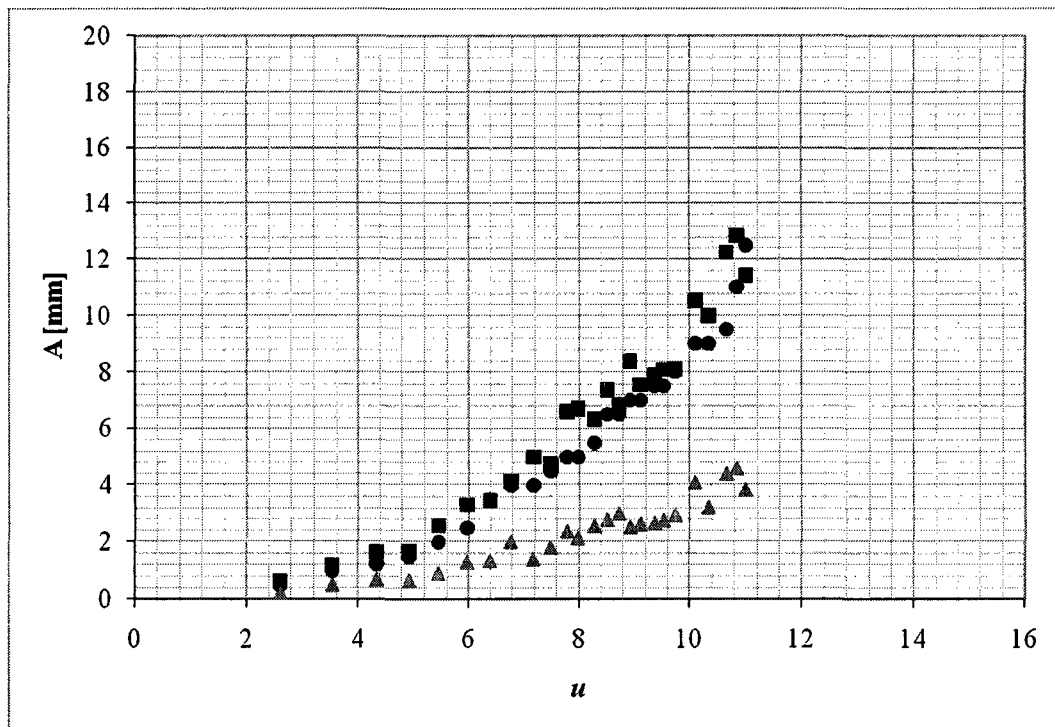


(a)

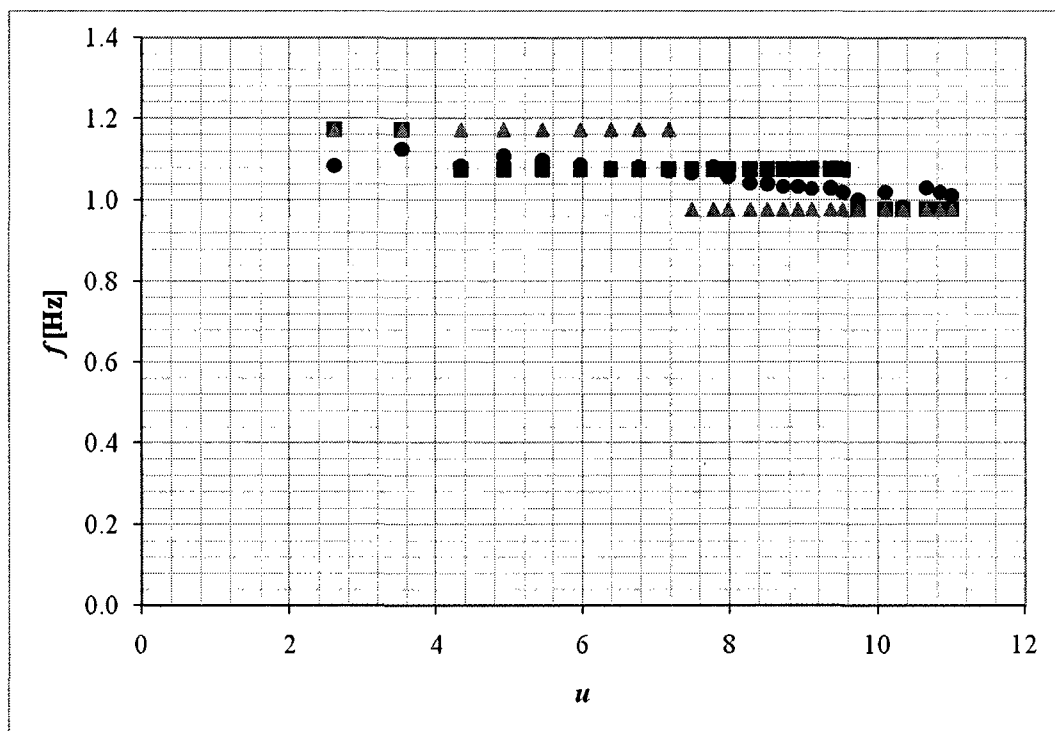


(b)

Figure 3.15. Results of Experiment 1B – Run #1 measured 5 mm above the free end of the pipe. (a) amplitude versus u : ● ruler estimate, ■ max amplitude, ▲ rms amplitude; (b) frequency versus u : ● chronometer estimate, ■ PSD (8 windows), ▲ PSD (16 windows).

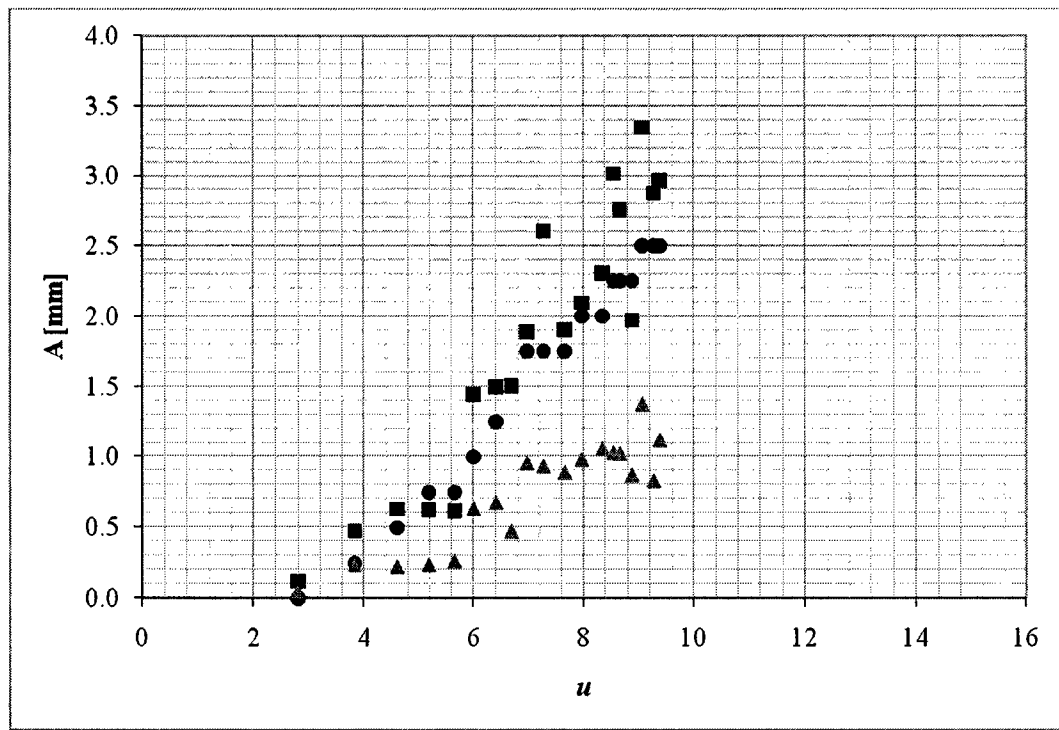


(a)

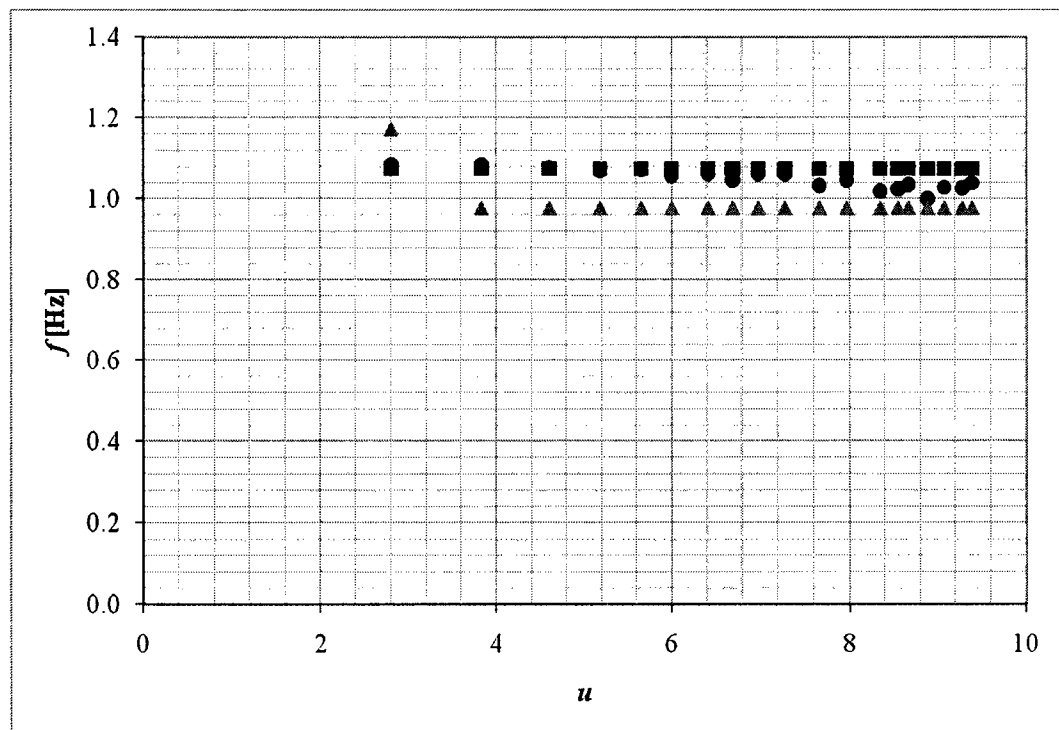


(b)

Figure 3.16. Results of Experiment 1C – Run #1 measured 5 mm above the free end of the pipe. (a) amplitude versus u : ● ruler estimate, ■ max amplitude, ▲ rms amplitude; (b) frequency versus u : ● chronometer estimate, ■ PSD (8 windows), ▲ PSD (16 windows).

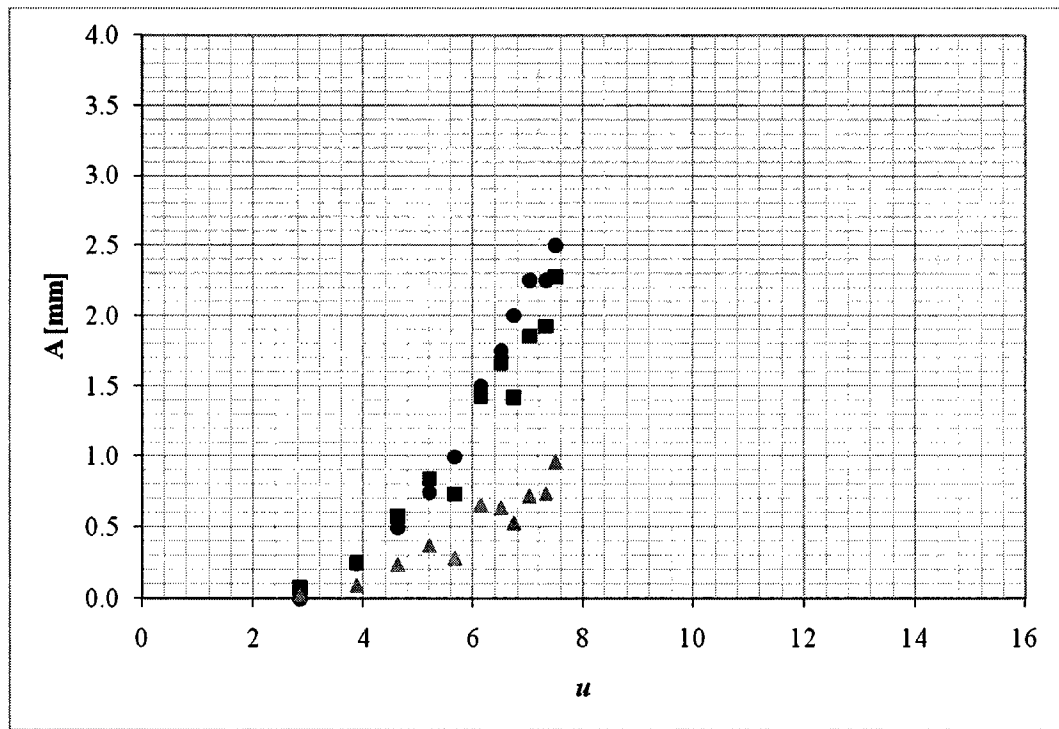


(a)

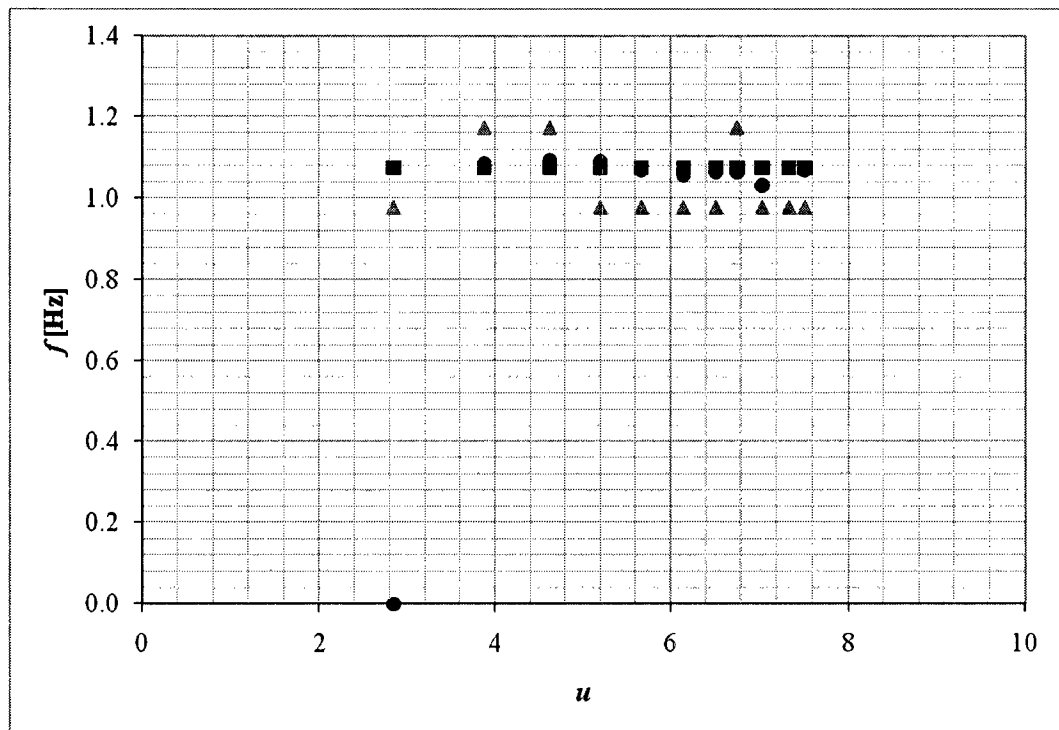


(b)

Figure 3.17. Results of Experiment 2A – Run #1 measured 8 mm above the free end of the pipe. (a) amplitude versus u : ● ruler estimate, ■ max amplitude, ▲ rms amplitude; (b) frequency versus u : ● chronometer estimate, ■ PSD (8 windows), ▲ PSD (16 windows).

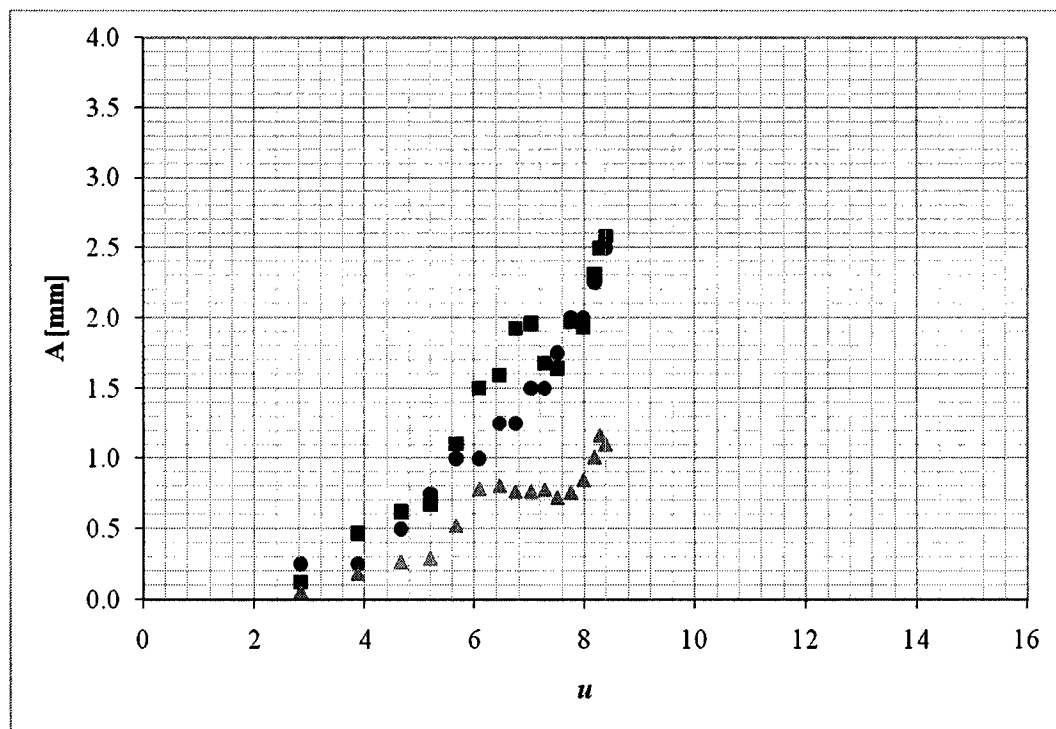


(a)

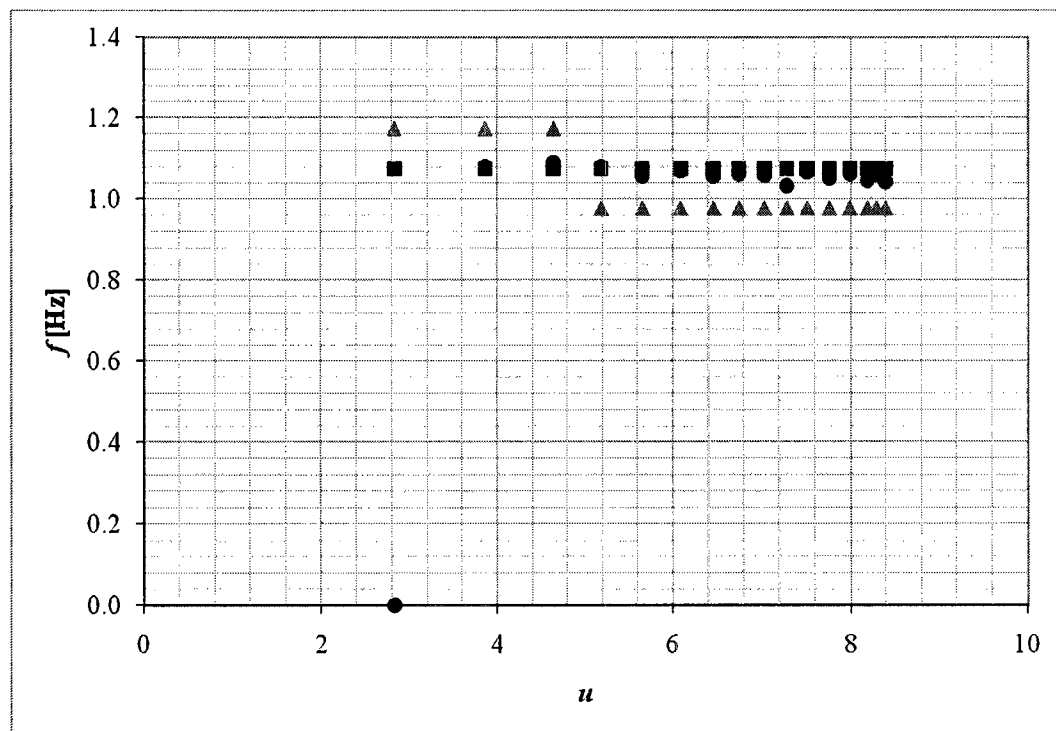


(b)

Figure 3.18. Results of Experiment 2A – Run #2 measured 8 mm above the free end of the pipe. (a) amplitude versus u : ● ruler estimate, ■ max amplitude, ▲ rms amplitude; (b) frequency versus u : ● chronometer estimate, ■ PSD (8 windows), ▲ PSD (16 windows).

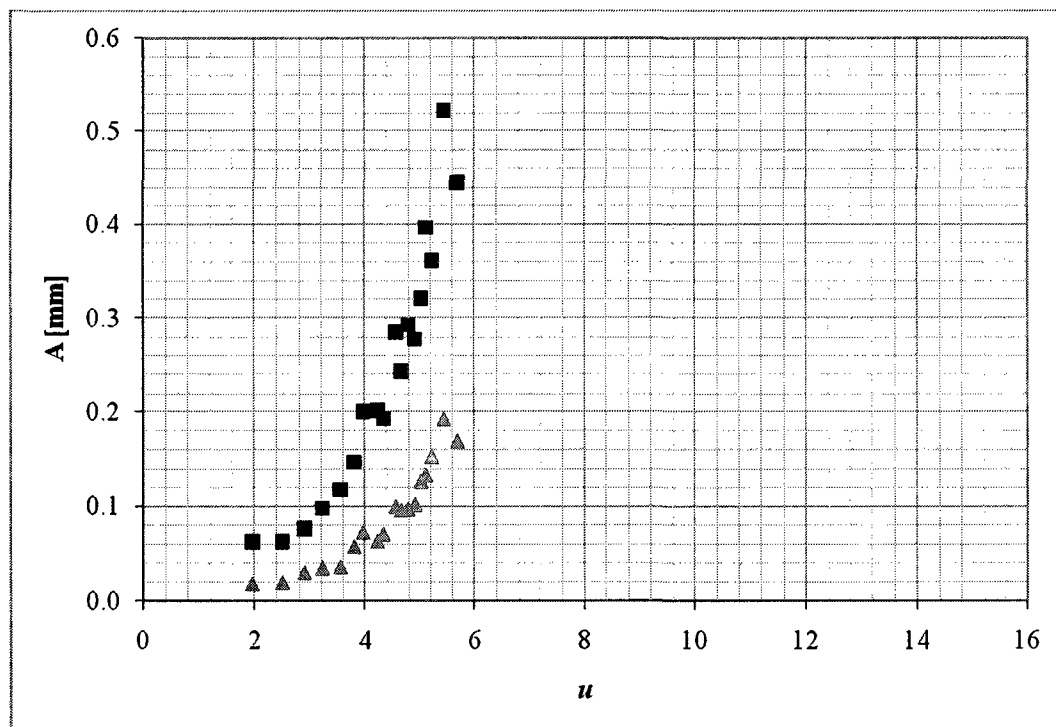


(a)

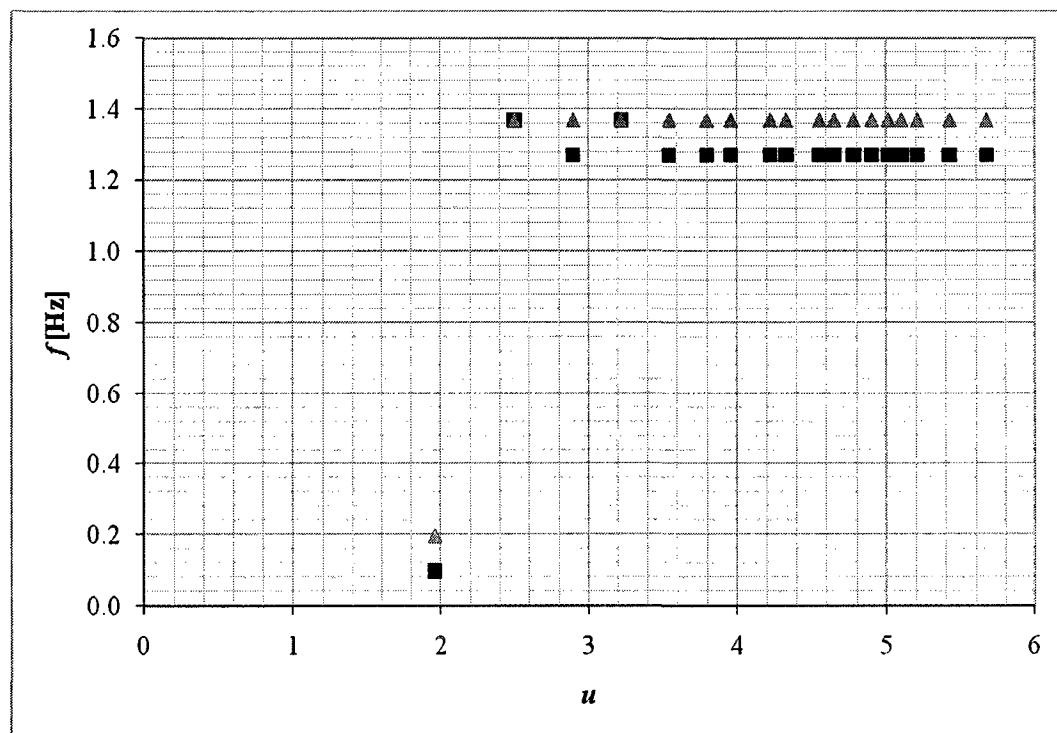


(b)

Figure 3.19. Results of Experiment 2A – Run #3 measured 8 mm above the free end of the pipe. (a) amplitude versus u : ● ruler estimate, ■ max amplitude, ▲ rms amplitude; (b) frequency versus u : ● chronometer estimate, ■ PSD (8 windows), ▲ PSD (16 windows).



(a)



(b)

Figure 3.20. Results of Experiment 3A – Run #1 measured 5 mm above the free end of the pipe. (a) amplitude versus u : ■ max amplitude, ▲ rms amplitude; (b) frequency versus u : ■ PSD (8 windows), ▲ PSD (16 windows).

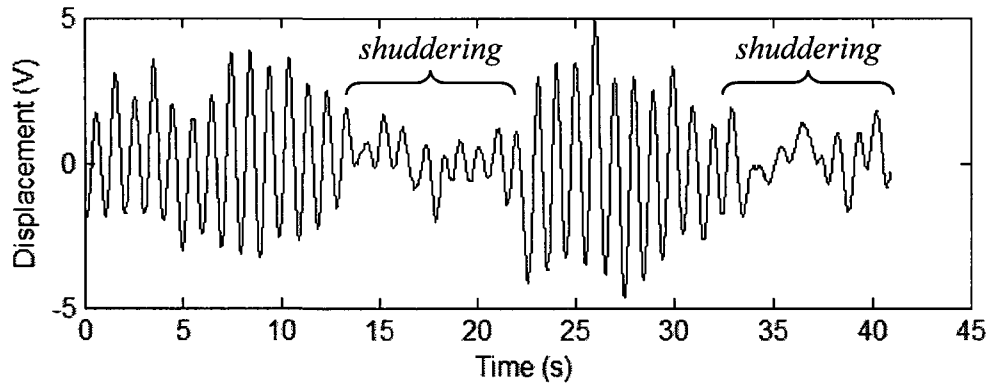


Figure 3.21. Time history signal of Experiment 1C – Run #1 for $u = 11.0$ illustrating the typical *shuddering* motion commonly encountered during experiments.

rather constant at approximately 1 Hz, but also exhibits zero, one, or sometimes two slight jumps, depending on the number of overlapping PSD windows, i.e. either 8 or 16 windows [see Table 3.8]. Moreover, the system, which is characterised predominantly by a three-dimensional, low frequency, first-mode type of flutter, also demonstrates an unexplainable intermittent *shuddering* motion, whereby the amplitude of oscillation decreases for brief periods of time, as seen in Figure 3.21. In addition, the pipe undergoes a slight extension, which is likely a Poisson-ratio-related effect due to depressurization.

3.4 Summary

In this chapter, the linear equation of motion for a cantilevered pipe aspirating fluid proposed by Païdoussis *et al.* (2005) was re-derived taking gravity into consideration. This theoretical model was then modified by introducing two distinct time delays: one in the axial direction, $\bar{\tau}_a$, and another in the lateral direction, $\bar{\tau}_\ell$. Overall, three delay and non-purely-tangential entry models were proposed, differing solely in the sequence of application of the delays. For model I, $\bar{\tau}_a$ and $\bar{\tau}_\ell$ were applied to F_ξ^* and F_ζ^* , respectively, in parallel. For model II, first $\bar{\tau}_a$ was applied to $F_\xi^* \approx F_x^*$, then F_ζ^* was determined from F_y^* and the updated F_x^* , and finally $\bar{\tau}_\ell$ was applied to the resulting F_ζ^* , thereby leading to a coupling of $\bar{\tau}_a$ and $\bar{\tau}_\ell$ in one of the inertial (or M_{sr}) terms of the equation of motion. For model III, $\bar{\tau}_a$ and $\bar{\tau}_\ell$ were applied to F_x and F_y , respectively, but

only to the terms involving the flow velocity within the pipe, U ; F_ξ^* and F_ζ^* were determined thereafter.

Furthermore, some key theoretical results were presented in tables, and a typical Argand diagram for the dynamical system as a function of u was plotted. In general, the theoretical results show that a realistic system with $\alpha = 0.40$, $\bar{\gamma} = 0.30$, and $\psi = 1.00$ becomes unstable by flutter in its first mode via a Hopf bifurcation if gravity and damping effects are included in the analysis. Moreover, $\bar{\tau}_a = D_i/U_{cr}$, $\bar{\tau}_\ell = 10^{-3}$ s, and $\kappa = 0.60$ are good estimates for the axial and lateral time delays, as well as for the shear force factor, κ , when compared to experimental results.

Moreover, a description of the experimental apparatus and a detailed procedure was provided, along with the main results for ten different aspirating pipe experiments, presented in both tabular and graphical form. In general, the amplitude of the system increased as the flow velocity increased, while the frequency of oscillation remained rather constant at about 1 Hz. Therefore, it can be concluded that the aspirating pipe flutters at very small flow velocities in its first mode, based on both theoretical and experimental evidence. Agreement between theory and experiment was very good for pipes 1 and 2; however, the same cannot be said for pipe 3. Note that, in every experiment, the pipe was observed to lose stability by flutter in its first mode from the very beginning; that is, from the lowest flow velocity recorded. In general, the theoretical nondimensional critical flow velocity for pipe 1 was, on the average, $u_{cr} \approx 2.5$, while the average experimental one was also $u_{cr} \approx 2.5$. For pipe 2, the average theoretical dimensionless critical flow velocity was $u_{cr} \approx 3.1$, while the average experimental one was $u_{cr} \approx 2.8$. For pipe 3, the theoretical nondimensional critical flow velocity was found to be $u_{cr} \approx 6.1$, while the experimental one was found to be only $u_{cr} \approx 2.0$. However, the maximum amplitude recorded for pipe 3 was very low, i.e. $A_{\max} = 0.445$ mm. Therefore, if higher flow velocities could have been attained with the experimental apparatus, it is possible that the system would exhibit much higher amplitudes, and that the dynamical behaviour would suggest a higher critical flow velocity.

Lastly, three interesting phenomena were also observed during the experiments, which included (i) an extension of the pipe as the flow velocity was increased, which is probably a Poisson-ratio-related effect, (ii) an intermittent *shuddering* motion, whereby

the amplitude of the system diminished considerably for reasons unknown, and (iii) an unexplainable (at present) shell-type flutter or dynamic divergence instability followed by a shell-type buckling collapse at the free end of the cantilevered pipe when no stiffening end-piece was attached.

CHAPTER 4

Dynamics of a Free-Clamped Cylinder in Confined Axial Flow

4.1 Introduction

Perhaps the earliest study regarding slender flexible cylindrical structures in axial flow was undertaken by Hawthorne (1961), who investigated the dynamics of the Dracone barge system, which is a towed, long flexible container with tapered ends that carries liquids lighter than seawater. His work then paved the way for a theoretical and experimental study of the dynamics of slender flexible cylinders in axial flow subject to different boundary conditions, i.e. clamped-free, pinned-pinned, and clamped-clamped, by Païdoussis (1966a,b). The resulting linear equation of motion, given by Eqn. (1.12), and repeated here, is

$$EI \frac{\partial^4 w}{\partial x^4} + \rho_f A \left(\frac{\partial}{\partial t} + U \frac{\partial}{\partial x} \right)^2 w - \frac{\partial}{\partial x} \left\{ \frac{1}{2} \rho_f D U^2 C_T \left[\left(1 - \frac{1}{2} \delta \right) L - x \right] \frac{\partial w}{\partial x} \right\} - \left[\delta \bar{T} + \frac{1}{2} \rho_f D^2 U^2 (1 - \delta) C_b \right] \frac{\partial^2 w}{\partial x^2} + \frac{1}{2} \rho_f D U C_N \left(\frac{\partial w}{\partial t} + U \frac{\partial w}{\partial x} \right) + m \frac{\partial^2 w}{\partial t^2} = 0, \quad (1.12)$$

where the standard boundary conditions apply if the two ends of the cylinder are supported, and Eqn. (1.13), repeated here,

$$EI \frac{\partial^2 w}{\partial x^2} = 0, \quad (1.13)$$

$$EI \frac{\partial^3 w}{\partial x^3} + f \rho_f A U \left(\frac{\partial w}{\partial t} + U \frac{\partial w}{\partial x} \right) - (m + f \rho_f A) x_e \frac{\partial^2 w}{\partial t^2} = 0,$$

applies at $x = L$ if the cylinder is cantilevered. Unfortunately, Eqn. (1.12) was incorrect because, in the derivation, F_N and F_L were taken in the x - and y -directions, instead of normal and longitudinal on the cylinder. Consequently, the correct, and more general, linear equation of motion for a slender flexible cylinder in confined axial flow was derived by Païdoussis (1973) [see also Païdoussis (1974, 2004)], which is given by Eqn. (1.16), and repeated here,

$$\begin{aligned}
 & \left(E^* \frac{\partial}{\partial t} + E \right) I \frac{\partial^4 w}{\partial x^4} + \chi \rho_f A \left(\frac{\partial}{\partial t} + U \frac{\partial}{\partial x} \right)^2 w - \left\{ \delta [\bar{T} + (1 - 2\nu)(\bar{p}A)] \right. \\
 & + \left[\frac{1}{2} \rho_f D U^2 C_f \left(1 + \frac{D}{D_h} \right) + (m - \rho_f A) g \right] \left[(1 - \frac{1}{2} \delta) L - x \right] \\
 & + \frac{1}{2} \rho_f D^2 U^2 (1 - \delta) C_b \} \frac{\partial^2 w}{\partial x^2} + \frac{1}{2} \rho_f D U C_f \left(\frac{\partial w}{\partial t} + U \frac{\partial w}{\partial x} \right) + \frac{1}{2} \rho_f D C_D \frac{\partial w}{\partial t} \\
 & + \left[(m - \rho_f A) g + \frac{1}{2} \rho_f D U^2 C_f \left(\frac{D}{D_h} \right) \right] \frac{\partial w}{\partial x} + m \frac{\partial^2 w}{\partial t^2} = 0.
 \end{aligned} \tag{1.16}$$

Note that, if the axial flow is unconfined, the equation of motion for this system can be recovered if χ is set equal to 1, D/D_h is set equal to 0, and $C_N = C_T \equiv C_f$.

A typical Argand diagram for a clamped-free cylinder in unconfined axial flow, where only the three lowest modes of the system are plotted as a function of the dimensionless flow velocity, u , is illustrated in Fig. 4.1. From this figure, it can be seen that, in all three modes, free motions of the cylinder are damped for small values of u . However, at $u \approx 2.04$, the system becomes unstable by divergence in its first mode. This occurs because the real component of the dimensionless complex frequency, $\text{Re}(\omega)$, is zero, while the imaginary component, $\text{Im}(\omega)$, becomes negative. The system is then restabilized before losing stability by flutter in its second mode via a Hopf bifurcation at $u \approx 5.16$. Thereafter, the system is restabilized once again; beforehand, it becomes unstable by flutter in its third mode via another Hopf bifurcation at $u \approx 8.17$. The reader is referred to Païdoussis (1973, 1974, 2004) for details concerning the dynamics of a cylinder subject to boundary conditions other than clamped-free.

The present study was motivated by the dynamics of a flexible cantilevered

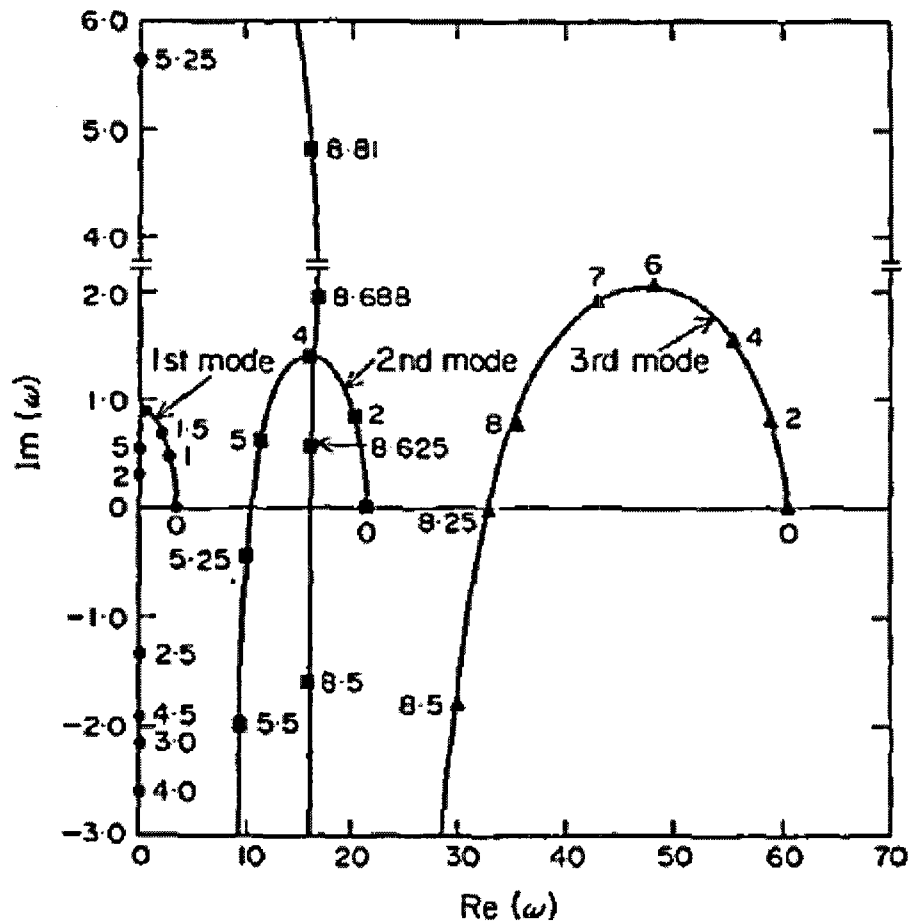


Figure 4.1. Argand diagram as a function of u for a clamped-free cylinder in unconfined axial flow with $\beta = 0.50$, $\varepsilon c_f = 1$, $\chi = 1$, $f = 0.80$, $\chi_e = 0.01$, $\bar{\alpha}^* = \delta = h = \gamma = c_b = 0$ [Païdoussis (1973)].

cylinder in confined axial flow, where the flow is directed from the free to the clamped end, as opposed to the case described above, where the flow is directed from the clamped to the free end. This system is of particular interest because its dynamical behaviour can be compared to that of a pipe aspirating fluid [see Chapter 3], just as the clamped-free cylinder has been compared to the pipe conveying fluid in Chapter 1. Note that, if the ends are supported, the cylinder behaves similarly to the pipe, at least up to the point of the first instability; however, the same cannot be concluded for the cantilevered system. Now, the scope of this chapter is to derive the linear equation of motion for the free-clamped cylinder in confined axial flow following Païdoussis' (1973) formulation, as well as to present the theoretical and experimental results of the analysis, and lastly, to compare these results.

4.2 Theoretical Investigation

4.2.1 Theoretical model

The linear equation of motion for small lateral motions of a free-clamped cylinder in confined axial flow is derived using the Newtonian approach, and closely following the formulation by Païdoussis (1973) for a cylindrical structure subjected to axial flow. The system, which consists of a uniform flexible cylinder of length L , cross-sectional area A , mass per unit length m , and flexural rigidity EI , which is immersed in an incompressible fluid of density ρ_f , and uniform flow velocity U , is illustrated in Fig. 4.2. Note that the cylinder is equipped with a tapered end-piece of length ℓ at its free end. Furthermore, the cylinder is considered to be inextensible, the undisturbed or equilibrium axis of the cylinder is assumed to be coincident with the x -axis of the system in the direction of gravity, and the effect of gravity is regarded as non-negligible. In addition, the curvilinear coordinate along the centreline of the cylinder, s , may be used interchangeably with the vertical coordinate, x , since the lateral motions, $y = w(x, t)$, are assumed to be small compared to the diameter of the cylinder, i.e. L/D is large, and the two-dimensional motion is assumed to be confined to the x - y plane.

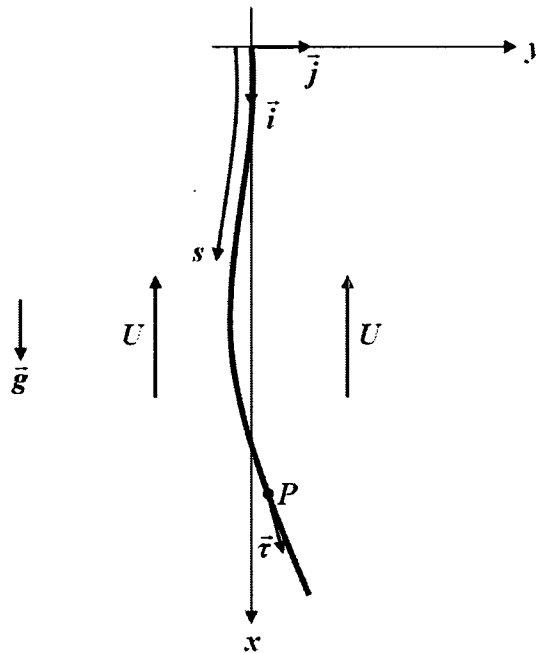


Figure 4.2. A free-clamped cylinder in axial flow.

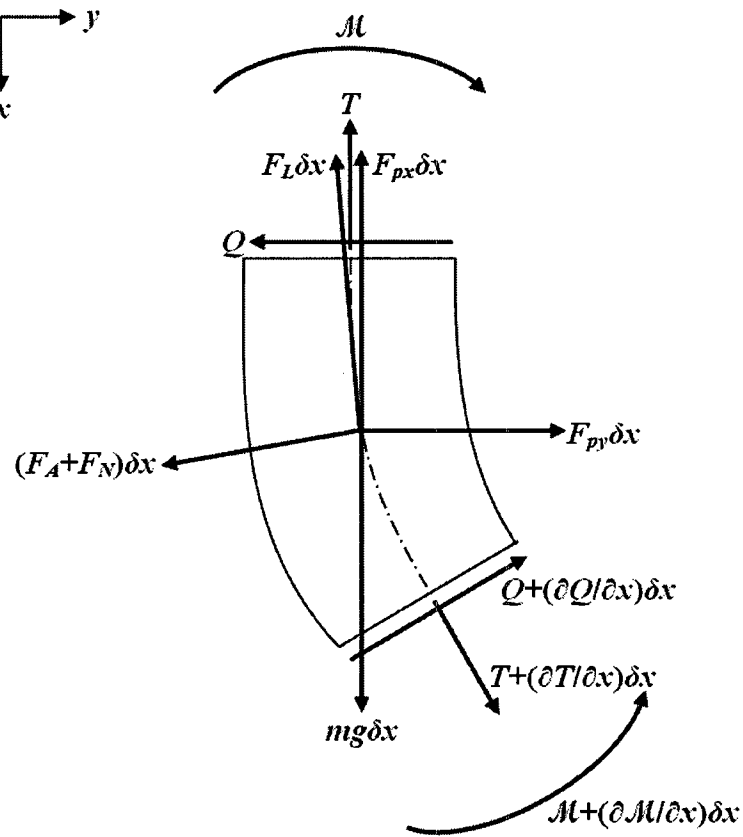


Figure 4.3. A small element δx of the cylinder showing applied forces and moments.

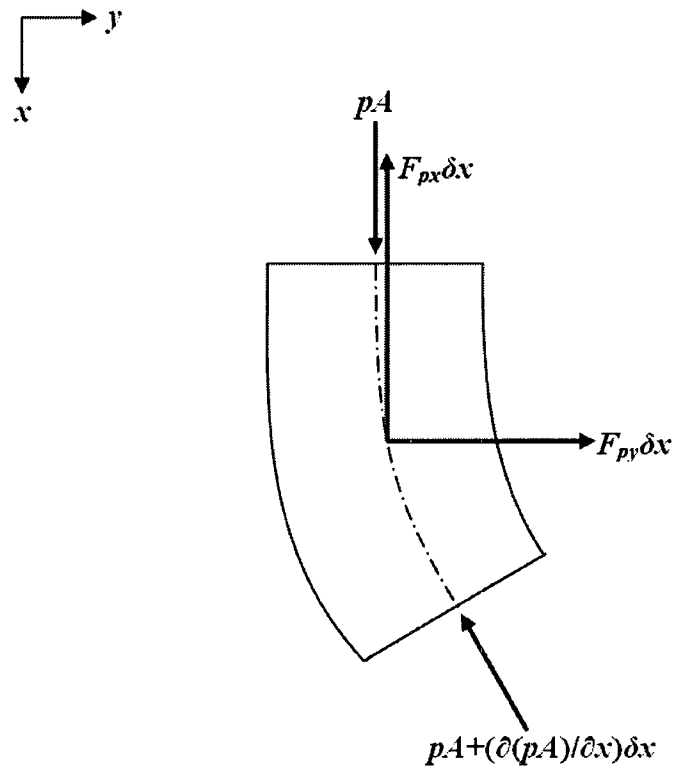


Figure 4.4. A small element δx of the cylinder surrounded by fluid on all sides.

Fig. 4.3 illustrates the forces and moments acting on a small element δx of the flexible cylinder, where Q is the lateral shear force, T is the axial tension, \mathcal{M} is the bending moment, $mg\delta x$ is the weight of the cylinder element, $F_{px}\delta x$ is the hydrostatic force in the x -direction, $F_{py}\delta x$ is the hydrostatic force in the y -direction, $F_A\delta x$ is the inviscid hydrodynamic force in the normal direction, $F_L\delta x$ is the viscous force in the longitudinal direction, and $F_N\delta x$ is the viscous force in the normal direction.

Newton's second law is now applied to the small element δx of the flexible cylinder shown in Fig. 4.3, yielding the equations of motion in the x - and y -direction, respectively

$$\frac{\partial T}{\partial x} + mg - F_{px} - F_L + (F_A + F_N) \frac{\partial w}{\partial x} = 0, \quad (4.1)$$

$$\frac{\partial Q}{\partial x} + \frac{\partial}{\partial x} \left(T \frac{\partial w}{\partial x} \right) + F_{py} - F_L \frac{\partial w}{\partial x} - (F_A + F_N) = m \frac{\partial^2 w}{\partial t^2}. \quad (4.2)$$

From Euler-Bernoulli beam theory, it is also known that

$$Q = -\frac{\partial \mathcal{M}}{\partial x} = -EI \left[1 + \left(\bar{\alpha} + \frac{\bar{\mu}^*}{\Omega} \right) \frac{\partial}{\partial t} \right] \frac{\partial^3 w}{\partial x^3}, \quad (4.3)$$

where the internal dissipation is a combination of hysteretic and viscoelastic damping [see Païdoussis & des Trois Maisons (1971)]. Note that the effects of angular acceleration, and terms of second order, such as the inertial forces in the axial direction, have been neglected from Eqns. (4.1) and (4.2).

The velocity of a small element δx of the flexible cylinder is

$$\vec{V}_c = \frac{\partial \vec{r}}{\partial t} = \frac{\partial x}{\partial t} \vec{i} + \frac{\partial y}{\partial t} \vec{j}, \quad (4.4)$$

where \vec{r} is the position vector measured from the origin to a point on the cylinder, denoted by P in Fig. 4.2. The resultant fluid velocity flowing past the cylinder is

$$\vec{V}_f = -U\vec{\tau} + \vec{V}_c, \quad (4.5)$$

where $\vec{\tau}$ is the unit vector tangential to the cylinder, and is given by

$$\vec{\tau} = \frac{\partial x}{\partial s} \vec{i} + \frac{\partial y}{\partial s} \vec{j}. \quad (4.6)$$

Hence, we may write

$$\vec{V}_f = -U \left(\frac{\partial x}{\partial s} \vec{i} + \frac{\partial y}{\partial s} \vec{j} \right) + \left(\frac{\partial x}{\partial t} \vec{i} + \frac{\partial y}{\partial t} \vec{j} \right) = \left(\frac{\partial}{\partial t} - U \frac{\partial}{\partial s} \right) (x \vec{i} + y \vec{j}) \quad (4.7)$$

As proposed by Lighthill (1960) and shown by Païdoussis (1973, 2004), the inviscid hydrodynamic force per unit length is equal and opposite to the rate of change of momentum per unit length, $[(\partial/\partial t) - U(\partial/\partial x)](Mv)$, where M is the added mass of the fluid per unit length, which is equal to $\chi \rho_f A$ for a cylindrical body in confined axial flow, and v is the resultant fluid velocity in the y -direction, which is given by the \vec{j} component in Eqn. (4.7). It should also be mentioned that χ is a confinement parameter that is equal to $(D_{ch}^2 + D^2)/(D_{ch}^2 - D^2)$, where D is the diameter of the cylinder, and D_{ch} is the diameter of the confining annular channel [see Fig. 4.5]. Therefore,

$$F_A = \chi \rho_f A \left(\frac{\partial}{\partial t} - U \frac{\partial}{\partial x} \right) \left(\frac{\partial w}{\partial t} - U \frac{\partial w}{\partial x} \right), \quad (4.8)$$

where we have utilized the fact that $y = w$ and $\partial x/\partial s \approx 1$.

Using the expressions proposed by Taylor (1952), but in a form modified by Païdoussis *et al.* (2008), the viscous forces per unit length in the longitudinal and normal directions are

$$F_L = \frac{1}{2} \rho_f D U^2 C_T, \quad (4.9)$$

$$F_N = \frac{1}{2} \rho_f D U C_N \left(\frac{\partial w}{\partial t} - U \frac{\partial w}{\partial x} \right) + c \frac{\partial w}{\partial t}, \quad (4.10)$$

where C_T and C_N are the tangential and normal friction drag coefficients, and c is the viscous damping due to the surrounding fluid, which is given by the expression

$$c = \frac{2\sqrt{2}}{\sqrt{S}} \frac{1 + \bar{\gamma}^3}{(1 - \bar{\gamma}^2)^2} \Omega \rho_f A, \quad (4.11)$$

where $\bar{\gamma} = D/D_{ch}$, $S = \Omega r^2/\nu$, $r = 1/2D$, Ω is the circular frequency of oscillation, and ν is the kinematic viscosity of the ambient fluid [see Païdoussis *et al.* (2008)].

The hydrostatic forces per unit length in the x - and y -direction are the resultants of the mean pressure, p , acting on the outer surfaces of the small element δx of the flexible cylinder illustrated in Fig. 4.3. If this element is temporarily frozen in time and completely immersed in fluid, then two additional forces, namely pA and $\{pA + [\partial(pA)/\partial x]\delta x\}$, which are shown in Fig. 4.4, will arise on the two remaining surfaces of the element. The resultant of these forces, and of the hydrostatic forces, F_{px} and F_{py} , is known: it is equal to the buoyancy force. Moreover, if p is assumed to be a linear function of x , which is a reasonable assumption, then

$$\begin{aligned} \left[-\frac{\partial(pA)}{\partial x} - F_{px} \right] \delta x \vec{i} + \left[F_{py} - \frac{\partial}{\partial x} \left(pA \frac{\partial w}{\partial x} \right) \right] \delta x \vec{j} &= -\iiint p \vec{n} dA \\ &= -\iiint_{vol} \vec{\nabla} p d(vol) = -\frac{\partial p}{\partial x} A \delta x \vec{i}. \end{aligned} \quad (4.12)$$

Consequently, we have

$$F_{px} = \frac{\partial p}{\partial x} A - \frac{\partial(pA)}{\partial x}, \quad (4.13)$$

$$F_{py} = \frac{\partial}{\partial x} \left(pA \frac{\partial w}{\partial x} \right). \quad (4.14)$$

The mean pressure, p , is now obtained by considering a fluid element of length δx and confined flow area A_{ch} , as shown in Fig. 4.5. A force balance of the flow in the annular channel region yields

$$-\frac{\partial p}{\partial x} A_{ch} + F_f + \rho_f g A_{ch} = 0, \quad (4.15)$$

where $A_{ch} = \frac{\pi}{4}(D_{ch}^2 - D^2)$, and F_f is the total frictional force, given by $F_f = F_L(S_{tot}/S_o)$, where $S_{tot} = \pi D_{ch} + \pi D$ is the total wetted area per unit length, and $S_o = \pi D$ is the outside wetted area per unit length. It is thus confirmed that $\partial p/\partial x > 0$, as it should be. Eqn. (4.15) is then integrated with respect to x to give

$$pA = \left[F_L \left(\frac{D}{D_h} \right) + \rho_f g A \right] x, \quad (4.16)$$

where $D_h \equiv 4A_{ch}/S_{tot} = D_{ch} - D$ is the hydraulic diameter of the annular channel region, and the mean pressure at $x = 0$, i.e. at the exit, is assumed to be zero.

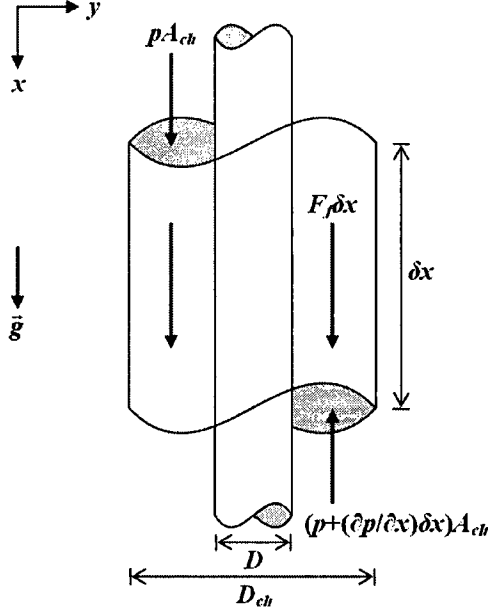


Figure 4.5. A small element δx of the fluid showing the total frictional force F_f .

Using Eqns. (4.8) to (4.10) and (4.13), the equation of motion in the x -direction, Eqn. (4.1), becomes

$$\frac{\partial T}{\partial x} + mg - \frac{\partial p}{\partial x} A + \frac{\partial(pA)}{\partial x} - \frac{1}{2} \rho_f D U^2 C_T = 0. \quad (4.17)$$

Thus, an expression for $\partial(T + pA)/\partial x$ is now determined from Eqn. (4.17). Upon rearranging,

$$\frac{\partial(T + pA)}{\partial x} = \frac{\partial p}{\partial x} A + \frac{1}{2} \rho_f D U^2 C_T - mg. \quad (4.18)$$

Combining Eqns. (4.9), (4.16), and (4.18) yields

$$\frac{\partial(T + pA)}{\partial x} = \frac{1}{2} \rho_f D U^2 C_T \left(1 + \frac{D}{D_h} \right) - (m - \rho_f A)g. \quad (4.19)$$

Eqn. (4.19) is now integrated from x to L to give an expression for $(T + pA)$ as follows:

$$(T + pA) = (T + pA)_L - \left[\frac{1}{2} \rho_f D U^2 C_T \left(1 + \frac{D}{D_h} \right) - (m - \rho_f A)g \right] (L - x). \quad (4.20)$$

From Païdoussis (1973, 2004), the term $(T + pA)_L$ in Eqn. (4.20) is

$$(T + pA)_L = (p_L - p_b)A = -\frac{1}{2} \rho_f D^2 U^2 C_b, \quad (4.21)$$

where p_b is the base pressure, and C_b is the base drag coefficient. Note that Eqn. (4.21) is negative since $p_b > p_L$ when the flow is directed from the free to the clamped end. Consequently, the cylinder will experience a compressive load, as opposed to a tension, at its free end.

The linear equation of motion for a flexible free-clamped cylinder in confined axial flow is now determined from the equation of motion in the y -direction, Eqn. (4.2), and from the other relevant expressions presented in the foregoing, to give

$$\begin{aligned} EI \left[1 + \left(\bar{\alpha} + \frac{\bar{\mu}^*}{\Omega} \right) \frac{\partial}{\partial t} \right] \frac{\partial^4 w}{\partial x^4} - \left[\frac{1}{2} \rho_f D U^2 C_T \left(\frac{D}{D_h} \right) - (m - \rho_f A)g \right] \frac{\partial w}{\partial x} \\ + \left\{ \frac{1}{2} \rho_f D^2 U^2 C_b + \left[\frac{1}{2} \rho_f D U^2 C_T \left(1 + \frac{D}{D_h} \right) - (m - \rho_f A)g \right] (L - x) \right\} \frac{\partial^2 w}{\partial x^2} \\ + \chi \rho_f A \left(\frac{\partial^2 w}{\partial t^2} - 2U \frac{\partial^2 w}{\partial x \partial t} + U^2 \frac{\partial^2 w}{\partial x^2} \right) + \frac{1}{2} \rho_f D U C_N \left(\frac{\partial w}{\partial t} - U \frac{\partial w}{\partial x} \right) \\ + c \frac{\partial w}{\partial t} + m \frac{\partial^2 w}{\partial t^2} = 0, \end{aligned} \quad (4.22)$$

which is subject to the appropriate boundary conditions; at $x = 0$,

$$w = \frac{\partial w}{\partial x} = 0, \quad (4.23)$$

and at $x = L$,

$$EI \frac{\partial^2 w}{\partial x^2} = 0, \quad (4.24)$$

$$EI \frac{\partial^3 w}{\partial x^3} + \left(\frac{1}{2} \rho_f D^2 U^2 C_b + f \chi \rho_f A U^2 \right) \frac{\partial w}{\partial x} - f \chi \rho_f A U \frac{\partial w}{\partial t} - (f \chi \rho_f A + m) x_e \frac{\partial^2 w}{\partial t^2} = 0,$$

where the shear boundary condition, given by the second expression in Eqn. (4.24), is derived in detail in Appendix G. Since $\ell/L \ll 1$, the boundary conditions are assumed to be applied at $x = L$. Now, Eqn. (4.24) may be inserted into Eqn. (4.22) by means of a Dirac delta function, $\delta(x - L)$, thus resulting in the final form of the equation of motion for a flexible free-clamped cylinder in confined axial flow,

$$\begin{aligned} EI \left[1 + \left(\bar{\alpha} + \frac{\bar{\mu}^*}{\Omega} \right) \frac{\partial}{\partial t} \right] \frac{\partial^4 w}{\partial x^4} - \left[\frac{1}{2} \rho_f D U^2 C_T \left(\frac{D}{D_h} \right) - (m - \rho_f A) g \right] \frac{\partial w}{\partial x} \\ + \left\{ \frac{1}{2} \rho_f D^2 U^2 C_b + \left[\frac{1}{2} \rho_f D U^2 C_T \left(1 + \frac{D}{D_h} \right) - (m - \rho_f A) g \right] (L - x) \right\} \frac{\partial^2 w}{\partial x^2} \\ + \chi \rho_f A \left(\frac{\partial^2 w}{\partial t^2} - 2U \frac{\partial^2 w}{\partial x \partial t} + U^2 \frac{\partial^2 w}{\partial x^2} \right) + \frac{1}{2} \rho_f D U C_N \left(\frac{\partial w}{\partial t} - U \frac{\partial w}{\partial x} \right) + c \frac{\partial w}{\partial t} \\ + m \frac{\partial^2 w}{\partial t^2} + \left[- \left(\frac{1}{2} \rho_f D^2 U^2 C_b + f \chi \rho_f A U^2 \right) \frac{\partial w}{\partial x} + f \chi \rho_f A U \frac{\partial w}{\partial t} \right] \delta(x - L) \\ + (f \chi \rho_f A + m) x_e \frac{\partial^2 w}{\partial t^2} \delta(x - L) = 0. \end{aligned} \quad (4.25)$$

The dimensionless form of Eqn. (4.25) is obtained by using the parameters

$$\xi = \frac{x}{L}, \quad \eta = \frac{w}{L}, \quad \tau = \left(\frac{EI}{\rho_f A + m} \right)^{\frac{1}{2}} \frac{t}{L^2}, \quad (4.26)$$

to yield

$$\begin{aligned} \left[1 + \left(\bar{\alpha}^* + \frac{\bar{\mu}^*}{\omega} \right) \frac{\partial}{\partial \tau} \right] \frac{\partial^4 \eta}{\partial \xi^4} + \left[\frac{1}{2} c_b u^2 + \frac{1}{2} \varepsilon c_T u^2 (1 + h)(1 - \xi) - \gamma(1 - \xi) + \chi u^2 \right] \frac{\partial^2 \eta}{\partial \xi^2} \\ - 2 \chi \beta^{\frac{1}{2}} u \frac{\partial^2 \eta}{\partial \xi \partial \tau} - \left(\frac{1}{2} \varepsilon c_T u^2 h - \gamma + \frac{1}{2} \varepsilon c_N u^2 \right) \frac{\partial \eta}{\partial \xi} + \left(\frac{1}{2} \varepsilon c_N \beta^{\frac{1}{2}} u + \sigma \right) \frac{\partial \eta}{\partial \tau} \\ + [1 + \beta(\chi - 1)] \frac{\partial^2 \eta}{\partial \tau^2} + \left[- \left(\frac{1}{2} c_b u^2 + f \chi u^2 \right) \frac{\partial \eta}{\partial \xi} + f \chi \beta^{\frac{1}{2}} u \frac{\partial \eta}{\partial \tau} \right] \delta(\xi - 1) \\ + [1 + \beta(f \chi - 1)] \chi_e \frac{\partial^2 \eta}{\partial \tau^2} \delta(\xi - 1) = 0, \end{aligned} \quad (4.27)$$

where

$$\begin{aligned}
 u &= \left(\frac{\rho_f A}{EI} \right)^{\frac{1}{2}} UL, \quad \beta = \frac{\rho_f A}{\rho_f A + m}, \quad \gamma = \frac{(m - \rho_f A)gL^3}{EI}, \\
 \bar{\alpha}^* &= \left(\frac{EI}{\rho_f A + m} \right)^{\frac{1}{2}} \frac{\bar{\alpha}}{L^2}, \quad \sigma = \frac{cL^2}{[EI(\rho_f A + m)]^{\frac{1}{2}}}, \quad \omega = \left(\frac{\rho_f A + m}{EI} \right)^{\frac{1}{2}} \Omega L^2, \\
 c_b &= \frac{4}{\pi} C_b, \quad c_T = \frac{4}{\pi} C_T, \quad c_N = \frac{4}{\pi} C_N, \quad \varepsilon = \frac{L}{D}, \quad h = \frac{D}{D_h}, \quad \chi_e = \frac{x_e}{L}.
 \end{aligned} \tag{4.28}$$

The system is discretized following the Galerkin procedure. Thus, a solution of the form

$$\eta(\xi, \tau) = \sum_{r=1}^N \phi_r(\xi) q_r(\tau) \tag{4.29}$$

is assumed, where $\phi_r(\xi)$ are the comparison functions, which are taken to be the cantilever beam eigenfunctions, and $q_r(\tau)$ are the generalized coordinates. This eventually leads to an expression of the following form:

$$[M]\ddot{\mathbf{q}} + [C]\dot{\mathbf{q}} + [K]\mathbf{q} = \mathbf{0}, \tag{4.30}$$

where $\mathbf{q} = \{q_1, q_2, \dots, q_N\}^T$. Combining Eqns. (4.27) and (4.29) yields

$$\begin{aligned}
 \sum_{r=1}^N \{ & \lambda_r^4 \phi_r q_r + (\bar{\alpha}^* + \bar{\mu}^*/\omega) \lambda_r^4 \phi_r \dot{q}_r + [\frac{1}{2} c_b u^2 + \frac{1}{2} \varepsilon c_T u^2 (1+h) - \gamma + \chi u^2] \phi_r'' q_r \\
 & - [\frac{1}{2} \varepsilon c_T u^2 (1+h) - \gamma] \phi_r'' q_r - 2\chi \beta^{\frac{1}{2}} u \phi_r' \dot{q}_r - (\frac{1}{2} \varepsilon c_T u^2 h - \gamma + \frac{1}{2} \varepsilon c_N u^2) \phi_r' q_r \\
 & + (\frac{1}{2} \varepsilon c_N \beta^{\frac{1}{2}} u + \sigma) \phi_r \dot{q}_r + [1 + \beta(\chi - 1)] \phi_r \ddot{q}_r - (\frac{1}{2} c_b u^2 + f\chi u^2) \phi_r' q_r \delta(\xi - 1) \\
 & + \{ f\chi \beta^{\frac{1}{2}} u \phi_r \dot{q}_r + [1 + \beta(f\chi - 1)] \chi_e \phi_r \ddot{q}_r \} \delta(\xi - 1) \} = 0.
 \end{aligned} \tag{4.31}$$

Multiplying Eqn. (4.31) by $\phi_s(\xi)$ and integrating over the domain $[0, 1]$ gives

$$\begin{aligned}
 \lambda_r^4 \delta_{sr} q_r + (\bar{\alpha}^* + \bar{\mu}^*/\omega) \lambda_r^4 \delta_{sr} \dot{q}_r + [\frac{1}{2} c_b u^2 + \frac{1}{2} \varepsilon c_T u^2 (1+h) - \gamma + \chi u^2] c_{sr} q_r \\
 - [\frac{1}{2} \varepsilon c_T u^2 (1+h) - \gamma] d_{sr} q_r - 2\chi \beta^{\frac{1}{2}} u b_{sr} \dot{q}_r - (\frac{1}{2} \varepsilon c_T u^2 h - \gamma + \frac{1}{2} \varepsilon c_N u^2) b_{sr} q_r \\
 + (\frac{1}{2} \varepsilon c_N \beta^{\frac{1}{2}} u + \sigma) \delta_{sr} \dot{q}_r + [1 + \beta(\chi - 1)] \delta_{sr} \ddot{q}_r - (\frac{1}{2} c_b u^2 + f\chi u^2) \phi_s(1) \phi_r'(1) q_r \\
 + f\chi \beta^{\frac{1}{2}} u \phi_s(1) \phi_r(1) \dot{q}_r + [1 + \beta(f\chi - 1)] \chi_e \phi_s(1) \phi_r(1) \ddot{q}_r = 0,
 \end{aligned} \tag{4.32}$$

where

$$b_{sr} = \frac{4}{(\lambda_s/\lambda_r)^2 + (-1)^{r+s}}, \quad b_{rr} = 2, \quad (4.33)$$

$$c_{sr} = \frac{4(\lambda_r\sigma_r - \lambda_s\sigma_s)}{(-1)^{r+s} - (\lambda_s/\lambda_r)^2}, \quad c_{rr} = \lambda_r\sigma_r(2 - \lambda_r\sigma_r), \quad (4.34)$$

$$d_{sr} = \frac{4(\lambda_r\sigma_r - \lambda_s\sigma_s + 2)}{1 - (\lambda_s/\lambda_r)^4}(-1)^{r+s} - \frac{3 + (\lambda_s/\lambda_r)^4}{1 - (\lambda_s/\lambda_r)^4}b_{sr}, \quad d_{rr} = \frac{1}{2}c_{rr}, \quad (4.35)$$

for a cantilevered pipe [see Païdoussis (1998, p. 87)]. From Eqn. (4.32), the elements of the mass $[M]$, damping $[C]$, and stiffness $[K]$ matrices in Eqn. (4.30) are determined to be the following:

$$M_{sr} = [1 + \beta(\chi - 1)]\delta_{sr} + [1 + \beta(f\chi - 1)]\chi_e\phi_s(1)\phi_r(1), \quad (4.36)$$

$$C_{sr} = [(\bar{\alpha}^* + \bar{\mu}^*/\omega)\lambda_r^4 + \frac{1}{2}\varepsilon c_N\beta^{1/2}u + \sigma]\delta_{sr} - 2\chi\beta^{1/2}ub_{sr} + f\chi\beta^{1/2}u\phi_s(1)\phi_r(1), \quad (4.37)$$

$$K_{sr} = \lambda_r^4\delta_{sr} - \left(\frac{1}{2}\varepsilon c_T u^2 h - \gamma + \frac{1}{2}\varepsilon c_N u^2\right)\delta_{sr} + \left[\frac{1}{2}c_b u^2 + \frac{1}{2}\varepsilon c_T u^2(1+h) - \gamma + \chi u^2\right]c_{sr} \\ - \left[\frac{1}{2}\varepsilon c_T u^2(1+h) - \gamma\right]d_{sr} - \left(\frac{1}{2}c_b u^2 + f\chi u^2\right)\phi_s(1)\phi_r'(1). \quad (4.38)$$

4.2.2 Theoretical results

In this section, a system with $\bar{\alpha}^* = 0.00030$, $\bar{\mu}^* = 0.03578$, $\beta = 1.14 \times 10^{-3}$, $\gamma = 17.6$, $\varepsilon = 25.3$, $h = 0.455$, $\chi = 1.22$, $\chi_e = 0.00792$, $c_N = 0.0100$, $c_T = 0.0125$, and $c_b = 1 - f$ (generally), which will be varied for different cases, is studied using linear theory. This corresponds to a physical system with the following dimensional characteristics: $D = 0.0159$ m, $D_{ch} = 0.0508$ m, $L = 0.401$ m, $EI = 7.63 \times 10^{-3}$ N·m², $m = 0.213$ kg/m, and $\rho_f A = 2.43 \times 10^{-4}$ kg/m. The Argand diagrams for the three lowest modes as a function of the nondimensional flow velocity, u , are presented in Figs. 4.6 to 4.9 for four separate cases, i.e. $f = 1.00$ ($c_b = 0$), $f = 0.80$ ($c_b = 0.20$), $f = 0.60$ ($c_b = 0.40$), and $f = 0.80$ ($c_b = 0.60$). Note that the multiplicative factor to switch from dimensionless u to U in m/s is 13.9, while that to switch from dimensionless ω to f in Hz is 0.187.

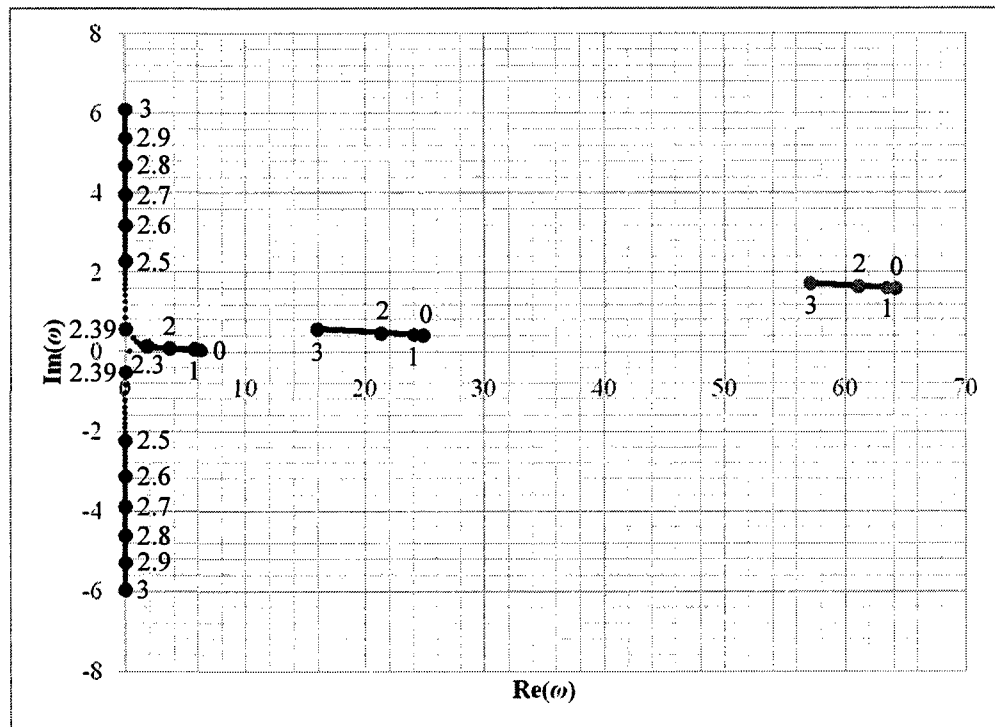


Figure 4.6. Argand diagram as a function of u for a free-clamped cylinder in confined axial flow with $f=1.00$ and $c_b=0$ using a five-mode Galerkin approximation.

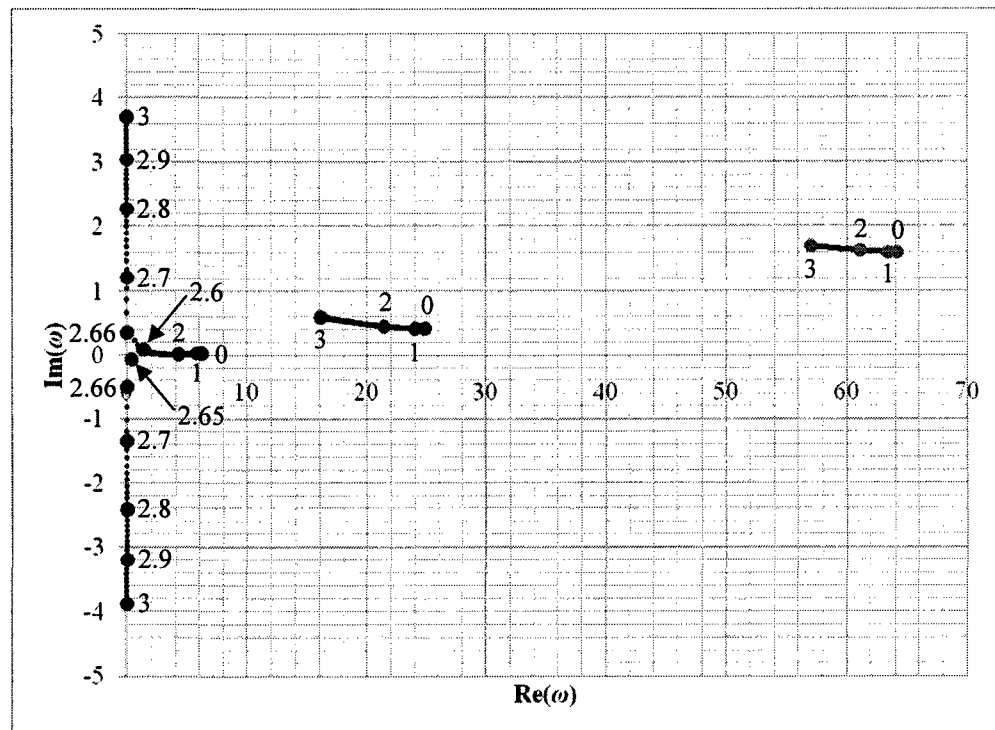


Figure 4.7. Argand diagram as a function of u for a free-clamped cylinder in confined axial flow with $f=0.80$ and $c_b=0.20$ using a five-mode Galerkin approximation.

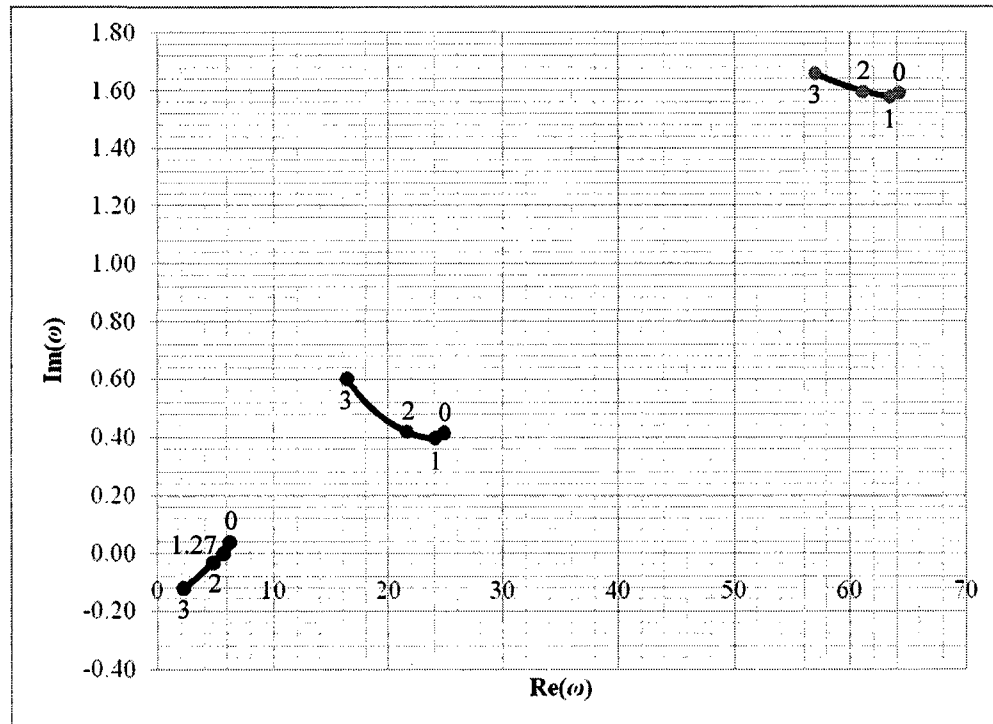


Figure 4.8. Argand diagram as a function of u for a free-clamped cylinder in confined axial flow with $f = 0.60$ and $c_b = 0.40$ using a five-mode Galerkin approximation.

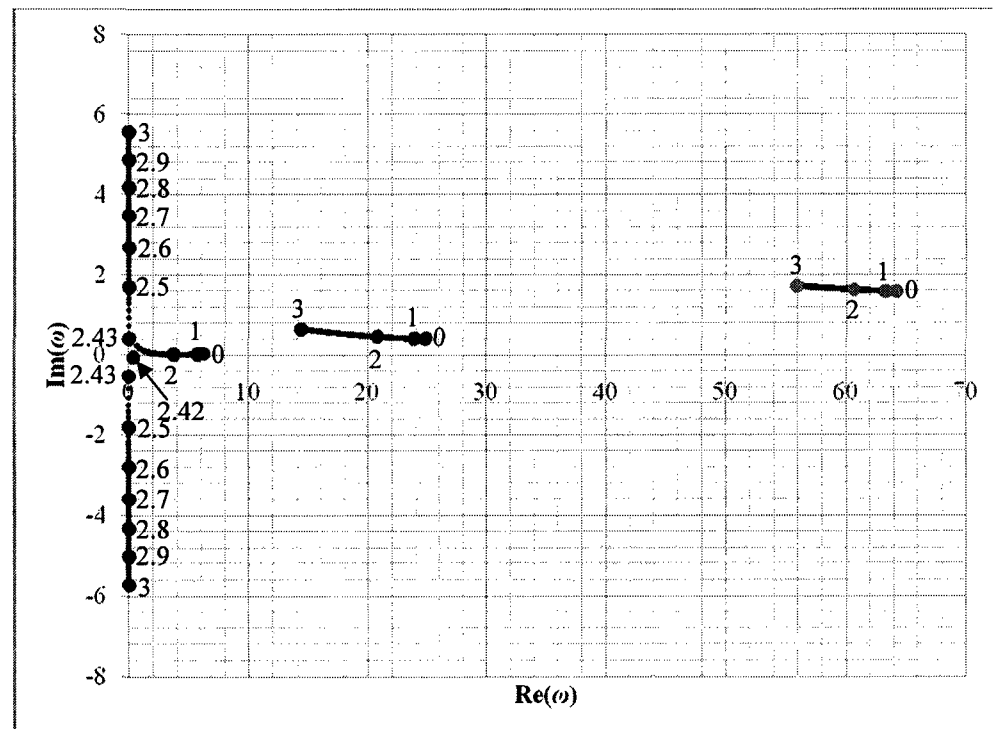


Figure 4.9. Argand diagram as a function of u for a free-clamped cylinder in confined axial flow with $f = 0.80$ and $c_b = 0.60$ using a five-mode Galerkin approximation.

From Fig. 4.6, the system with $f = 1.00$ and $c_b = 0$ loses stability by divergence in its first mode at $u_{cr,d} = 2.39$, since the dimensionless complex frequency, ω , becomes purely imaginary and negative at this critical flow velocity. Prior to $u_{cr,d} = 2.39$, however, the flow actually induces damping in the first mode of the system. Moreover, for the full range of flow velocities studied, i.e. $0 \leq u \leq 3$, the damping of the system is increased with flow velocity for the second and third modes too, since $\text{Im}(\omega)$ increases and $\text{Re}(\omega)$ decreases. Note that the damping ratio is given by $\zeta = \text{Im}(\omega)/\text{Re}(\omega)$.

From Fig. 4.7, the system with $f = 0.80$ and $c_b = 0.20$ loses stability by divergence in its first mode at $u_{cr,d} = 2.66$, since $\text{Re}(\omega)$ becomes zero and $\text{Im}(\omega)$ becomes negative at this critical value. However, just prior to $u_{cr,d} = 2.66$, the system becomes unstable by flutter in its first mode via a Hopf bifurcation at $u_{cr,f} = 2.65$ with a frequency of oscillation of $\text{Re}(\omega_{cr,f}) = 0.417$, since $\text{Re}(\omega)$ remains positive, while $\text{Im}(\omega)$ becomes negative at this critical value. Furthermore, for values of u in the range $0 \leq u \leq 2.64$, the flow induces damping in the first mode of the system. The latter also holds true for values of u in the full range of flow velocities studied, i.e. $0 \leq u \leq 3$, for the second and third modes of the free-clamped system. In addition, the system with $f = 0.80$ and $c_b = 0.60$, whose Argand diagram is shown in Fig. 4.9, behaves similarly to the above system; however, in this case, $u_{cr,f} = 2.42$, $\text{Re}(\omega_{cr,f}) = 0.415$, and $u_{cr,d} = 2.43$.

From Fig. 4.8, the system with $f = 0.60$ and $c_b = 0.40$ loses stability by flutter in its first mode via a Hopf bifurcation at $u_{cr,f} = 1.27$ with a frequency of oscillation of $\text{Re}(\omega_{cr,f}) = 5.68$, since the first-mode locus enters the unstable region of the Argand diagram at this critical flow velocity, while $\text{Re}(\omega)$ remains positive. For the full flow range investigated, i.e. $0 \leq u \leq 3$, the system remains stable in its second and third modes, and the first mode is not restabilized after $u_{cr,f} = 1.27$, since $\text{Im}(\omega)$ remains negative.

4.3 Experimental Investigation

4.3.1 Experimental apparatus

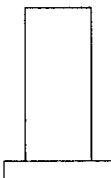
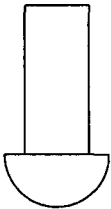
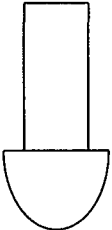
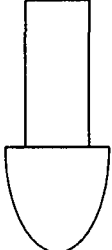
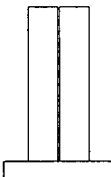
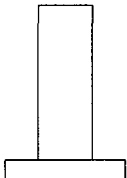
The air experiments of a free-clamped cylindrical structure in confined axial flow were performed using three flexible cylinders: (i) an ordinary elastomer cylinder, (ii) a

blade-stiffened elastomer cylinder, and (iii) a denser elastomer cylinder. These cylinders are essentially the same pipes that were used during the experiments of a cantilevered pipe aspirating fluid; here, however, pipes 1 and 2 are filled with stagnant water. The reader is referred to Section 3.3.1 of Chapter 3 for information concerning the three cylinders mentioned above, and for a description of the experimental set-up and apparatus. Note that the aspirating configuration, shown in Fig. 3.8 of Chapter 3, was used for the confined axial air-flow experiments presented here; however, an annular channel was added to the set-up. This annulus was made from plexiglas, and was attached to a brass support by means of an adaptor and four pins, which were secured with set-screws. The reader is referred to Appendix F for the technical drawings of the brass support, pins, adaptor, and annulus. Table 4.1 presents the geometrical and physical properties of each cylinder, while Table 4.2 presents the profiles of the different end-pieces that were fitted at the free end of a cylinder during an experiment. Note that $c_N = 0.0100$ and $c_T = 0.0125$ were used for the normalized normal and tangential friction drag coefficients, respectively. Throughout this chapter, Experiment 1A refers to the use of cylinder 1 and end-piece A, Experiment 1B refers to the use of cylinder 1 and end-piece B, and so on and so forth, as illustrated in Table 4.2.

Table 4.1. The geometrical and physical properties of the cylinders

Properties	Cylinder 1	Cylinder 2	Cylinder 3
D [m]	0.0159	0.0159	0.0159
D_{ch} [m]	0.0508	0.0508	0.0508
L [m]	0.401	0.412	0.346
EI [$N \cdot m^2$]	7.63×10^{-3}	8.25×10^{-3}	1.10×10^{-2}
m [kg/m]	0.213	0.233	0.355
$\rho_f A$ [kg/m]	$f(\text{fluid density})$	$f(\text{fluid density})$	$f(\text{fluid density})$
β [-]	$f(\text{fluid density})$	$f(\text{fluid density})$	$f(\text{fluid density})$
γ [-]	$f(\text{fluid density})$	$f(\text{fluid density})$	$f(\text{fluid density})$
$\bar{\alpha}^*$ [-]	0.00030	0.00030	0.00023
$\bar{\mu}^*$ [-]	0.03578	0.03914	0.04863
f_1 [Hz]	1.27	1.20	1.34
f_2 [Hz]	5.47	5.08	5.86
f_3 [Hz]	14.8	12.5	15.6
δ_1 [-]	0.0423	0.0438	0.0587
δ_2 [-]	0.119	0.101	0.141
δ_3 [-]	0.160	0.215	0.183
δ_n [-]	$0.0590n - 0.0107$	$0.0854n - 0.0511$	$0.0623n + 0.0030$

Table 4.2. The various end-pieces used during the air experiments

	End-piece A	End-piece B	End-piece C	End-piece D
Cylinder 1	 $x_e = 0.00318 \text{ m}$	 $x_e = 0.00529 \text{ m}$	 $x_e = 0.00794 \text{ m}$	 $x_e = 0.0106 \text{ m}$
Cylinder 2	 $x_e = 0.00318 \text{ m}$			
Cylinder 3	 $x_e = 0.00318 \text{ m}$			

4.3.2 Experimental procedure

The experimental procedure for a typical air experiment involving a free-clamped cylinder subjected to external confined axial flow is the same as that described in Section 3.3.2 of Chapter 3 for a cantilevered pipe aspirating fluid. The reader is referred to Figs. 3.9 and 3.10 of Chapter 3, once more, for schematics of the manometer valves and the experimental set-up, respectively.

4.3.3 Experimental results

Table 4.3 presents some of the main experimental and theoretical results for six different confined air-flow experiments of a free-clamped cylinder, including the multiplicative factors to convert values of nondimensional u and ω to dimensional U

(m/s) and f (Hz), the smallest and largest experimental amplitudes of oscillation, i.e. A_{\min} and A_{\max} , for both maximum and root-mean-square readings from the recorded time history signals, as well as the critical flow velocities and frequencies at the onset of flutter and/or buckling. Additionally, Figs. 4.10 to 4.15 illustrate how the amplitude of oscillation and the dominant frequency vary with increasing dimensionless flow velocity. Note that the experimental amplitude readings were determined either from ruler measurements or from the recorded time history signals, whereas the frequency readings were found either from chronometer measurements or from the PSD plots of the time history signals using 8 or 16 windows for averaging [see Appendix E]. Moreover, the experimental critical flow velocity for divergence, $u_{cr,d}$, was determined by fitting a parabolic regression line through the experimental data points of the frequency versus dimensionless flow velocity graph. The critical flow velocity was then approximated by extending the regression line to the u -axis of the graph; the point where the regression line crossed the u -axis was considered to be the critical point for the onset of buckling.

In general, the air-flow experiments for a free-clamped cylinder demonstrate that the system loses stability in its first mode by flutter at very low flow velocities ($u = u_{cr,f} \approx 0.3$ to 0.4), and then, at higher flow velocities ($u = u_{cr,d} \approx 1.1$ to 1.7), the system exhibits a static instability, and thereby buckles in a first-mode configuration. Theoretically, the frequency of the system is zero at the onset of buckling. However, this condition is never fully realized in the experiments presented here; in fact, it is never realized due to nonlinear effects [see Païdoussis (1998, 2004)]. As a consequence, the critical flow velocity for buckling must be extrapolated from the available experimental data points by means of a parabolic regression line, as described in the previous paragraph.

Moreover, the experiments illustrate that, while the cylinder is fluttering, the amplitude of oscillation of the system increases rather rapidly before attaining a maximum; thereafter, the amplitude of oscillation ceases to increase. Note that the amplitudes presented in Figs. 4.10 to 4.15 are the amplitudes of oscillation, which are not to be confused with the transverse buckling displacement. Therefore, an amplitude of oscillation equal to zero would imply that the cylinder has become unstable by

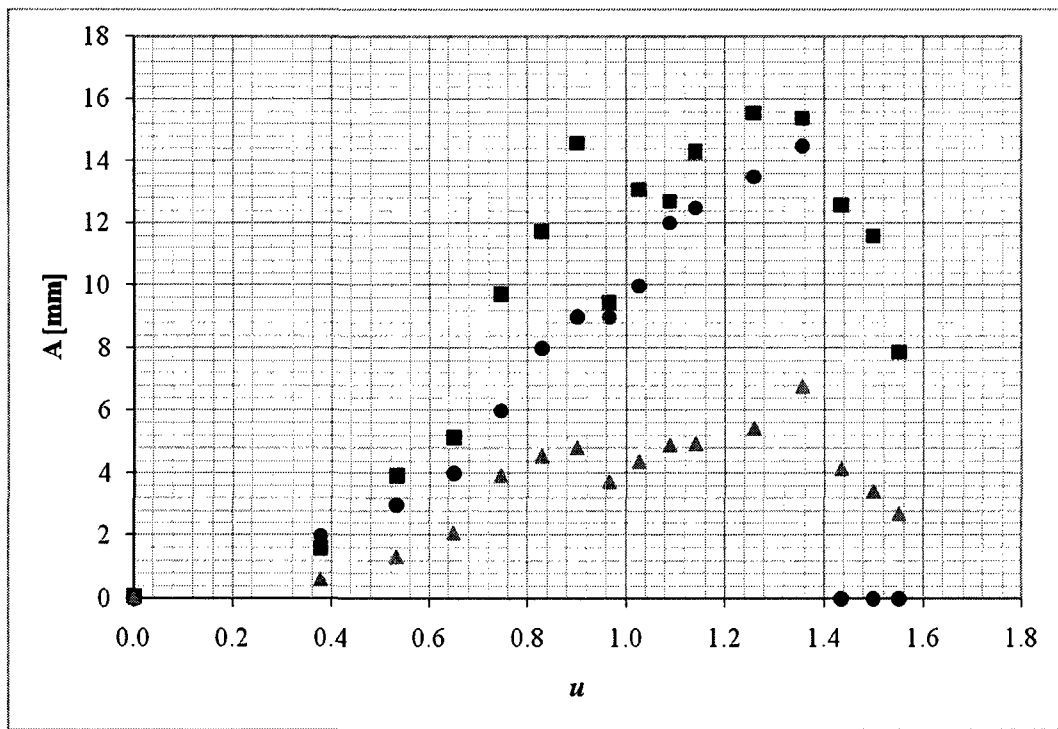
Table 4.3. Key results including multiplicative factors, vibration amplitudes, flow velocities, and vibration frequencies

Exp.	Multiplicative factors		Experimental max amplitudes		Experimental rms amplitudes	
	$u \rightarrow U$	$\omega \rightarrow f$	A_{\min} [mm]	A_{\max} [mm]	A_{\min} [mm]	A_{\max} [mm]
1A	13.9	0.187	0.0851	15.5	0.0182	6.77
1B	13.7	0.187	0.0668	8.04	0.0247	3.16
1C	13.9	0.187	0.0737	12.6	0.0186	4.16
1D	13.9	0.187	0.0736	14.4	0.0196	4.69
2A	14.4	0.176	0.0792	6.94	0.0202	3.05
3A	19.4	0.234	0.0843	8.45	0.0196	3.06

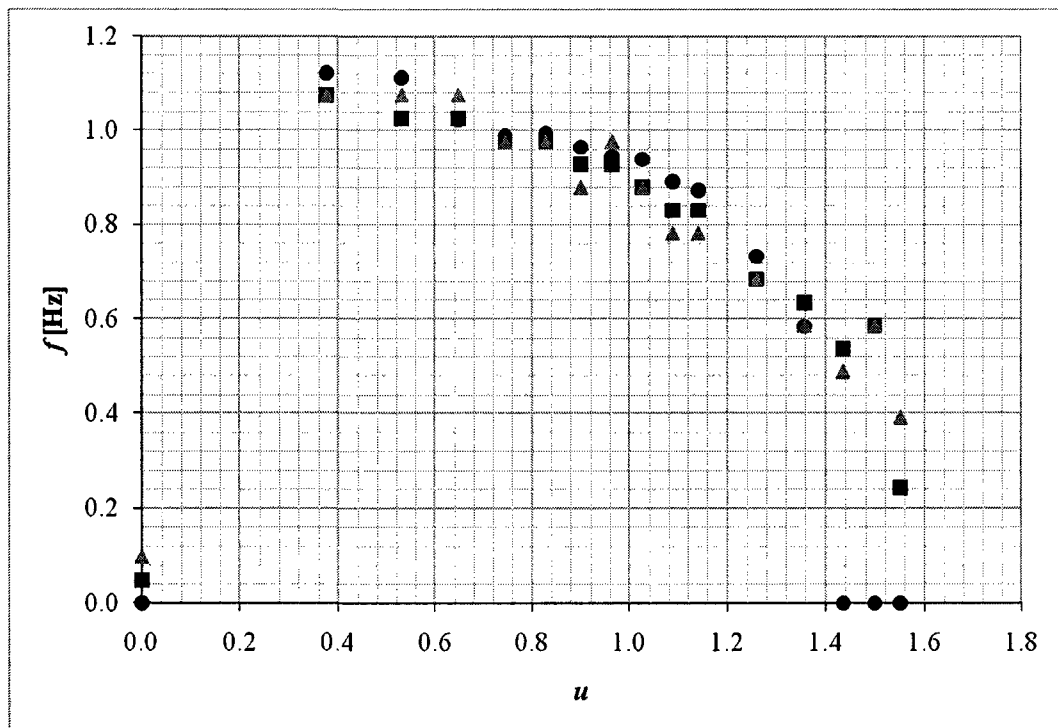
Exp.	Experimental flutter and buckling results				Theoretical flutter and buckling results			
	$u_{cr,f}$	$f_{cr,f}$ [Hz]		$u_{cr,d}$	$f = 1.00, c_b = 0$			
		PSD 8	PSD 16		$u_{cr,f}$	$\text{Re}(\omega_{cr,f})$	$u_{cr,d}$	$\text{Re}(\omega_{cr,d})$
1A	0.377	1.07	1.07	1.70	None	None	2.39	0
1B	0.380	1.12	1.17	1.64	None	None	2.39	0
1C	0.380	1.12	1.17	1.64	None	None	2.39	0
1D	0.376	1.12	1.07	1.67	None	None	2.39	0
2A	0.371	1.03	1.07	1.23	None	None	2.46	0
3A	0.270	1.32	1.27	1.08	None	None	2.20	0

Exp.	Theoretical flutter and buckling results				Theoretical flutter and buckling results			
	$f = 0.80, c_b = 0.20$				$f = 0.60, c_b = 0.40$			
	$u_{cr,f}$	$\text{Re}(\omega_{cr,f})$	$u_{cr,d}$	$\text{Re}(\omega_{cr,d})$	$u_{cr,f}$	$\text{Re}(\omega_{cr,f})$	$u_{cr,d}$	$\text{Re}(\omega_{cr,d})$
1A	2.65	0.417	2.66	0	1.27	5.68	None	None
1B	2.65	0.412	2.66	0	1.27	5.62	None	None
1C	2.65	0.406	2.66	0	1.28	5.54	None	None
1D	2.65	0.400	2.66	0	1.28	5.47	None	None
2A	2.73	0.424	2.74	0	1.40	5.80	None	None
3A	2.42	0.708	2.44	0	2.89	0.423	2.90	0

Exp.	Theoretical flutter and buckling results			
	$f = 0.80, c_b = 0.60$			
	$u_{cr,f}$	$\text{Re}(\omega_{cr,f})$	$u_{cr,d}$	$\text{Re}(\omega_{cr,d})$
1A	2.42	0.415	2.43	0
1B	2.42	0.410	2.43	0
1C	2.42	0.404	2.43	0
1D	2.42	0.397	2.43	0
2A	None	None	2.50	0
3A	2.22	0.450	2.23	0

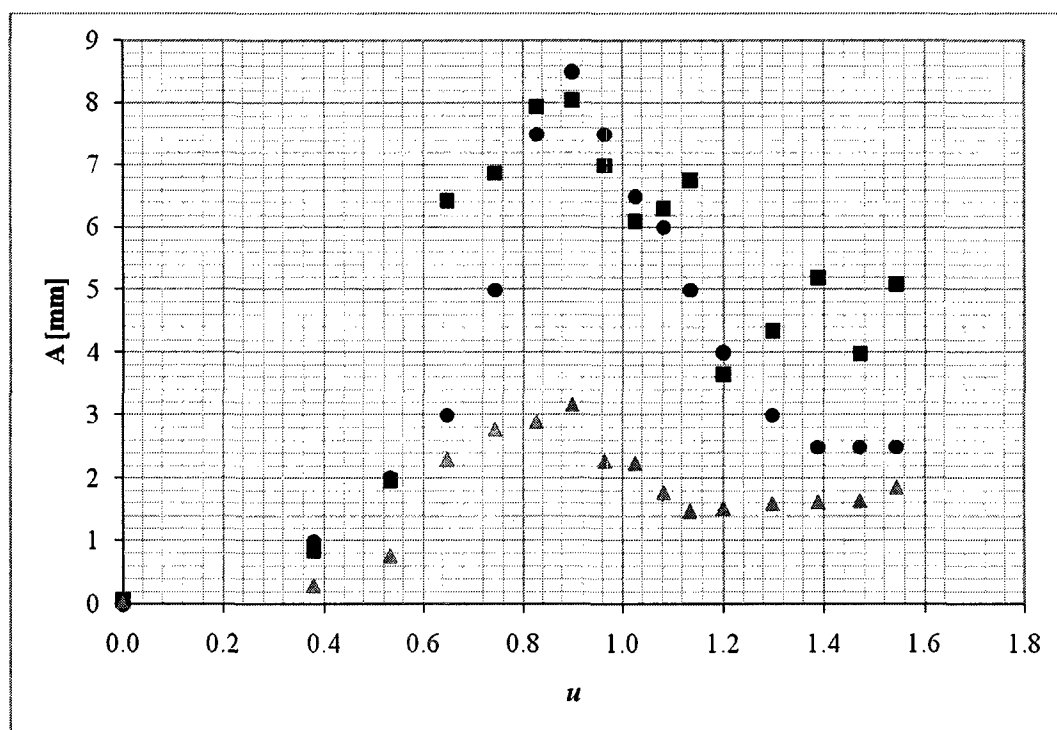


(a)

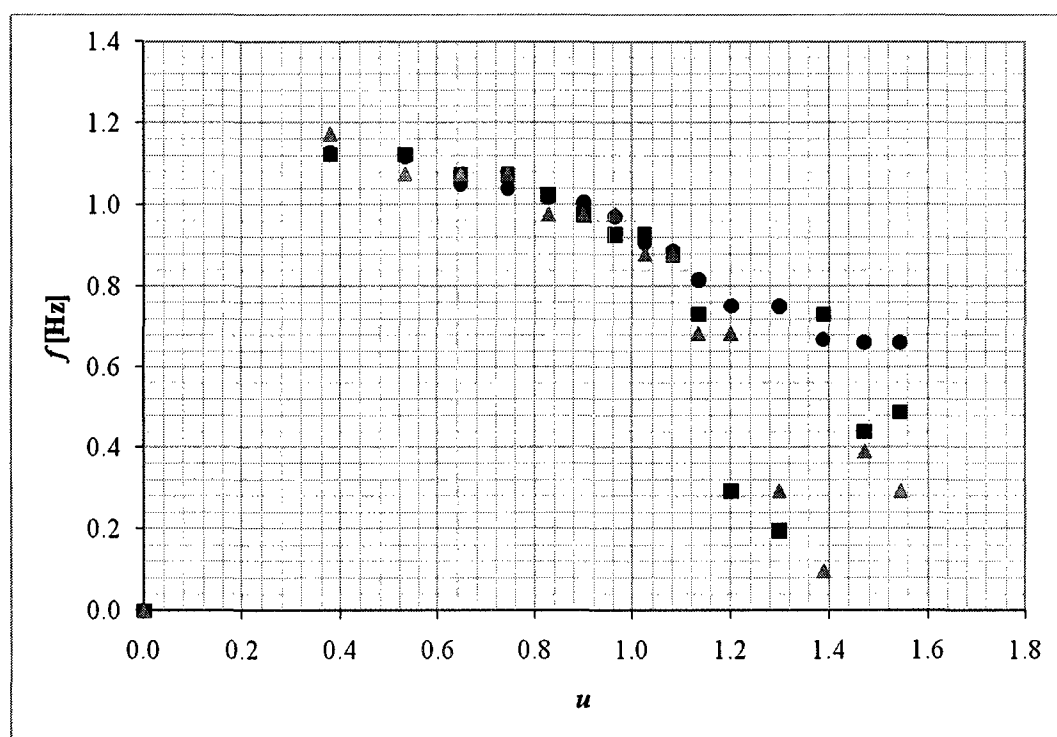


(b)

Figure 4.10. Results of Experiment 1A measured 5 mm above the free end of the cylinder. (a) amplitude versus u : ● ruler estimate, ■ max amplitude, ▲ rms amplitude; (b) frequency versus u : ● chronometer estimate, ■ PSD (8 windows), ▲ PSD (16 windows).

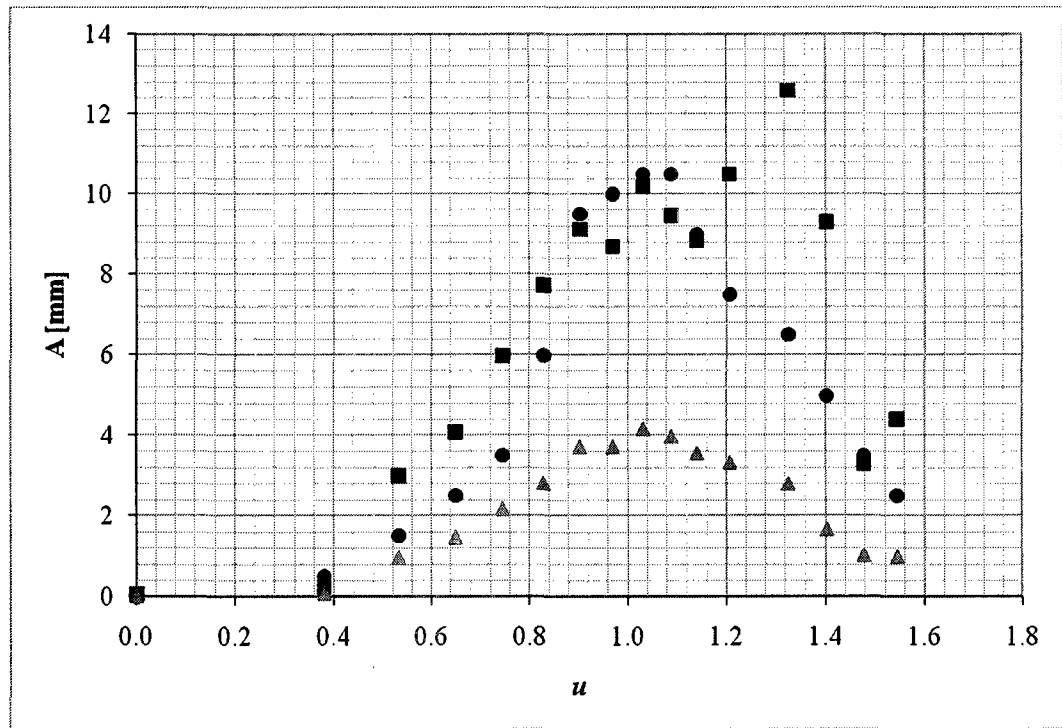


(a)

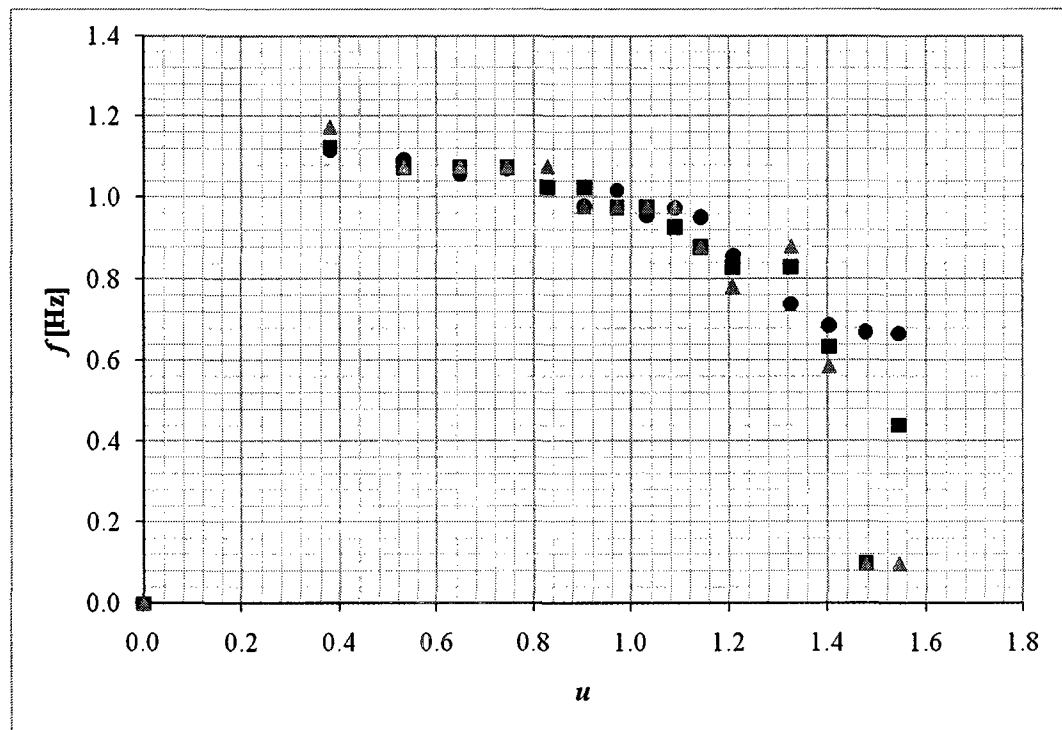


(b)

Figure 4.11. Results of Experiment 1B measured 5 mm above the free end of the cylinder. (a) amplitude versus u : ● ruler estimate, ■ max amplitude, ▲ rms amplitude; (b) frequency versus u : ● chronometer estimate, ■ PSD (8 windows), ▲ PSD (16 windows).

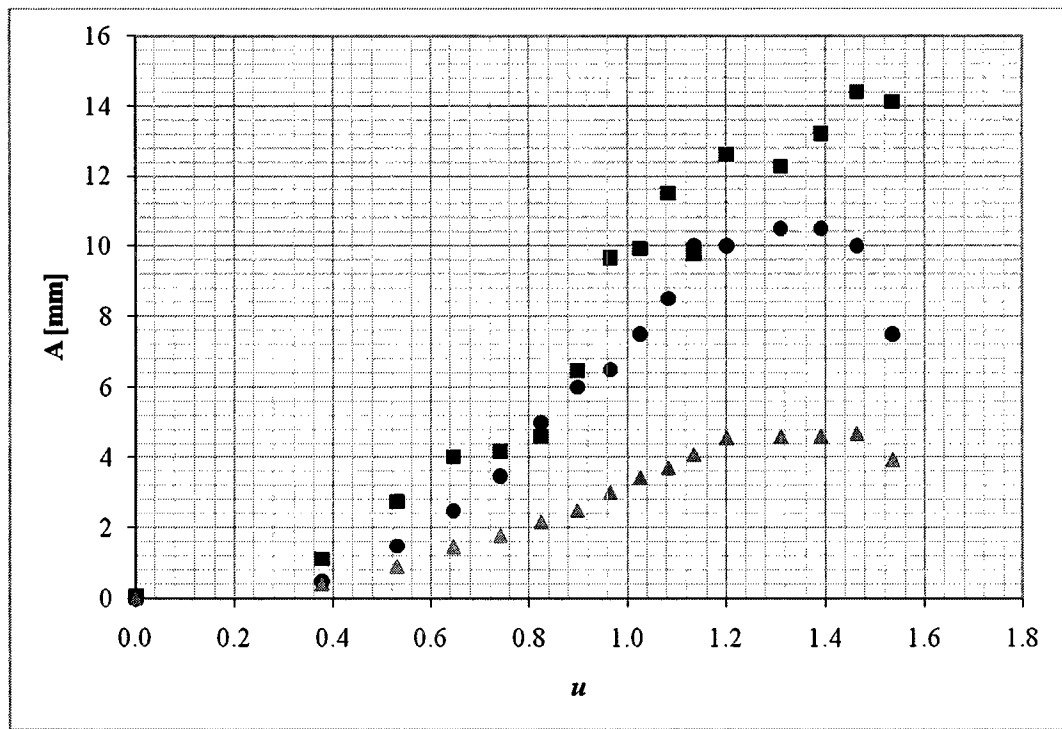


(a)

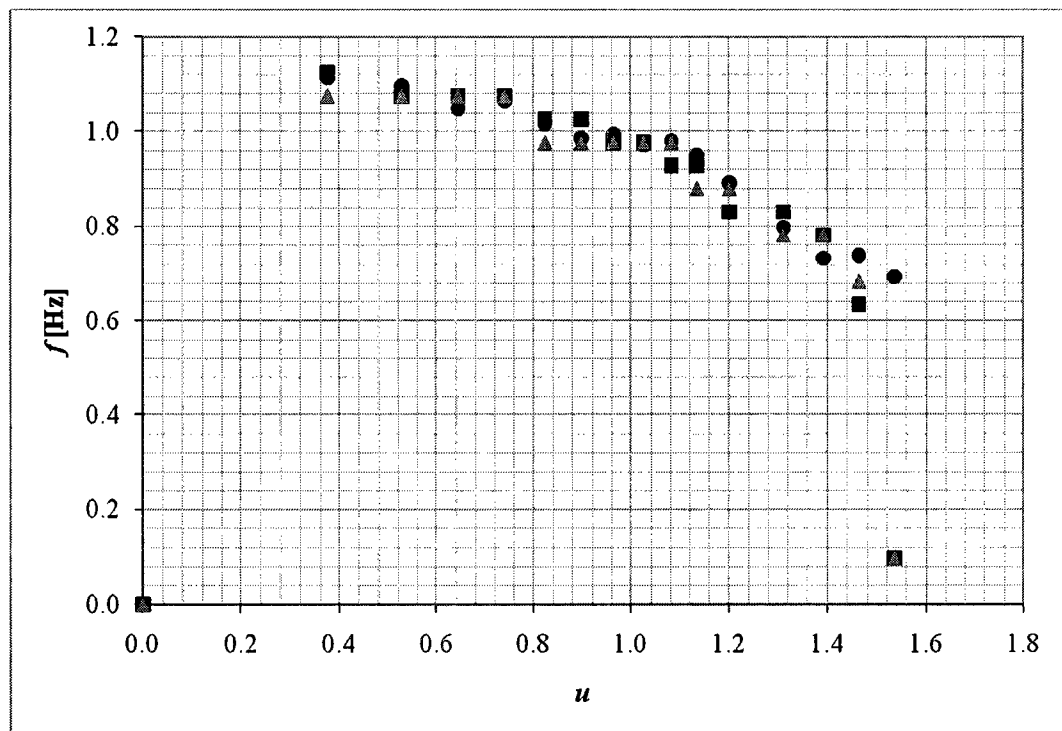


(b)

Figure 4.12. Results of Experiment 1C measured 5 mm above the free end of the cylinder. (a) amplitude versus u : ● ruler estimate, ■ max amplitude, ▲ rms amplitude; (b) frequency versus u : ● chronometer estimate, ■ PSD (8 windows), ▲ PSD (16 windows).

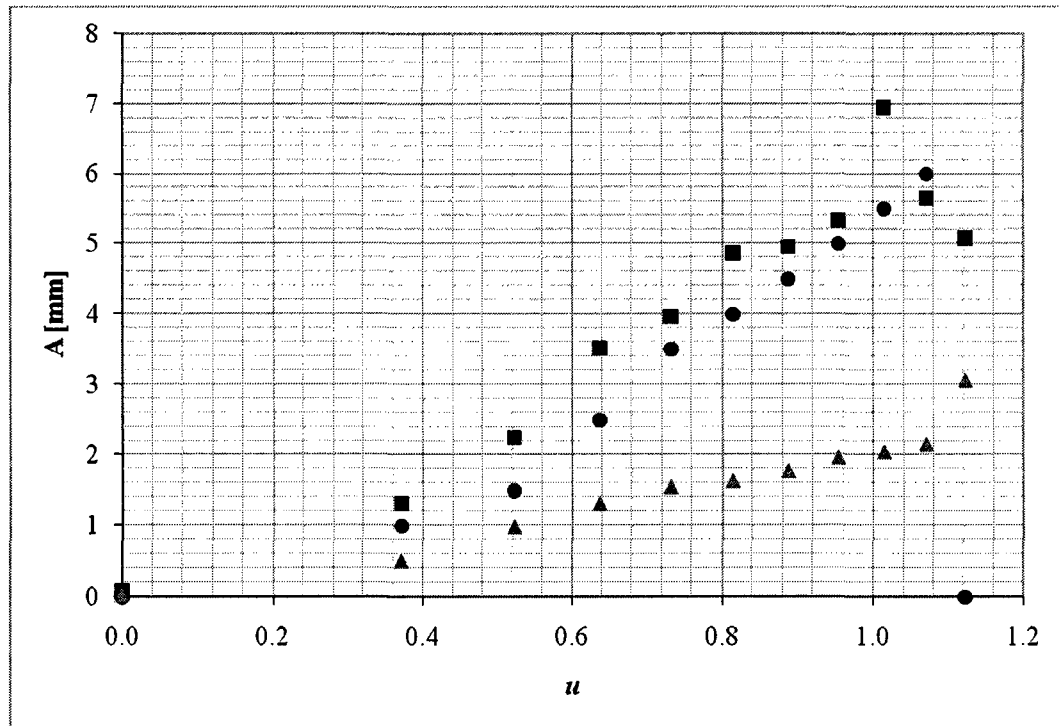


(a)

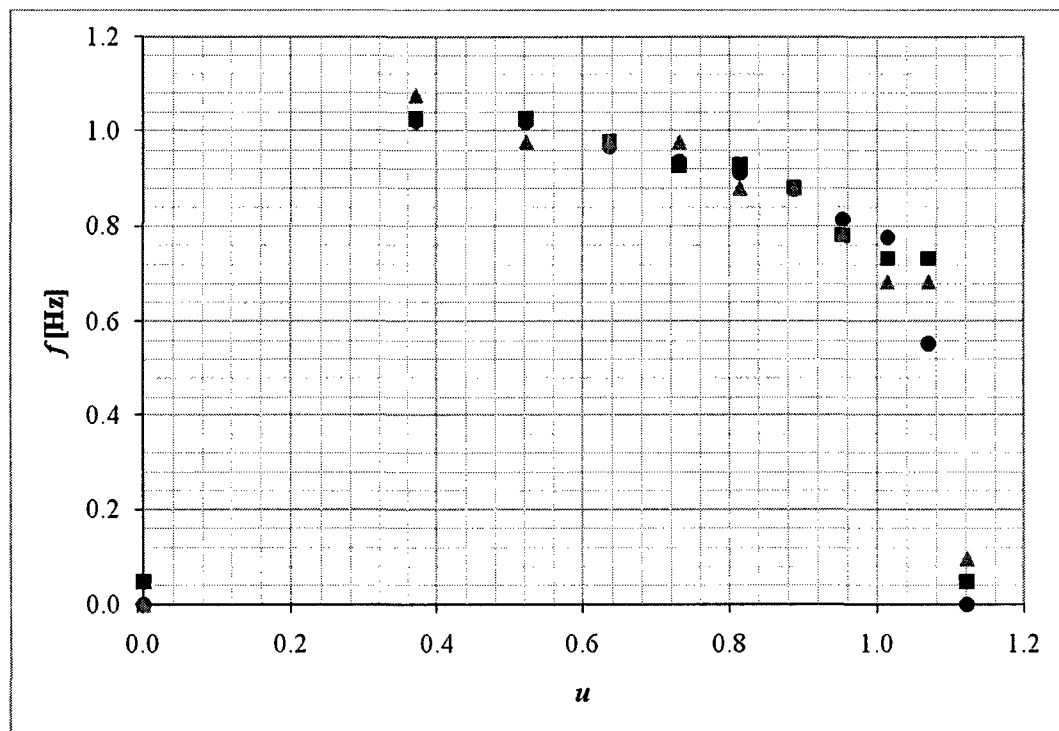


(b)

Figure 4.13. Results of Experiment 1D measured 5 mm above the free end of the cylinder. (a) amplitude versus u : ● ruler estimate, ■ max amplitude, ▲ rms amplitude; (b) frequency versus u : ● chronometer estimate, ■ PSD (8 windows), ▲ PSD (16 windows).

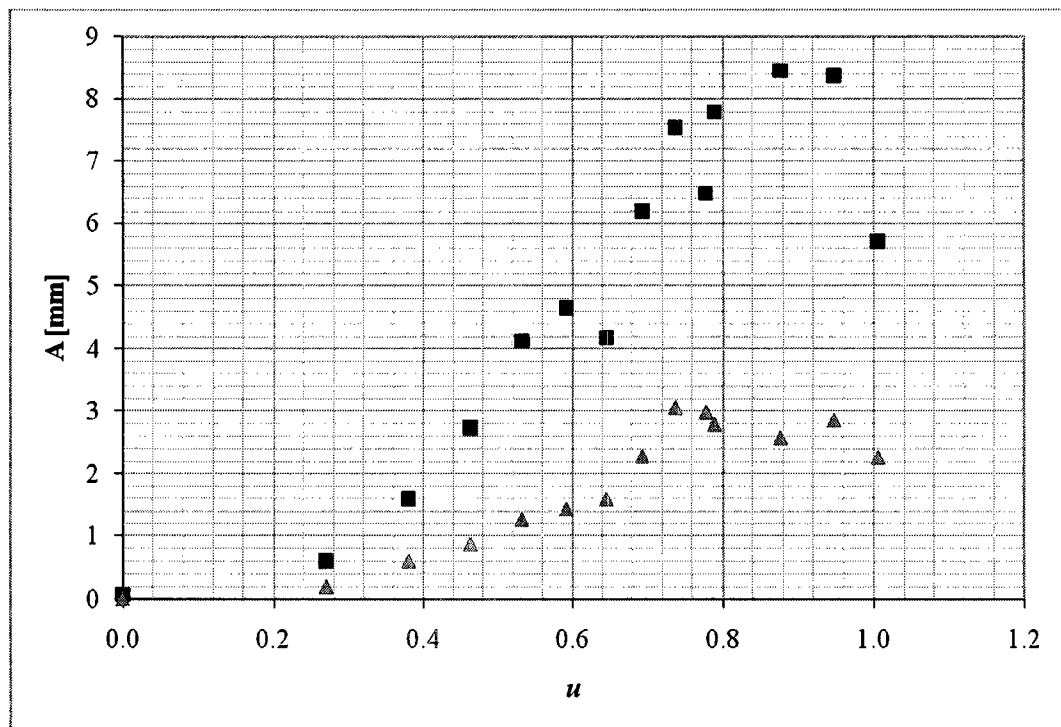


(a)

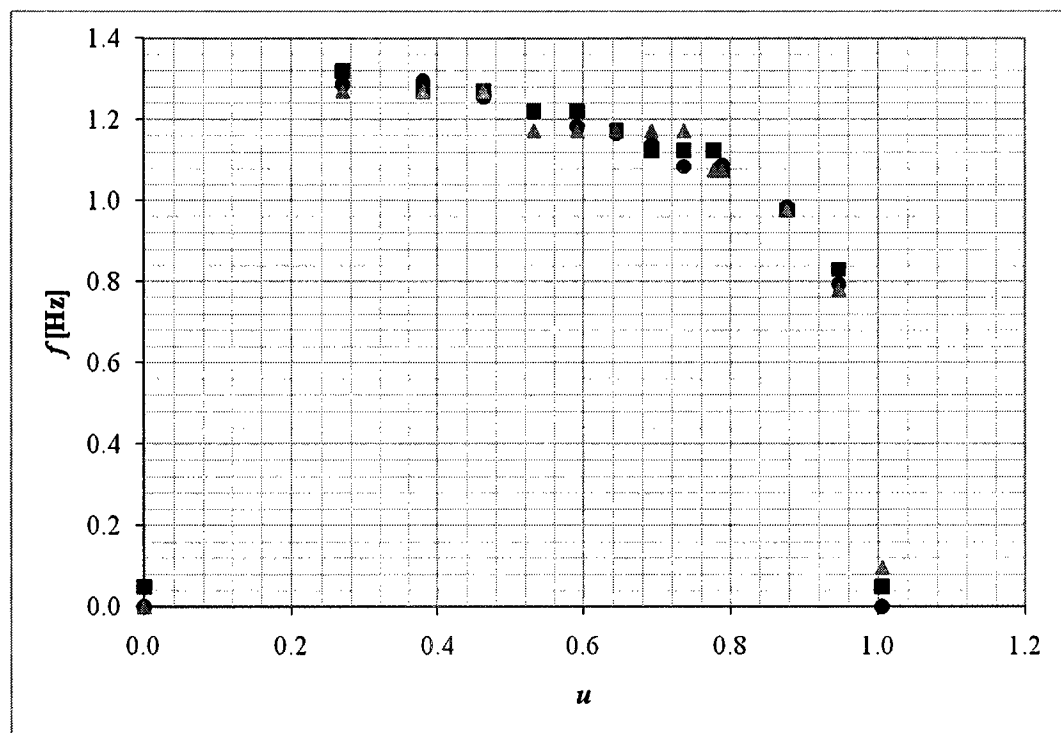


(b)

Figure 4.14. Results of Experiment 2A measured 5 mm above the free end of the cylinder. (a) amplitude versus u : ● ruler estimate, ■ max amplitude, ▲ rms amplitude; (b) frequency versus u : ● chronometer estimate, ■ PSD (8 windows), ▲ PSD (16 windows).



(a)



(b)

Figure 4.15. Results of Experiment 3A measured 5 mm above the free end of the cylinder. (a) amplitude versus u : ■ max amplitude, ▲ rms amplitude; (b) frequency versus u : ● chronometer estimate, ■ PSD (8 windows), ▲ PSD (16 windows).

divergence, since the frequency is zero, and oscillations no longer occur. This condition is never fully realized either, unless we consider the ruler estimates, as in Figs. 4.10 and 4.14.

Unfortunately, the behaviour of the cylinder at, and beyond, the onset of buckling could not be studied due to flow limitations of the experimental apparatus, since the experiments were generally terminated when the largest possible flow velocity was attained. It should also be mentioned that the experimental data reveals that cylinder 1 develops the largest amplitudes of oscillation because it is the most flexible, while cylinder 3 develops the largest critical frequencies for flutter because it is the shortest.

For each experiment, a comparison between theoretical and experimental results can be found in Table 4.3. Note that the theoretical results in the flow velocity range $0 \leq u \leq 3$ have been presented for four different cases: (i) $f = 1.00$ and $c_b = 0$, (ii) $f = 0.80$ and $c_b = 0.20$, (iii) $f = 0.60$ and $c_b = 0.40$, and (iv) $f = 0.80$ and $c_b = 0.60$. Regrettably, none of these cases accurately corresponds to what is observed in experiments; that is, flutter at very low flow velocities, followed by buckling at higher flow velocities. More specifically, if we consider the first case, divergence is the only predicted instability. Similarly, if we consider the third case, the system becomes unstable solely by flutter (for cylinders 1 and 2), yet the experimental results for $f_{cr,f}$ match the theoretical ones quite nicely, i.e. $f_{cr,f} \approx 1$ Hz. On the other hand, if the second or fourth case is considered, both flutter and buckling are predicted; however, the experimental results for $u_{cr,f}$, $f_{cr,f}$, and $u_{cr,d}$ do not agree very well with the theoretical ones. Furthermore, if we consider the second and fourth cases, wherein f is set equal to 0.80 and c_b is increased from 0.20 to 0.60, it is found that the critical flow velocities for both the onset of flutter and divergence are decreased as c_b is increased; thus, the system becomes less stable, as expected, since the compressive load at the free end ($x = L$) is increased.

It should be noted that buckling is an instability that is quite sensitive to imperfections within the pipe. Therefore, it is likely that the predicted theoretical critical flow velocities for divergence have actually been overestimated, and are thus closer in value to those determined experimentally. Nevertheless, the current linear model for a free-clamped cylinder in axial flow needs to be modified, perhaps by reassessing the boundary conditions at $x = L$, in order to validate, or otherwise, the experimental results presented in this chapter. A first-attempt at improving the model is made in Appendix H.

4.4 Summary

In this chapter, the linear equation of motion for a free-clamped cylinder subjected to confined axial flow was derived using a Newtonian approach, and the theoretical results were presented in Argand diagrams as a function of the nondimensional flow velocity using a five-mode Galerkin approximation. Four combinations of f , which is a parameter related to the tapering of the end-piece, and c_b , which is the normalized base drag coefficient, were investigated, namely (i) $f = 1.00$ and $c_b = 0$, (ii) $f = 0.80$ and $c_b = 0.20$, (iii) $f = 0.60$ and $c_b = 0.40$, and (iv) $f = 0.80$ and $c_b = 0.60$. For the first combination, the cylinder became unstable by buckling in its first mode at $u_{cr,d} = 2.39$. For the second combination, the system lost stability by flutter in its first mode via a Hopf bifurcation at $u_{cr,f} = 2.65$ with a frequency of $\text{Re}(\omega_{cr,f}) = 0.417$; afterwards, the cylinder became unstable via first-mode divergence at $u_{cr,d} = 2.66$. For the third combination, the system lost stability by flutter in its first mode via a Hopf bifurcation at $u_{cr,f} = 1.27$ with a frequency of $\text{Re}(\omega_{cr,f}) = 5.68$. For the fourth combination, the system became unstable by first-mode flutter via a Hopf bifurcation at $u_{cr,f} = 2.42$ with $\text{Re}(\omega_{cr,f}) = 0.415$; thereafter, the cylinder lost stability by first-mode divergence at $u_{cr,d} = 2.43$. Note that the second and third modes of the cylindrical structure remained stable for the full range of flow velocities considered, i.e. $0 \leq u \leq 3$, regardless of the combination of f and c_b chosen.

Moreover, confined air-flow experiments of a free-clamped cylinder were performed, and the experimental results were compared to theoretical ones. Unfortunately, the linear model proposed in Section 4.2.1 was incapable of accurately predicting the dynamical behaviour of the system. Therefore, modifications to the boundary conditions at $x = L$, or to the linear model itself, are suggested for future work. The reader is referred to Appendix H for a possible improvement to the model.

In any case, in the experiments, the cylinder was observed to exhibit first-mode flutter at very low flow velocities, i.e. $u_{cr,f} \approx 0.3$ to 0.4 . It should be mentioned that the motion of the free-clamped cylinder in axial flow during flutter was very similar to that of the cantilevered pipe aspirating fluid. However, at higher flow velocities, i.e. $u_{cr,d} \approx 1.1$ to 1.7 , the cylinder was observed to lose stability by first-mode buckling as well, but the cantilevered pipe aspirating fluid did not experience a second instability [see Chapter 3].

Furthermore, the experimental amplitudes of oscillation for the cylindrical structures were found to increase relatively quickly before reaching a maximum, and then began decreasing afterwards. Additionally, the experimental plots of frequency versus dimensionless flow velocity revealed the typical parabolic behaviour that characterizes a buckling instability. Consequently, a parabolic regression line was utilized to estimate the critical flow velocity of divergence for each of the experiments presented in this chapter. Lastly, the largest amplitudes were recorded with cylinder 1, and the highest frequencies were found with cylinder 3, respectively the most and least flexible cylinder.

CHAPTER 5

Dynamics of a Cantilevered Pipe Subjected Simultaneously to Counter-current Internal and Confined External Axial Flows

5.1 Introduction

The historical account of cylindrical structures subjected concurrently to internal and external axial flows is fairly limited. Perhaps Cesari & Curioni (1971) were the first to carry out a study of the topic. They investigated the buckling instability of the system subject to six different restraint conditions: clamped-free, clamped-clamped, pinned-supported, clamped-supported, clamped-pinned, and pinned-pinned. Possibly the most complete theoretical and experimental treatment of the subject, however, was carried out by Hannoyer & Païdoussis (1978), who studied the dynamics of the system when the internal and external flows do not depend on each other. In this case, the linear equation of motion is given by Eqn. (1.21),

$$\begin{aligned}
 & \left(E^* \frac{\partial}{\partial t} + E \right) I \frac{\partial^4 w}{\partial x^4} + \rho_i A_i \left(\frac{\partial}{\partial t} + U_i \frac{\partial}{\partial x} \right)^2 w \\
 & + \rho_e A_e \left(\frac{\partial}{\partial t} + U_e^* \frac{\partial}{\partial x} \right) \left(\frac{\partial w}{\partial t} + U_e \frac{\partial w}{\partial x} \right) - (\rho_e A_e - \rho_i A_i - m) g \frac{\partial w}{\partial x} \\
 & - \left\{ (T + A_e p_e - A_i p_i)_L + [(\rho_e A_e - \rho_i A_i - m) g - \frac{1}{2} C_{fj} \rho_e D_o U_e^2] (L - x) \right\} \frac{\partial^2 w}{\partial x^2} \\
 & + \frac{1}{2} C_{fj} \rho_e D_o U_e \left(\frac{\partial w}{\partial t} + U_e \frac{\partial w}{\partial x} \right) + \frac{1}{2} \mu_e C_D \frac{\partial w}{\partial t} + m \frac{\partial^2 w}{\partial t^2} = 0,
 \end{aligned} \tag{1.21}$$

where the standard boundary conditions for a cantilevered pipe apply, except for the one related to the shear force at $x = L$, which is given by Eqn. (1.22),

$$\begin{aligned}
 & [(\rho + f\rho_e)\bar{A}_e + (\rho_i - \rho)A_i]\ell\left(\frac{\partial^2 w}{\partial t^2}\right)_L - f\rho_e(A_e - A_i)U_e^*\left(\frac{\partial w}{\partial t}\right)_L \\
 & + [f\rho_e(A_i U_e^* - \bar{A}_e U_e) + 2\rho_i A_i U_i]\ell\left(\frac{\partial^2 w}{\partial x \partial t}\right)_L - \left(E^* \frac{\partial}{\partial t} + E\right)I\left(\frac{\partial^3 w}{\partial x^3}\right)_L \\
 & - \{f\rho_e(A_e - A_i)U_e U_e^* + [(\rho_e - \rho)\bar{A}_e + (\rho - \rho_i)A_i]g\ell\}\left(\frac{\partial w}{\partial x}\right)_L = 0,
 \end{aligned} \tag{1.22}$$

where U_e^* is a reduced external flow velocity, ℓ is the length of the tapered end, and \bar{A}_e is an average area given by Eqn. (1.23),

$$\bar{A}_e = \frac{1}{\ell} \int_L^{L+\ell} A_e(x) dx. \tag{1.23}$$

Hannoyer & Païdoussis (1978) found that the dynamical behaviour of the system is generally complex, and cannot be predicted from an analysis of the internal and external flows separately. Furthermore, the dynamics is not only dependent on the combined effect of the internal and external flow velocities, but also on the shape of the free end of the cantilevered pipe. In fact, the dynamics is dominated by the internal flow if the free end is blunt, and as a consequence, the system becomes unstable by flutter only. On the other hand, depending on the parameters of the system, both buckling and flutter may occur if the free end is nicely streamlined.

Some years later, Païdoussis *et al.* (2008) revisited the topic. This time, however, the internal and external flows were considered counter-current, and related through continuity. Moreover, the external axial flow was confined to an annular region. This work was inspired mainly by the fallacious patent for a drill-string system, consisting of an idealized hollow drill-rod and a floating fluid-powered drill-bit, which was described by Den Hartog (1969) in a lecture. The reader is referred to Chapter 1 for additional details on the drill-string system. The linear equation of motion for this system, as derived by Païdoussis *et al.* (2008), is given by Eqn. (1.25),

$$\begin{aligned}
& EI \frac{\partial^4 w}{\partial x^4} + m \frac{\partial^2 w}{\partial t^2} + \rho_i A_i \left(\frac{\partial^2 w}{\partial t^2} + 2U_i \frac{\partial^2 w}{\partial x \partial t} + U_i^2 \frac{\partial^2 w}{\partial x^2} \right) \\
& + \chi \rho_e A_e \left(\frac{\partial^2 w}{\partial t^2} - 2U_e \frac{\partial^2 w}{\partial x \partial t} + U_e^2 \frac{\partial^2 w}{\partial x^2} \right) - \{ (T - A_i p_i + A_e p_e)_L \\
& + [(m + \rho_i A_i - \rho_e A_e)g - \tfrac{1}{2} C_f \rho_e D_o U_e^2 (1 + D_o/D_h)](L - x) \} \frac{\partial^2 w}{\partial x^2} \\
& + [(m + \rho_i A_i - \rho_e A_e)g - \tfrac{1}{2} C_f \rho_e D_o U_e^2 (1 + D_o/D_h)] \frac{\partial w}{\partial x} \\
& + \tfrac{1}{2} C_f \rho_e D_o U_e \frac{\partial w}{\partial t} + c \frac{\partial w}{\partial t} = 0,
\end{aligned} \tag{1.25}$$

where $\rho_i = \rho_e \equiv \rho_f$ and $\rho_i A_i \equiv M$, and the standard boundary conditions for a cantilevered pipe apply. Theoretically, Païdoussis *et al.* (2008) found that the dynamics is dominated by the internal flow if the annular flow region is wide; therefore, the system is damped at low flow velocities, and eventually loses stability by flutter via a Hopf bifurcation at higher flow velocities. In contrast, the dynamics is dominated by the external flow if the annular flow region is narrow. Consequently, the system loses stability by flutter via a Hopf bifurcation at very low flow velocities since the external annular flow is destabilizing. Hence, the resulting dynamical behaviour of this system is very similar to that of a free-clamped cylinder in confined axial flow at low flow velocities [see Chapter 4].

The present study was motivated by the dynamics of a cantilevered pipe subjected simultaneously to counter-current internal and confined external axial flows, which are related through continuity, and thus not independent of each other. The scope of this chapter is to re-derive the linear equation of motion proposed by Païdoussis *et al.* (2008), while including some modifications, such as the presence of an end-mass and/or nozzle at the free end of the cantilevered pipe. More importantly, however, the results obtained through experimentation will be presented, and compared to those obtained through application of the theoretical model.

5.2 Theoretical Investigation

5.2.1 Paidoussis, Luu & Prabhakar (2008) model

In this section, the Newtonian approach is used to re-derive the theoretical model of Paidoussis *et al.* (2008) for small lateral, two-dimensional motions of a cantilevered pipe subjected simultaneously to counter-current internal and confined external axial flows. Fig. 5.1 depicts the system being considered, which consists of a uniform flexible pipe of length L , internal cross-sectional area A_i , based on the inner pipe diameter D_i , external cross-sectional area A_e , based on the outer pipe diameter D_o , mass per unit length m , and flexural rigidity EI . Furthermore, the pipe conveys an incompressible fluid of density ρ_f , and mass per unit length M , with an internal flow velocity U_i . The fluid leaving the free end of the pipe then flows upwards in an annular channel of cross-sectional area A_{ch} , based on the outer pipe diameter D_o and the annular channel diameter D_{ch} , with an external flow velocity U_e . Note that U_i and U_e are related through continuity, i.e. $U_i A_i = U_e A_{ch}$. The pipe is considered to be inextensible, and is also vertically hung, thus the effect of gravity is taken into consideration in the derivation of the equation of motion. Moreover, the x -axis, which is in the direction of gravity, is assumed to be coincident with the undisturbed or equilibrium axis of the pipe, and the curvilinear coordinate along the centreline of the pipe, s , is used interchangeably with the vertical coordinate, x , since lateral motions of the system, $y = w(x, t)$, are assumed to be small.

The forces and moments acting on a small element δx of the internal fluid and pipe are shown in Figs. 5.2 and 5.3, respectively. Note that p_i is the mean gauge pressure for the internal flow region, p_e is the mean gauge pressure for the external annular flow region, $F_{in}\delta x$ is the hydrodynamic force in the normal direction due to the internal flow, $F_{it}\delta x$ is the hydrodynamic force in the tangential direction due to the internal flow, $Mg\delta x$ is the weight of the internal fluid element, T is the axial tension, Q is the lateral shear force, \mathcal{M} is the bending moment, $mg\delta x$ is the weight of the pipe element, $F_{px}\delta x$ is the hydrostatic force in the x -direction, $F_{py}\delta x$ is the hydrostatic force in the y -direction, $F_A\delta x$ is the inviscid hydrodynamic force in the normal direction, $F_L\delta x$ is the viscous force in the longitudinal direction, and $F_N\delta x$ is the viscous force in the normal direction.

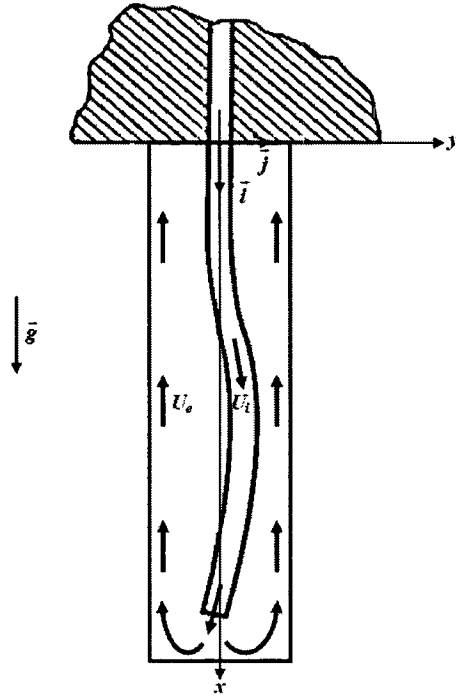


Figure 5.1. A cantilevered pipe subjected simultaneously to dependent, counter-current internal and confined external axial flows [Païdoussis & Issid (1974)].

The equations of motion in the x - and y -direction for the internal fluid are found by applying Newton's second law to the small element δx illustrated in Fig. 5.2 to give

$$-A_i \frac{\partial p_i}{\partial x} - F_u + F_m \frac{\partial w}{\partial x} + Mg = Ma_{fx}, \quad (5.1)$$

$$-A_i \frac{\partial}{\partial x} \left(p_i \frac{\partial w}{\partial x} \right) - F_u \frac{\partial w}{\partial x} - F_m = Ma_{fy}, \quad (5.2)$$

where a_{fx} and a_{fy} are the accelerations of the internal fluid element in the x - and y -direction, and are determined following the formulation presented in Section 3.2.1 of Chapter 3 to be

$$a_{fx} = 0, \quad a_{fy} = \frac{\partial^2 w}{\partial t^2} + 2U_i \frac{\partial^2 w}{\partial x \partial t} + U_i^2 \frac{\partial^2 w}{\partial x^2}. \quad (5.3)$$

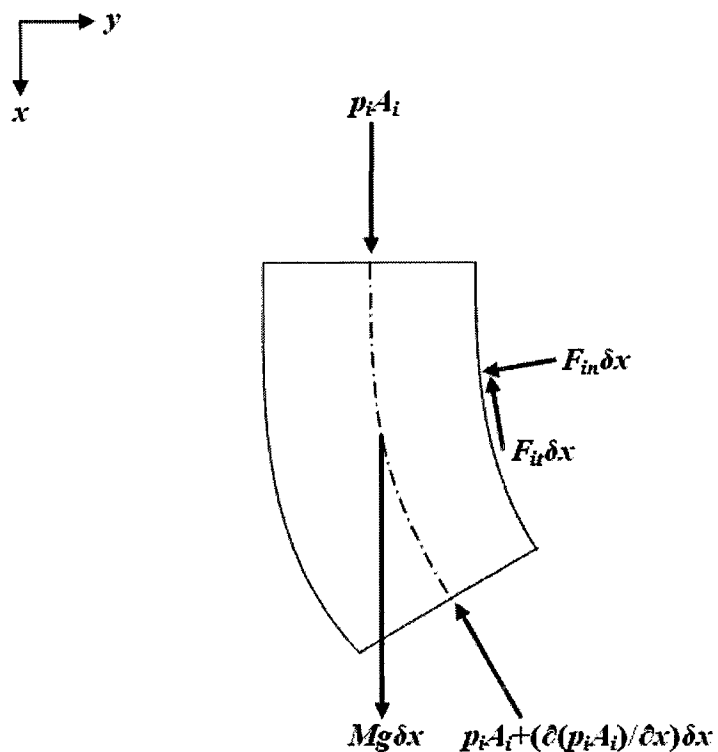


Figure 5.2. A small element δx of the internal fluid showing applied forces.

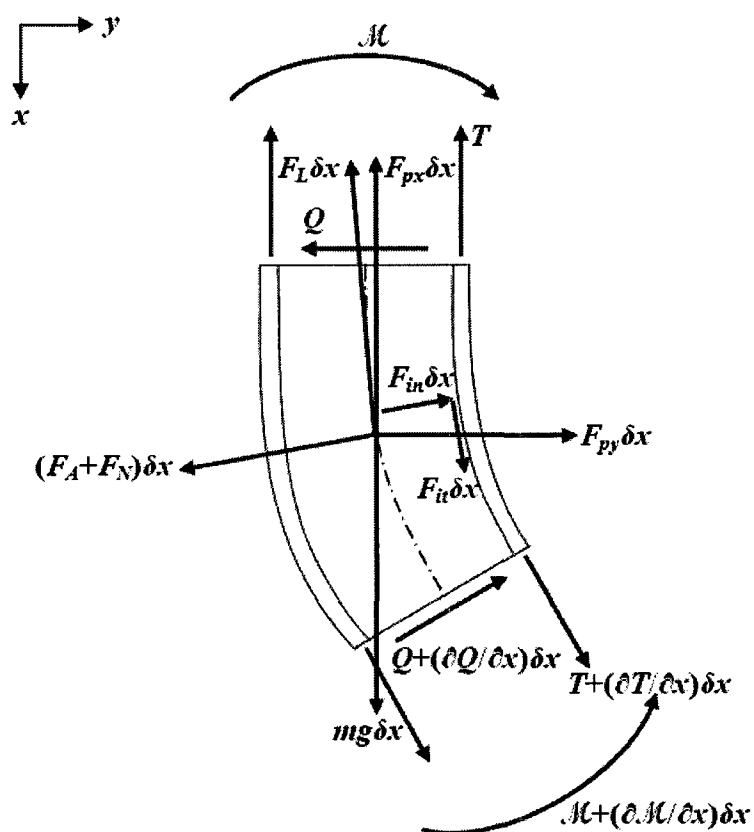


Figure 5.3. A small element δx of the pipe showing applied forces and moments.

In the same way, the equations of motion in the x - and y -direction for the pipe are found by applying Newton's second law to the small element δx shown in Fig. 5.3, yielding

$$\frac{\partial T}{\partial x} + F_{it} - F_{in} \frac{\partial w}{\partial x} - F_{px} - F_L + (F_A + F_N) \frac{\partial w}{\partial x} + mg = 0, \quad (5.4)$$

$$\frac{\partial Q}{\partial x} + \frac{\partial}{\partial x} \left(T \frac{\partial w}{\partial x} \right) + F_{it} \frac{\partial w}{\partial x} + F_{in} + F_{py} - F_L \frac{\partial w}{\partial x} - (F_A + F_N) = ma_{py}, \quad (5.5)$$

where a_{py} is the acceleration of the pipe element in the y -direction, and was found in Section 3.2.1 of Chapter 3 to be

$$a_{py} = \frac{\partial^2 w}{\partial t^2}. \quad (5.6)$$

Moreover, from Euler-Bernoulli beam theory,

$$Q = -\frac{\partial \mathcal{M}}{\partial x} = -EI \left[1 + \left(\bar{\alpha} + \frac{\bar{\mu}^*}{\Omega} \right) \frac{\partial}{\partial t} \right] \frac{\partial^3 w}{\partial x^3}, \quad (5.7)$$

where the internal dissipation in the material of the pipe is assumed to be a combination of hysteretic and viscoelastic damping [see Païdoussis & des Trois Maisons (1971)]. It should be mentioned that the effects of angular acceleration, as well as second order terms, were not included in the foregoing expressions.

The inviscid hydrodynamic force in the normal direction, $F_A \delta x$, the viscous force in the longitudinal direction, $F_L \delta x$, the viscous force in the normal direction, $F_N \delta x$, the hydrostatic force in the x -direction, $F_{px} \delta x$, and the hydrostatic force in the y -direction, $F_{py} \delta x$, were all previously derived. The reader is referred to Section 4.2.1 of Chapter 4 for more details. Thus, we have

$$F_A = \chi \rho_f A_e \left(\frac{\partial}{\partial t} - U_e \frac{\partial}{\partial x} \right) \left(\frac{\partial w}{\partial t} - U_e \frac{\partial w}{\partial x} \right), \quad (5.8)$$

where the confinement parameter is given by $\chi = (D_{ch}^2 + D_o^2) / (D_{ch}^2 - D_o^2)$,

$$F_L = \frac{1}{2} \rho_f D_o U_e^2 C_f, \quad (5.9)$$

$$F_N = \frac{1}{2} \rho_f D_o U_e C_f \left(\frac{\partial w}{\partial t} - U_e \frac{\partial w}{\partial x} \right) + c \frac{\partial w}{\partial t}, \quad (5.10)$$

where we have set $C_T = C_N \equiv C_f$, and

$$F_{px} = \frac{\partial p_e}{\partial x} A_e - \frac{\partial (p_e A_e)}{\partial x}, \quad (5.11)$$

$$F_{py} = \frac{\partial}{\partial x} \left(p_e A_e \frac{\partial w}{\partial x} \right). \quad (5.12)$$

Note that the viscous damping due to the surrounding fluid, c , in Eqn. (5.10) is given by

$$c = \frac{2\sqrt{2}}{\sqrt{S}} \frac{1 + \bar{\gamma}^3}{(1 - \bar{\gamma}^2)^2} \Omega \rho_f A_e, \quad (5.13)$$

where $\bar{\gamma} = D_o/D_{ch}$, $S = \Omega r_o^2/\nu$, $r_o = \frac{1}{2}D_o$, Ω is the circular frequency of oscillation, and ν is the kinematic viscosity of the surrounding fluid [see Païdoussis *et al.* (2008)]. Furthermore, the mean external gauge pressure, p_e , in Eqns. (5.11) and (5.12) is found by performing a force balance on a small element δx of the external flowing fluid, which is contained in the annular region formed by the pipe on one side and by the rigid channel on the other, as shown in Fig. 5.4, to yield

$$-\frac{\partial p_e}{\partial x} A_{ch} + F_f + \rho_f g A_{ch} = 0, \quad (5.14)$$

where $A_{ch} = \frac{\pi}{4} (D_{ch}^2 - D_o^2)$, and F_f is the total frictional force, given by $F_f = F_L(S_{tot}/S_o)$, where $S_{tot} = \pi D_{ch} + \pi D_o$ is the total wetted area per unit length, and $S_o = \pi D_o$ is the outside wetted area per unit length. Integrating Eqn. (5.14) with respect to x gives

$$p_e A_e = \left[F_L \left(\frac{D_o}{D_h} \right) + \rho_f g A_e \right] x, \quad (5.15)$$

where $D_h \equiv 4A_{ch}/S_{tot} = D_{ch} - D_o$ is the hydraulic diameter of the annular channel. Note that the mean external gauge pressure at $x = 0$ is assumed to be zero.

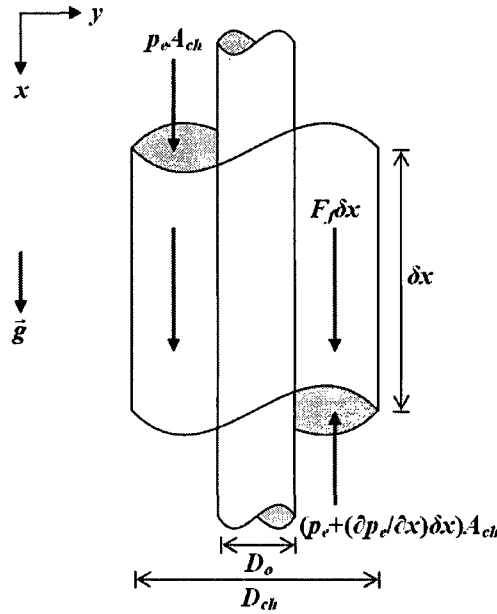


Figure 5.4. A small element δx of the external fluid showing the total frictional force F_f .

The linear equation of motion is now obtained by combining Eqns. (5.2), (5.3), (5.5) to (5.10), and (5.12) to yield

$$\begin{aligned}
 EI \left[1 + \left(\bar{\alpha} + \frac{\bar{\mu}^*}{\Omega} \right) \frac{\partial}{\partial t} \right] \frac{\partial^4 w}{\partial x^4} + m \frac{\partial^2 w}{\partial t^2} + M \left(\frac{\partial^2 w}{\partial t^2} + 2U_i \frac{\partial^2 w}{\partial x \partial t} + U_i^2 \frac{\partial^2 w}{\partial x^2} \right) \\
 - \frac{\partial}{\partial x} \left[(T - p_i A_i + p_e A_e) \frac{\partial w}{\partial x} \right] + \chi \rho_f A_e \left(\frac{\partial^2 w}{\partial t^2} - 2U_e \frac{\partial^2 w}{\partial x \partial t} + U_e^2 \frac{\partial^2 w}{\partial x^2} \right) \\
 + \frac{1}{2} \rho_f D_o U_e C_f \frac{\partial w}{\partial t} + c \frac{\partial w}{\partial t} = 0,
 \end{aligned} \quad (5.16)$$

where $(T - p_i A_i + p_e A_e)$ is found by combining Eqns. (5.1), (5.3), (5.4), (5.8) to (5.11), and (5.15) to give

$$\frac{\partial (T - p_i A_i + p_e A_e)}{\partial x} = \frac{1}{2} \rho_f D_o U_e^2 C_f (1 + D_o/D_h) - (m + M - \rho_f A_e) g. \quad (5.17)$$

Integrating Eqn. (5.17) from x to L gives

$$\begin{aligned}
 (T - p_i A_i + p_e A_e) &= (T - p_i A_i + p_e A_e)_L - \frac{1}{2} \rho_f D_o U_e^2 C_f \left(1 + \frac{D_o}{D_h} \right) (L - x) \\
 &+ (m + M - \rho_f A_e) g (L - x).
 \end{aligned} \quad (5.18)$$

Introducing Eqns. (5.17) and (5.18) into Eqn. (5.16) yields

$$\begin{aligned}
 EI & \left[1 + \left(\bar{\alpha} + \frac{\bar{\mu}^*}{\Omega} \right) \frac{\partial}{\partial t} \right] \frac{\partial^4 w}{\partial x^4} + m \frac{\partial^2 w}{\partial t^2} + M \left(\frac{\partial^2 w}{\partial t^2} + 2U_i \frac{\partial^2 w}{\partial x \partial t} + U_i^2 \frac{\partial^2 w}{\partial x^2} \right) \\
 & - \left[(T - p_i A_i + p_e A_e)_L - \frac{1}{2} \rho_f D_o U_e^2 C_f \left(1 + \frac{D_o}{D_h} \right) (L - x) \right] \frac{\partial^2 w}{\partial x^2} \\
 & - (m + M - \rho_f A_e) g (L - x) \frac{\partial^2 w}{\partial x^2} \\
 & + \left[(m + M - \rho_f A_e) g - \frac{1}{2} \rho_f D_o U_e^2 C_f \left(1 + \frac{D_o}{D_h} \right) \right] \frac{\partial w}{\partial x} \\
 & + \chi \rho_f A_e \left(\frac{\partial^2 w}{\partial t^2} - 2U_e \frac{\partial^2 w}{\partial x \partial t} + U_e^2 \frac{\partial^2 w}{\partial x^2} \right) + \frac{1}{2} \rho_f D_o U_e C_f \frac{\partial w}{\partial t} + c \frac{\partial w}{\partial t} = 0.
 \end{aligned} \tag{5.19}$$

The presence of an end-mass at the free end of the pipe may be accounted for by replacing the quantity $(m + M)$ by $[m + M + m_e \delta(x - L)]$ in Eqn. (5.19), where $\delta(x - L)$ is a Dirac delta function. Hence, the final form of the equation of motion, correct to first order, for a cantilevered pipe subjected simultaneously to counter-current internal and confined external axial flows is

$$\begin{aligned}
 EI & \left[1 + \left(\bar{\alpha} + \frac{\bar{\mu}^*}{\Omega} \right) \frac{\partial}{\partial t} \right] \frac{\partial^4 w}{\partial x^4} + m \frac{\partial^2 w}{\partial t^2} + M \left(\frac{\partial^2 w}{\partial t^2} + 2U_i \frac{\partial^2 w}{\partial x \partial t} + U_i^2 \frac{\partial^2 w}{\partial x^2} \right) \\
 & + m_e \delta(x - L) \frac{\partial^2 w}{\partial t^2} - \left[(T - p_i A_i + p_e A_e)_L - \frac{1}{2} \rho_f D_o U_e^2 C_f \left(1 + \frac{D_o}{D_h} \right) (L - x) \right] \frac{\partial^2 w}{\partial x^2} \\
 & - \left\{ \int_x^L [m + M + m_e \delta(x - L) - \rho_f A_e] g dx \right\} \frac{\partial^2 w}{\partial x^2} \\
 & + \left\{ [m + M + m_e \delta(x - L) - \rho_f A_e] g - \frac{1}{2} \rho_f D_o U_e^2 C_f \left(1 + \frac{D_o}{D_h} \right) \right\} \frac{\partial w}{\partial x} \\
 & + \chi \rho_f A_e \left(\frac{\partial^2 w}{\partial t^2} - 2U_e \frac{\partial^2 w}{\partial x \partial t} + U_e^2 \frac{\partial^2 w}{\partial x^2} \right) + \frac{1}{2} \rho_f D_o U_e C_f \frac{\partial w}{\partial t} + c \frac{\partial w}{\partial t} = 0,
 \end{aligned} \tag{5.20}$$

which is subject to the standard cantilevered boundary conditions; at $x = 0$,

$$w = \frac{\partial w}{\partial x} = 0, \tag{5.21}$$

and at $x = L$,

$$\frac{\partial^2 w}{\partial x^2} = \frac{\partial^3 w}{\partial x^3} = 0. \quad (5.22)$$

The only undefined quantity in Eqn. (5.20) is the term $(T - p_i A_i + p_e A_e)_L$. Now, the end-mass attached to the free end of the pipe is assumed to be a very short convergent nozzle. In Païdoussis (1998, p. 76), where we have a cantilevered pipe discharging to atmosphere,

$$(T - p_i A_i)_L = -(p_i A_i)_L = -MU_i(U_j - U_i) \quad (5.23)$$

where $U_j = U_i(A_i/A_j)$ is the discharge velocity, and A_j is the cross-sectional area of the nozzle exit. In Eqn. (5.23), it is understood that T_L , which is the tension at $x = L$, is zero. Nevertheless, \bar{T}_L , which is an externally applied tension, is retained for generality. Consequently, Eqn. (5.23) becomes

$$(T - p_i A_i)_L = \bar{T}_L - MU_i(U_j - U_i) \quad (5.24)$$

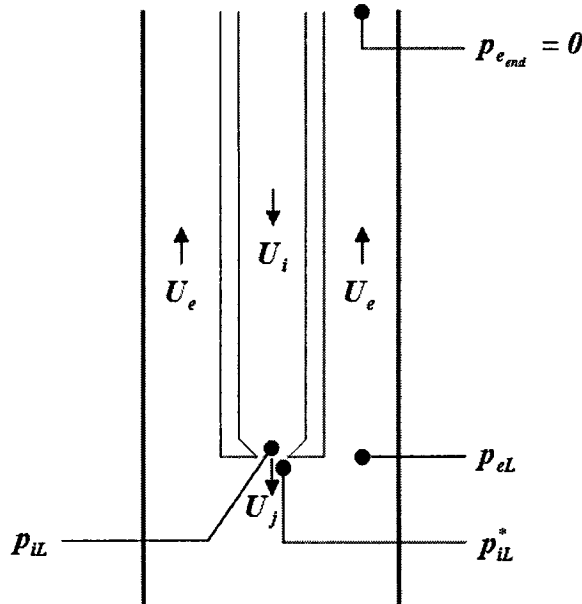


Figure 5.5. Diagram showing the locations of the mean pressures and flow velocities.

Furthermore, the pressure just outside the free end of the pipe, p_{iL}^* , which is shown in Fig. 5.5, is related to p_{eL} through the relationship

$$p_{iL}^* + \frac{1}{2} \rho_f U_j^2 = p_{eL} + \frac{1}{2} \rho_f U_e^2 + \rho_f g h_o, \quad (5.25)$$

where h_o is the head loss arising from the sudden expansion in flow area from A_j to A_{ch} , and is given by the expression

$$h_o = \frac{1}{2g} C (U_j - U_e)^2, \quad (5.26)$$

where $C = 1$ is taken [see Païdoussis *et al.* (2008)]. Combining Eqns. (5.25) and (5.26) yields

$$p_{iL}^* = p_{eL} + \rho_f U_e (U_e - U_j) \quad (5.27)$$

A further reduction in pressure arises because of the presence of the nozzle; so, we can write the following:

$$p_{iL} = p_{iL}^* + \rho_f U_i (U_j - U_i) \quad (5.28)$$

Introducing Eqn. (5.27) into Eqn. (5.28) gives

$$p_{iL} = p_{eL} + \rho_f U_e (U_e - U_j) + \rho_f U_i (U_j - U_i) \quad (5.29)$$

where, from Eqn. (5.15),

$$p_{eL} = \left[\frac{F_L}{A_e} \left(\frac{D_o}{D_h} \right) + \rho_f g \right] L. \quad (5.30)$$

Note that, in the absence of the nozzle, $U_j = U_i$ in Eqn. (5.29), and the expression for p_{iL} in Païdoussis *et al.* (2008) is recovered; in the case of an infinite external annular flow area, $U_e = 0$, and assuming that $p_{eL} = 0$, the expression for p_{iL} in Païdoussis (1998, p. 76) is recovered, as expected. Therefore, we have

$$\begin{aligned} (T - p_i A_i + p_e A_e)_L &= \bar{T}_L - M U_e (U_e - U_j) - M U_i (U_j - U_i) \\ &+ \left[F_L \left(\frac{D_o}{D_h} \right) + \rho_f g A_e \right] \left[1 - \left(\frac{D_i}{D_o} \right)^2 \right] L. \end{aligned} \quad (5.31)$$

Now, the linear equation of motion is rendered dimensionless by substituting the following dimensionless parameters in Eqn. (5.20):

$$\xi = \frac{x}{L}, \quad \eta = \frac{w}{L}, \quad \tau = \left(\frac{EI}{m + M + \rho_f A_e} \right)^{1/2} \frac{t}{L^2}. \quad (5.32)$$

This eventually leads to the expression

$$\begin{aligned} & \left[1 + \left(\bar{\alpha}^* + \frac{\bar{\mu}^*}{\omega} \right) \frac{\partial}{\partial \tau} \right] \frac{\partial^4 \eta}{\partial \xi^4} + [1 + \beta_e (\chi - 1) + \Gamma_e \delta (\xi - 1)] \frac{\partial^2 \eta}{\partial \tau^2} \\ & + 2(u_i \beta_i^{1/2} - \chi u_e \beta_e^{1/2}) \frac{\partial^2 \eta}{\partial \xi \partial \tau} + (u_i^2 + \chi u_e^2) \frac{\partial^2 \eta}{\partial \xi^2} \\ & - \left[(\Gamma_L - \Pi_{iL} + \Pi_{eL}) + \gamma \left(1 - \xi + \frac{\Gamma_e}{1 - 2\beta_e} \right) - \frac{1}{2} c_f \varepsilon u_e^2 (1 + h)(1 - \xi) \right] \frac{\partial^2 \eta}{\partial \xi^2} \\ & + \left\{ \gamma \left[1 + \frac{\Gamma_e \delta (\xi - 1)}{1 - 2\beta_e} \right] - \frac{1}{2} c_f \varepsilon u_e^2 (1 + h) \right\} \frac{\partial \eta}{\partial \xi} + \frac{1}{2} c_f \varepsilon u_e \beta_e^{1/2} \frac{\partial \eta}{\partial \tau} + \sigma \frac{\partial \eta}{\partial \tau} = 0, \end{aligned} \quad (5.33)$$

where

$$\begin{aligned} \bar{\alpha}^* &= \left(\frac{EI}{m + M + \rho_f A_e} \right)^{1/2} \frac{\bar{\alpha}}{L^2}, \quad \omega = \left(\frac{m + M + \rho_f A_e}{EI} \right)^{1/2} \Omega L^2, \\ u_i &= \left(\frac{M}{EI} \right)^{1/2} U_i L, \quad u_e = \left(\frac{\rho_f A_e}{EI} \right)^{1/2} U_e L, \\ \beta_i &= \frac{M}{m + M + \rho_f A_e}, \quad \beta_e = \frac{\rho_f A_e}{m + M + \rho_f A_e}, \quad \Gamma_e = \frac{m_e}{(m + M + \rho_f A_e)L}, \\ \gamma &= \frac{(m + M - \rho_f A_e)gL^3}{EI}, \quad \Gamma_L = \frac{T_L L^2}{EI}, \quad \Pi_{iL} = \frac{p_{iL} A_i L^2}{EI}, \quad \Pi_{eL} = \frac{p_{eL} A_e L^2}{EI}, \\ c_f &= \frac{4}{\pi} C_f, \quad \varepsilon = \frac{L}{D_o}, \quad h = \frac{D_o}{D_h}, \quad \sigma = \frac{cL^2}{[EI(m + M + \rho_f A_e)]^{1/2}}. \end{aligned} \quad (5.34)$$

After some manipulation, the dimensionless form of Eqn. (5.31) may be expressed as

$$\begin{aligned} (\Gamma_L - \Pi_{iL} + \Pi_{eL}) &= \bar{\Gamma}_L - \alpha_i^2 u_e^2 [1 - (\alpha_{ch}^2 - 1)/\alpha_j^2] - u_i^2 [(\alpha_i/\alpha_j)^2 - 1] \\ &+ \frac{1}{2} c_f \varepsilon u_e^2 h (1 - \alpha_i^2) + \rho_f g A_e L^3 (1 - \alpha_i^2)/EI, \end{aligned} \quad (5.35)$$

where

$$\bar{\Gamma}_L = \frac{\bar{T}_L L^2}{EI}, \quad \alpha_i = \frac{D_i}{D_o}, \quad \alpha_j = \frac{D_j}{D_o}, \quad \alpha_{ch} = \frac{D_{ch}}{D_o}, \quad u_e = \frac{\alpha_i}{(\alpha_{ch}^2 - 1)} u_i. \quad (5.36)$$

The Galerkin method is used to discretize the system by assuming a solution of the form

$$\eta(\xi, \tau) = \sum_{r=1}^N \phi_r(\xi) q_r(\tau), \quad (5.37)$$

where $\phi_r(\xi)$ are the comparison functions, i.e. the cantilever beam eigenfunctions, and $q_r(\tau)$ are the generalized coordinates. This leads to N decoupled ordinary differential equations, which may be expressed concisely as

$$[M]\ddot{\mathbf{q}} + [C]\dot{\mathbf{q}} + [K]\mathbf{q} = \mathbf{0}, \quad (5.38)$$

where $\mathbf{q} = \{q_1, q_2, \dots, q_N\}^T$. Using Eqn. (5.37), Eqn. (5.33) becomes

$$\begin{aligned} \sum_{r=1}^N \{ & \lambda_r^4 \phi_r q_r + (\bar{\alpha}^* + \bar{\mu}^*/\omega) \lambda_r^4 \phi_r \dot{q}_r + [1 + \beta_e(\chi - 1) + \Gamma_e \delta(\xi - 1)] \phi_r \ddot{q}_r \\ & + 2(u_i \beta_i^{1/2} - \chi u_e \beta_e^{1/2}) \phi_r' \dot{q}_r + (u_i^2 + \chi u_e^2) \phi_r'' q_r - (\Gamma_L - \Pi_{iL} + \Pi_{eL}) \phi_r'' q_r \\ & - \left\{ \gamma [1 + \Gamma_e/(1 - 2\beta_e)] - \frac{1}{2} c_f \epsilon u_e^2 (1 + h) \right\} \phi_r'' q_r + \left[\gamma - \frac{1}{2} c_f \epsilon u_e^2 (1 + h) \right] \xi \phi_r'' q_r \\ & + \left\{ \gamma [1 + \Gamma_e \delta(\xi - 1)/(1 - 2\beta_e)] - \frac{1}{2} c_f \epsilon u_e^2 (1 + h) \right\} \phi_r' q_r \\ & + \left(\frac{1}{2} c_f \epsilon u_e \beta_e^{1/2} + \sigma \right) \phi_r \dot{q}_r \} = 0. \end{aligned} \quad (5.39)$$

Multiplying Eqn. (5.39) by $\phi_s(\xi)$ and integrating over the domain $[0, 1]$ yields

$$\begin{aligned} & \lambda_r^4 \delta_{sr} q_r + (\bar{\alpha}^* + \bar{\mu}^*/\omega) \lambda_r^4 \delta_{sr} \dot{q}_r + [1 + \beta_e(\chi - 1)] \delta_{sr} \ddot{q}_r + \Gamma_e \phi_s(1) \phi_r(1) \ddot{q}_r \\ & + 2(u_i \beta_i^{1/2} - \chi u_e \beta_e^{1/2}) b_{sr} \dot{q}_r + (u_i^2 + \chi u_e^2) c_{sr} q_r - (\Gamma_L - \Pi_{iL} + \Pi_{eL}) c_{sr} q_r \\ & - \left\{ \gamma [1 + \Gamma_e/(1 - 2\beta_e)] - \frac{1}{2} c_f \epsilon u_e^2 (1 + h) \right\} c_{sr} q_r + \left[\gamma - \frac{1}{2} c_f \epsilon u_e^2 (1 + h) \right] d_{sr} q_r \\ & + \left[\gamma - \frac{1}{2} c_f \epsilon u_e^2 (1 + h) \right] b_{sr} q_r + \gamma [\Gamma_e/(1 - 2\beta_e)] \phi_s(1) \phi_r'(1) q_r \\ & + \left(\frac{1}{2} c_f \epsilon u_e \beta_e^{1/2} + \sigma \right) \delta_{sr} \dot{q}_r = 0, \end{aligned} \quad (5.40)$$

where we have

$$b_{sr} = \frac{4}{(\lambda_s/\lambda_r)^2 + (-1)^{r+s}}, \quad b_{rr} = 2, \quad (5.41)$$

$$c_{sr} = \frac{4(\lambda_r\sigma_r - \lambda_s\sigma_s)}{(-1)^{r+s} - (\lambda_s/\lambda_r)^2}, \quad c_{rr} = \lambda_r\sigma_r(2 - \lambda_r\sigma_r), \quad (5.42)$$

$$d_{sr} = \frac{4(\lambda_r\sigma_r - \lambda_s\sigma_s + 2)}{1 - (\lambda_s/\lambda_r)^4}(-1)^{r+s} - \frac{3 + (\lambda_s/\lambda_r)^4}{1 - (\lambda_s/\lambda_r)^4}b_{sr}, \quad d_{rr} = \frac{1}{2}c_{rr}, \quad (5.43)$$

for a cantilevered pipe [see Païdoussis (1998, p. 87)]. The elements of the mass $[M]$, damping $[C]$, and stiffness $[K]$ matrices in Eqn. (5.38) are found by inspection of Eqn. (5.40) to be

$$M_{sr} = [1 + \beta_e(\chi - 1)]\delta_{sr} + \Gamma_e\phi_s(1)\phi_r(1), \quad (5.44)$$

$$C_{sr} = [(\bar{\alpha}^* + \bar{\mu}^*/\omega)\lambda_r^4 + \frac{1}{2}c_f\epsilon u_e\beta_e^{1/2} + \sigma]\delta_{sr} + 2(u_i\beta_i^{1/2} - \chi u_e\beta_e^{1/2})b_{sr}, \quad (5.45)$$

$$\begin{aligned} K_{sr} = & \lambda_r^4\delta_{sr} + [\gamma - \frac{1}{2}c_f\epsilon u_e^2(1+h)]b_{sr} - (\Gamma_L - \Pi_{iL} + \Pi_{eL})c_{sr} \\ & + \{u_i^2 + \chi u_e^2 - \gamma[1 + \Gamma_e/(1 - 2\beta_e)] + \frac{1}{2}c_f\epsilon u_e^2(1+h)\}c_{sr} \\ & + [\gamma - \frac{1}{2}c_f\epsilon u_e^2(1+h)]d_{sr} + \gamma[\Gamma_e/(1 - 2\beta_e)]\phi_s(1)\phi_r'(1). \end{aligned} \quad (5.46)$$

Note that the case of no end-mass is recovered if Γ_e is set equal to zero in Eqns. (5.44) to (5.46). Furthermore, $(\Gamma_L - \Pi_{iL} + \Pi_{eL})$ is given by Eqn. (5.35).

5.2.2 Theoretical results

The system studied in this section has the following dimensionless characteristics: $\bar{\alpha}^* = 0.00021$, $\bar{\mu}^* = 0.04920$, $\beta_i = 0.0542$, $\beta_e = 0.339$, $\Gamma_e = 7.49 \times 10^{-3}$, $\gamma = 7.14$, $\bar{\Gamma}_L = 0$, $c_f = 0.0159$, $\epsilon = 21.6$, $h = 1.00$ (or 1.67), $\alpha_i = 0.400$, $\alpha_j = 0.320$, $\alpha_{ch} = 2.00$ (or 1.60), and $\chi = 1.67$ (or 2.28). These quantities correspond to a physical system defined by $D_o = 0.0159$ m, $D_i = 0.00635$ m, $D_j = 0.00508$ m, $D_{ch} = 0.0318$ m (or 0.0254 m), $L = 0.343$ m, $EI = 1.05 \times 10^{-2}$ N·m², $m = 0.355$ kg/m, $M = 0.0317$ kg/m, $\rho_f A_e = 0.198$ kg/m, and $m_e = 1.50 \times 10^{-3}$ kg. The Argand diagrams for the three lowest modes as a function of the dimensionless internal flow velocity, u_i , for the two values of α_{ch} investigated are

presented in Figs. 5.6 and 5.7. It should be mentioned that the multiplicative factor to switch from u_i to U_i in m/s is 1.68, that to switch from u_e to U_e in m/s is 0.671, and that to switch from ω to f in Hz is 0.181. Additionally, we have that

$$\begin{aligned} u_e &= 0.133u_i \text{ for } \alpha_{ch} = 2.00, \\ u_e &= 0.256u_i \text{ for } \alpha_{ch} = 1.60. \end{aligned} \tag{5.47}$$

From Fig. 5.6, it is seen that for wide annular channels, here $\alpha_{ch} = 2.00$, the cantilevered pipe becomes unstable by flutter in its second mode at an internal flow velocity of $u_{i,cr} = 4.42$, and with a frequency of oscillation of $\text{Re}(\omega_{cr}) = 11.4$. This dynamic instability occurs via a Hopf bifurcation, since the imaginary component of the dimensionless complex frequency, $\text{Im}(\omega)$, becomes negative at this critical point, while the real component, $\text{Re}(\omega)$, remains greater than zero. Note that the internal flow plays a dominant role here: the system exhibits similar behaviour to that when it is simply discharging internal fluid [see Chapter 2]. It should also be mentioned that both the first and third modes of the system remain stable; the flow induces damping for the entire range of internal flow velocities considered, i.e. for $0 \leq u_i \leq 8$.

From Fig. 5.7, it is determined that for a narrow annular channel, here $\alpha_{ch} = 1.60$, the cantilevered pipe loses stability by flutter in its first mode via a Hopf bifurcation at an internal flow velocity of $u_{i,cr} = 2.25$, and with a frequency of oscillation of $\text{Re}(\omega_{cr}) = 4.16$. On the other hand, the second-mode locus of the system remains stable over the full range of internal flow velocities investigated. In fact, an increase in the internal flow velocity causes an increase in system damping. The cantilevered pipe also exhibits single-mode flutter when the fluid attains an internal flow velocity of $u_{i,cr} = 7.55$, this time in its third mode with a critical frequency of oscillation $\text{Re}(\omega_{cr}) = 20.7$. Thus, it can be concluded that the critical flow velocity, as well as the frequency of oscillation for the first encountered instability are much lower for $\alpha_{ch} = 1.60$ than for $\alpha_{ch} = 2.00$. The latter is expected since the first-mode frequencies of the system are generally lower than the second-mode ones for fairly small flow velocities. Lastly, it is interesting to note that the unstable modes for $\alpha_{ch} = 1.60$ are stable for $\alpha_{ch} = 2.00$; similarly, the unstable mode for $\alpha_{ch} = 2.00$ is stable for $\alpha_{ch} = 1.60$.

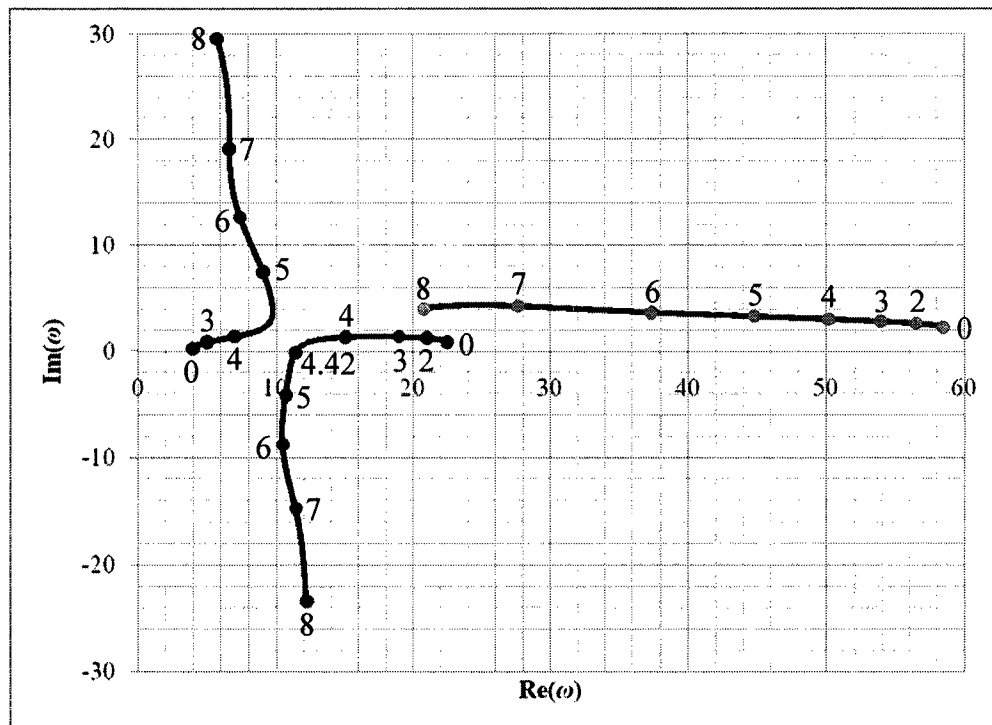


Figure 5.6. Argand diagram as a function of u_i for $\alpha_{ch} = 2.00$ using a fifteen-mode Galerkin approximation.

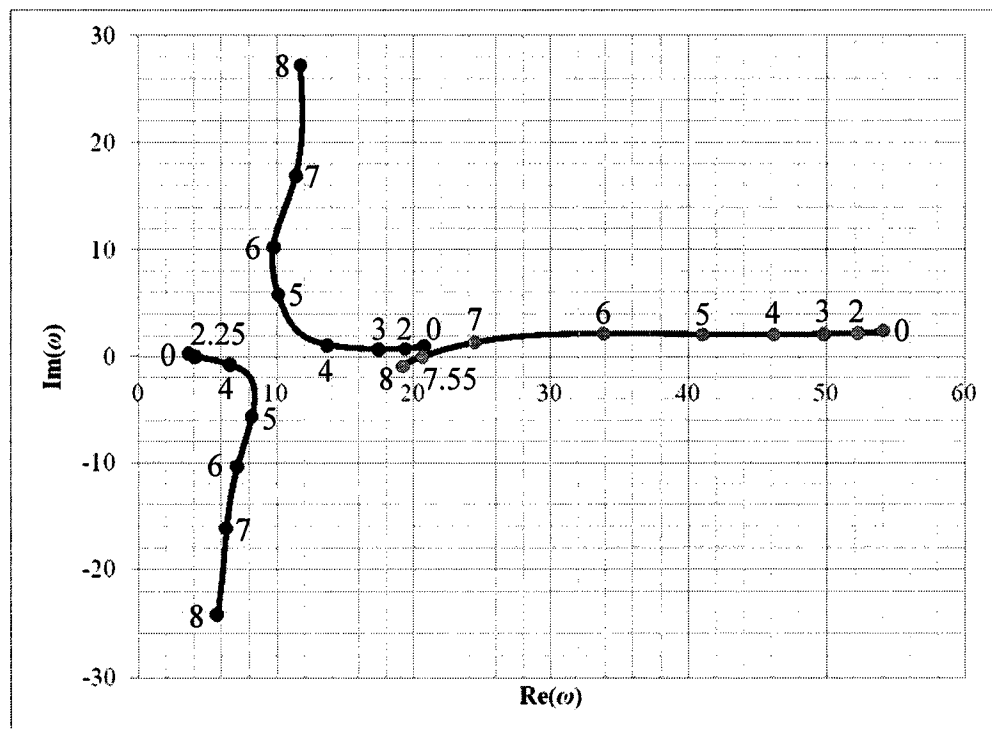


Figure 5.7. Argand diagram as a function of u_i for $\alpha_{ch} = 1.60$ using a fifteen-mode Galerkin approximation.

5.3 Experimental Investigation

5.3.1 *Experimental apparatus*

The water experiments of a cantilevered pipe subjected simultaneously to internal and confined external axial flow were carried out with a flexible elastomer pipe, in which fine copper particles were added in the two-part silicone rubber mixture during the casting process [see Appendix A]. The geometrical and physical properties of the pipe are presented in Table 5.1. Note that the logarithmic decrements of the system for modes greater than $n = 3$ are approximated by $\delta_n = 0.0623n + 0.0030$. The reader is referred to Appendix B for an account of the determination of the natural frequencies, flexural rigidity, and logarithmic decrements of the pipe, and also to Section 2.3.1 of Chapter 2 for a complete description and a schematic of the experimental set-up.

A variety of plastic end-pieces, including a nozzle with diameter $D_j = 0.00508$ m ($\alpha_j = 0.320$) and mass $m_e = 1.50 \times 10^{-3}$ kg ($\Gamma_e = 7.49 \times 10^{-3}$), a semi-spherical end-piece with mass $m_e = 2.10 \times 10^{-3}$ kg ($\Gamma_e = 1.05 \times 10^{-2}$), and four sets of rings with thicknesses varying from 4.76 mm to 12.7 mm were employed during the experiments, as illustrated in Fig. 5.8. It should be mentioned that the rings, which were used to prompt a leakage-flow instability, were placed approximately 3 mm from the free end of the pipe, and that each set of rings consisted of: one of 20.6 mm in width, which was used for the narrow channel experiments ($\alpha_{ch} = 1.60$), and another of 27.0 mm in width, which was used for the wide channel experiments ($\alpha_{ch} = 2.00$).

The reader is also referred to Fig. 5.9 for a sketch of the experimental apparatus and to Appendix F for the technical drawings of the individual components, and an assembly of the rigid annular channel, which surrounds the cantilevered pipe and confines the external axial flow. It should be mentioned that this apparatus was fabricated almost entirely from plexiglas, and was enclosed within square plexiglas tubing, which allowed easier viewing and recording of the motion of the cantilevered system during experiments. Moreover, a screen and honeycomb were incorporated into the design in order to straighten the flow emerging from the free end of the pipe, and subsequently

Table 5.1. The geometrical and physical properties of the pipe

D_o [m]	D_i [m]	L [m]	EI [N·m ²]	m [kg/m]	M [kg/m]
0.0159	0.00635	0.343	1.05×10^{-2}	0.355	0.0317
$\rho_f A_e$ [kg/m]	β_e [-]	β_i [-]	γ [-]	$\bar{\alpha}^*$ [-]	$\bar{\mu}^*$ [-]
0.198	0.339	0.0542	7.14	0.00021	0.04920
f_1 [Hz]	f_2 [Hz]	f_3 [Hz]	δ_1 [-]	δ_2 [-]	δ_3 [-]
1.34	5.86	15.6	0.0587	0.141	0.183

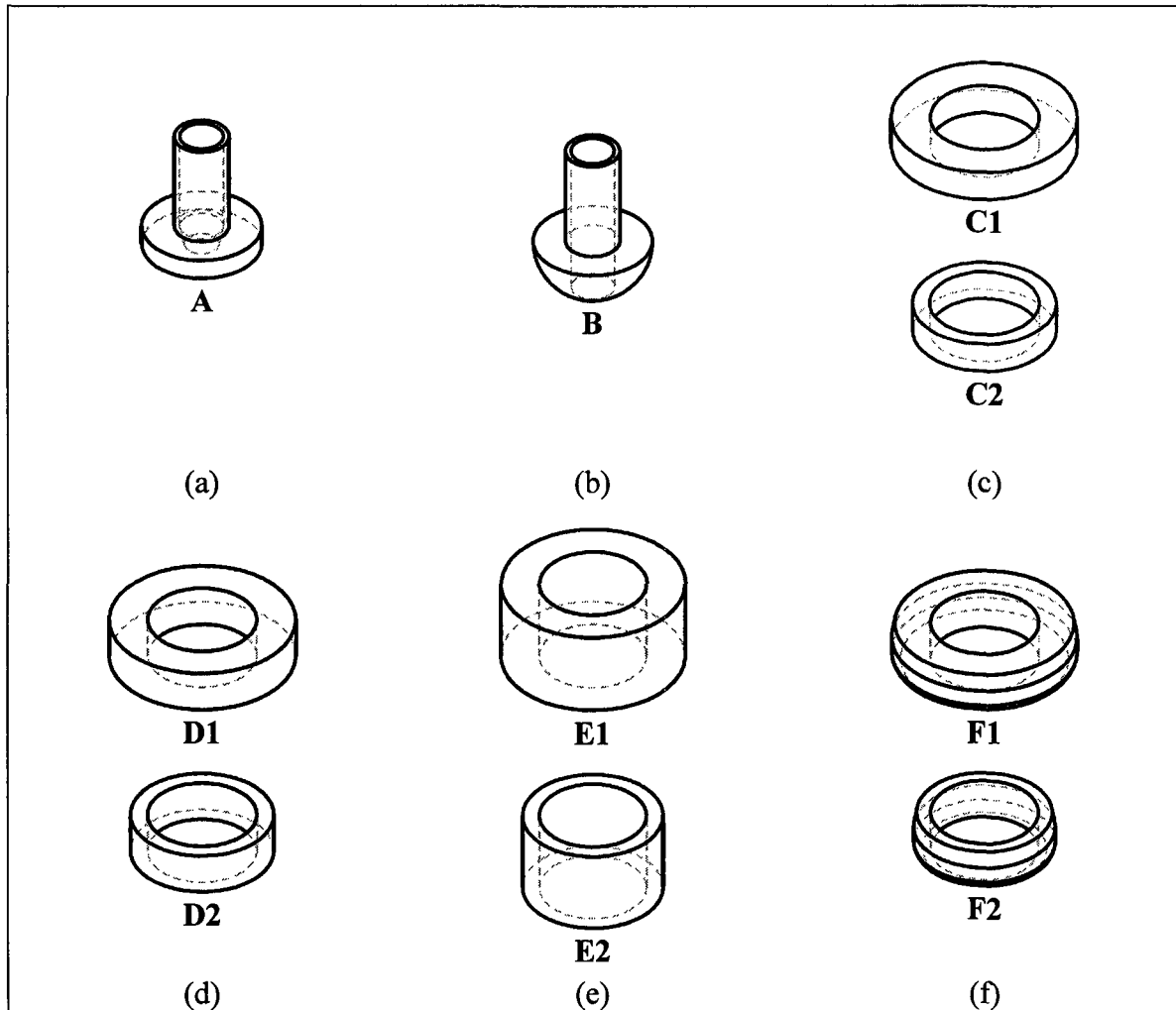


Figure 5.8. Schematic of the plastic end-pieces used in experiments: (a) nozzle with $D_j = 0.00508$ m and $m_e = 1.50 \times 10^{-3}$ kg; (b) semi-spherical end-piece with $m_e = 2.10 \times 10^{-3}$ kg; (c) 4.76 mm thick rings; (d) 6.35 mm thick rings; (e) 12.7 mm thick rings; and (f) 6.35 mm thick profiled rings.

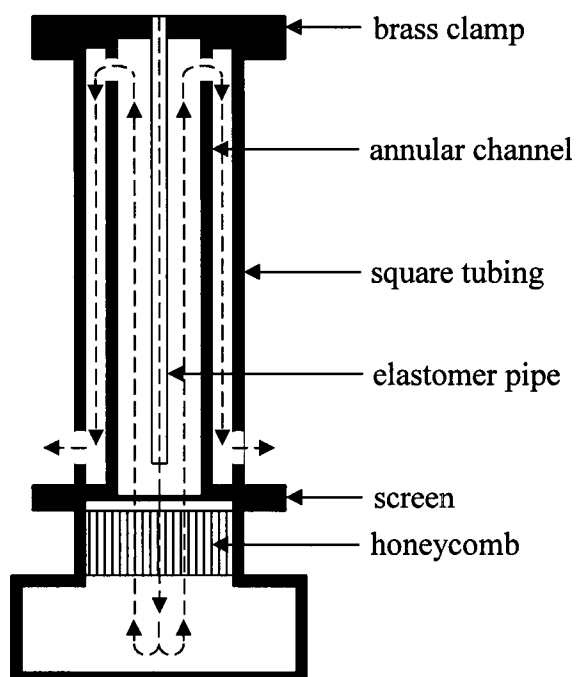


Figure 5.9. Sketch of the experimental apparatus showing the direction of flow.

hitting the bottom surface of the experimental apparatus. Note that the assembly components that required gluing were chemically bonded using methylene chloride. Moreover, both the cantilevered pipe and the annular channel were mounted onto a brass support, which was located at the water flow outlet of the piping system. A two-piece brass clamp was then used to secure the upstream end of the cantilevered pipe. The reader is referred to Figs. F.8 and F.9 in Appendix F for the technical drawings of the brass support and two-piece brass clamp.

5.3.2 *Experimental procedure*

The experimental procedure for a typical water experiment involving a cantilevered pipe subjected simultaneously to counter-current internal and confined external axial flows is essentially the same as that described in Section 2.3.2 of Chapter 2 for a cantilevered pipe conveying fluid that is fitted with a stabilizing end-piece. However, one of the additional steps at the beginning of the procedure is the securing of the plexiglas annular channel to the brass support using four long bolts and four nuts. An additional step, which is to be carried out after step 13 and prior to step 14, is the

calibration of the *Optron* system for amplitude measurements in millimetres as per Appendix C. Moreover, step 18 should also include the determination of the amplitude of oscillation from the recorded time history signals for each measurement.

5.3.3 Experimental results

Some important quantitative results, including the critical flow velocities and frequencies of oscillation, i.e. $u_{i,cr}$ and f_{cr} , as well as the initial and final amplitude values, i.e. A_i and A_f , for both maximum and root-mean-square readings from the experimental time history signals, for a cantilevered pipe subjected simultaneously to internal and confined external axial flow are presented in Table 5.2 for experiments involving a wide annular channel, i.e. $\alpha_{ch} = 2.00$, and in Table 5.3 for those involving a narrow one, i.e. $\alpha_{ch} = 1.60$. It should be mentioned that the name given to a particular experiment was selected based on the end-piece or ring that was mounted at, or very close to, the free end of the cantilevered pipe [see Fig. 5.8]. For Experiment X, however, no end-piece or ring was used. Moreover, the multiplicative factors to convert from dimensionless u_i , u_e , and ω to dimensional U_i (m/s), U_e (m/s), and f (Hz), respectively, are given in Table 5.4, along with the multiplicative factor which relates u_i to u_e for $\alpha_{ch} = 2.00$ and $\alpha_{ch} = 1.60$. Furthermore, some important qualitative results, including the variation of both amplitude and frequency with dimensionless internal flow velocity, are presented in Figs. 5.10 to 5.23. Note that the frequency readings were obtained from PSD plots of the acquired time history signals using either 8 or 16 averaging windows [see Appendix E], and that the f versus u_i graphs include the theoretical first- and second-mode frequencies for comparison purposes.

The observed dynamical behaviour of the system during experiments indicates that the cantilevered pipe becomes unstable by flutter in its first mode at practically zero internal flow velocity, regardless of the amount of confinement; that is, for $\alpha_{ch} = 2.00$, we have $u_{i,cr} \approx 0.2$ to 0.7 , and for $\alpha_{ch} = 1.60$, we have $u_{i,cr} \approx 0.1$ to 0.6 . Note that the actual critical internal flow velocities may well be lower than those presented in Tables 5.2 and 5.3, since the critical values were chosen to be the lowest possible internal flow velocity measurements after $u_i = 0$.

Table 5.2. Key results including amplitudes, velocities, and frequencies for $\alpha_{ch} = 2.00$

Exp.	Theoretical critical values		Experimental critical values		Experimental max amplitudes		Experimental rms amplitudes	
	$u_{i,cr}$	$Re(\omega_{cr})$	$u_{i,cr}$	f_{cr} [Hz]	A_i [mm]	A_f [mm]	A_i [mm]	A_f [mm]
X	5.51	11.7	0.59	0.684	0.0790	2.14	0.0114	0.726
A	4.42	11.4	0.19	0.806	0.0557	2.52	0.0118	0.837
B	5.50	11.7	0.49	0.781	0.0587	2.33	0.0104	0.786
C1	5.51	11.7	0.36	0.684	0.0613	1.39	0.0121	0.359
D1	5.51	11.7	0.72	0.854	0.0713	1.85	0.0117	0.563
E1	5.51	11.7	0.68	0.903	0.0796	2.23	0.0127	0.656
F1	5.51	11.7	0.69	0.781	0.0630	1.84	0.0120	0.609

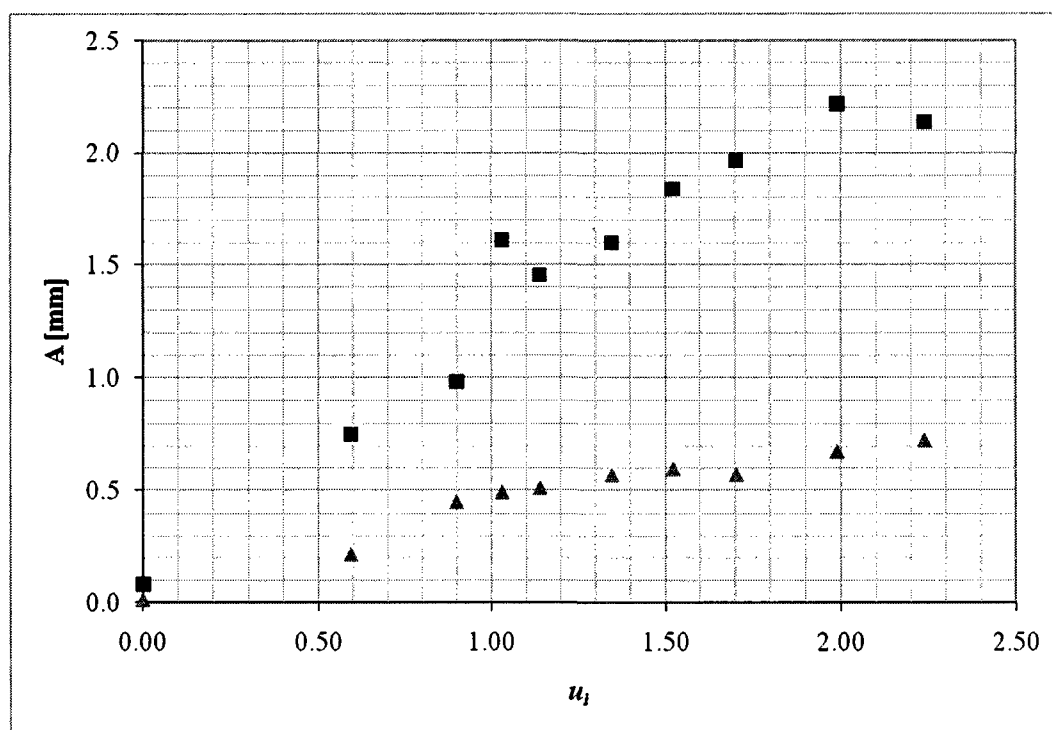
Table 5.3. Key results including amplitudes, velocities, and frequencies for $\alpha_{ch} = 1.60$

Exp.	Theoretical critical values		Experimental critical values		Experimental max amplitudes		Experimental rms amplitudes	
	$u_{i,cr}$	$Re(\omega_{cr})$	$u_{i,cr}$	f_{cr} [Hz]	A_i [mm]	A_f [mm]	A_i [mm]	A_f [mm]
X	2.30	3.97	0.21	0.684	0.0636	2.47	0.0135	0.799
A	2.25	4.16	0.21	0.806	0.0584	2.11	0.0165	0.692
B	2.32	4.01	0.53	0.659	0.0723	2.01	0.0127	0.699
C2	2.30	3.97	0.42	0.659	0.0645	2.04	0.0114	0.595
D2	2.30	3.97	0.63	0.781	0.0714	2.13	0.0135	0.650
E2	2.30	3.97	0.10	0.684	0.0646	2.62	0.0144	0.682
F2	2.30	3.97	0.57	0.806	0.0626	2.04	0.0128	0.681

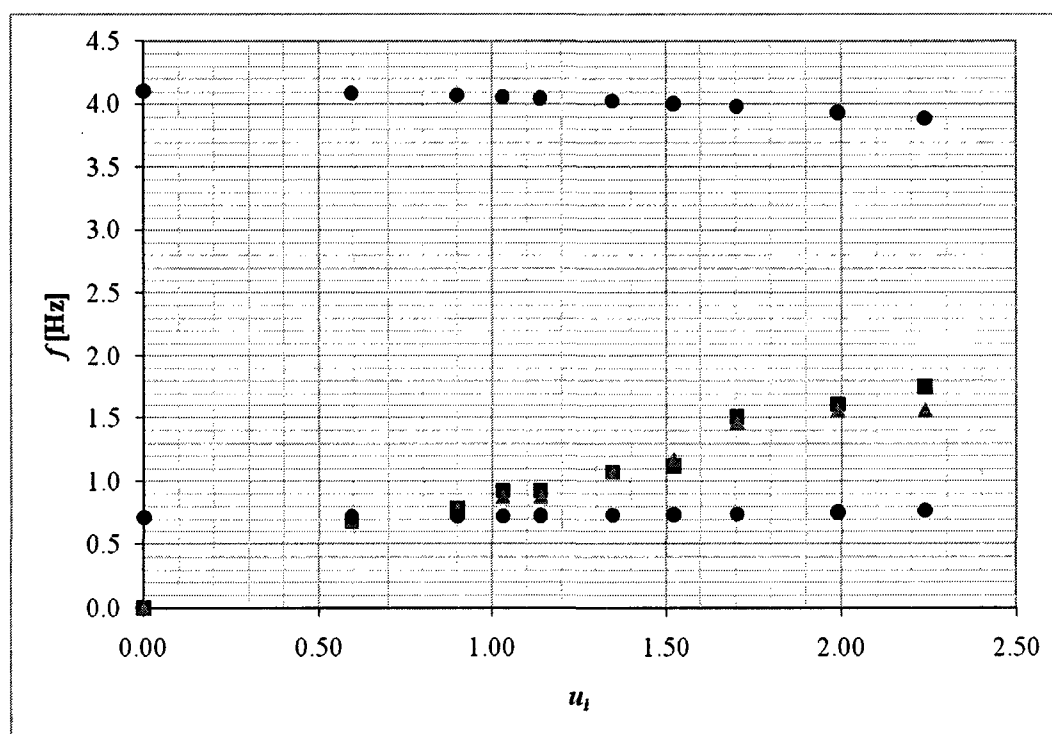
Table 5.4. Relevant multiplicative factors

Multiplicative factors	$\alpha_{ch} = 2.00$	$\alpha_{ch} = 1.60$
$u_i \rightarrow U_i$	1.68	1.68
$u_e \rightarrow U_e$	0.671	0.671
$u_i \rightarrow u_e$	0.133	0.256
$\omega \rightarrow f$	0.181	0.181

From Figs. 5.10 to 5.23, it can be seen that the vibration amplitude of the cantilevered pipe increases almost linearly as the internal flow velocity is increased, which is suggestive of a dynamic instability, regardless of the amount of confinement, and may be followed by one, or even a combination of the following: (i) a small decrease in amplitude with increasing flow, and/or (ii) a saturation amplitude, where an almost constant amplitude is recorded with increasing flow. Although it is tempting to attribute

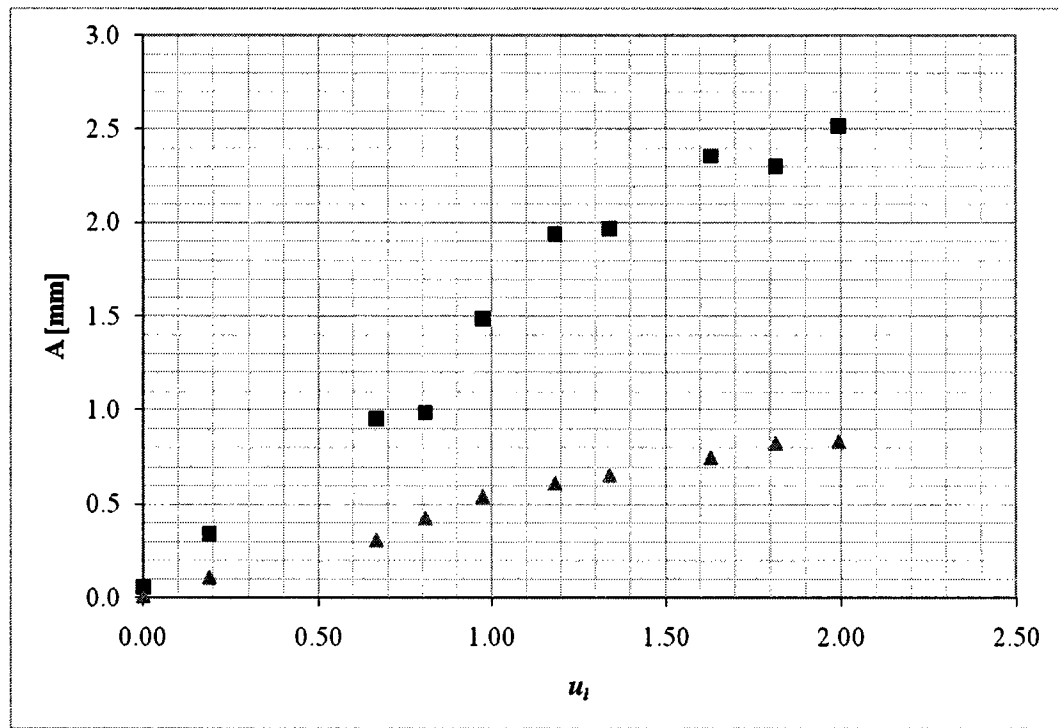


(a)

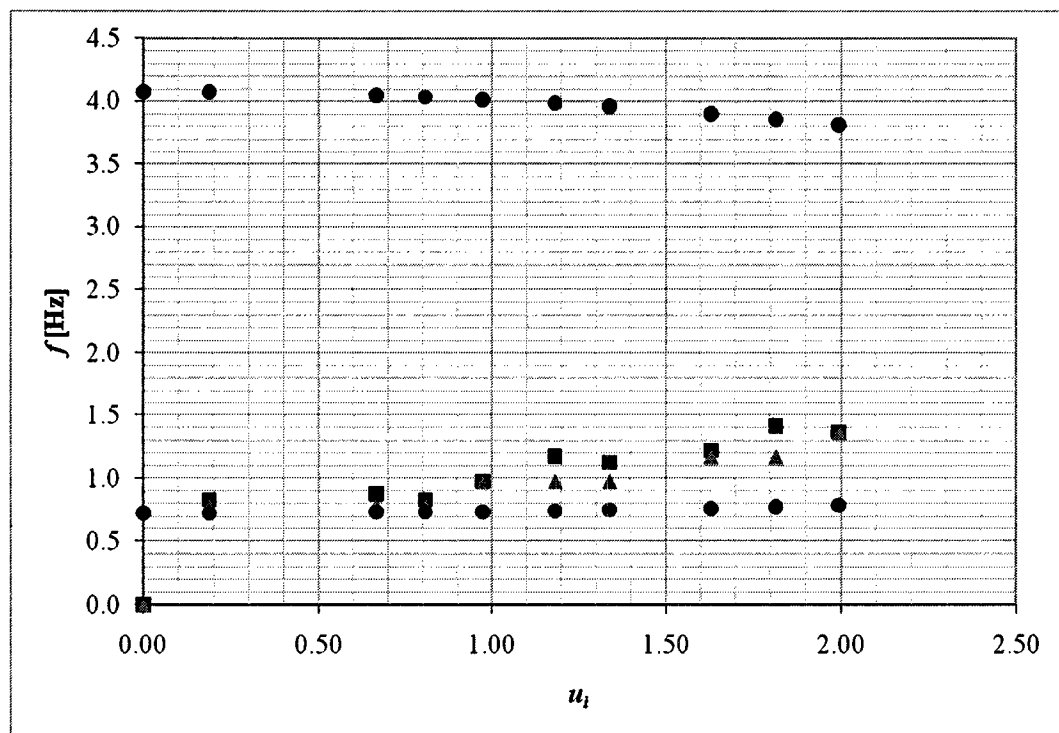


(b)

Figure 5.10. Results of Experiment X ($\alpha_{ch} = 2.00$) measured 16.0 cm below the clamped end of the pipe. (a) amplitude versus u_i : ■ max amplitude, ▲ rms amplitude; (b) frequency versus u_i : ● mode 1 (theoretical), ● mode 2 (theoretical), ■ PSD (8 windows), ▲ PSD (16 windows).

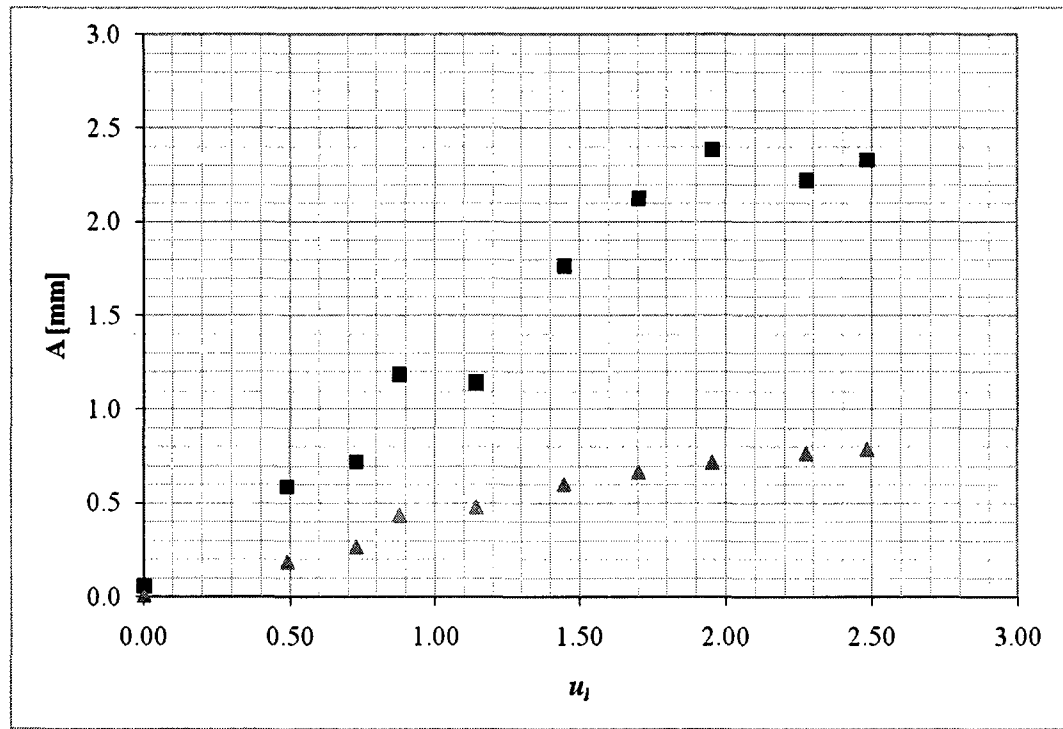


(a)

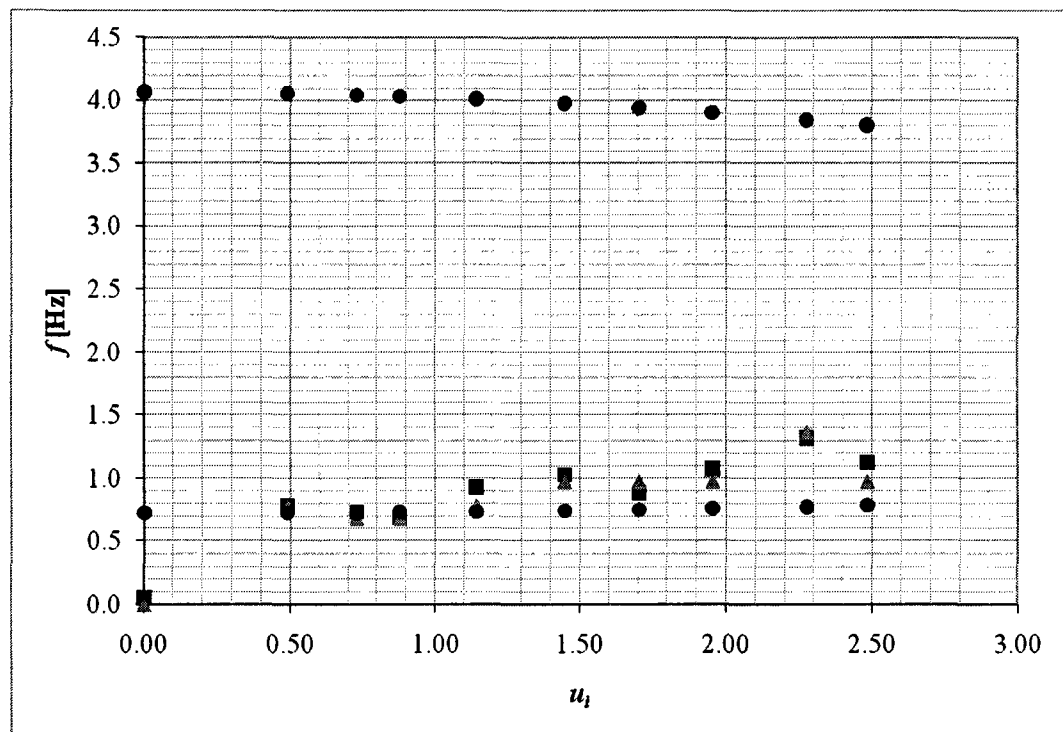


(b)

Figure 5.11. Results of Experiment A ($\alpha_{ch} = 2.00$) measured 16.0 cm below the clamped end of the pipe. (a) amplitude versus u_i : ■ max amplitude, ▲ rms amplitude; (b) frequency versus u_i : ● mode 1 (theoretical), ● mode 2 (theoretical), ■ PSD (8 windows), ▲ PSD (16 windows).

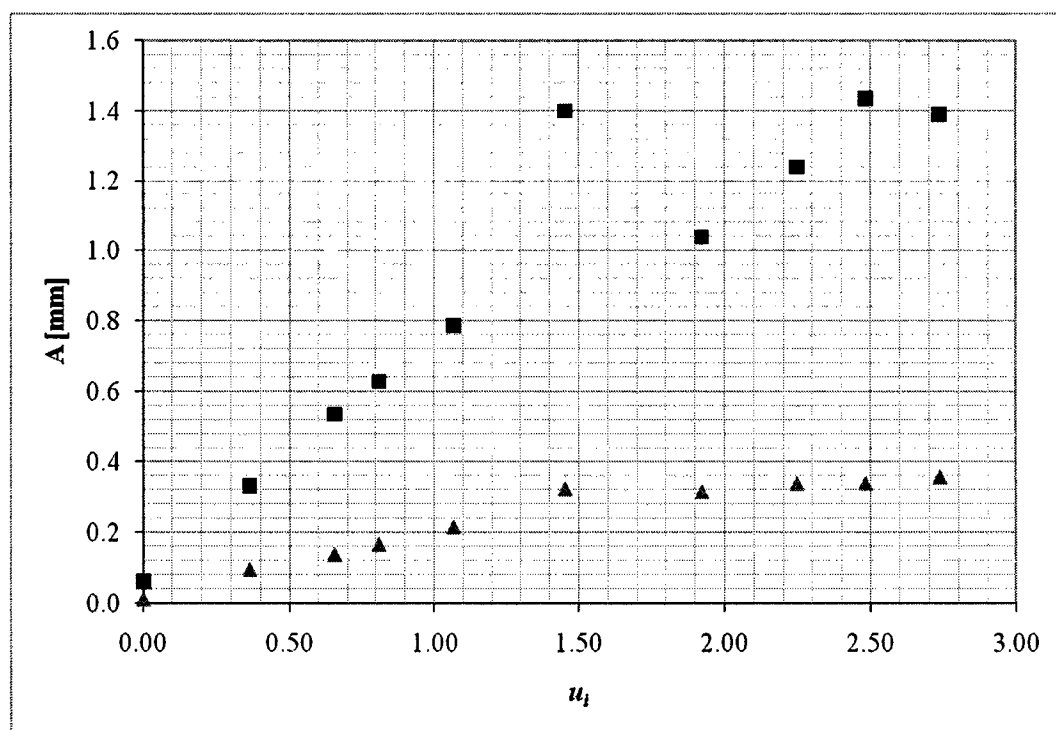


(a)

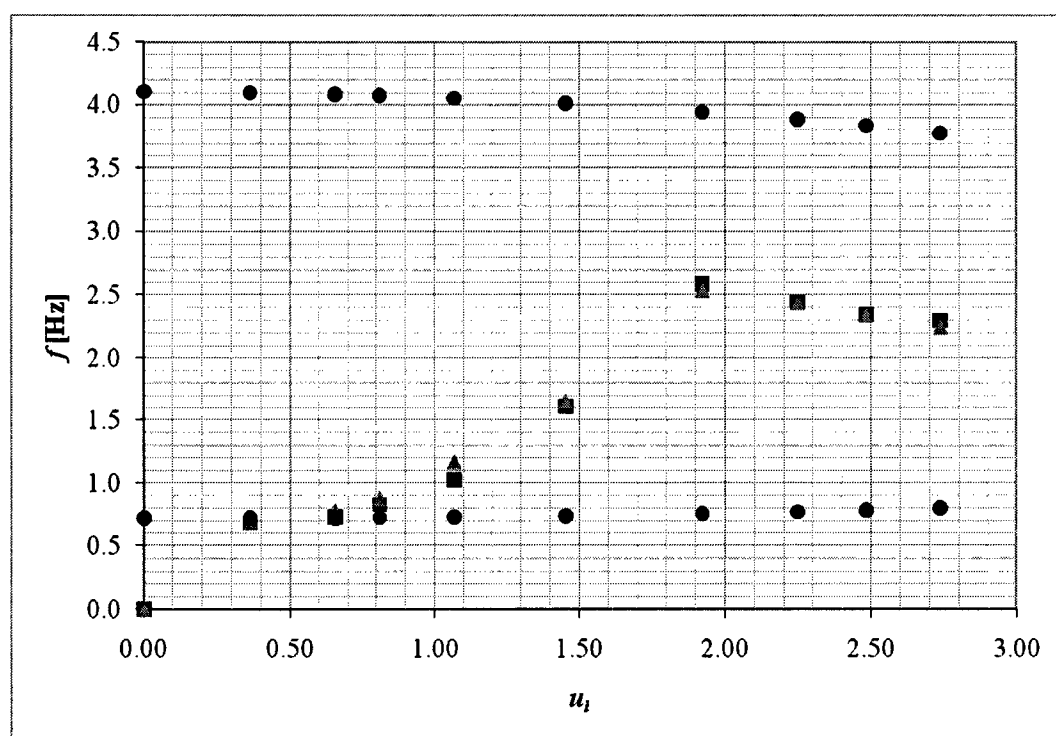


(b)

Figure 5.12. Results of Experiment B ($\alpha_{ch} = 2.00$) measured 16.0 cm below the clamped end of the pipe. (a) amplitude versus u_i : ■ max amplitude, ▲ rms amplitude; (b) frequency versus u_i : ● mode 1 (theoretical), ● mode 2 (theoretical), ■ PSD (8 windows), ▲ PSD (16 windows).

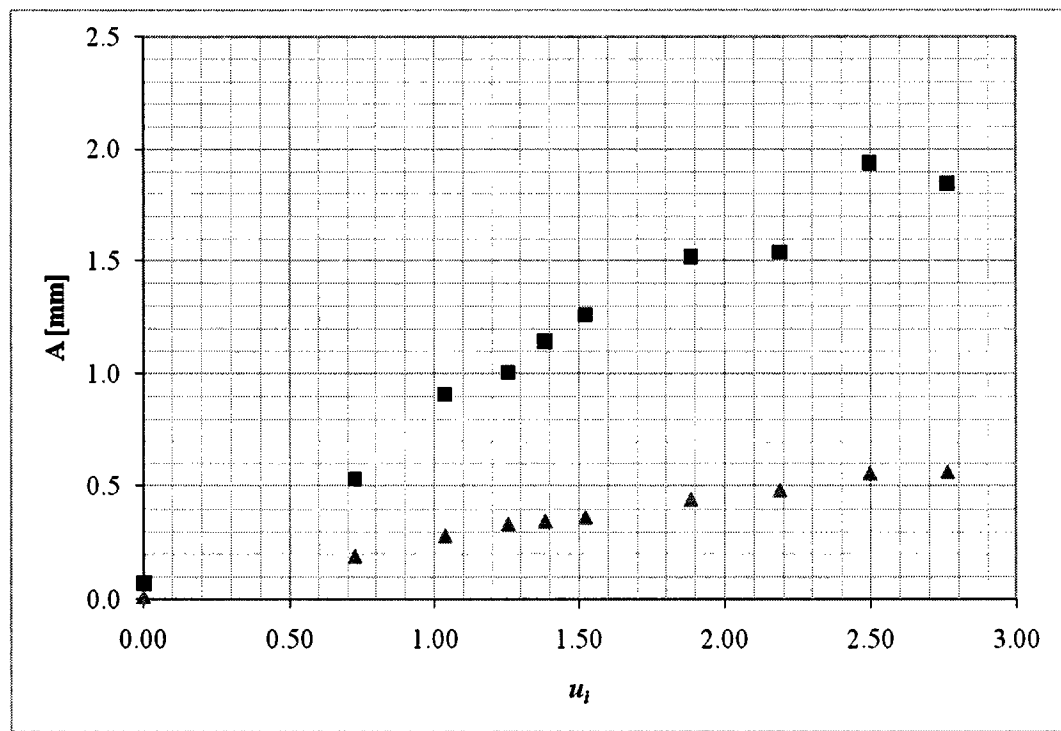


(a)

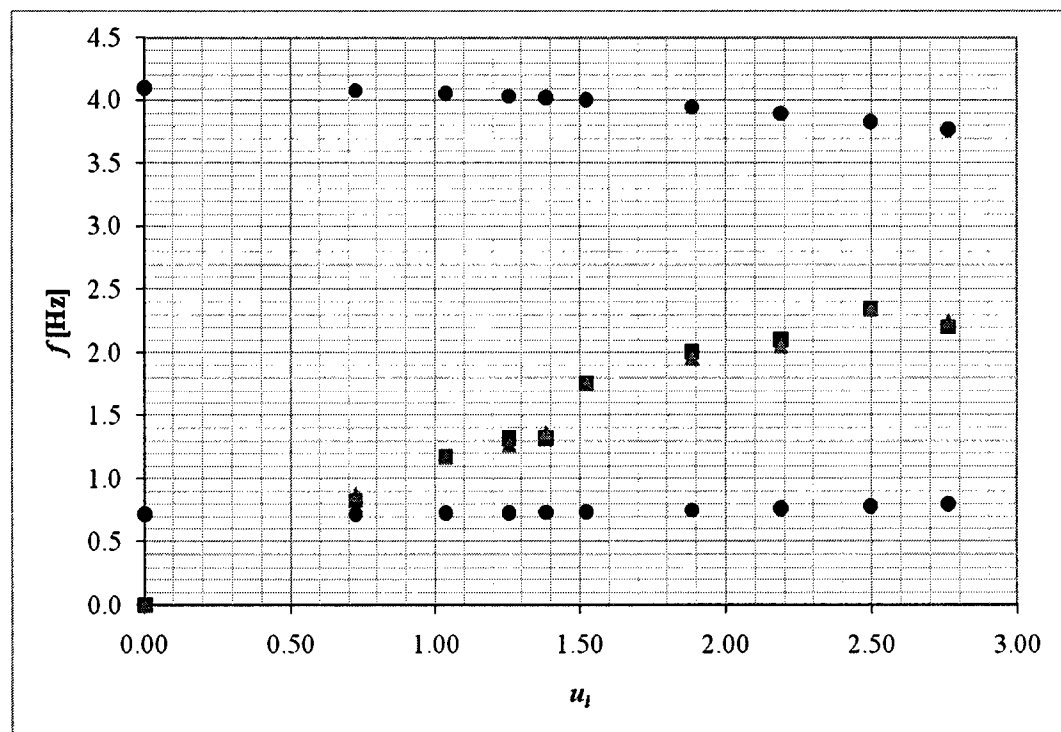


(b)

Figure 5.13. Results of Experiment C1 ($\alpha_{ch} = 2.00$) measured 16.0 cm below the clamped end of the pipe. (a) amplitude versus u_i : ■ max amplitude, ▲ rms amplitude; (b) frequency versus u_i : ● mode 1 (theoretical), ● mode 2 (theoretical), ■ PSD (8 windows), ▲ PSD (16 windows).

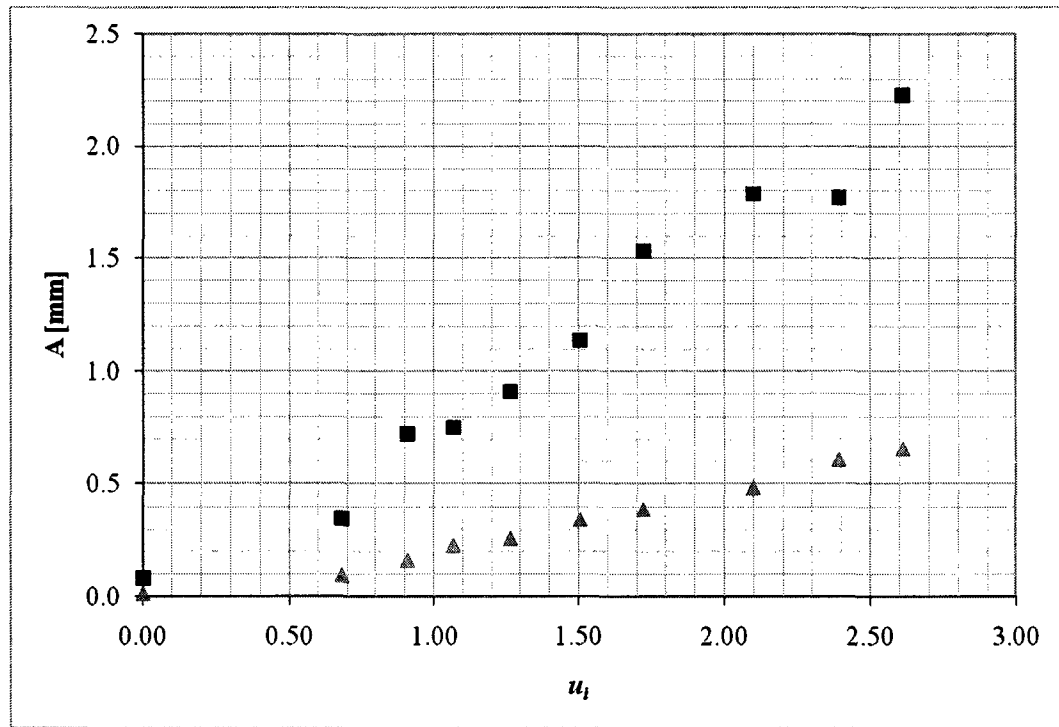


(a)

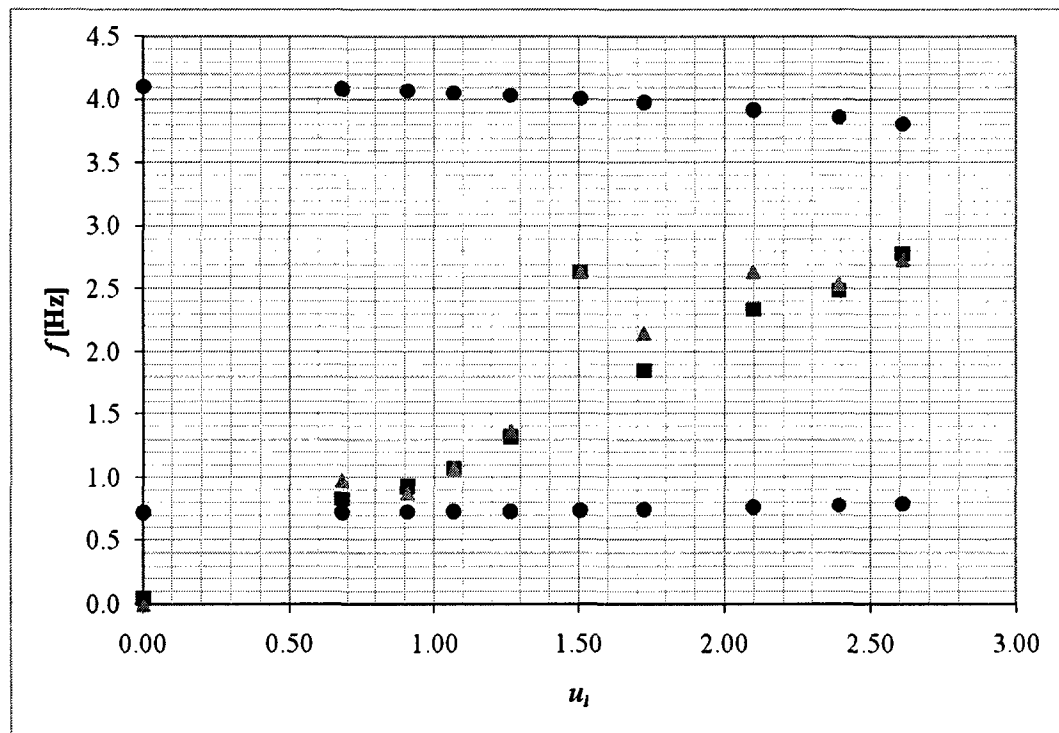


(b)

Figure 5.14 Results of Experiment D1 ($\alpha_{ch} = 2.00$) measured 16.0 cm below the clamped end of the pipe. (a) amplitude versus u_i : ■ max amplitude, ▲ rms amplitude; (b) frequency versus u_i : ● mode 1 (theoretical), ● mode 2 (theoretical), ■ PSD (8 windows), ▲ PSD (16 windows).

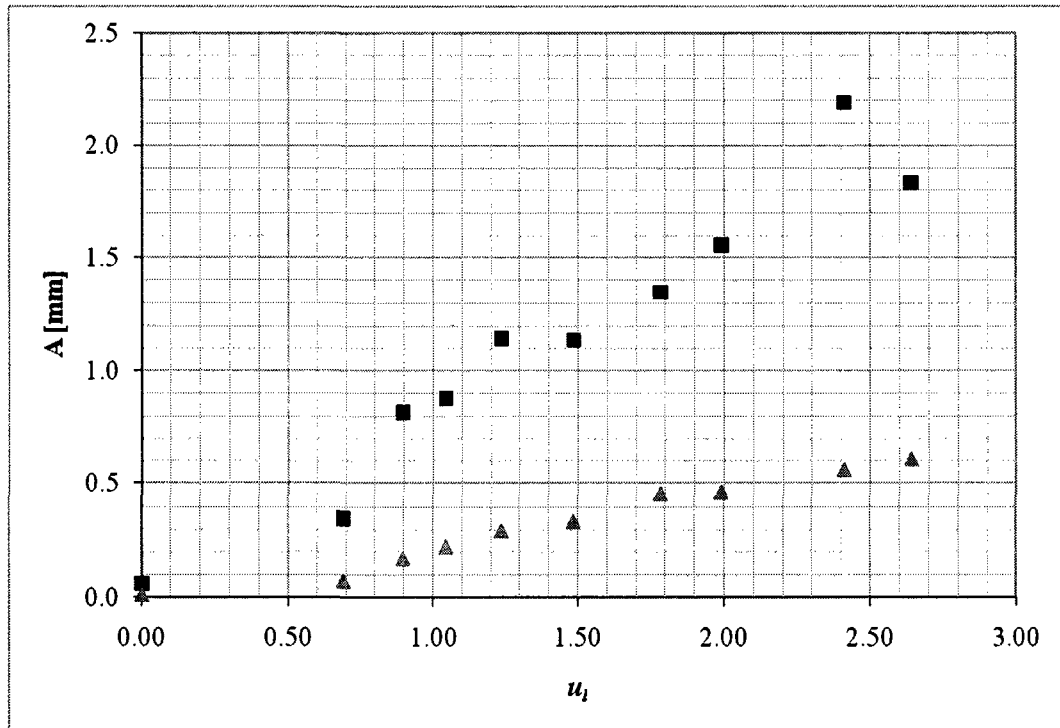


(a)

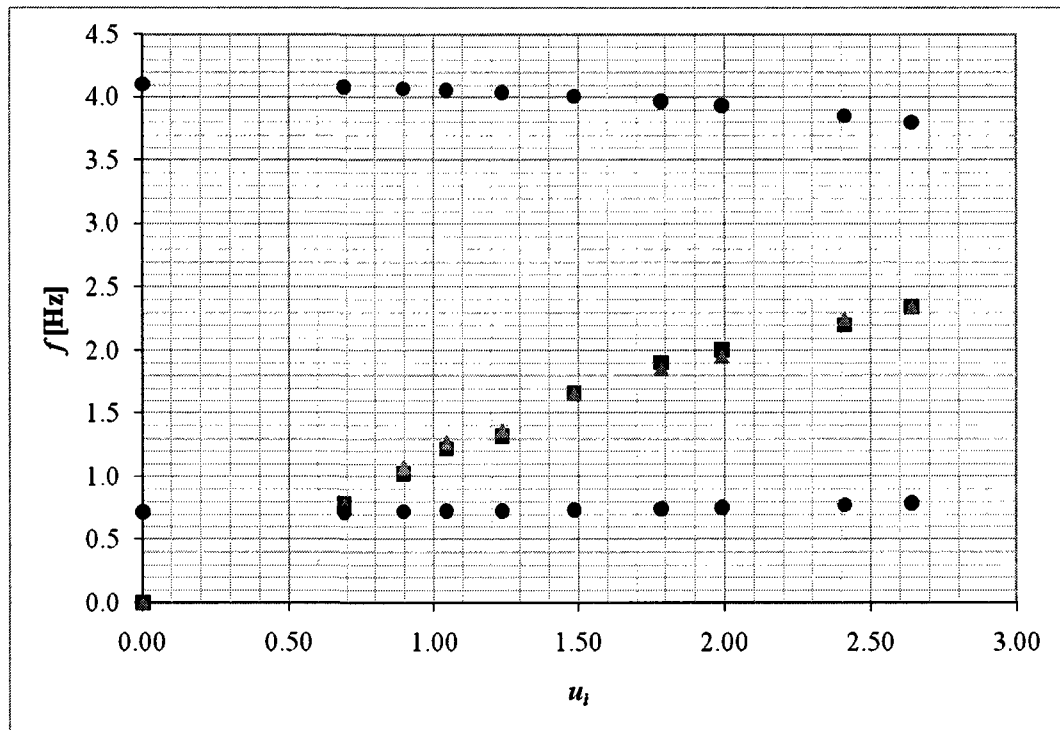


(b)

Figure 5.15. Results of Experiment E1 ($\alpha_{ch} = 2.00$) measured 16.0 cm below the clamped end of the pipe. (a) amplitude versus u_i : ■ max amplitude, ▲ rms amplitude; (b) frequency versus u_i : ● mode 1 (theoretical), ● mode 2 (theoretical), ■ PSD (8 windows), ▲ PSD (16 windows).

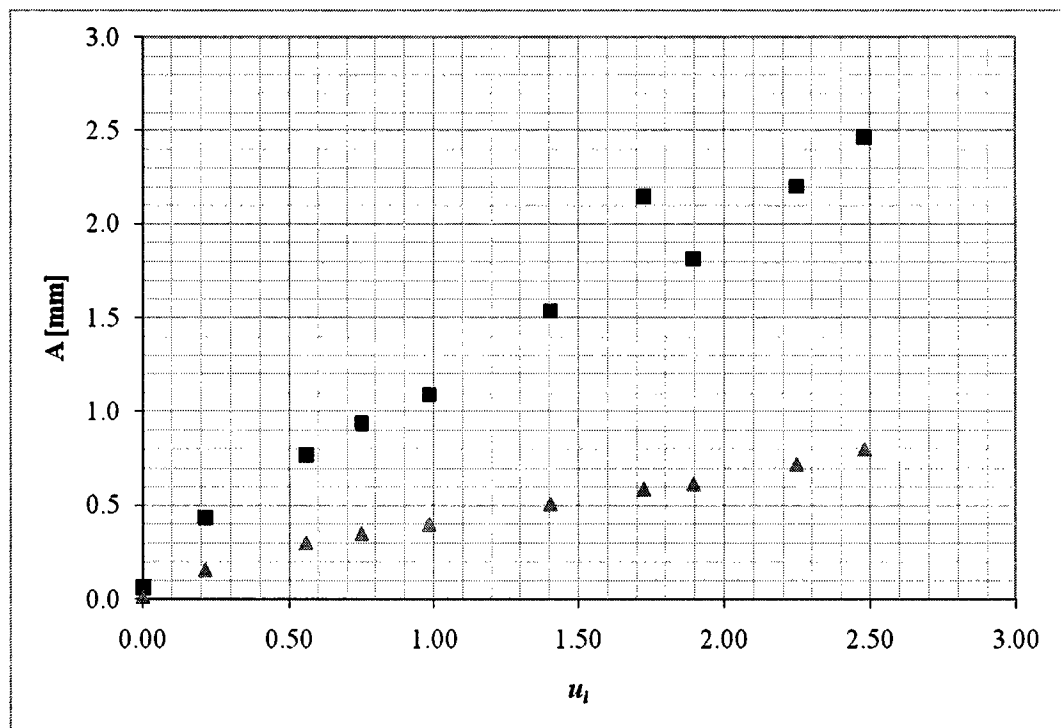


(a)

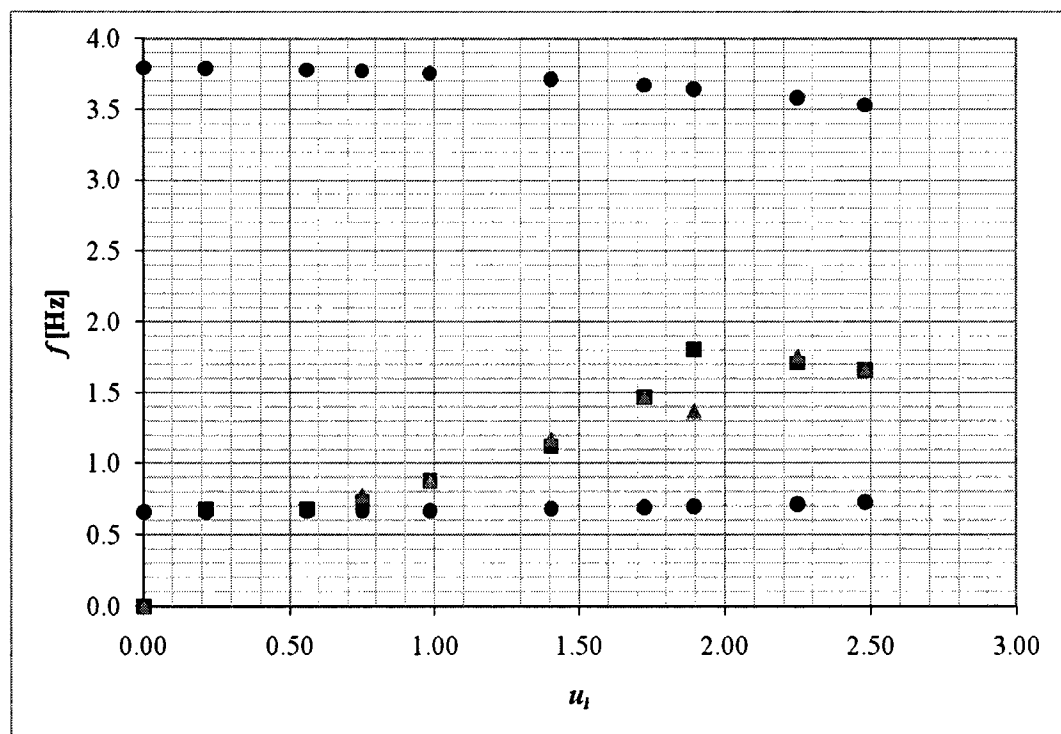


(b)

Figure 5.16. Results of Experiment F1 ($\alpha_{ch} = 2.00$) measured 16.0 cm below the clamped end of the pipe. (a) amplitude versus u_i : ■ max amplitude, ▲ rms amplitude; (b) frequency versus u_i : ● mode 1 (theoretical), ● mode 2 (theoretical), ■ PSD (8 windows), ▲ PSD (16 windows).

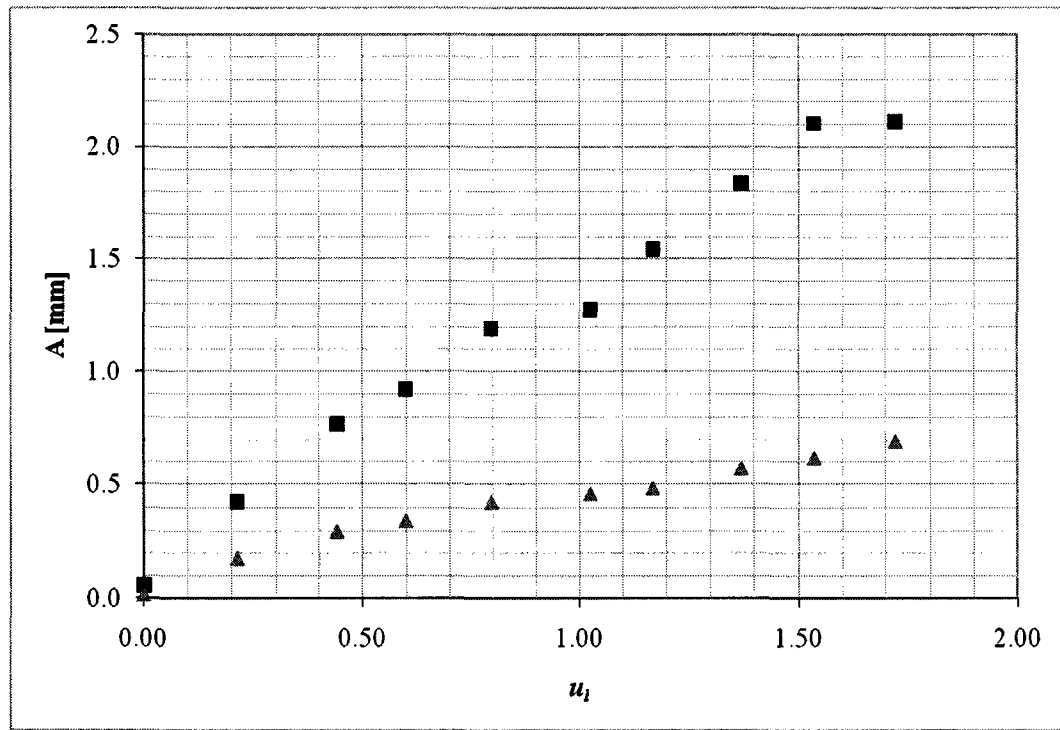


(a)

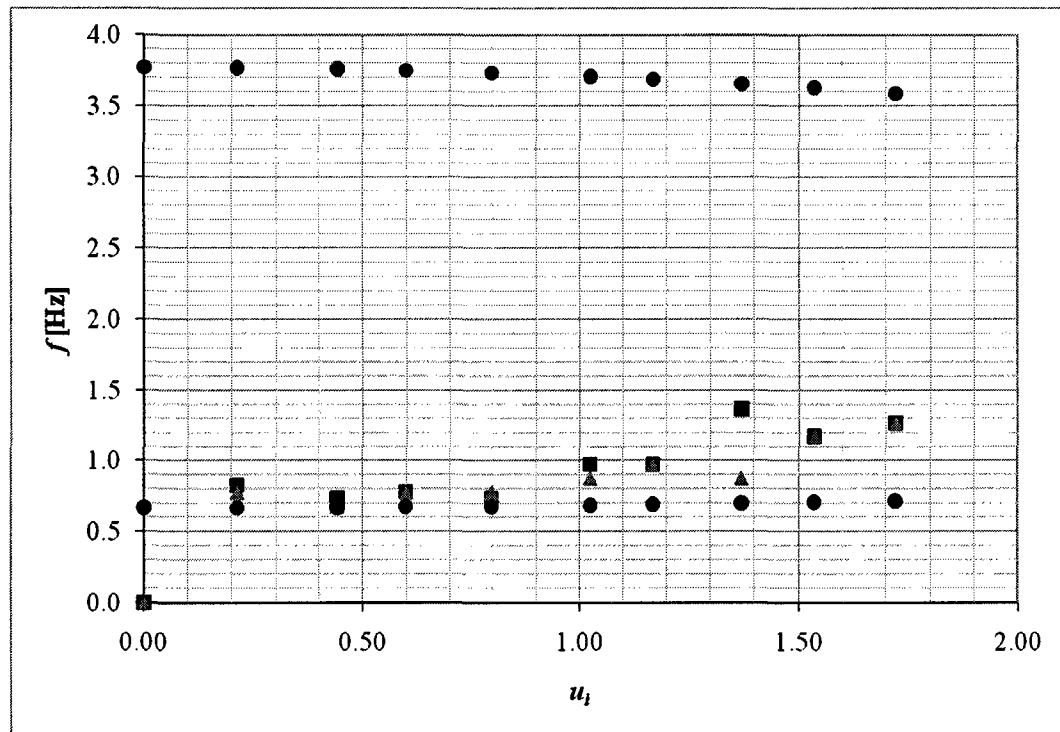


(b)

Figure 5.17. Results of Experiment X ($\alpha_{ch} = 1.60$) measured 16.0 cm below the clamped end of the pipe. (a) amplitude versus u_i : ■ max amplitude, ▲ rms amplitude; (b) frequency versus u_i : ● mode 1 (theoretical), ● mode 2 (theoretical), ■ PSD (8 windows), ▲ PSD (16 windows).

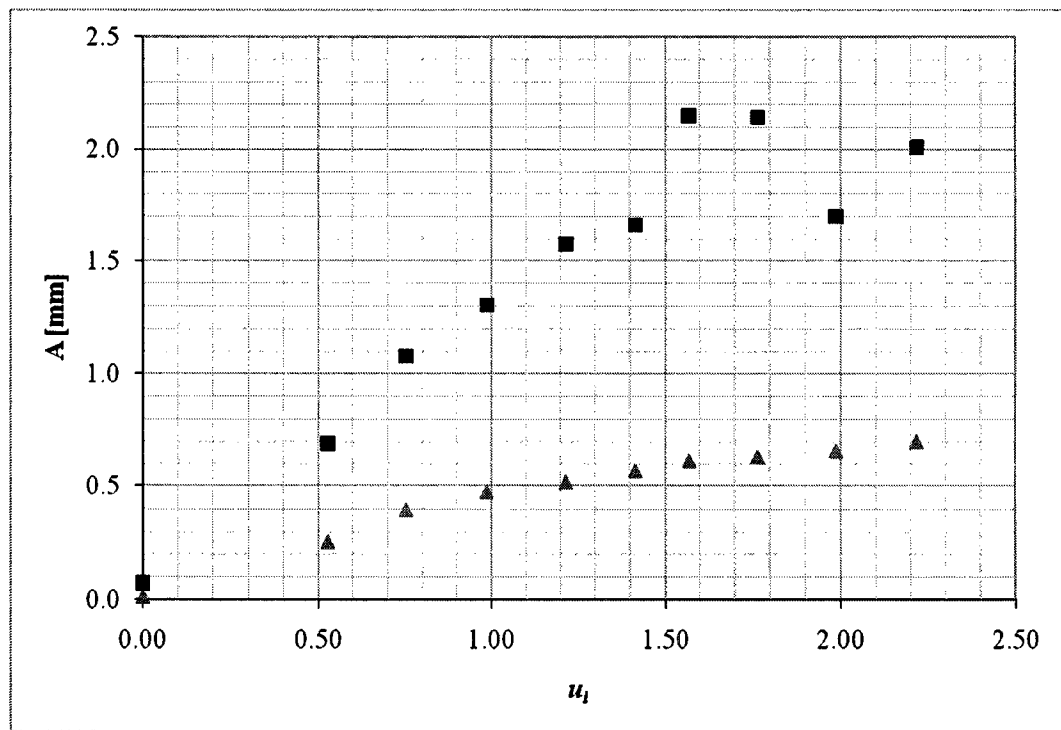


(a)

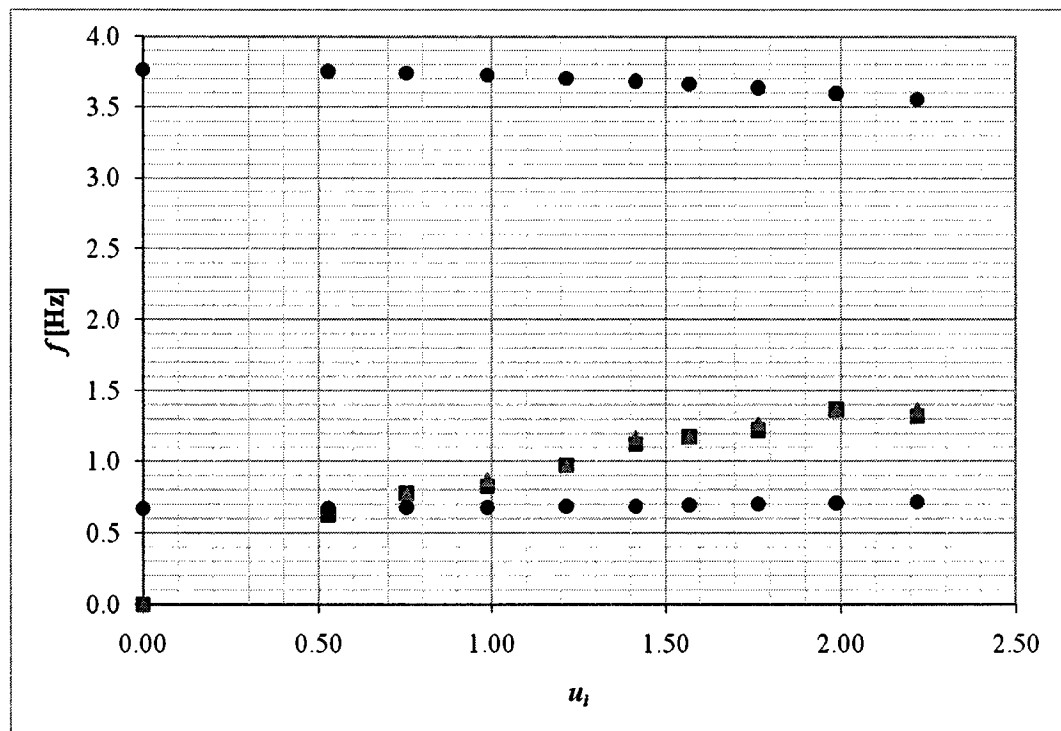


(b)

Figure 5.18. Results of Experiment A ($\alpha_{ch} = 1.60$) measured 16.0 cm below the clamped end of the pipe. (a) amplitude versus u_i : ■ max amplitude, ▲ rms amplitude; (b) frequency versus u_i : ● mode 1 (theoretical), ● mode 2 (theoretical), ■ PSD (8 windows), ▲ PSD (16 windows).

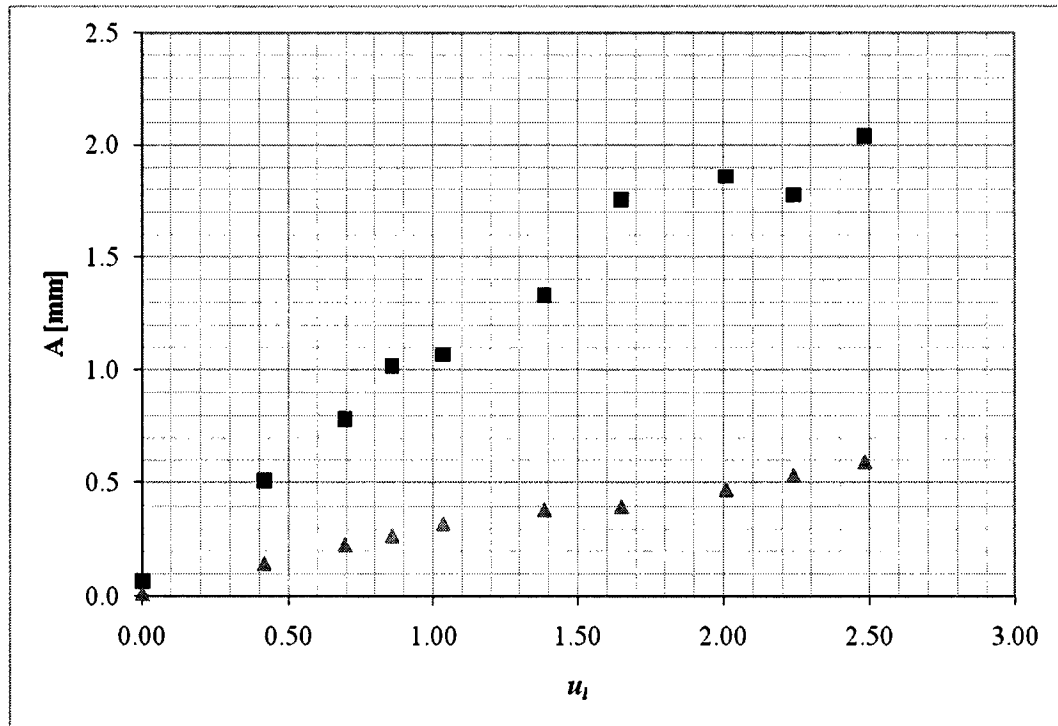


(a)

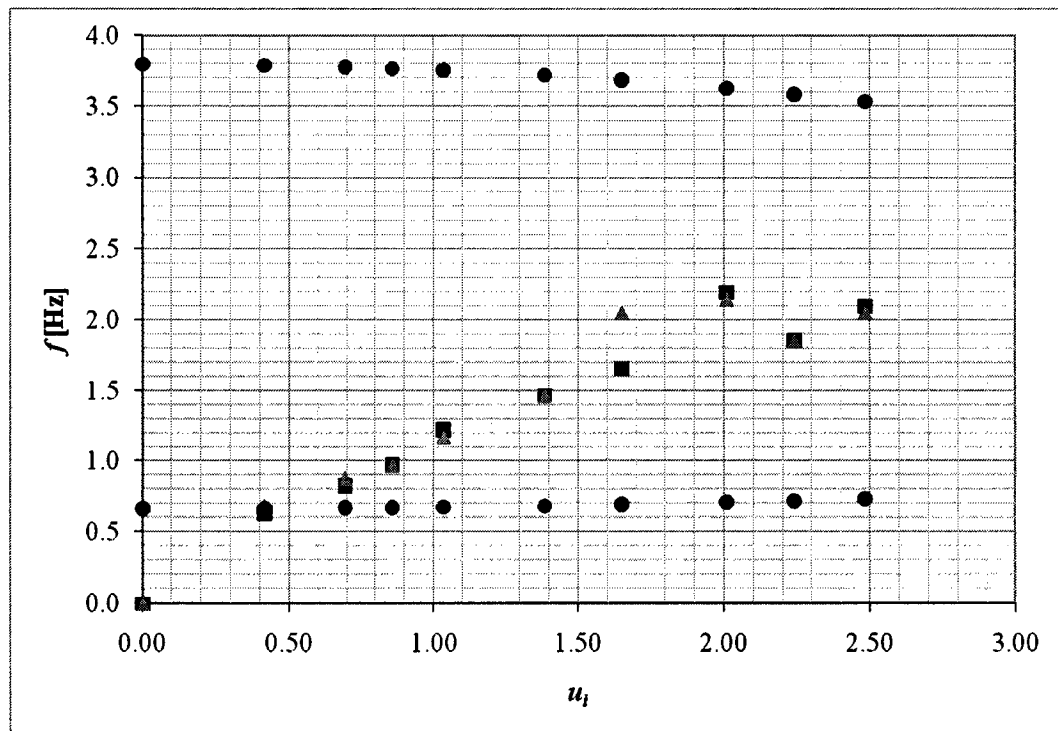


(b)

Figure 5.19. Results of Experiment B ($\alpha_{ch} = 1.60$) measured 16.0 cm below the clamped end of the pipe. (a) amplitude versus u_i : ■ max amplitude, ▲ rms amplitude; (b) frequency versus u_i : ● mode 1 (theoretical), ● mode 2 (theoretical), ■ PSD (8 windows), ▲ PSD (16 windows).

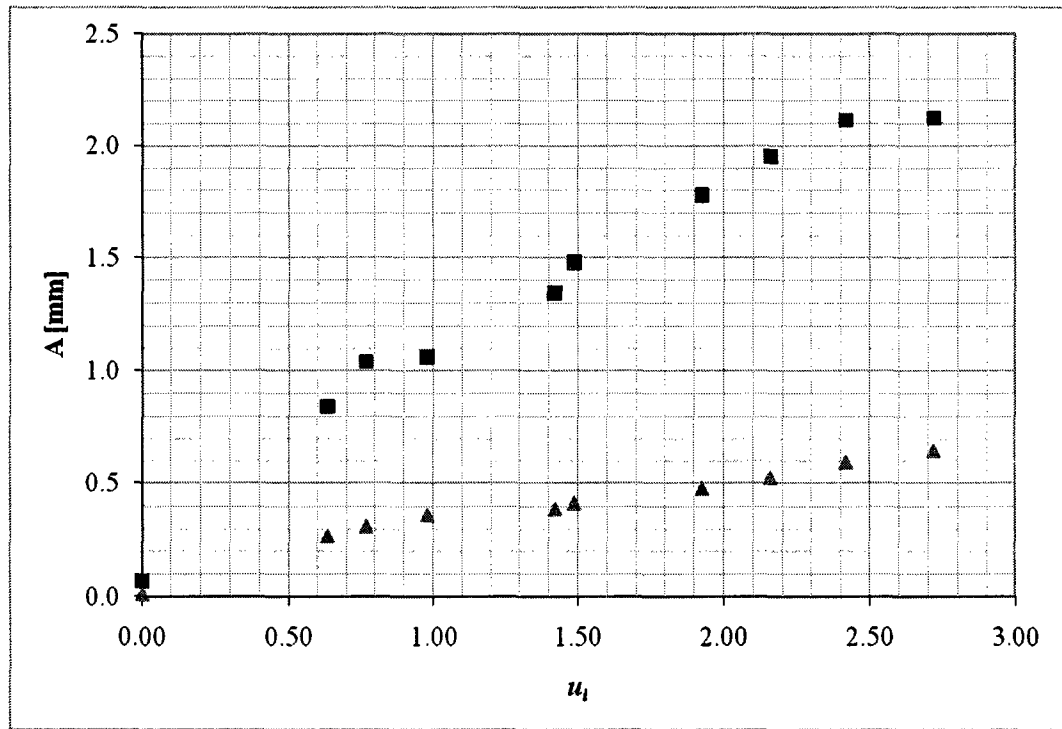


(a)

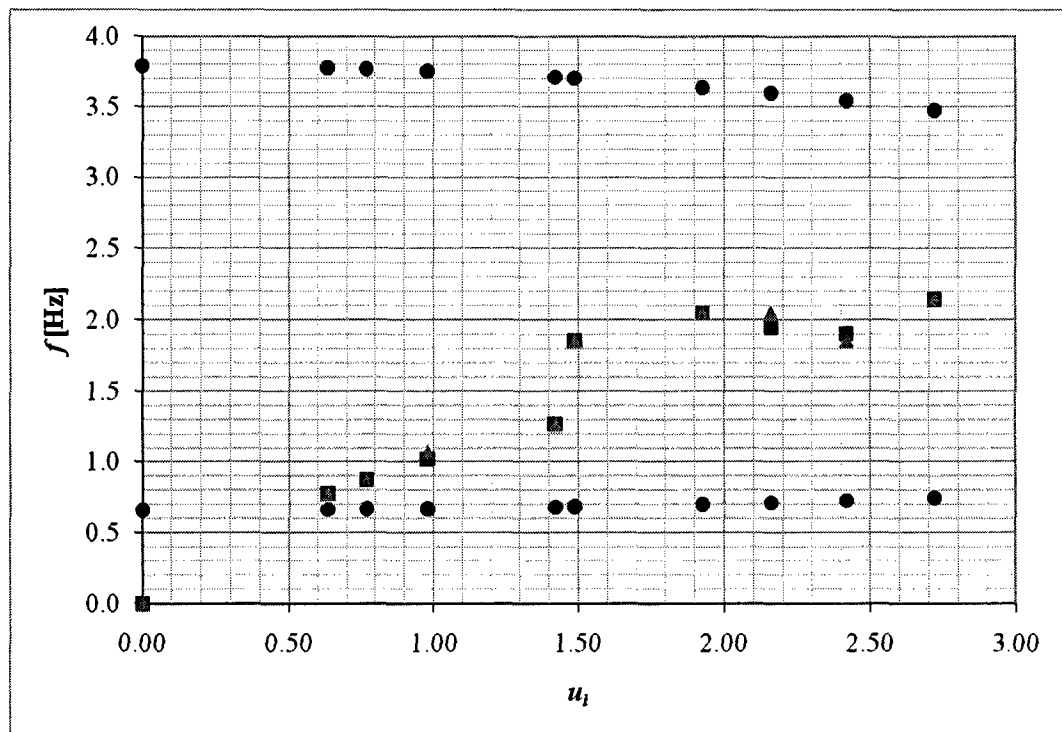


(b)

Figure 5.20. Results of Experiment C2 ($\alpha_{ch} = 1.60$) measured 16.0 cm below the clamped end of the pipe. (a) amplitude versus u_i : ■ max amplitude, ▲ rms amplitude; (b) frequency versus u_i : ● mode 1 (theoretical), ● mode 2 (theoretical), ■ PSD (8 windows), ▲ PSD (16 windows).

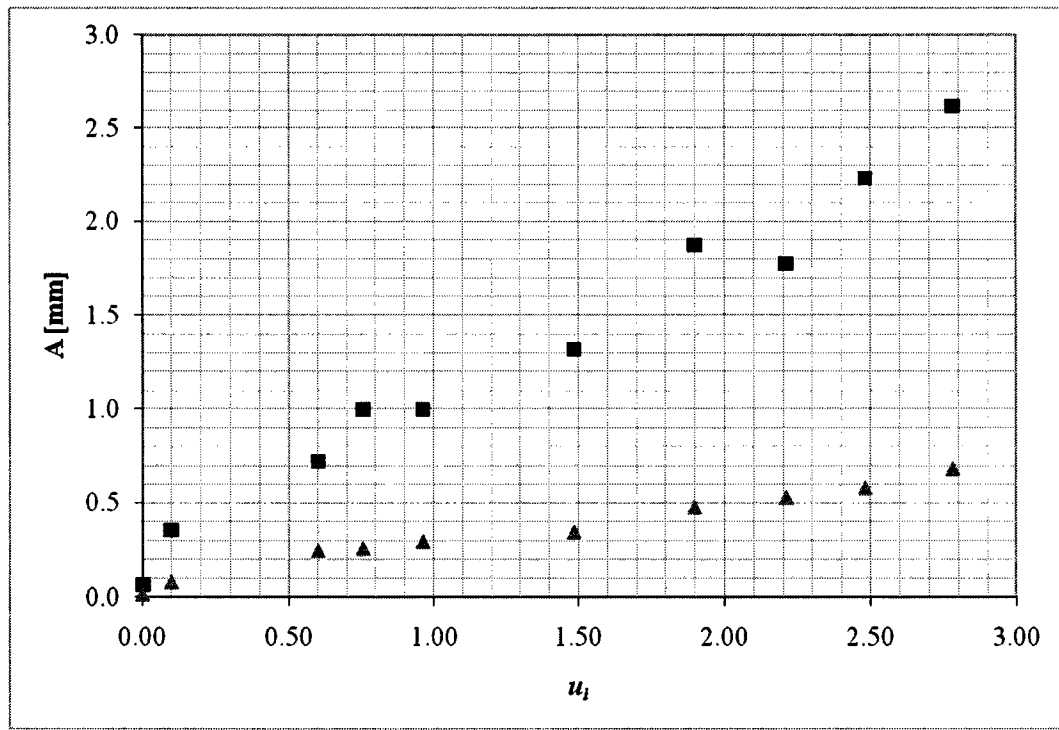


(a)

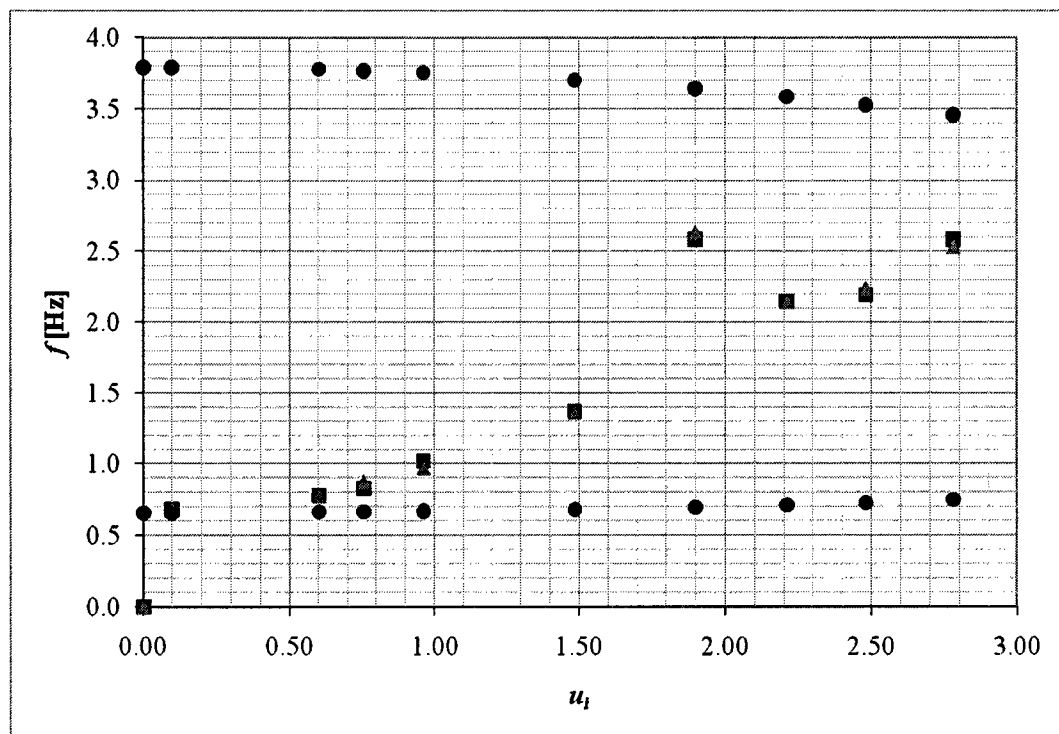


(b)

Figure 5.21. Results of Experiment D2 ($\alpha_{ch} = 1.60$) measured 16.0 cm below the clamped end of the pipe. (a) amplitude versus u_i : ■ max amplitude, ▲ rms amplitude; (b) frequency versus u_i : ● mode 1 (theoretical), ● mode 2 (theoretical), ■ PSD (8 windows), ▲ PSD (16 windows).

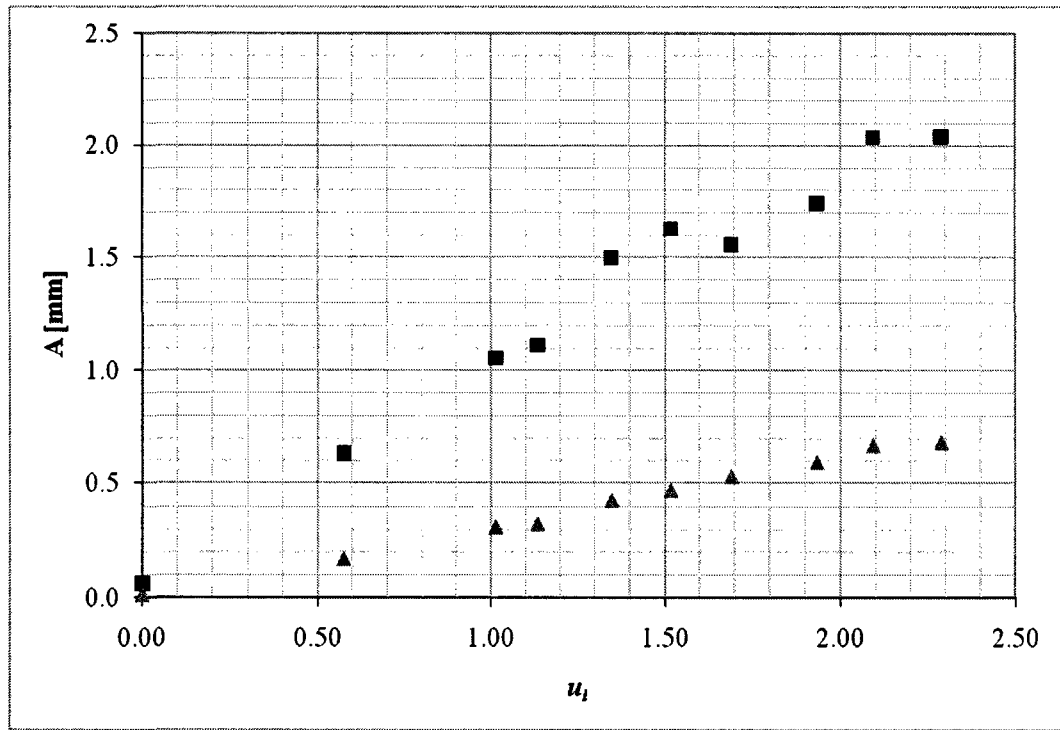


(a)

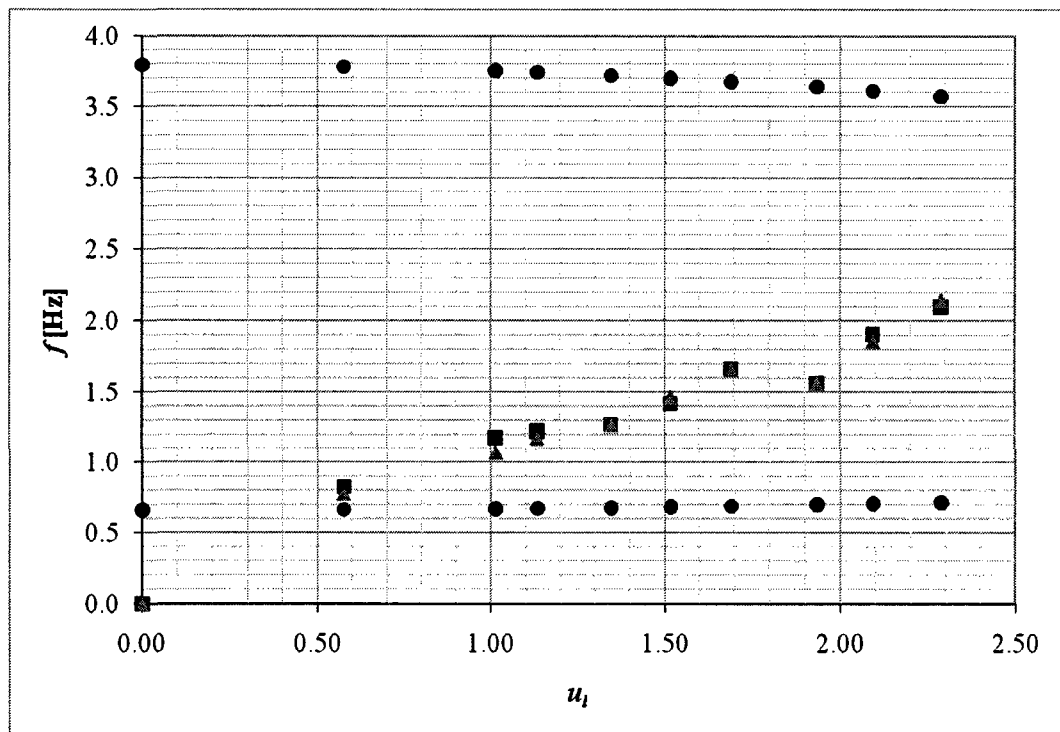


(b)

Figure 5.22. Results of Experiment E2 ($\alpha_{ch} = 1.60$) measured 16.0 cm below the clamped end of the pipe. (a) amplitude versus u_l : ■ max amplitude, ▲ rms amplitude; (b) frequency versus u_l : ● mode 1 (theoretical), ● mode 2 (theoretical), ■ PSD (8 windows), ▲ PSD (16 windows).



(a)



(b)

Figure 5.23. Results of Experiment F2 ($\alpha_{ch} = 1.60$) measured 16.0 cm below the clamped end of the pipe. (a) amplitude versus u_i : ■ max amplitude, ▲ rms amplitude; (b) frequency versus u_i : ● mode 1 (theoretical), ● mode 2 (theoretical), ■ PSD (8 windows), ▲ PSD (16 windows).

the small amplitude measurements, i.e. $A_{f,\max} \approx 1.4$ mm to 2.5 mm for $\alpha_{ch} = 2.00$ and $A_{f,\max} \approx 2.0$ mm to 2.6 mm for $\alpha_{ch} = 1.60$, to turbulence, the empirical expression proposed by Païdoussis (2004, p. 869) for predicting small-amplitude vibrations has shown otherwise. The empirical expression was applied to the data acquired in Experiment X for $\alpha_{ch} = 1.60$, and it predicted that the turbulence-induced vibration amplitudes would lie between 0 mm and 0.075 mm if the empirical factor, K , was set equal to 1 for quiet, laboratory-type conditions, and in the worse case, between 0 mm and 0.375 mm, if K was set equal to 5 for realistic, industrial conditions.

Furthermore, from Figs. 5.10 to 5.23, it is observed that the vibration frequency also exhibits an almost linear increase as the internal flow velocity is increased, regardless of the confinement. However, this effect is more pronounced for the experiments involving an external ring rather than an end-piece, which is somewhat expected because the rings were introduced to prompt a leakage-flow instability in an effort to decrease the critical internal flow velocity, thus leading to an earlier occurrence of the instability [see Païdoussis (2004)]. It should be mentioned that the theoretical model of Section 5.2.1 does not consider the presence of a ring attached to the external surface of the cantilevered pipe. Consequently, the theoretical critical flow velocities presented in Tables 5.2 and 5.3 are equivalent to those of the simple system, which includes neither an end-mass nor a nozzle. Additionally, the cantilevered pipe did not show signs of a second instability beyond the first one; in fact, the system became chaotic at relatively low internal flow velocities, which was apparent from the time history signals and their corresponding PSD plots, and violent impacting of the pipe occurred with the sides of the rigid channel surrounding it.

Unfortunately, from Tables 5.2 and 5.3, it can be seen that the theoretical results do not correspond well to the dynamical behaviour recorded in experiments. More specifically, if we consider the experiments with $\alpha_{ch} = 2.00$, the theoretical results predict that the cantilevered pipe loses stability by flutter in its second mode instead of its first mode, as observed experimentally, at $u_{i,cr} \approx 5.4$ with $f_{cr} \approx 2.1$ Hz, on the average. However, the experimental results suggest much lower critical flow velocities and vibration frequencies. Moreover, if we consider the experiments with $\alpha_{ch} = 1.60$, the theoretical results predict that the system becomes unstable by flutter in its first mode at

$u_{i,cr} \approx 2.3$ with $f_{cr} \approx 0.72$ Hz, on the average. Although the theoretical vibration frequencies agree quite well with the experimental ones, the theoretical critical flow velocities are still much too high compared to the experimental ones. Consequently, it is obvious that the theoretical model of Section 5.2.1 is flawed, and that modifications need to be made in order to accurately predict the dynamical behaviour of a cantilevered pipe subjected simultaneously to internal and confined external axial flow. Lastly, it is interesting to note that the experimental vibration frequencies are bounded between the first- and second-mode theoretical ones for the full range of experimental flow velocities studied, and that the system displays more second-mode behaviour at higher flow velocities when the pipe is mounted with an external ring.

5.4 Summary

In this chapter, the linear equation of motion proposed by Païdoussis *et al.* (2008) for a cantilevered pipe subjected simultaneously to internal and confined external axial flow is re-derived using a Newtonian approach, and the effect of an end-mass and/or nozzle mounted at the free end of the pipe is incorporated into the derivation. It should be mentioned that the standard model of Païdoussis *et al.* (2008) is recovered if the end-mass parameter, Γ_e , is set equal to zero, and if the dimensionless diameter of the nozzle exit, α_j , is set equal to the dimensionless inner diameter of the pipe, α_i .

Furthermore, the dynamical behaviour of a typical bench-top system was studied using a fifteen-mode Galerkin approximation for both a wide ($\alpha_{ch} = 2.00$) and a narrow ($\alpha_{ch} = 1.60$) annular confinement, and the theoretical results were presented in Argand diagrams as a function of the nondimensional internal flow velocity, u_i . In general, the cantilevered system with $\alpha_{ch} = 2.00$ behaved similarly to the standard discharging pipe, thereby losing stability solely by flutter via a second-mode Hopf bifurcation, since the internal flow plays a dominant role in such circumstances. Moreover, the critical flow velocity was found to be $u_{i,cr} = 4.42$, and the corresponding vibration frequency was determined to be $\text{Re}(\omega_{cr}) = 11.4$. On the other hand, the cantilevered system with $\alpha_{ch} = 1.60$ became unstable by flutter via a first-mode Hopf bifurcation at a critical flow velocity of $u_{i,cr} = 2.25$, and with a frequency equal to $\text{Re}(\omega_{cr}) = 4.16$. Then, at a much

higher flow velocity, i.e. $u_{i,cr} = 7.55$, the pipe lost stability in its third mode via another Hopf bifurcation. Here, the corresponding frequency of oscillation was $\text{Re}(\omega_{cr}) = 20.7$.

Moreover, the results for eleven separate experiments involving a cantilevered pipe subjected simultaneously to internal and confined external axial flow were presented in both tabular and graphical form. Experimentally, the system became unstable by flutter at very low flow velocities, even without a ring-related annular confinement, regardless of the value of α_{ch} , and the dynamical behaviour was very similar to that observed for a free-clamped cylinder in confined axial flow [see Chapter 4], as expected. More specifically, for $\alpha_{ch} = 2.00$, the critical flow velocities were found to be in the range $0.2 \leq u_{i,cr} \leq 0.7$, and for $\alpha_{ch} = 1.60$, it was found that $0.1 \leq u_{i,cr} \leq 0.6$. From the A versus u_i graphs, it was determined that the vibration amplitude of the pipe increased almost linearly as the internal flow velocity was increased. Note that the maximum vibration amplitudes for experiments with $\alpha_{ch} = 2.00$ were found to lie in the range $1.4 \text{ mm} \leq A_{f,max} \leq 2.5 \text{ mm}$, and for $\alpha_{ch} = 1.60$, it was found that $2.0 \text{ mm} \leq A_{f,max} \leq 2.6 \text{ mm}$. Similarly, from the f versus u_i graphs, it was observed that the vibration frequency of the pipe increased almost linearly as the internal flow velocity was increased, but the rise was more prominent for experiments involving an external ring, as opposed to an end-piece. At higher flow velocities, yet still reasonably low, the motion of the cantilevered pipe was chaotic, and impacting occurred with the rigid channel.

The theoretical and experimental results were compared, and it was regrettably concluded that the theoretical model derived in Section 5.2.1 was inadequate for predicting the dynamical behaviour of this system. Therefore, modification to the current linear model is suggested for future work. For the experiments with $\alpha_{ch} = 2.00$, a number of discrepancies can be singled out from the theoretical results, such as the overestimated critical flow velocities and vibration frequencies, in addition to an incorrect prediction of the unstable mode. Theoretically, it was found that $u_{i,cr} \approx 5.4$ and $f_{cr} \approx 2.1 \text{ Hz}$, on the average, and that the unstable mode was the second one. On the other hand, for the experiments with $\alpha_{ch} = 1.60$, the theoretical critical flow velocities were also overestimated, but the vibration frequencies and the unstable mode were in good agreement with the experimental results. Theoretically, it was found that $u_{i,cr} \approx 2.3$ and $f_{cr} \approx 0.72 \text{ Hz}$, on the average, and that the unstable mode was the first one.

CHAPTER 6

Conclusion

6.1 Concluding Remarks

6.1.1 *Dynamics of a cantilevered pipe conveying fluid fitted with a stabilizing end-piece*

In this thesis, Chapter 2 was motivated by the dynamics of a cantilevered pipe conveying fluid fitted with an end-piece, wherein the fluid, chosen to be water, was allowed to either pass straight through, representing the standard discharging case, or was diverted by 90° at the free end, corresponding to the instability-free case. This work was not particularly applications-oriented, but rather curiosity-driven, and was motivated by the desire to acquire new knowledge. The dynamics of the system was studied both theoretically and experimentally.

Theoretically, the linear dynamics of a typical bench-top system was studied using a five-mode Galerkin approximation. In general, the unblocked cantilevered pipe fitted with either the four-holed ($\Gamma_e = 0.196$) or the eight-holed ($\Gamma_e = 0.200$) end-piece became unstable in the second mode by single-mode flutter at relatively high flow velocity. Not unexpectedly, however, linear theory could not adequately predict the second bifurcation, which was observed experimentally, and it was necessary to resort to nonlinear theory, which was implemented in *Fortran* using Dr. Yahya Modarres-Sadeghi's code with $N = 4$ modes. From the nonlinear perspective, the cantilevered pipe became unstable by travelling-wave type flutter first, followed by fixed-node type flutter afterwards, regardless of the end-piece tested – which agreed with observation. On the other hand, the blocked cantilevered pipe remained stable for all flow velocities because the centrifugal

term, $MU^2(\partial^2 w/\partial x^2)$, which is essential in bringing about flutter, was cancelled by the blockage-induced tension on the pipe, \bar{T} .

Experimentally, the unblocked cantilevered pipe experienced a first bifurcation in its second mode, which was characterized by two-dimensional planar, travelling-wave type flutter, regardless of the end-piece studied. Then, at a higher flow velocity, the system experienced a second bifurcation in its third mode, which was characterized by two-dimensional planar, fixed-node type flutter, and a higher vibration frequency. At even higher flow velocities, the motion of the cantilevered pipe became more complex, and the vibration frequency increased even further, eventually leading the system to chaos. In contrast, the blocked cantilevered pipe did not display any instability for the full range of flow velocities studied. Therefore, it can be concluded that an end-piece plugging the straight-through flow of fluid is a stabilizing device if mounted on a cantilevered pipe.

6.1.2 Dynamics of a cantilevered pipe aspirating fluid

Chapter 3 was concerned with the dynamics of a cantilevered pipe aspirating fluid. Here, the working fluid was chosen to be air because earlier experiments with water proved unfruitful. The system was studied both theoretically and experimentally in an effort to answer the notorious question: *Does a cantilevered pipe aspirating fluid lose stability by flutter at small flow velocities?* The theoretical model proposed by Païdoussis *et al.* (2005) was re-derived; however, this time, the effect of gravity was included in the equation of motion, in addition to an axial and a lateral time delay of the forces acting at the free end of the pipe. Moreover, universal values were chosen for some key parameters, such as α , $\bar{\gamma}$, and ψ , based on the numerical *ANSYS* work of a colleague, Dana Blake Giacobbi. A number of experiments, using three different flexible elastomer pipes, and a number of profiled end-pieces, were also performed in a pressurized steel tank, wherein air was forced into the tank and up the pipe. Note that some important engineering applications for this system include the ocean mining of minerals from the sea floor, such as manganese nodules, the liquefying of natural gas onboard ships by

aspirating cold seawater, and the exploitation of gas hydrate deposits, such as methane crystals.

Three delay and non-purely-tangential entry models, differing primarily in the sequence of application of the time delays, were studied. Theoretically, the best model was model III; that is, where the axial and lateral delays, $\bar{\tau}_a$ and $\bar{\tau}_\ell$, were applied only to the terms involving U in the expressions for F_x and F_y , and F_ξ^* and F_ζ^* were determined afterwards, with $\alpha = 0.40$, $\bar{\gamma} = 0.30$, $\psi = 1.00$, $\kappa = 0.60$, $\bar{\tau}_a = D_i/U_{cr}$, and $\bar{\tau}_\ell = 10^{-3}$ s. Note that gravity and damping effects should also be taken into consideration. In general, this system was subject to a Hopf bifurcation in its first mode at relatively low flow velocity, while the second and third modes exhibited flow-induced damping.

From the experimental perspective, the vibration amplitude of the cantilevered pipe increased as the flow velocity increased from the very beginning, but the vibration frequency remained constant throughout at about 1 Hz, which is close to the first-mode natural frequency of the system. Consequently, together with the numerical results of Giacobbi (2007) and Giacobbi *et al.* (2008b), it was concluded that the cantilevered pipe aspirating fluid does indeed flutter at small flow velocities in its first mode. It should be mentioned that some additional interesting phenomena were also observed in the experiments, such as (i) a Poisson-ratio-related extension of the pipe with increasing flow, (ii) an intermittent *shuddering* motion, and (iii) in the absence of a stiffening end-piece, a shell-type flutter instability (or perhaps, a dynamic divergence) followed by a shell-type buckling collapse at the free end of the cantilevered pipe.

6.1.3 Dynamics of a free-clamped cylinder in confined axial flow

Chapter 4 was concerned with the dynamics of a free-clamped cylinder in confined axial flow, where the chosen fluid – air – was directed from the free to the clamped end. The linear equation of motion of the system was derived using a Newtonian approach, and closely following the formulation of Païdoussis (1973) for cylindrical structures subjected to axial flow. The resulting theoretical results were then compared with the available experimental ones. Here, too, the research was curiosity-driven, and thus academic in nature.

The dynamical behaviour of a typical bench-top system was studied using linear theory for four combinations of the parameters f and c_b , namely (i) $f = 1.00$ and $c_b = 0$, (ii) $f = 0.80$ and $c_b = 0.20$, (iii) $f = 0.60$ and $c_b = 0.40$, and (iv) $f = 0.80$ and $c_b = 0.60$. For the first case, the free-clamped cylinder became unstable solely by buckling in its first mode. For the second and fourth cases, the system initially lost stability by flutter via a Hopf bifurcation in its first mode, followed immediately thereafter by divergence in its first mode as well. For the third case, however, first-mode flutter was the only instability predicted by linear theory for the full range of flow velocities investigated, i.e. $0 \leq u \leq 3$.

Three different flexible elastomer cylinders were tested experimentally, along with a number of tapered end-pieces. Generally, the cylinder became unstable by flutter in its first mode at very low flow velocity, i.e. from the very beginning of the experiment, and the vibration amplitude of the system increased quickly with increasing flow until reaching a maximum. Then, at higher flow velocities, the system lost stability by divergence in its first mode, and the vibration frequency of the system decreased parabolically to practically zero. Note that the vibration amplitude also ceased to grow during the buckling instability.

Furthermore, it was concluded that the theoretical results do not agree well with the behaviour observed in experiments. Although, theoretically, a system with $f = 0.80$ and $c_b = 0.20$ or $f = 0.80$ and $c_b = 0.60$ does exhibit both flutter and divergence, the predicted critical flow velocities are too high compared with those found experimentally. However, it is likely that the critical flow velocities for the onset of buckling are higher in theory than in practice because divergence is sensitive to imperfections. It should also be mentioned that, prior to buckling, the observed dynamical behaviour of the free-clamped cylinder in confined axial flow was very similar to that observed in the experiments of a cantilevered pipe aspirating fluid.

6.1.4 Dynamics of a cantilevered pipe subjected simultaneously to counter-current internal and confined external axial flows

Chapter 5 dealt with the dynamics of a cantilevered pipe subjected simultaneously to counter-current internal and confined external axial flows, where the internal and

external flows were related through continuity, and the working fluid was chosen to be water. The linear equation of motion of the system proposed by Païdoussis *et al.* (2008) was re-derived using the Newtonian approach; however, this time, the possibility of an end-mass and/or nozzle mounted at the free end of the cantilevered pipe was accounted for in the derivation. Furthermore, the results of a number of experiments were discussed, and also compared with the predicted theoretical behaviour of the system. This work was partly motivated by the fallacious drill-string patent described by Den Hartog (1969) in a lecture. Another more reasonable application deals with the design of MEMS devices, such as microcantilevers and microchannels, which are expected to possess high Q factors, i.e. low damping, for atomic force microscopy and biomolecular detection in viscous fluids.

From the theoretical perspective, a typical bench-top model with $\alpha_{ch} = 2.00$, i.e. wide annular confinement, became unstable by flutter in its second mode via a Hopf bifurcation, much like a cantilevered pipe discharging fluid does. Consequently, it was concluded that the internal fluid plays the dominant role for systems subjected to wide annular confinement. On the other hand, a typical bench-top model with $\alpha_{ch} = 1.60$, i.e. narrow annular confinement, lost stability by single-mode flutter; but, this time, the unstable mode was the first one. Furthermore, at a much higher flow velocity, the third mode of the system also became unstable by flutter via a Hopf bifurcation. Thus, it was concluded that the external fluid plays the dominant role for systems subjected to narrow annular confinement.

The corresponding experiments were performed with a flexible elastomer pipe, wherein fine copper particles were introduced during the casting process, and a variety of plastic end-pieces and rings were mounted at, or very close to, the free end of the pipe. Qualitatively, the cantilevered system became unstable at very low flow velocities, i.e. from the very beginning of the experiment, regardless of the amount of confinement and whether a ring was used or not, and behaved similarly to the free-clamped cylinder in confined axial flow. Moreover, both the vibration amplitude and the vibration frequency were observed to increase almost linearly with increasing flow velocity, but the effect of the latter was more pronounced for experiments in which an external ring was mounted at the free end. This was expected because the rings were included to create a leakage-flow

instability, thereby making the system less stable. Then, at higher, yet still low, flow velocities the cantilevered system was observed to behave chaotically, and impacting occurred with the sides of the rigid annular channel surrounding the pipe. Unfortunately, it was concluded that, once again, the theoretical results did not match the experimental ones very well, thus paving the way to some suggestions for future work.

6.2 Future Work

In general, this thesis was concerned with the dynamics of cylindrical or tubular cantilevered systems subjected to internal and/or external axial flows. While ample work has been presented thus far, both theoretically and experimentally, there still exists much work to be carried out in the near future.

To begin with, for the cantilevered pipe aspirating fluid, it has been determined that the flow is, in fact, compressible within the pipe, since the Mach number is very close to, and generally exceeds, $M = 0.30$ for the majority of flow velocities investigated in a single experiment. Thus, it is essential to include the effects of compressibility in the equation of motion; in other words, density changes within the aspirating pipe, which result in significant changes in all other properties of the system, including temperature and pressure, must be accounted for. Moreover, it is very likely that a number of circulation cells, which give rise to lift forces, are formed within the region delineated by the pipe and the rigid annular channel while the cantilevered pipe is aspirating fluid. Consequently, the effect of these lift forces should also be included in the equation of motion in a suitable manner. In addition, both the intermittent *shuddering* motion, and the shell-type flutter (or dynamic divergence), followed by a shell-type buckling collapse of the flexible elastomer pipe should be studied further experimentally.

Moreover, for the free-clamped cylinder in confined axial flow, and the cantilevered pipe subjected simultaneously to counter-current internal and confined external axial flows, the equations of motion need to be re-visited, and modifications need to be made to the boundary conditions at the free end, i.e. at $x = L$, in an effort to better model the dynamical behaviour that was observed experimentally. For example, it is likely that the boundary condition stating that the bending moment is zero, as it has been

assumed throughout Chapters 4 and 5, is incorrect. Although, perhaps, computationally expensive, it would be worthwhile to perform numerical simulations in *ANSYS* for both the cylinder and pipe systems mentioned above. This would aid in visualizing the flow field in the vicinity of the free end, in addition to providing some valuable information concerning the forces that are developed there. The reader is referred to Appendix H for a first-attempt at improving the theoretical model of Chapter 4 for a free-clamped cylinder in confined axial flow. Additionally, for the cantilevered pipe subjected simultaneously to counter-current internal and confined external axial flows, it would be interesting to devise an experiment wherein the damping of the system may be measured.

Lastly, it would be worthwhile to extend the work of this thesis to include nonlinear effects once, of course, the linear equations of motion have been adequately modified and perfected. This would be useful in predicting the vibration amplitudes of the systems, as well as the instabilities which occur after the first one. Moreover, additional experiments should be performed, in which the minimum attainable flow velocities are lowered for the water experiments, while the maximum attainable flow velocities are raised for the air experiments. However, this would require some modifications to the existing experimental apparatus, such as the *Omega* FMG710 magnetic flowmeter for the water experiments, as well as the size of the air control valve for the air experiments.

Bibliography

- Ashley, H. & Haviland, G. (1950) Bending vibrations of a pipe line containing flowing fluid. *Journal of Applied Mechanics* **17**, 229–232.
- Basak, S., Raman, A. & Garimella, S.V. (2006) Hydrodynamic loading of microcantilevers vibrating in viscous fluids. *Journal of Applied Physics* **99**, 114906-1–114906-10.
- Benjamin, T.B. (1961a) Dynamics of a system of articulated pipes conveying fluid. I. Theory. *Proceedings of the Royal Society of London. Series A, Mathematical and Physical Sciences* **261**, 457–486.
- Benjamin, T.B. (1961b) Dynamics of a system of articulated pipes conveying fluid. II. Experiments. *Proceedings of the Royal Society of London. Series A, Mathematical and Physical Sciences* **261**, 487–499.
- Bourrières, F.-J. (1939) Sur un phénomène d'oscillation auto-entretenu en mécanique des fluides réels. *Publications Scientifiques et Techniques du Ministère de l'Air*, No. 147.
- Burg, T.P. & Manalis, S.R. (2003) Suspended microchannel resonators for biomolecular detection. *Applied Physics Letters* **83**, 2698–2700.
- Cesari, F. & Curioni S. (1971) Buckling instability in tubes subject to internal and external axial fluid flow. *Proceedings of the 4th Conference on Dimensioning and Strength Calculations*. Hungarian Academy of Sciences, Budapest, 301–311.
- Chen, S.-S. & Jendrzejczyk, J.A. (1985) General characteristics, transition, and control of instability of tubes conveying fluid. *Journal of the Acoustical Society of America* **77**, 887–895.
- Chen, S.-S. & Wambsganss, M.W. (1972) Parallel-flow-induced vibration of fuel rods. *Nuclear Engineering and Design* **18**, 253–278.
- Copeland, G.S. & Moon, F.C. (1992) Chaotic flow-induced vibration of a flexible tube with end mass. *Journal of Fluids and Structures* **6**, 705–718.
- de Langre, E., Païdoussis, M.P., Doaré, O. & Modarres-Sadeghi, Y. (2007) Flutter of long flexible cylinders in axial flow. *Journal of Fluid Mechanics* **571**, 371–389.

- Den Hartog, J.P. (1969) John Orr memorial lecture: Recent cases of mechanical vibration. *The South African Mechanical Engineer* **19**, 53–68.
- Dowling, A.P. (1988a) The dynamics of towed flexible cylinders. Part 1. Neutrally buoyant elements. *Journal of Fluid Mechanics* **187**, 507–532.
- Dowling, A.P. (1988b) The dynamics of towed flexible cylinders. Part 2. Negatively buoyant elements. *Journal of Fluid Mechanics* **187**, 533–571.
- Feodos'ev, V.P. (1951) Vibrations and stability of a pipe when liquid flows through it. *Inzhenernyi Sbornik* **10**, 169–170.
- Fukuma, T., Kobayashi, K., Matsushige, K. & Yamada, H. (2005) True atomic resolution in liquid by frequency-modulation atomic force microscopy. *Applied Physics Letters* **87**, 034101-1–034101-3.
- Giacobbi, D.B. (2007) A numerical and experimental study of the dynamics of aspirating cantilever pipes. B.Eng. Honours Thesis, McGill University.
- Giacobbi, D.B., Semler, C. & Païdoussis, M.P. (2008a) Private communication.
- Giacobbi, D.B., Semler, C. & Païdoussis, M.P. (2008b) Numerical fluid-structure interaction study of a cantilevered pipe discharging or aspirating fluid via a computational fluid dynamics and finite element analysis model. *Proceedings of the 6th International Conference on Engineering Computational Technology, ECT2008*. 2-5 September 2008, Athens, Greece, Paper 48, ISBN 978-1-905088-25-6 CD-ROM, Civil Comp Press, Stirlingshire, Scotland.
- Gregory, R.W. & Païdoussis, M.P. (1966a) Unstable oscillation of tubular cantilevers conveying fluid. I. Theory. *Proceedings of the Royal Society of London. Series A, Mathematical and Physical Sciences* **293**, 512–527.
- Gregory, R.W. & Païdoussis, M.P. (1966b) Unstable oscillation of tubular cantilevers conveying fluid. II. Experiments. *Proceedings of the Royal Society of London. Series A, Mathematical and Physical Sciences* **293**, 528–542.
- Grigoriev, J.V. (1978) Stability of a drill tube column with an initial curvature in the axial stream (in Russian). *Journal of Bauman Moscow State Technical University: Mashinostronye* **5**, 23–28.

- Hannoyer, M.J. & Païdoussis, M.P. (1978) Instabilities of tubular beams simultaneously subjected to internal and external axial flows. *ASME Journal of Mechanical Design* **100**, 328–336.
- Hawthorne, W.R. (1961) The early development of the Dracone flexible barge. *Proceedings of the Institution of Mechanical Engineers* **175**, 52–83.
- Hill, J.L. & Swanson, C.P. (1970) Effects of lumped masses on the stability of fluid conveying tubes. *Journal of Applied Mechanics* **37**, 494–497.
- Housner, G.W. (1952) Bending vibrations of a pipe line containing flowing fluid. *Journal of Applied Mechanics* **19**, 205–208.
- Jendrzejczyk, J.A. & Chen, S.-S. (1985) Experiments on tubes conveying fluid. *Thin-Walled Structures* **3**, 109–134.
- Kuiper, G.L. (2008) Stability of offshore risers conveying fluid. Ph.D. Thesis, Delft University of Technology.
- Kuiper, G.L. & Metrikine, A.V. (2005) Dynamic stability of a submerged, free-hanging riser conveying fluid. *Journal of Sound and Vibration* **280**, 1051–1065.
- Kuiper, G.L. & Metrikine, A.V. (2008) Experimental investigation of dynamic stability of a cantilever pipe aspirating fluid. *Journal of Fluids and Structures* **24**, 541–558.
- Kuiper, G.L., Metrikine, A.V. & Battjes, J.A. (2007a) A new time-domain drag description and its influence on the dynamic behaviour of a cantilever pipe conveying fluid. *Journal of Fluids and Structures* **23**, 429–445.
- Kuiper, G.L., Metrikine, A.V. & Efthymiou, M. (2007b) Experimental investigation of the dynamic behaviour of a water intake riser. *Proceedings of the 26th International Conference on Offshore Mechanics and Arctic Engineering, OMAE2007-29401*. 10-15 June 2007, San Diego, USA.
- Lighthill, M.J. (1960) Note on the swimming of slender fish. *Journal of Fluid Mechanics* **9**, 305–317.
- Lopes, J.-L., Païdoussis, M.P. & Semler, C. (1999a) Nonlinear equations of a cylinder in steady axial flow. MERL Report No. 99-1, Department of Mechanical Engineering, McGill University.

- Lopes, J.-L., Païdoussis, M.P. & Semler, C. (1999b) Nonlinear dynamics of a cylinder in steady axial flow. MERL Report No. 99-2, Department of Mechanical Engineering, McGill University.
- Lopes, J.-L., Païdoussis, M.P. & Semler, C. (2002) Linear and nonlinear dynamics of cantilevered cylinders in axial flow. Part 2: The equations of motion. *Journal of Fluids and Structures* **16**, 715–737.
- Luu, T.P. (1983) On the dynamics of three systems involving tubular beams conveying fluid. M.Eng. Thesis, McGill University.
- Modarres-Sadeghi, Y., Semler, C., Wadham-Gagnon, M. & Païdoussis, M.P. (2007) Dynamics of cantilevered pipes conveying fluid. Part 3: Three-dimensional dynamics in the presence of an end-mass. *Journal of Fluids and Structures* **23**, 589–603.
- Niordson, F.I. (1953) Vibrations of a cylindrical tube containing flowing fluid. *Kungliga Tekniska Hogskolans Handlingar (Stockholm)* No. 73.
- Païdoussis, M.P. (1963) Oscillations of liquid-filled flexible tubes. Ph.D. Thesis, University of Cambridge.
- Païdoussis, M.P. (1966a) Dynamics of flexible slender cylinders in axial flow. Part 1. Theory. *Journal of Fluid Mechanics* **26**, 717–736.
- Païdoussis, M.P. (1966b) Dynamics of flexible slender cylinders in axial flow. Part 2. Experiments. *Journal of Fluid Mechanics* **26**, 737–751.
- Païdoussis, M.P. (1968) Stability of towed, totally submerged flexible cylinders. *Journal of Fluid Mechanics* **34**, 273–297.
- Païdoussis, M.P. (1970a) Dynamics of tubular cantilevers conveying fluid. *Journal of Mechanical Engineering Science* **12**, 85–103.
- Païdoussis, M.P. (1970b) Dynamics of submerged towed cylinders. *Eighth Symposium on Naval Hydrodynamics: Hydrodynamics in the Ocean Environment*. United States Office of Naval Research, ARC-179, 981–1016.
- Païdoussis, M.P. (1973) Dynamics of cylindrical structures subjected to axial flow. *Journal of Sound and Vibration* **29**, 365–385.
- Païdoussis, M.P. (1974) The dynamical behaviour of cylindrical structures in axial flow. *Annals of Nuclear Science and Engineering* **1**, 83–106.

- Païdoussis, M.P. (1987) Flow-induced instabilities of cylindrical structures. *Applied Mechanics Reviews* **40**, 163–175.
- Païdoussis, M.P. (1993) 1992 Calvin Rice lecture: Some curiosity-driven research in fluid structure interactions and its current applications. *ASME Journal of Pressure Vessel Technology* **115**, 2–14.
- Païdoussis, M.P. (1998) *Fluid-Structure Interactions: Slender Structures and Axial Flow*, Volume 1. London: Academic Press Limited.
- Païdoussis, M.P. (1999) Aspirating pipes do not flutter at infinitesimally small flow. *Journal of Fluids and Structures* **13**, 419–425.
- Païdoussis, M.P. (2004) *Fluid-Structure Interactions: Slender Structures and Axial Flow*, Volume 2. London: Elsevier Academic Press.
- Païdoussis, M.P. (2005) Some unresolved issues in fluid-structure interactions. *Journal of Fluids and Structures* **20**, 871–890.
- Païdoussis, M.P. (2008a) The canonical problem of the fluid-conveying pipe and radiation of the knowledge gained to other dynamics problems across Applied Mechanics. *Journal of Sound and Vibration* **310**, 462–492.
- Païdoussis, M.P. (2008b) Dynamics of cantilevers subjected to internal and/or external axial flow: New developments and insights. *Proceedings of the 9th International Conference on Flow-Induced Vibration, FIV2008*. 30 June - 3 July 2008, Prague, Czech Republic, 9–20.
- Païdoussis, M.P. & Besançon, P. (1981) Dynamics of arrays of cylinders with internal and external axial flow. *Journal of Sound and Vibration* **76**, 361–379.
- Païdoussis, M.P. & Deksnis, E.B. (1970) Articulated models of cantilevers conveying fluid: The study of a paradox. *Journal of Mechanical Engineering Science* **12**, 288–300.
- Païdoussis, M.P. & des Trois Maisons, P.E. (1969) Free vibration of a heavy, damped cantilever in a plane inclined to the vertical. MERL Report No. 69-6, Department of Mechanical Engineering, McGill University.
- Païdoussis, M.P. & des Trois Maisons, P.E. (1971) Free vibration of a heavy, damped, vertical cantilever. *Journal of Applied Mechanics* **38**, 524–526.

- Païdoussis, M.P. & Issid, N.T. (1974) Dynamic stability of pipes conveying fluid. *Journal of Sound and Vibration* **33**, 267–294.
- Païdoussis, M.P. & Li, G.X. (1993) Pipes conveying fluid: A model dynamical problem. *Journal of Fluids and Structures* **7**, 137–204.
- Païdoussis, M.P. & Luu, T.P. (1985) Dynamics of a pipe aspirating fluid such as might be used in ocean mining. *ASME Journal of Energy Resources Technology* **107**, 250–255.
- Païdoussis, M.P. & Semler, C. (1998) Non-linear dynamics of a fluid-conveying cantilevered pipe with a small mass attached at the free end. *International Journal of Non-Linear Mechanics* **33**, 15–32.
- Païdoussis, M.P. & Yu, B.-K. (1976) Elastohydrodynamics of towed slender bodies: The effect of nose and tail shapes on stability. *AIAA Journal of Hydronautics* **10**, 127–134.
- Païdoussis, M.P., Grinevich, E., Adamovic, D. & Semler, C. (2002) Linear and nonlinear dynamics of cantilevered cylinders in axial flow. Part 1: Physical dynamics. *Journal of Fluids and Structures* **16**, 691–713.
- Païdoussis, M.P., Semler, C. & Wadham-Gagnon, M. (2005) A reappraisal of why aspirating pipes do not flutter at infinitesimal flow. *Journal of Fluids and Structures* **20**, 147–156.
- Païdoussis, M.P., Luu, T.P. & Prabhakar, S. (2008) Dynamics of a long tubular cantilever conveying fluid downwards, which then flows upwards around the cantilever as a confined annular flow. *Journal of Fluids and Structures* **24**, 111–128.
- Pao, H.P. (1970) Dynamical stability of a towed thin flexible cylinder. *AIAA Journal of Hydronautics* **4**, 144–150.
- Putman, C.A.J., Van der Werf, K.O., De Grooth, B.G., Van Hulst, N.F. & Greve, J. (1994) Tapping mode atomic force microscopy in liquid. *Applied Physics Letters* **64**, 2454–2456.
- Rinaldi, S. & Païdoussis, M.P. (2007) Dynamics of a cantilevered pipe conveying fluid fitted with a stabilizing end-piece. *Proceedings of the 21st Canadian Congress of Applied Mechanics, CANCAM 2007*. 3-7 June 2007, Toronto, Canada, 507–508.
- Semler, C. & Païdoussis, M.P. (1995) Intermittency route to chaos of a cantilevered pipe conveying fluid with a mass defect at the free end. *Journal of Applied Mechanics* **62**, 903–907.

- Semler, C., Li, G.X. & Païdoussis, M.P. (1994) The non-linear equations of motion of pipes conveying fluid. *Journal of Sound and Vibration* **169**, 577–599.
- Semler, C., Lopes, J.-L., Augu, N. & Païdoussis, M.P. (2002) Linear and nonlinear dynamics of cantilevered cylinders in axial flow. Part 3: Nonlinear dynamics. *Journal of Fluids and Structures* **16**, 739–759.
- Taylor, G.I. (1952) Analysis of the swimming of long and narrow animals. *Proceedings of the Royal Society of London. Series A, Mathematical and Physical Sciences* **214**, 158–183.
- Triantafyllou, G.S. & Chryssostomidis, C. (1984) Analytic determination of the buckling speed of towed slender cylindrical beams. *ASME Journal of Energy Resources Technology* **106**, 246–249.
- Triantafyllou, G.S. & Chryssostomidis, C. (1985) Stability of a string in axial flow. *ASME Journal of Energy Resources Technology* **107**, 421–425.
- Triantafyllou, G.S. & Chryssostomidis, C. (1989) The dynamics of towed arrays. *ASME Journal of Offshore Mechanics and Arctic Engineering* **111**, 208–213.
- Wadham-Gagnon, M., Païdoussis, M.P. & Semler, C. (2007) Dynamics of cantilevered pipes conveying fluid. Part 1: Nonlinear equations of three-dimensional motion. *Journal of Fluids and Structures* **23**, 545–567.
- Wang, X. & Bloom, F. (1999) Dynamics of a submerged and inclined concentric pipe system with internal and external flows. *Journal of Fluids and Structures* **13**, 443–460.
- Zhang, Q. & Miska, S. (2005) Effects of flow-pipe interaction on drill pipe buckling and dynamics. *ASME Journal of Pressure Vessel Technology* **127**, 129–136.

APPENDIX A

Pipe Casting Process

The flexible elastomer pipes used during experiments are made from *Silastic® E RTV* Silicone Rubber from Dow Corning, which is a two-part silicone rubber kit consisting of a base and a curing agent. The pipe casting tools are illustrated in Fig. A.1. Additional information can be found in Païdoussis (1998, Appendix D). The pipe casting process is:

1. Clean the mould and plexiglas piston to remove any grease, dirt, or additional residue left over from a previous casting.
2. Apply a thin coat of release agent (*PAM®* cooking spray works well) on the inner surfaces of the mould, and on the central rod for easier pipe removal afterwards.
3. Tightly secure the two sections of the mould by fastening its fourteen bolts using an open-end wrench. Apply an approximately equal amount of torque to each bolt.
4. Attach the two brass end-pieces to the mould using four screws for each end-piece. The brass end-pieces are needed to connect the central rod and the mould, in addition to facilitating the injection of the silicone rubber via small holes. Attach braid-reinforced tubing to both brass end-pieces using worm-drive hose clamps.
5. Affix the assembled mould to the tripod found in the laboratory using two C-clamps.
6. Prepare the silicone rubber by thoroughly mixing the base and curing agent in a plastic container using a hand-held drill and a mixing paddle. The base-to-curing-agent weight ratio must be 10:1, and can easily be measured with a weighing scale. Note that the silicone rubber remains pourable for up to two hours after being mixed.
7. Carefully pour the silicone rubber into the plexiglas piston. Make certain to limit the amount of air introduced into the mixture.

8. Connect the plexiglas piston to the vacuum pump, which is equipped with a regulator valve, to de-aerate the mixture and eliminate the occurrence of air voids within the pipe. De-aerate the mixture for approximately ten to fifteen minutes.
9. Attach the plexiglas piston to the lower end of the assembled mould using a worm-drive hose clamp via the braid-reinforced tubing that is already attached to the mould.
10. Slowly turn the lead screw of the plexiglas piston clockwise to inject the silicone rubber and totally fill the mould. Be very careful to never reverse the turning. Stop turning once the mixture has entered the braid-reinforced tubing at the upper end of the assembled mould.
11. Let the silicone rubber mixture cure for approximately 48 hours at room temperature. Note that the polymerization of the base and curing agent requires only 24 hours.
12. Remove the flexible elastomer pipe from the mould. This step can be simplified by introducing compressed air into the mould using a blowgun.

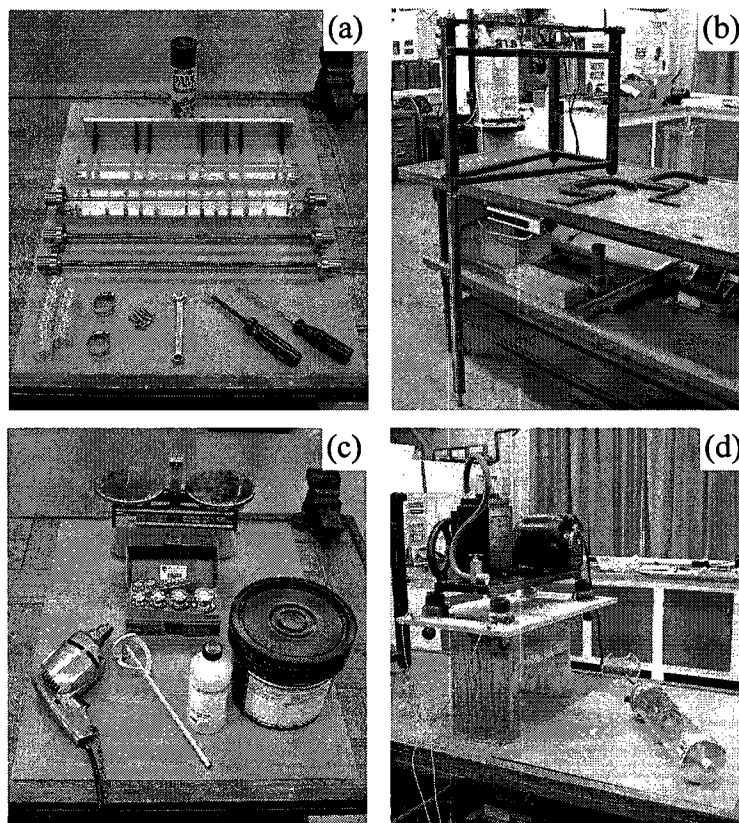


Figure A.1. Tools required for the pipe casting process: (a) mould and release agent; (b) tripod; (c) weighing scale, mixing tools, and silicone rubber (curing agent and base); (d) plexiglas piston and vacuum pump.

APPENDIX B

Determination of Flexural Rigidity and Damping

Flexible elastomer pipes made using *Silastic*® E RTV Silicone Rubber from Dow Corning possess practically the same physical properties if, and only if, they are cast from the same batch of silicone rubber. If not, their physical properties, such as their flexural rigidity and damping constants, will differ considerably from one pipe to another. The method used to determine the flexural rigidity and damping constants of a flexible elastomer pipe is based on the work by Païdoussis & des Trois Maisons (1969, 1971). Additional information can also be found in Païdoussis (1998, Appendix D).

B.1 Determination of Flexural Rigidity

The flexural rigidity, EI , of a flexible elastomer pipe is determined by planar free-vibration experiments of a cantilevered pipe containing no fluid that is hung vertically and excited in its first-mode natural frequency. This can be achieved rather effortlessly by displacing and releasing the free end of the cantilevered pipe such that it oscillates in its first mode. The displacement of the pipe is then measured using the *Optron* system, which is a non-contacting optical tracking system. A PSD plot is then constructed using the resultant time signal [see Appendix E] in order to determine the first-mode natural frequency of the system. From Païdoussis & des Trois Maisons (1969),

$$\frac{\gamma}{[\text{Re}(\omega_1)]^2} = \frac{g}{[\text{Re}(\Omega_1)]^2 L}, \quad (\text{B.1})$$

where γ is a gravity parameter, ω_1 is the nondimensional first-mode natural frequency, g is the gravitational constant, L is the effective length of the pipe, and $\Omega_1 = 2\pi f_1$ is the dimensional first-mode natural frequency in radians/second. Using the right-hand side of Eqn. (B.1) and Table A.1 from Païdoussis & des Trois Maisons (1969), the corresponding value of γ can be found by linear interpolation. The flexural rigidity, EI , of the pipe is then calculated from the expression

$$\gamma = \frac{mgL^3}{EI}, \quad (\text{B.2})$$

where m is the mass per unit length of the pipe, and all other quantities were defined previously.

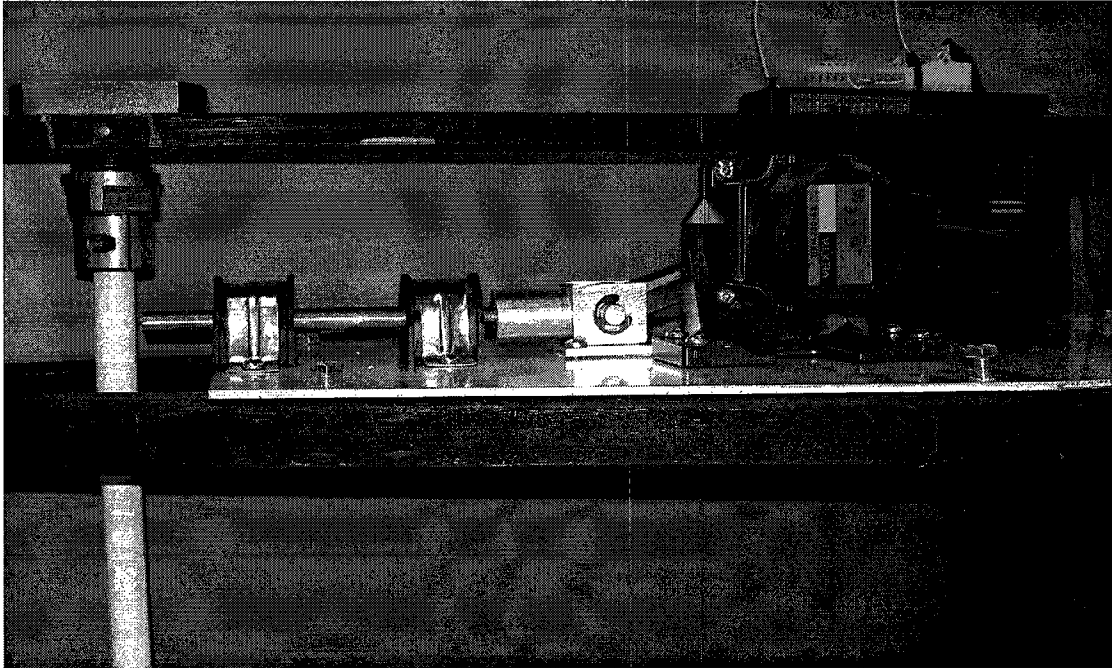


Figure B.1. The small DC motor and crank-slider that are used to excite the pipe.

B.2 Determination of Logarithmic Decrements

The logarithmic decrements, δ_n , of a flexible elastomer pipe are also determined by planar free-vibration experiments of a cantilevered pipe containing no fluid that is

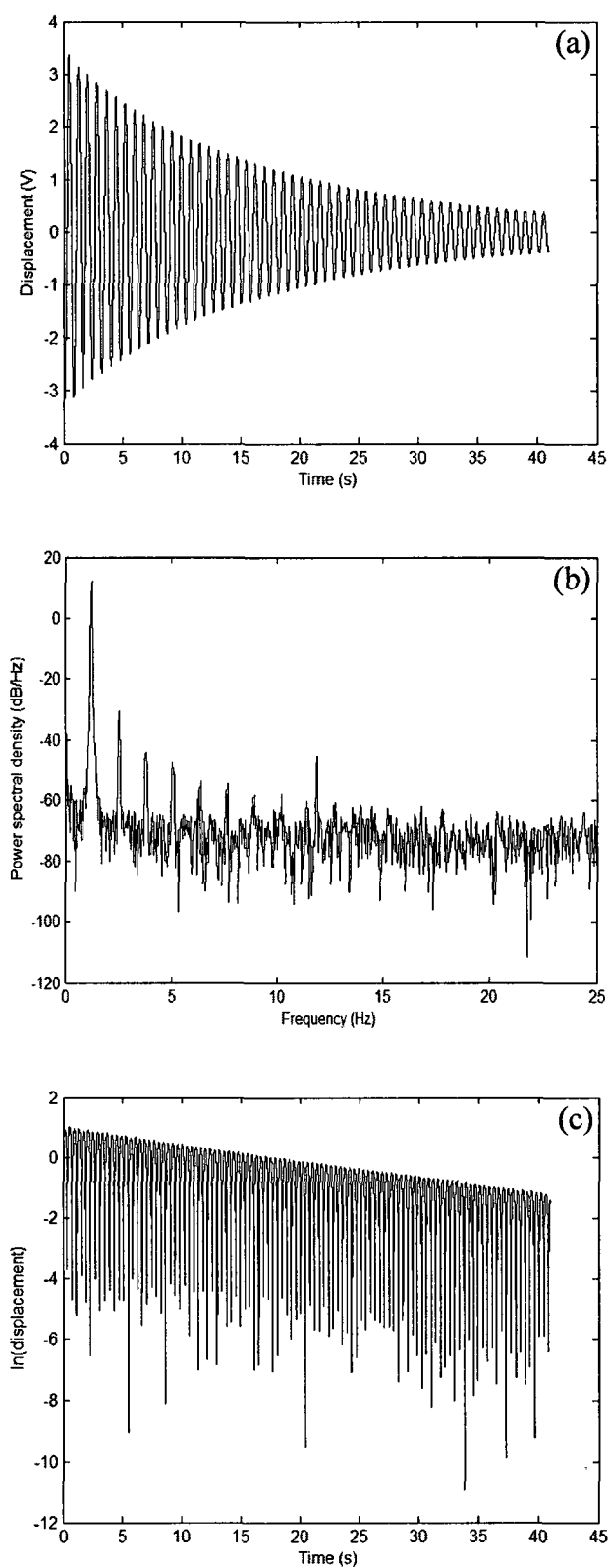


Figure B.2. Typical first mode (a) time signal, (b) PSD plot, and (c) $\ln(\text{displacement})$ versus time plot.

hung vertically and excited in its first-, second-, and third-mode natural frequencies. The first mode is, once again, excited manually; however, the second and third modes are excited mechanically with a small DC motor that is equipped with a crank-slider. The experimental set-up is shown in Fig. B.1. When the DC motor is turned off abruptly, the pipe oscillates in only the mode of interest. The decaying pipe vibration is then measured using the *Optron* system, and the natural frequency of the mode of interest is determined from a PSD plot of the time signal [see Appendix E]. Note that a low-pass Chebyshev Type 1 filter is applied in *MATLAB* to the first-mode time signal, whereas band-pass Chebyshev Type 1 filters are applied to the second- and third-mode time signals, in order to remove any noise or unwanted components from the signals. The filtered time signals are then used to plot $\ln(\text{displacement})$ versus time graphs [see Fig. B.2], whereby the linear slope of the decaying peaks is used to determine the logarithmic decrement of the mode of interest, which is found from the expression

$$\delta_n = \frac{\text{slope}}{f_n}. \quad (\text{B.3})$$

It is then assumed that the logarithmic decrements for higher modes, i.e. for $n > 3$, increase linearly with modal number.

B.3 Determination of Hysteretic and Viscoelastic Damping Constants

If internal dissipation in the material of the flexible elastomer pipe is to be considered, the hysteretic damping constant, $\bar{\mu}^*$, and the dimensionless viscoelastic damping constant, $\bar{\alpha}^*$, must be determined from the experimental first-, second-, and third-mode dimensionless natural frequencies and logarithmic decrements, as well as from the resultant gravity parameter, γ . Then, using Figs. 1 and 2 from Païdoussis & des Trois Maisons (1971), the values of δ_1^* , δ_2^* , and δ_3^* , whereby

$$\delta_n^* = \frac{\delta_n}{\bar{\mu}^* + \bar{\alpha}^* \text{Re}(\omega_n)}, \quad (\text{B.4})$$

can be read directly from the graphs. This leads to three independent equations but only two unknowns, namely $\bar{\mu}^*$ and $\bar{\alpha}^*$. Fig. B.3 shows an example plot of three such independent equations. The hysteretic and viscoelastic damping constants are then chosen simultaneously by trial-and-error such that the error in computing δ_1^* , δ_2^* , and δ_3^* is minimized on the whole. Referring to Fig. B.3, $\bar{\mu}^*$ is chosen as the average of $\bar{\mu}_1^*$ and $\bar{\mu}_2^*$ as an initial trial; similarly, $\bar{\alpha}^*$ is chosen as the average of $\bar{\alpha}_1^*$ and $\bar{\alpha}_2^*$. Once these initial values of $\bar{\mu}^*$ and $\bar{\alpha}^*$ are calculated, they can be tweaked in order to minimize the error in computing δ_1^* , δ_2^* , and δ_3^* from Eqn. (B.4).

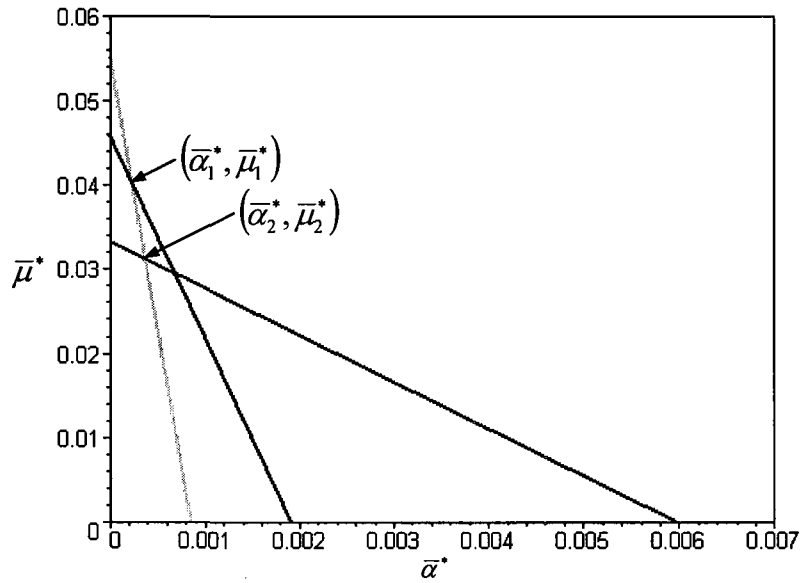


Figure B.3. Typical plot used to determine the hysteretic, $\bar{\mu}^*$, and viscoelastic, $\bar{\alpha}^*$, damping constants of a flexible elastomer pipe.

APPENDIX C

Optron Displacement Calibration

The *Optron* system is an electro-optical biaxial displacement follower system that tracks the motion of an object along a vertical and/or horizontal axis. In order for tracking to take place, the object must possess a light-dark or dark-light interface. If such an interface does not exist, then a sharp discontinuity in illumination can be achieved with the help of a DC lamp. Note that the *Optron* system has been designed to provide the user with a measure of displacement.

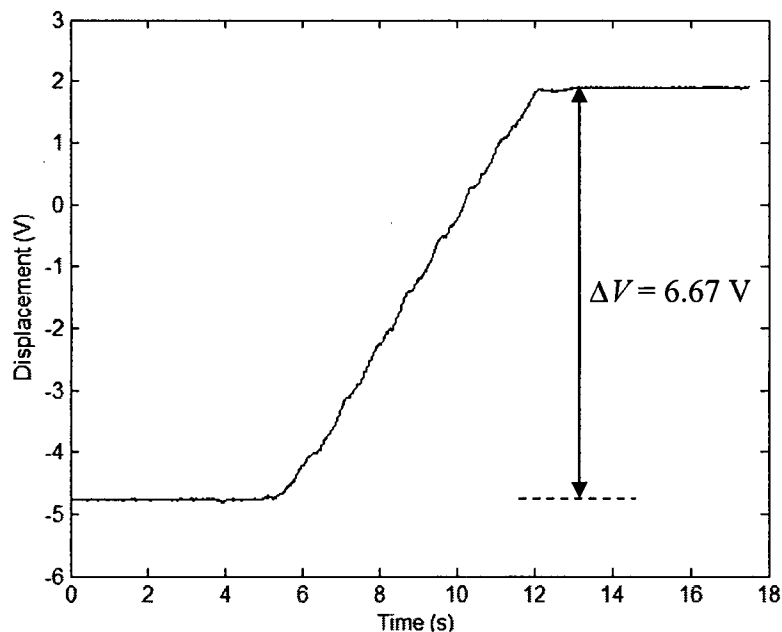


Figure C.1. Typical displacement calibration curve for the *Optron* system.

Since the output of the *Optron* system is a voltage rather than a physical displacement, the displacement of the object cannot be determined directly from the time

signals recorded in *LabVIEW*. As a result, the *Optron* system must be calibrated so that the amplitude scale of the time signal corresponds to a displacement in millimetres rather than a voltage. This can be achieved rather effortlessly by moving the optical head of the *Optron* system through a fixed distance that completely traverses the object from its light to dark area, or *vice versa*. Note that the object should remain stationary, or motionless, throughout the entire calibration process for accurate readings. Fig. C.1 shows a typical calibration curve from which a voltage difference can be read for a specified displacement. Since the relationship between voltage and displacement is linear, the two can be correlated using the resultant calibration curve.

APPENDIX D

Experimental Measurement of Flow Velocity

The only measurement taken during water experiments is the volumetric flow rate, Q . However, the air experiments were a little more involved, and six key measurements were taken, namely (i) the pressure upstream of the orifice plate, P_1 , (ii) the pressure differential across the orifice plate, ΔP , (iii) the pressure at location 3 on the large steel tank, P_3 , (iv) the pressure at location 4 on the large steel tank, P_4 , (v) the pressure at location 5 on the large steel tank, P_5 , and (vi) the air temperature, T . Refer to Fig. 3.10 for a schematic of the experimental set-up.

D.1 Water Flow Velocity Measurements

During water experiments, the volumetric flow rate, Q , is simply read from the *Omega* DPF64 ratemeter, which receives an input signal from the *Omega* FMG710 magnetic flowmeter. However, since the units being read were initially unknown, it was necessary to calibrate the ratemeter before any water experiments could take place. This was done by recording the time needed to collect 25 pounds of water at five specified dial positions on the controller. Referring to Table D.1 and Fig. D.1, it was found that the ratemeter displays the volumetric flow rate, Q , in litres/second, which can easily be converted to a flow velocity, U , in meters/second using the following expression:

$$U = \frac{Q \times 10^{-3}}{A}, \quad (\text{D.1})$$

where $A = \frac{\pi}{4} D_i^2$ is the flow area of interest, and D_i is the inner diameter of the pipe in meters.

Table D.1. Ratemeter calibration data

DIAL POSITION 20					
Trial	Weight [lbs]	Time [s]	Q [L/s]	Reading [?]	Difference [%]
1	25	88.62	0.1281	0.1280	0.069
2	25	88.97	0.1276	0.1280	0.325
3	25	89.28	0.1271	0.1280	0.671
Average	25	88.96	0.1276	0.1280	0.309

DIAL POSITION 40					
Trial	Weight [lbs]	Time [s]	Q [L/s]	Reading [?]	Difference [%]
1	25	52.04	0.2181	0.2170	0.518
2	25	52.69	0.2154	0.2170	0.722
3	25	52.34	0.2169	0.2170	0.058
Average	25	52.36	0.2168	0.2170	0.088

DIAL POSITION 60					
Trial	Weight [lbs]	Time [s]	Q [L/s]	Reading [?]	Difference [%]
1	25	41.87	0.2711	0.2725	0.512
2	25	41.75	0.2719	0.2725	0.226
3	25	41.93	0.2707	0.2725	0.654
Average	25	41.85	0.2712	0.2725	0.464

DIAL POSITION 80					
Trial	Weight [lbs]	Time [s]	Q [L/s]	Reading [?]	Difference [%]
1	25	34.97	0.3246	0.3275	0.886
2	25	34.28	0.3311	0.3275	1.109
3	25	34.72	0.3269	0.3275	0.173
Average	25	34.66	0.3276	0.3275	0.017

DIAL POSITION 100					
Trial	Weight [lbs]	Time [s]	Q [L/s]	Reading [?]	Difference [%]
1	25	29.55	0.3841	0.3825	0.427
2	25	29.77	0.3813	0.3825	0.315
3	25	29.48	0.3850	0.3825	0.666
Average	25	29.60	0.3835	0.3825	0.259

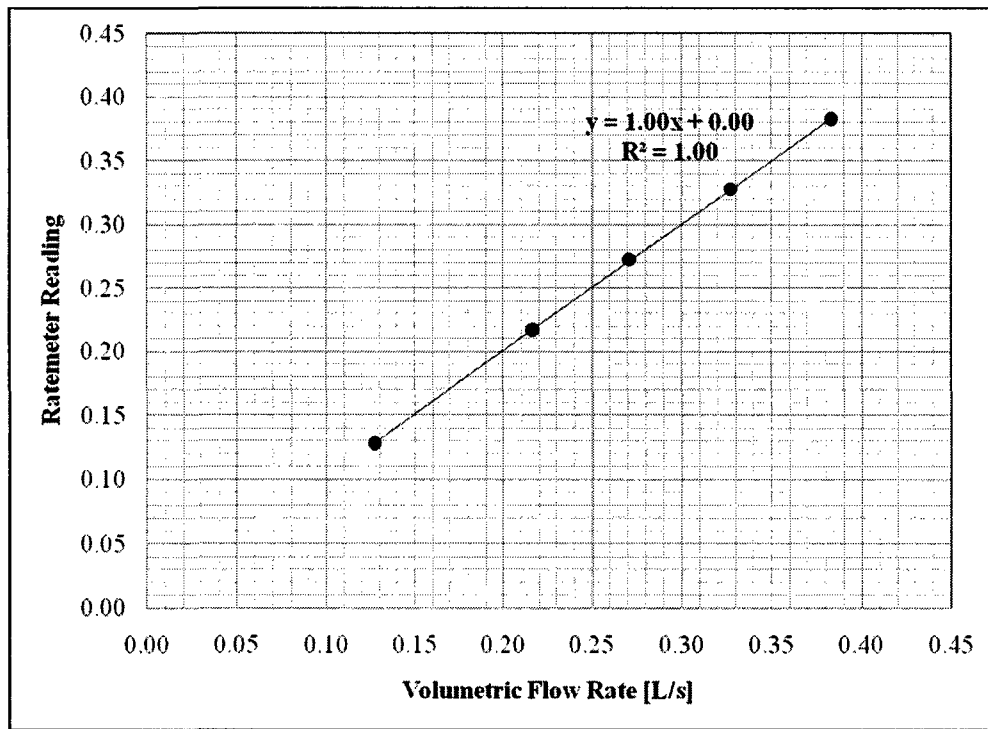


Figure D.1. Ratemeter calibration curve.

D.2 Air Flow Velocity Measurements

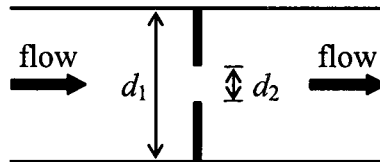


Figure D.2. Schematic of the orifice plate.

The mass flow rate of air supplied to the large steel tank during air experiments is found using an orifice plate, which is a flowmeter device that works based on Bernoulli's principle. Assuming steady-state, inviscid, incompressible flow in a horizontal pipe, and negligible frictional losses, Bernoulli's principle reduces to

$$P_1 + \frac{1}{2} \rho_1 V_1^2 = P_2 + \frac{1}{2} \rho_1 V_2^2, \quad (\text{D.2})$$

where P_1 and P_2 are the fluid pressure upstream and downstream of the orifice plate, respectively, ρ_1 is the fluid density, V_1 is the fluid velocity upstream the orifice plate, V_2 is

the fluid velocity through the orifice hole, and the volumetric flow rate is given by $Q = V_1 A_1 = V_2 A_2$. This leads to

$$P_1 - P_2 = \frac{1}{2} \rho_1 (Q^2 / A_2^2 - Q^2 / A_1^2), \quad (\text{D.3})$$

where A_1 is the cross-sectional area of the pipe, and A_2 is the cross-sectional area of the orifice hole. Rearranging for Q gives

$$Q = A_2 \sqrt{\frac{2(P_1 - P_2)/\rho_1}{1 - (A_2/A_1)^2}}. \quad (\text{D.4})$$

Introducing the beta factor, $\beta = d_2/d_1$, the coefficient of discharge, $C_d \approx 0.60$ for fully-developed turbulent flows, and the expansion factor, $Y \approx 1$ for air and small pressure differences, to account for compressibility effects, leads to the following expression for the volumetric flow rate, Q :

$$Q = \frac{\pi}{4} d_2^2 C_d Y \sqrt{\frac{2(P_1 - P_2)/\rho_1}{1 - \beta^4}}. \quad (\text{D.5})$$

Multiplying Eqn. (D.5) by the density of the fluid upstream the orifice plate, ρ_1 , gives the expression for the mass flow rate, \dot{m} :

$$\dot{m} = \frac{\pi}{4} d_2^2 C_d Y \sqrt{\frac{2\rho_1(P_1 - P_2)}{1 - \beta^4}}. \quad (\text{D.6})$$

Assuming air to be an ideal gas, the density of the fluid upstream the orifice plate, ρ_1 , is given by

$$\rho_1 = \frac{P_1}{RT_1}, \quad (\text{D.7})$$

where P_1 and $T_1 \approx T$ are measured directly, and $R = 286.9 \text{ J/(kg}\cdot\text{K)}$ is the ideal gas constant for air. Assuming a constant air density, ρ , the axial flow velocity, U , is given by

$$U = \frac{\dot{m}}{\rho A_f}, \quad (\text{D.8})$$

where \dot{m} is the mass flow rate given by Eqn. (D.6), and A_f is the flow area of interest. Unfortunately, the air density, ρ , cannot be measured directly. Therefore, a preliminary guess for ρ can be made using the ideal gas law,

$$\rho = \frac{P}{RT}, \quad (\text{D.9})$$

where P is the average of P_4 and P_5 :

$$\rho = \frac{\frac{1}{2}(P_4 + P_5)}{RT}. \quad (\text{D.10})$$

Now, compressibility effects must be taken into account if the Mach number is greater than $M = 0.30$ for the majority of flow velocities investigated, which is the case for an aspirating pipe. This can be accomplished through the use of the following isentropic flow expressions:

$$\frac{T^*}{T_o} = \left[1 + \left(\frac{\gamma - 1}{2} \right) M^2 \right]^{-1}, \quad (\text{D.11})$$

$$\frac{\rho^*}{\rho_o} = \left[1 + \left(\frac{\gamma - 1}{2} \right) M^2 \right]^{\frac{1}{1-\gamma}}, \quad (\text{D.12})$$

where T_o is the stagnation temperature, ρ_o is the stagnation density, $\gamma = 1.4$ is the specific heat ratio for air, $M = U/c$ is the Mach number, and $c = \sqrt{\gamma RT^*}$ is the speed of sound in air. Since the Mach number is small everywhere but inside the flexible elastomer pipe, the temperature, T , and the density, ρ , are assumed to be stagnation values, i.e. $T_o = T$ and $\rho_o = \rho$. In order for the solution to converge to more accurate axial flow velocities inside the flexible elastomer pipe, an iterative process is established whereby the updated values of temperature and density, T^* and ρ^* , are determined from the stagnation values, T_o and ρ_o , as well as from the previously calculated Mach numbers, M . Although T^* does not appear in Eqn. (D.8) explicitly, it is nevertheless needed to calculate ρ^* in Eqn. (D.12) because of the presence of a non-negligible M .

APPENDIX E

Experimental Measurement of Frequency

The main frequency of a time signal is determined using Welch's method. This technique can be used to produce power spectral density plots, i.e. PSD plots, which describe how the power of a signal is distributed with frequency. In a PSD plot, the frequency resulting in the largest peak yields the main frequency of the system. Fortunately, Welch's method can easily be implemented in *MATLAB* using the *pwelch* command.

More specifically, Welch's method divides a time signal into a specified number of overlapping sections, and then computes, as well as averages, the power spectral density of each individual section. Fig. E.1 illustrates a typical *MATLAB* code that is used to produce PSD plots from time signals. In this example, the acquired time signals are truncated to 2^{14} discrete sample points, and divided into eight sections with 50% overlap. Furthermore, each section is windowed with a Hanning window. Fig. E.2 illustrates a typical PSD plot in *MATLAB*.

In Fig. E.1, note that *A* is a vector containing the original time signal, while *B* is the truncated time signal from which the mean value of *A* has been subtracted. In addition, *Fs* is the sampling frequency in Hertz, *N* is the total number of discrete sample points, *WINDOW* specifies the type of window used, i.e. Hanning, as well as the length of each windowed section, *NOVERLAP* specifies the number of discrete sample points to overlap from section to section, and *NFFT* is the number of fast Fourier transform points used to calculate the power spectral density estimate. *NFFT* is typically chosen to be the maximum between 256 and the next power of 2 greater than the length of each windowed section. Moreover, note that the units for power spectral density in Fig. E.2 are dB/Hz.

```

clear all; clc;

format long

Fs = 400;
N = 2^14;
WINDOW = HANNING(3640);
NOVERLAP = 1820;
NFFT = 4096;

load('signal');

A(:,1) = sig1.data;
A(:,2) = sig2.data;
A(:,3) = sig3.data;
A(:,4) = sig4.data;
A(:,5) = sig5.data;

for I = 1:N
    t(I) = I/Fs;
end

for J = 1:5
    figure(J)
    B = A(1:N,J) - mean(A(1:N,J));
    [Pxx,F] = pwelch(B,WINDOW,NOVERLAP,NFFT,Fs);
    P = 10*log10(Pxx);
    subplot(2,1,1), plot(t,B);
    xlabel('Time (s)');
    ylabel('Displacement (V)');
    axis([0 45 -2 2]);
    subplot(2,1,2), plot(F,P);
    xlabel('Frequency (Hz)');
    ylabel('Power spectral density (dB/Hz)');
    axis([0 50 -80 0]);
    filename = sprintf('figure_%d.bmp',J);
    saveas(J,filename,'bmp');
    F(find(P==max(P)))
end

```

Figure E.1. Typical *MATLAB* code for producing PSD plots from time signals.

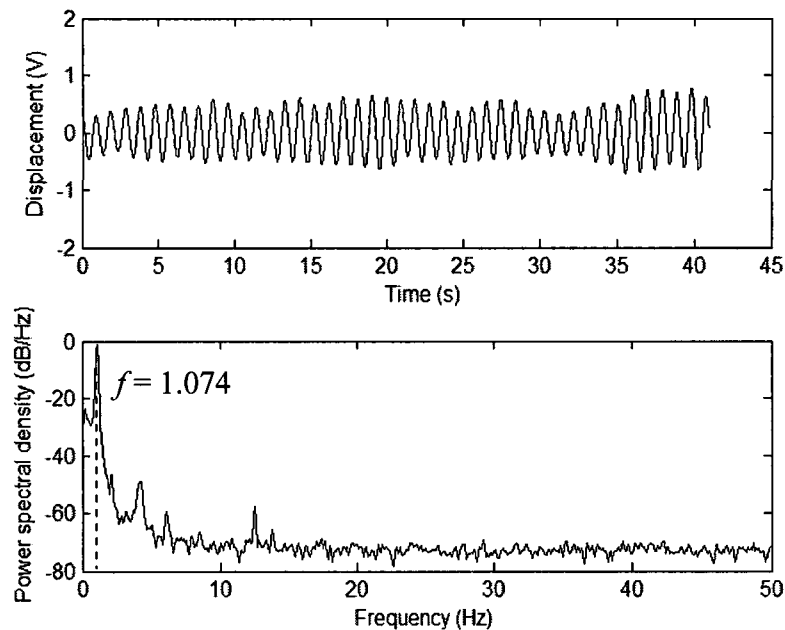


Figure E.2. Typical PSD plot produced in *MATLAB* from a time signal.

APPENDIX F

Technical Drawings

F.1 Technical Drawings for Chapter 4

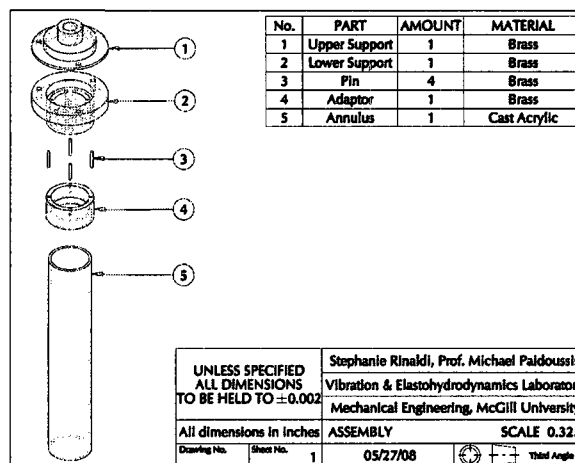


Figure F.1. Assembly technical drawing.

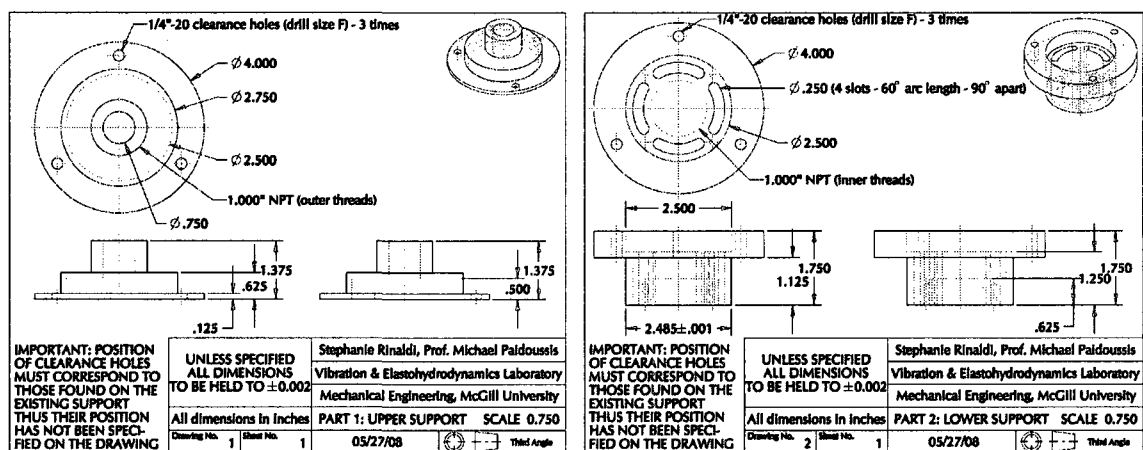


Figure F.2. Component technical drawings.

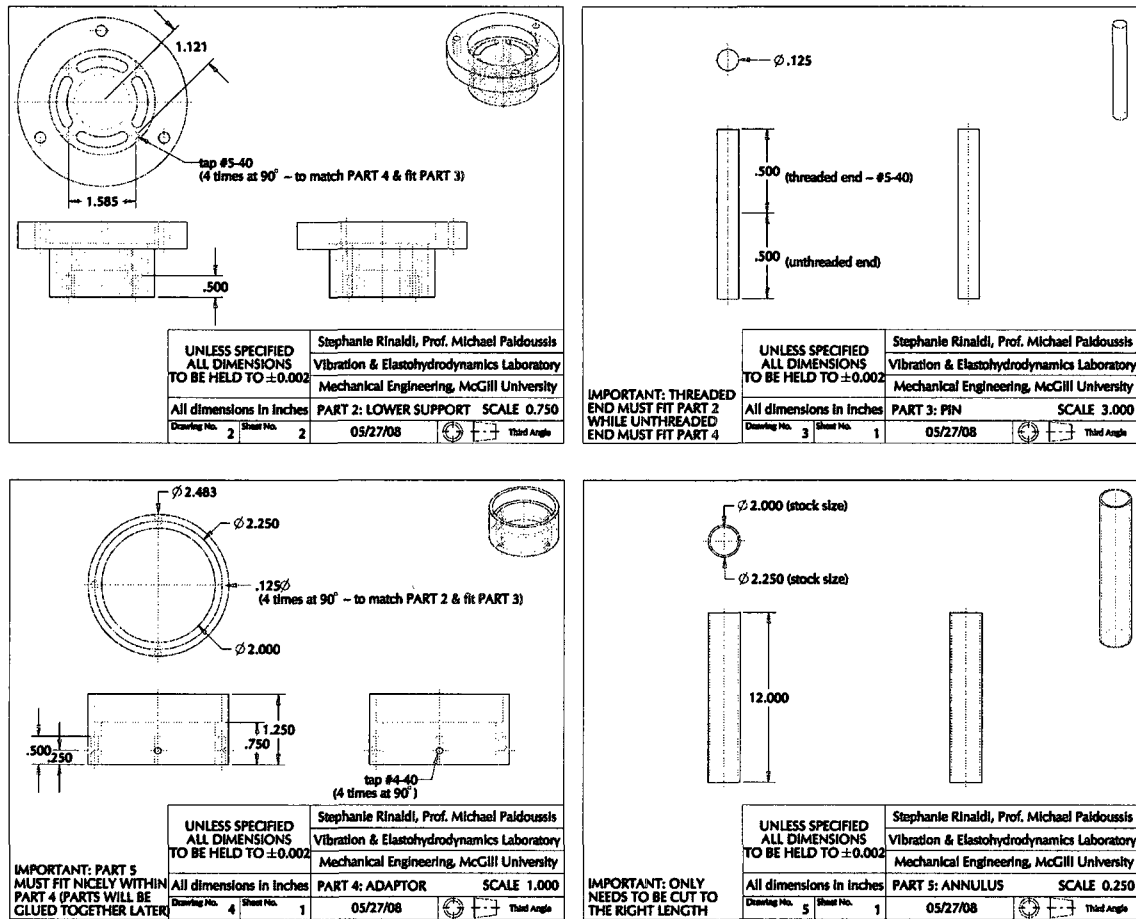


Figure F.2. cont'd.

F.2 Technical Drawings for Chapter 5

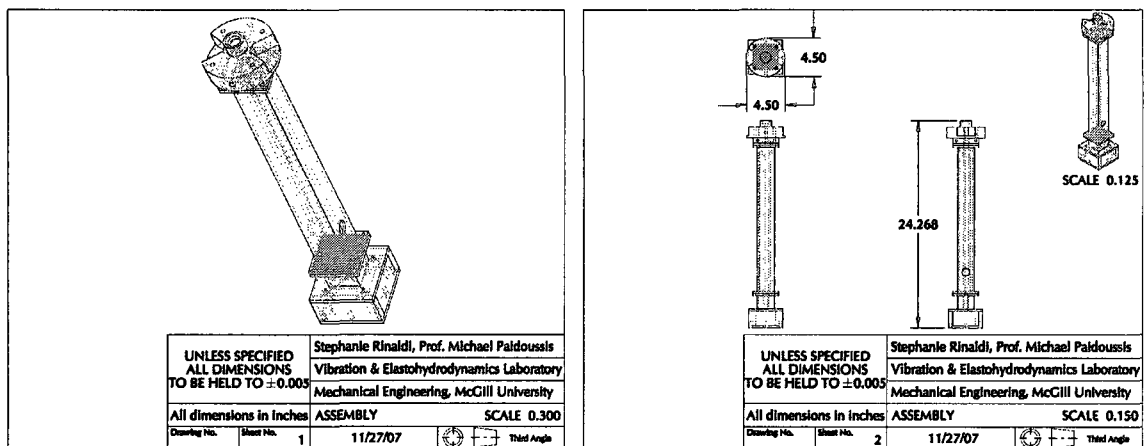


Figure F.3. Assembly technical drawings.

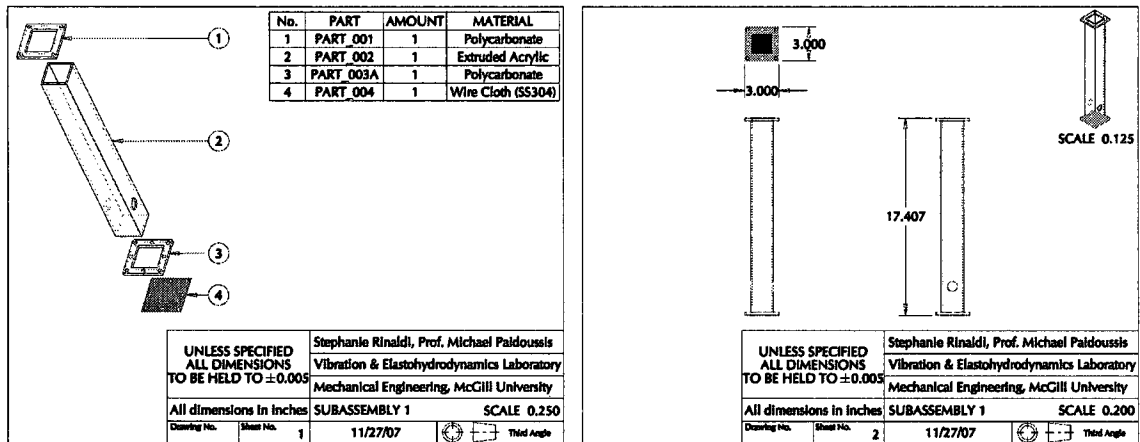


Figure F.4. Subassembly #1 technical drawings.

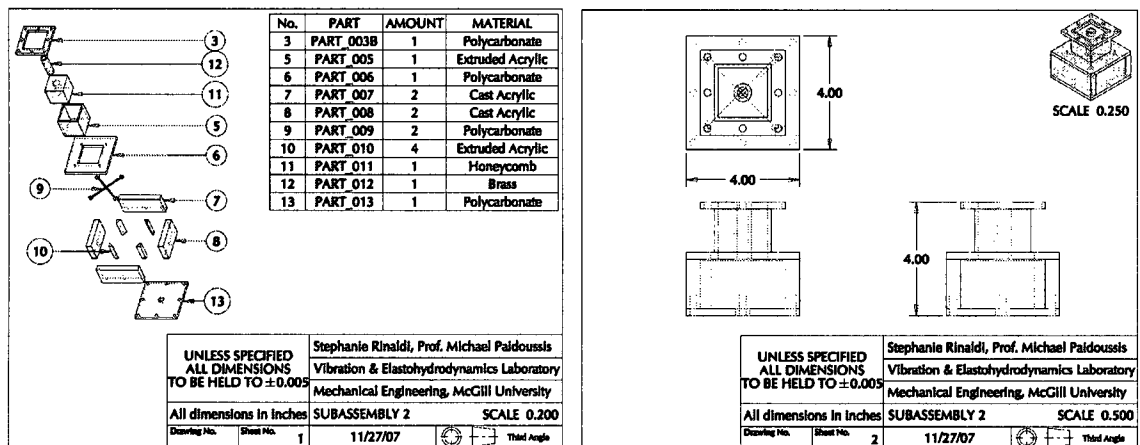


Figure F.5. Subassembly #2 technical drawings.

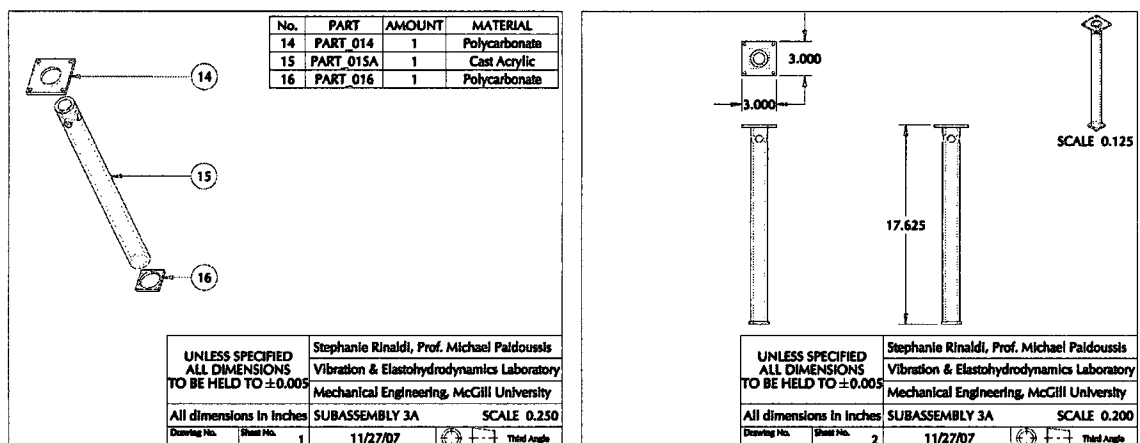


Figure F.6. Subassembly #3A technical drawings.

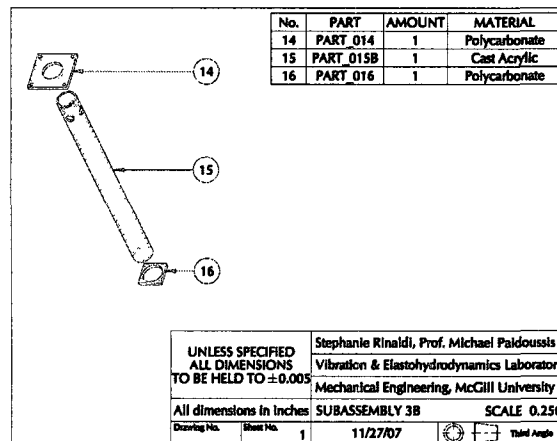


Figure F.7. Subassembly #3B technical drawing.

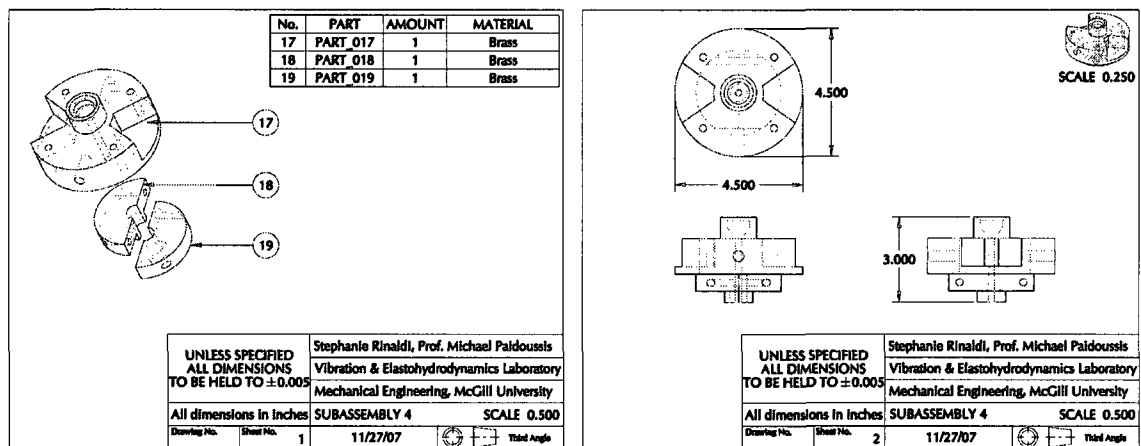


Figure F.8. Subassembly #4 technical drawings.

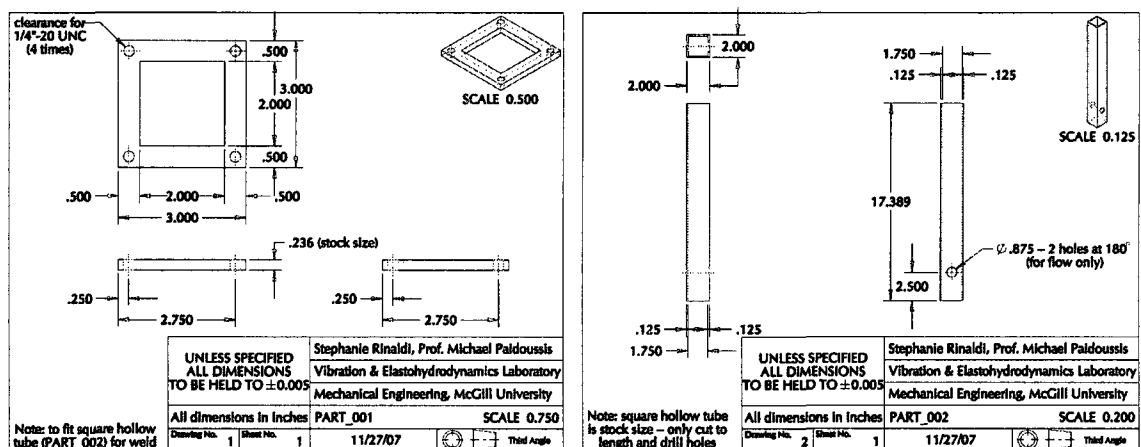


Figure F.9. Component technical drawings.

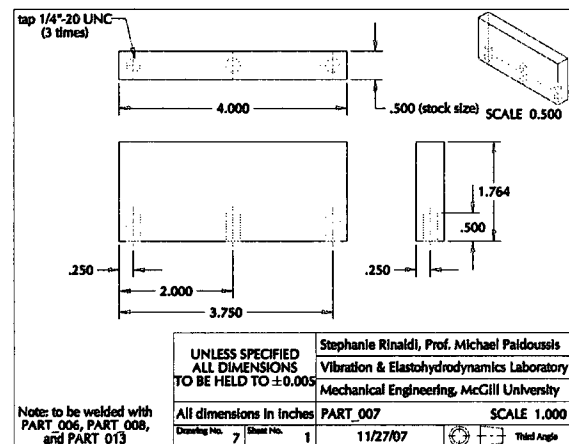
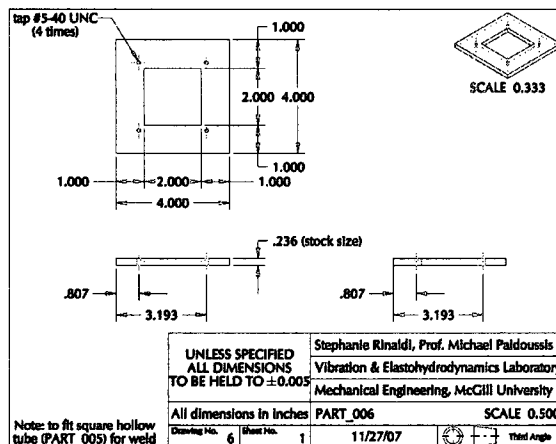
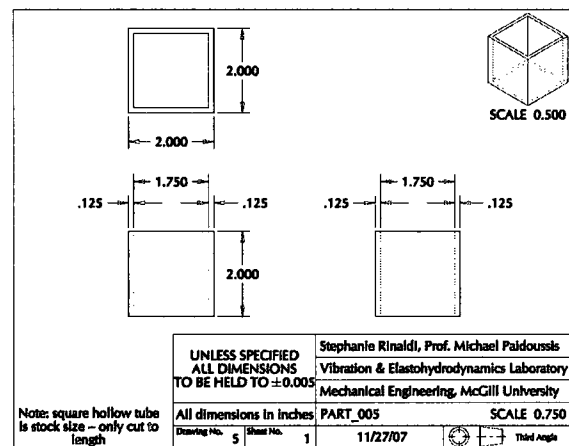
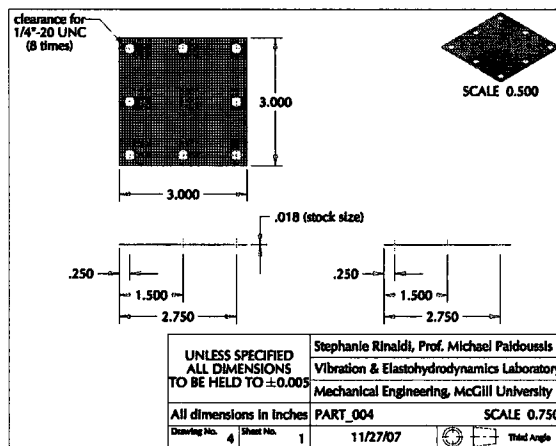
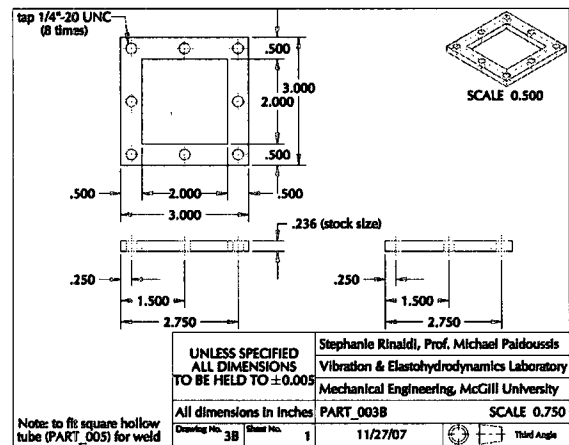
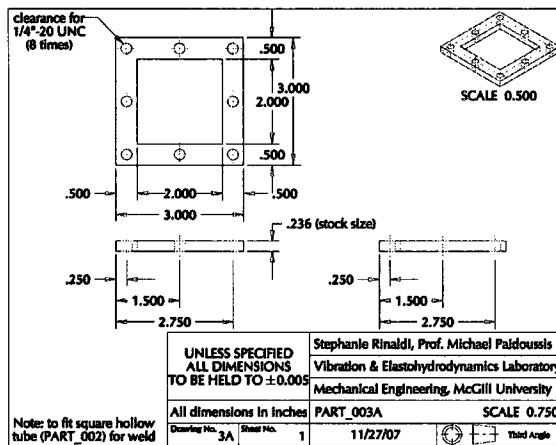


Figure F.9. cont'd.

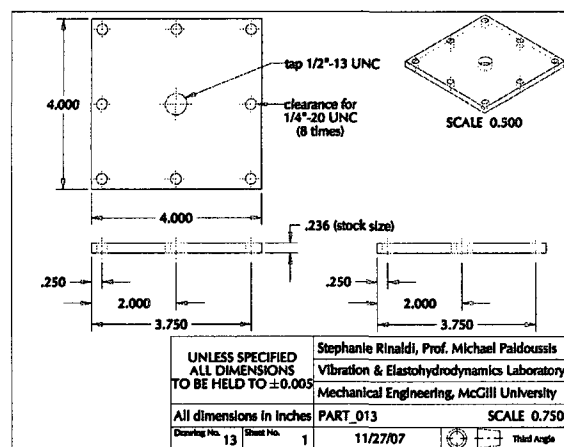
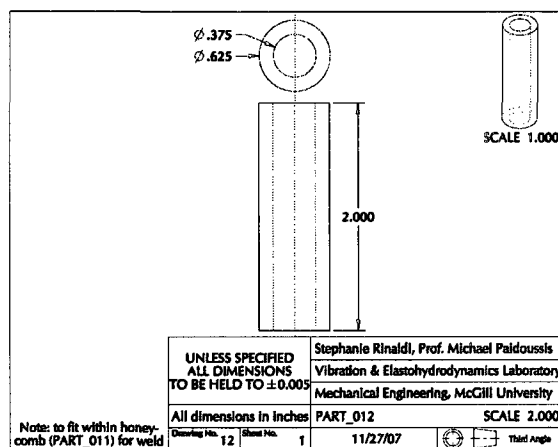
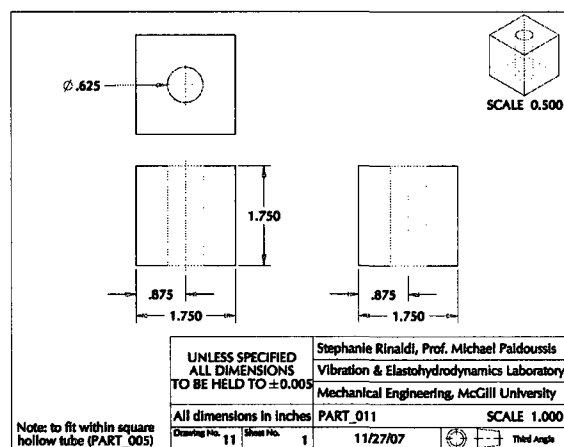
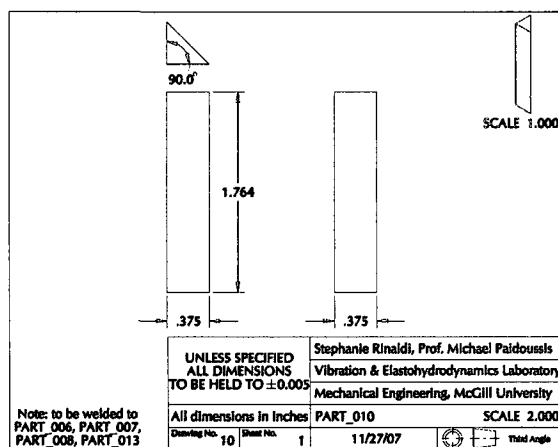
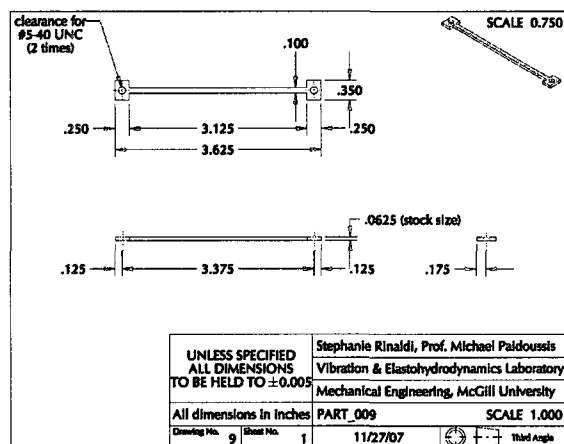
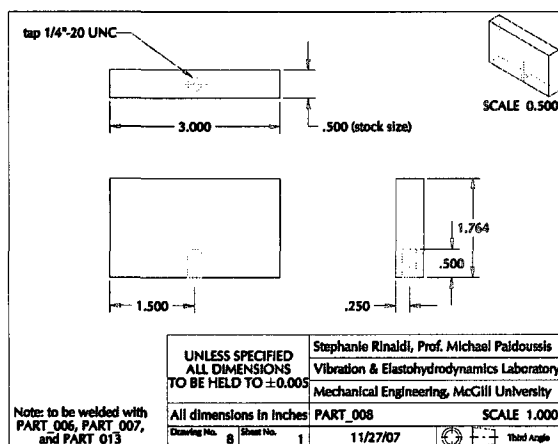


Figure F.9. cont'd.

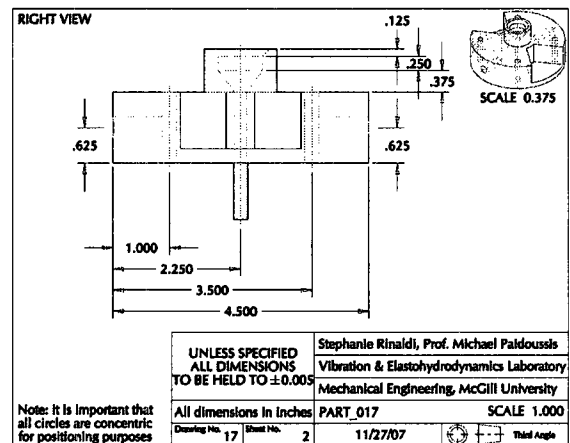
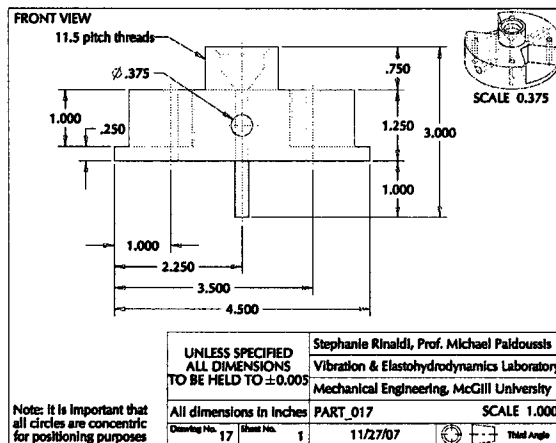
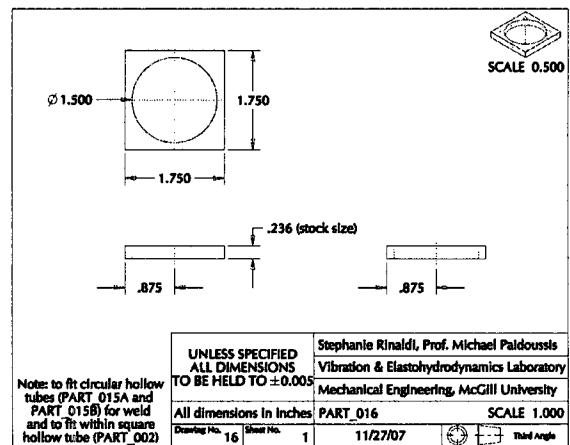
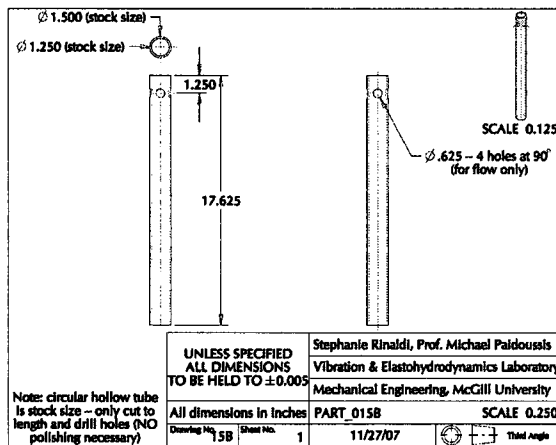
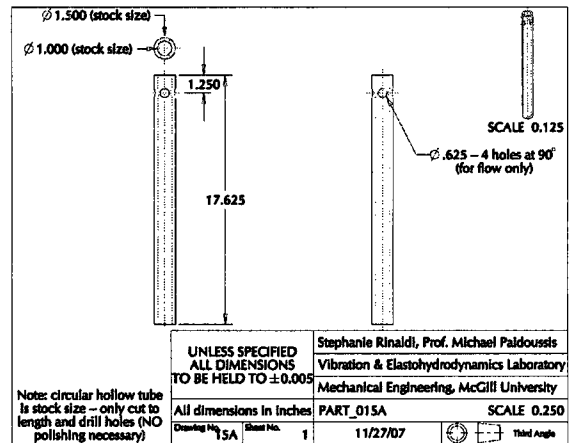
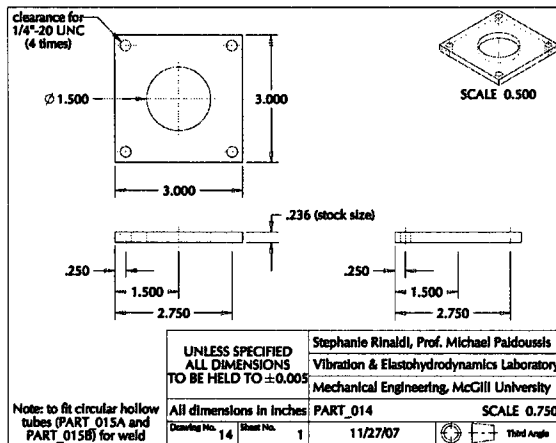


Figure F.9. cont'd.

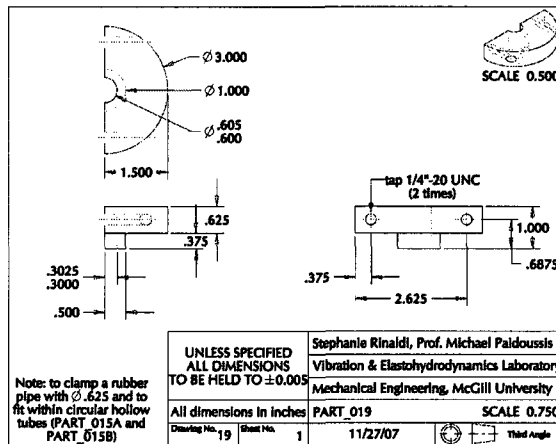
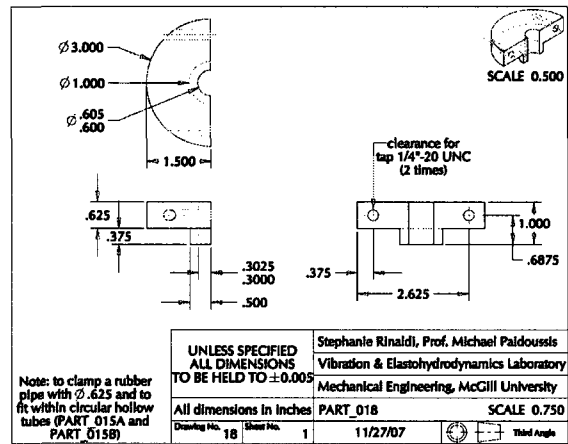
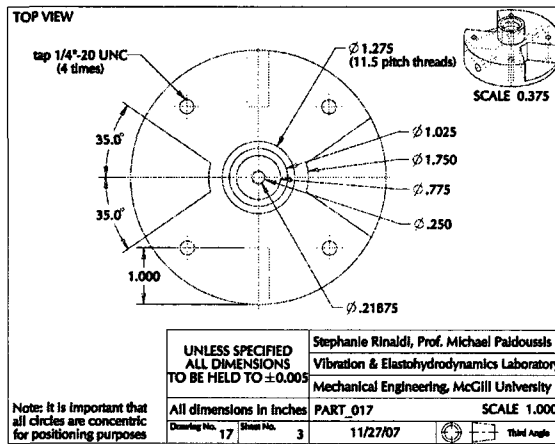


Figure F.9. cont'd.

APPENDIX G

Shear Boundary Condition for a Free-Clamped Cylinder in Confined Axial Flow

It is assumed that the free end of the free-clamped cylinder in confined axial flow is fitted with a rigid tapered end-piece of length ℓ , where $\ell/L \ll 1$, and has a cross-sectional area $A(x)$, which varies smoothly from A at $x = L$ to zero at $x = L + \ell$. The forces being applied to the tapered end-piece are illustrated in Fig. G.1. It should be noted that the forthcoming derivation of the shear boundary condition at $x = L$ is correct to first order. Furthermore, the derivation follows the formulation of Lopes *et al.* (2002), but in a simplified manner.

The variation of the Lagrangian of the tapered end-piece is

$$\delta \int_{t_1}^{t_2} \mathcal{L} dt = - \int_{t_1}^{t_2} \int_L^{L+\ell} m(x) \frac{\partial^2 w}{\partial t^2} \delta y dx dt, \quad (\text{G.1})$$

where $m(x) = \rho_b A(x)$, and ρ_b is the density of the tapered end-piece. Thus, Eqn. (G.1) reduces to

$$\delta \int_{t_1}^{t_2} \mathcal{L} dt = - \int_{t_1}^{t_2} m \frac{\partial^2 w}{\partial t^2} x_e \delta y dt, \quad (\text{G.2})$$

where

$$x_e = \frac{1}{A} \int_L^{L+\ell} A(x) dx. \quad (\text{G.3})$$

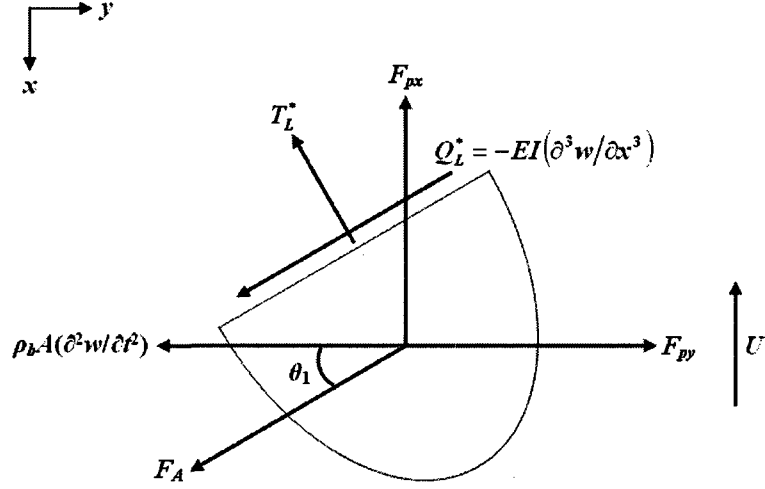


Figure G.1. Schematic of the tapered end-piece showing applied forces.

Considering only the virtual work done by the inviscid hydrodynamic force in the transverse direction, F_A , and the hydrostatic forces in the x - and y -direction, F_{px} and F_{py} , acting on the tapered end-piece, yields

$$\int_{t_1}^{t_2} \delta \mathcal{W} dt = \int_{t_1}^{t_2} \int_L^{L+\ell} \left\{ (-F_{px} + F_A \sin \theta_1) \delta x + (F_{py} - F_A \cos \theta_1) \delta y \right\} dx dt, \quad (\text{G.4})$$

where $\cos \theta_1 \approx 1$, $\sin \theta_1 \approx \partial w / \partial x$, and

$$\begin{aligned} F_{px} &= -p \frac{dA(x)}{dx}, \\ F_{py} &= \frac{\partial}{\partial x} \left(pA(x) \frac{\partial w}{\partial x} \right), \\ F_A &= f\chi\rho_f A(x) \left(\frac{\partial}{\partial t} - U \frac{\partial}{\partial x} \right) v = f\chi\rho_f A \frac{\partial v}{\partial t} \frac{1}{A} A(x) - f\chi\rho_f U v \frac{dA(x)}{dx}, \end{aligned} \quad (\text{G.5})$$

where $v = [\partial w / \partial t - U(\partial w / \partial x)]$. Simplifying Eqn. (G.4), and eliminating second order terms gives

$$\begin{aligned} \int_{t_1}^{t_2} \delta \mathcal{W} dt &= \int_{t_1}^{t_2} \int_L^{L+\ell} \left\{ -F_{px} \delta x + (F_{py} - F_A) \delta y \right\} dx dt, \\ \int_{t_1}^{t_2} \delta \mathcal{W} dt &= - \int_{t_1}^{t_2} \left\{ (pA)_L \delta x + \left\{ (pA)_L \frac{\partial w}{\partial x} + f\chi\rho_f A \left[\frac{\partial^2 w}{\partial t^2} x_e + U \left(\frac{\partial w}{\partial t} - U \frac{\partial w}{\partial x} \right) \right] \right\} \delta y \right\} dt. \end{aligned} \quad (\text{G.6})$$

Thus, combining Eqns. (G.2) and (G.6) gives

$$\begin{aligned} \delta \int_{t_1}^{t_2} \mathcal{L} dt + \int_{t_1}^{t_2} \delta \mathcal{W} dt = & - \int_{t_1}^{t_2} (pA)_L \delta x dt \\ & - \int_{t_1}^{t_2} \left\{ m \frac{\partial^2 w}{\partial t^2} x_e + (pA)_L \frac{\partial w}{\partial x} + f\chi\rho_f A \left[\frac{\partial^2 w}{\partial t^2} x_e + U \left(\frac{\partial w}{\partial t} - U \frac{\partial w}{\partial x} \right) \right] \right\} \delta y dt. \end{aligned} \quad (G.7)$$

The term in the curly brackets in Eqn. (G.7) is equal to the following:

$$-Q_L^* - T_L^* \frac{\partial w}{\partial x} = - \left\{ m \frac{\partial^2 w}{\partial t^2} x_e + (pA)_L \frac{\partial w}{\partial x} + f\chi\rho_f A \left[\frac{\partial^2 w}{\partial t^2} x_e + U \left(\frac{\partial w}{\partial t} - U \frac{\partial w}{\partial x} \right) \right] \right\}. \quad (G.8)$$

The shear force and tension acting on the tapered end-piece, Q_L^* and T_L^* , are equal in magnitude but opposite in direction to those acting on the pipe, Q_L and T_L , such that

$$Q_L + T_L \frac{\partial w}{\partial x} = - \left\{ m \frac{\partial^2 w}{\partial t^2} x_e + (pA)_L \frac{\partial w}{\partial x} + f\chi\rho_f A \left[\frac{\partial^2 w}{\partial t^2} x_e + U \left(\frac{\partial w}{\partial t} - U \frac{\partial w}{\partial x} \right) \right] \right\}. \quad (G.9)$$

Rearranging Eqn. (G.9) for Q_L yields

$$Q_L = -m \frac{\partial^2 w}{\partial t^2} x_e - (T + pA)_L \frac{\partial w}{\partial x} - f\chi\rho_f A \frac{\partial^2 w}{\partial t^2} x_e - f\chi\rho_f A U \left(\frac{\partial w}{\partial t} - U \frac{\partial w}{\partial x} \right), \quad (G.10)$$

where it was found that $(T + pA)_L = -\frac{1}{2} \rho_f D^2 U^2 C_b$. Therefore, Eqn. (G.10) becomes

$$Q_L = \left(\frac{1}{2} \rho_f D^2 U^2 C_b + f\chi\rho_f A U^2 \right) \frac{\partial w}{\partial x} - f\chi\rho_f A U \frac{\partial w}{\partial t} - (f\chi\rho_f A + m) x_e \frac{\partial^2 w}{\partial t^2}, \quad (G.11)$$

and the shear boundary condition at $x = L$ for a free-clamped cylinder in confined axial flow is thus

$$EI \frac{\partial^3 w}{\partial x^3} + \left(\frac{1}{2} \rho_f D^2 U^2 C_b + f\chi\rho_f A U^2 \right) \frac{\partial w}{\partial x} - f\chi\rho_f A U \frac{\partial w}{\partial t} - (f\chi\rho_f A + m) x_e \frac{\partial^2 w}{\partial t^2} = 0. \quad (G.12)$$

APPENDIX H

Improvements to the Model for a Free-Clamped Cylinder in Confined Axial Flow

Here, it is presumed that two additional forces – similar to those introduced in Chapter 3 for a cantilevered pipe aspirating fluid – arise at the free end of the cylinder, in addition to those already presented in Chapter 4. The forces exerted by the fluid on the cylinder at $x = L$ for both the (x, y) - and (ζ, ξ) -coordinate system are shown in Fig. H.1. It should be noted that a mean flow velocity, v , is shown facing the free end of the cylinder; thus, it is assumed, once again, that the fluid velocity undergoes a sudden change from $-v$ to $-U$, giving rise to the parameter $\alpha = v/U$.

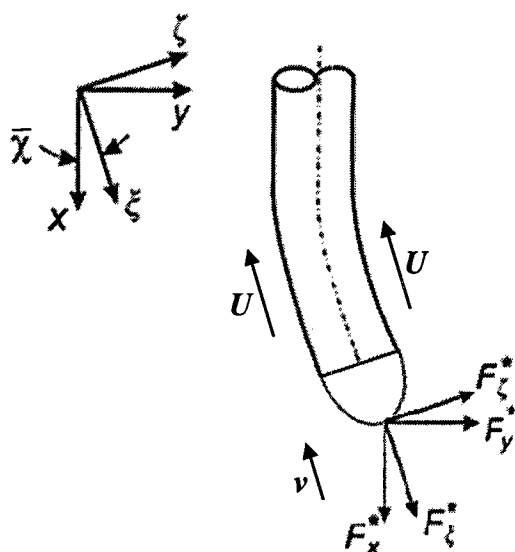


Figure H.1. Schematic of the forces exerted by the fluid on the cylinder at the free end, the (x, y) - and (ζ, ξ) -coordinate systems, and the angle $\bar{\chi}$ [Païdoussis *et al.* (2005)].

In Eqn. (4.20) of Chapter 4, an expression for $(T + pA)$ is provided as follows:

$$(T + pA) = (T + pA)_L - \left[\frac{1}{2} \rho_f D U^2 C_T \left(1 + \frac{D}{D_h} \right) - (m - \rho_f A)g \right] (L - x), \quad (\text{H.1})$$

where

$$(T + pA)_L = (T_L + p_L A) + \bar{T}. \quad (\text{H.2})$$

Note that T_L is the tension and p_L is the pressure at $x = L$, while \bar{T} is a newly added externally applied tension at $x = L$. Furthermore, from Eqn. (4.21), it is known that

$$(T_L + p_L A) = -\frac{1}{2} \rho_f D^2 U^2 C_b. \quad (\text{H.3})$$

Therefore, combining Eqns. (H.1), (H.2), and (H.3) gives

$$(T + pA) = \bar{T} - \frac{1}{2} \rho_f D^2 U^2 C_b - \left[\frac{1}{2} \rho_f D U^2 C_T \left(1 + \frac{D}{D_h} \right) - (m - \rho_f A)g \right] (L - x). \quad (\text{H.4})$$

Now, \bar{T} and the additional term in the shear boundary condition, which is given by the second expression in Eqn. (4.24), are determined from the forces F_x^* and F_y^* , which act on the cylinder at $x = L$, and are equal to the change in momentum, $\chi \rho_f A U (\Delta U)$. Referring to Fig. H.1,

$$F_x^* = -\chi \rho_f A U [-U \cos \bar{\chi} - (-v \cos \bar{\chi})], \quad (\text{H.5})$$

$$F_y^* = -\chi \rho_f A U [(-\dot{w}_L - U \sin \bar{\chi}) - (-v \sin \bar{\chi})], \quad (\text{H.6})$$

where $\cos \bar{\chi} \approx 1$, $\sin \bar{\chi} \approx \bar{\chi} \approx w'_L$, and $\alpha = v/U$. Thus,

$$F_x^* \approx \chi \rho_f A U^2 (1 - \alpha), \quad (\text{H.7})$$

$$F_y^* \approx \chi \rho_f A U [\dot{w}_L + (1 - \alpha) U w'_L] \quad (\text{H.8})$$

Furthermore, the forces exerted by the fluid on the cylinder at $x = L$ in the ξ - and ζ -direction, respectively, are determined to be

$$F_\xi^* = F_x^* \cos \bar{\chi} + F_y^* \sin \bar{\chi} \approx \chi \rho_f A U^2 (1 - \alpha), \quad (\text{H.9})$$

$$F_\zeta^* = F_y^* \cos \bar{\chi} - F_x^* \sin \bar{\chi} \approx \chi \rho_f A U \dot{w}_L. \quad (\text{H.10})$$

Consequently, the expressions for the newly added externally applied tension, and the updated shear boundary condition are

$$\bar{T} = F_\xi^* \approx \chi \rho_f A U^2 (1 - \alpha), \quad (\text{H.11})$$

$$\begin{aligned} EI \frac{\partial^3 w}{\partial x^3} + \left(\frac{1}{2} \rho_f D^2 U^2 C_b + f \chi \rho_f A U^2 \right) \frac{\partial w}{\partial x} - (f-1) \chi \rho_f A U \frac{\partial w}{\partial t} \\ - (f \chi \rho_f A + m) x_e \frac{\partial^2 w}{\partial t^2} = 0. \end{aligned} \quad (\text{H.12})$$

The updated equation of motion for a free-clamped cylinder in confined axial flow is

$$\begin{aligned} EI \left[1 + \left(\bar{\alpha} + \frac{\bar{\mu}^*}{\Omega} \right) \frac{\partial}{\partial t} \right] \frac{\partial^4 w}{\partial x^4} - \left[\frac{1}{2} \rho_f D U^2 C_T \left(\frac{D}{D_h} \right) - (m - \rho_f A) g \right] \frac{\partial w}{\partial x} \\ + \left\{ \frac{1}{2} \rho_f D^2 U^2 C_b + \left[\frac{1}{2} \rho_f D U^2 C_T \left(1 + \frac{D}{D_h} \right) - (m - \rho_f A) g \right] (L - x) \right\} \frac{\partial^2 w}{\partial x^2} \\ - \chi \rho_f A U^2 (1 - \alpha) \frac{\partial^2 w}{\partial x^2} + \chi \rho_f A \left(\frac{\partial^2 w}{\partial t^2} - 2U \frac{\partial^2 w}{\partial x \partial t} + U^2 \frac{\partial^2 w}{\partial x^2} \right) \\ + \frac{1}{2} \rho_f D U C_N \left(\frac{\partial w}{\partial t} - U \frac{\partial w}{\partial x} \right) + c \frac{\partial w}{\partial t} + m \frac{\partial^2 w}{\partial t^2} \\ + \left[- \left(\frac{1}{2} \rho_f D^2 U^2 C_b + f \chi \rho_f A U^2 \right) \frac{\partial w}{\partial x} + (f-1) \chi \rho_f A U \frac{\partial w}{\partial t} \right] \delta(x-L) \\ + (f \chi \rho_f A + m) x_e \frac{\partial^2 w}{\partial t^2} \delta(x-L) = 0. \end{aligned} \quad (\text{H.13})$$

Eqn. (H.13) is rendered nondimensional by using the parameters appearing in Eqn. (4.26), and the system is discretized using the Galerkin method. Two additional terms arise as a result of the modifications just made: one in the damping matrix, $[C]$, and the other in the stiffness matrix, $[K]$. The updated elements of the mass $[M]$, damping $[C]$, and stiffness $[K]$ matrices for the system are thus

$$M_{sr} = [1 + \beta(\chi - 1)] \delta_{sr} + [1 + \beta(f\chi - 1)] \chi_e \phi_s(1) \phi_r(1), \quad (\text{H.14})$$

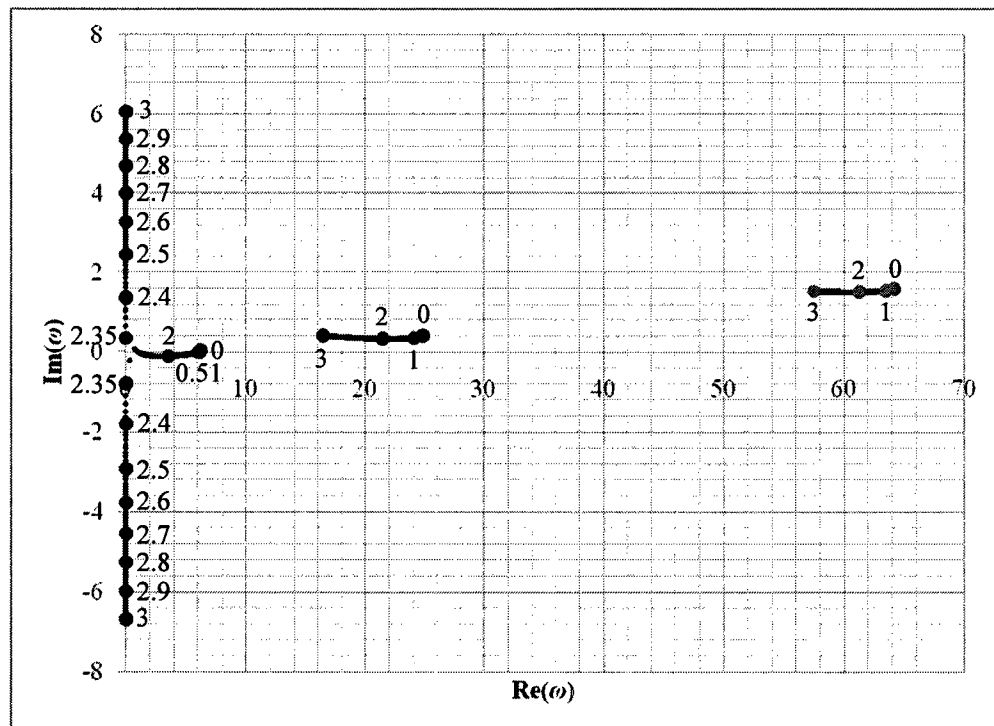


Figure H.2. Argand diagram as a function of u for a free-clamped cylinder in confined axial flow with $f=1.00$ and $c_b=0$ using a five-mode Galerkin approximation.

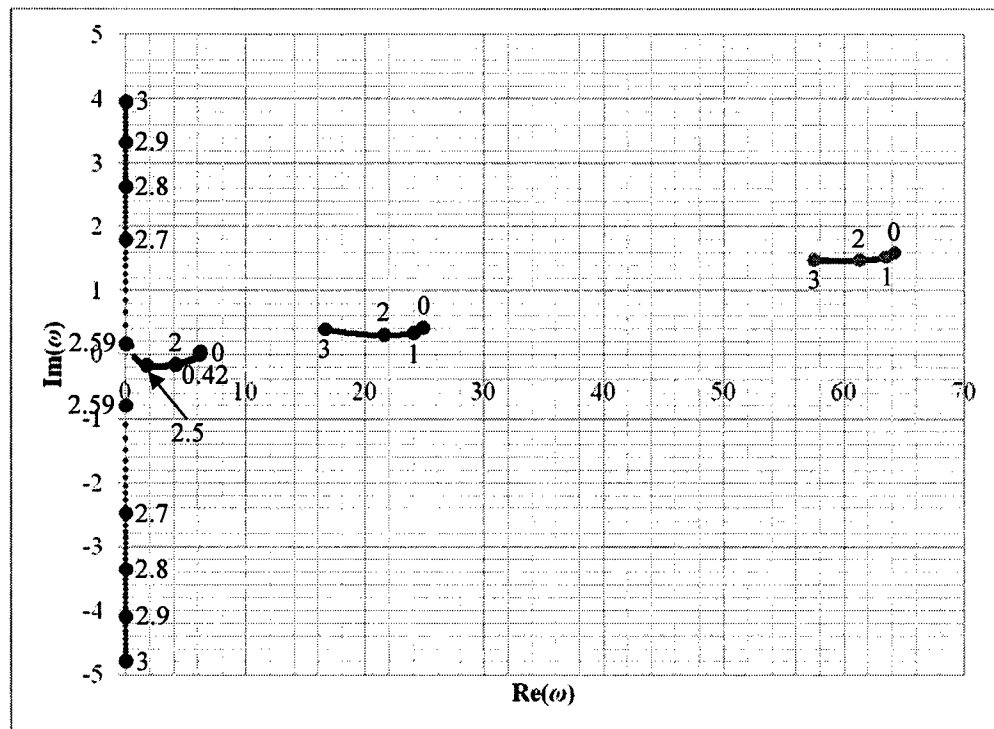


Figure H.3. Argand diagram as a function of u for a free-clamped cylinder in confined axial flow with $f=0.80$ and $c_b=0.20$ using a five-mode Galerkin approximation.

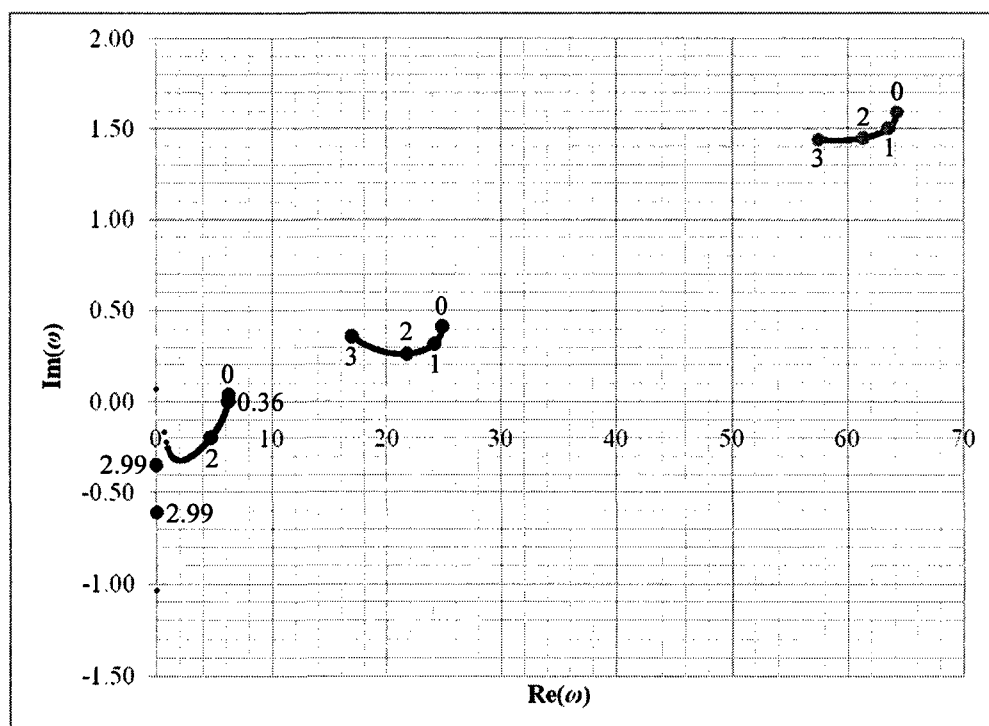


Figure H.4. Argand diagram as a function of u for a free-clamped cylinder in confined axial flow with $f = 0.60$ and $c_b = 0.40$ using a five-mode Galerkin approximation.

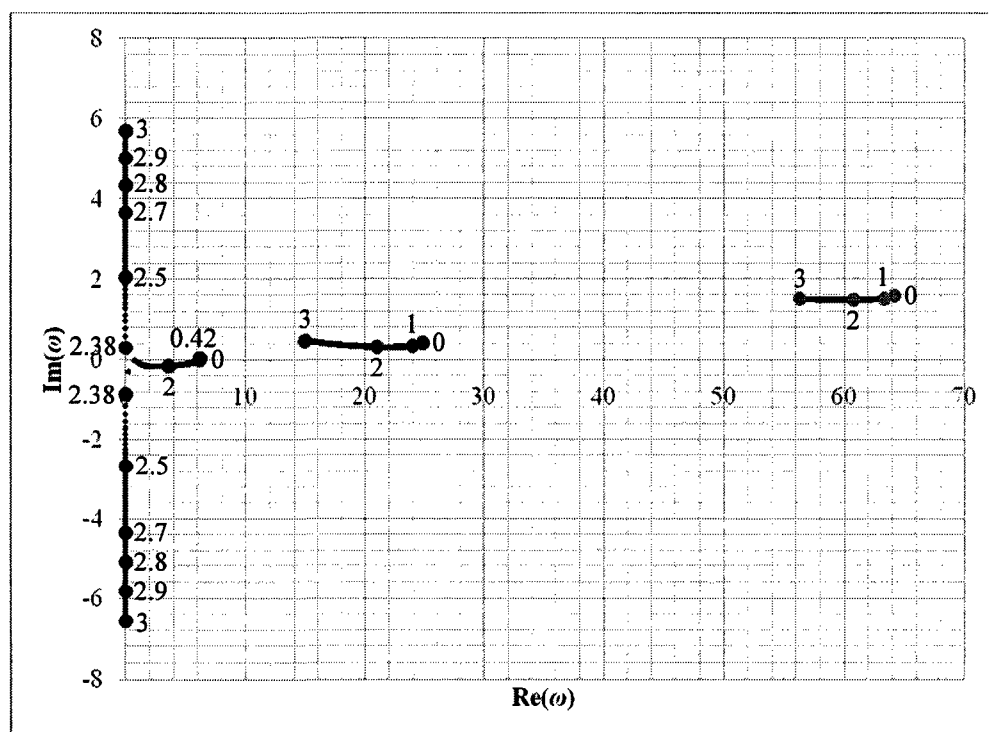


Figure H.5. Argand diagram as a function of u for a free-clamped cylinder in confined axial flow with $f = 0.80$ and $c_b = 0.60$ using a five-mode Galerkin approximation.

Table H.1. Key results including multiplicative factors, vibration amplitudes, flow velocities, and vibration frequencies

Exp.	Multiplicative factors		Experimental max amplitudes		Experimental rms amplitudes	
	$u \rightarrow U$	$\omega \rightarrow f$	A_{\min} [mm]	A_{\max} [mm]	A_{\min} [mm]	A_{\max} [mm]
1A	13.9	0.187	0.0851	15.5	0.0182	6.77
1B	13.7	0.187	0.0668	8.04	0.0247	3.16
1C	13.9	0.187	0.0737	12.6	0.0186	4.16
1D	13.9	0.187	0.0736	14.4	0.0196	4.69
2A	14.4	0.176	0.0792	6.94	0.0202	3.05
3A	19.4	0.234	0.0843	8.45	0.0196	3.06

Exp.	Experimental flutter and buckling results				Theoretical flutter and buckling results			
	$u_{cr,f}$	$f_{cr,f}$ [Hz]		$u_{cr,d}$	$f = 1.00, c_b = 0$			
		PSD 8	PSD 16		$u_{cr,f}$	$\text{Re}(\omega_{\sigma f})$	$u_{cr,d}$	$\text{Re}(\omega_{\sigma d})$
1A	0.377	1.07	1.07	1.70	0.51	6.09	2.35	0
1B	0.380	1.12	1.17	1.64	0.51	6.03	2.35	0
1C	0.380	1.12	1.17	1.64	0.52	5.95	2.35	0
1D	0.376	1.12	1.07	1.67	0.52	5.88	2.35	0
2A	0.371	1.03	1.07	1.23	0.57	6.28	2.41	0
3A	0.270	1.32	1.27	1.08	0.97	5.11	2.16	0

Exp.	Theoretical flutter and buckling results				Theoretical flutter and buckling results			
	$f = 0.80, c_b = 0.20$				$f = 0.60, c_b = 0.40$			
	$u_{cr,f}$	$\text{Re}(\omega_{\sigma f})$	$u_{cr,d}$	$\text{Re}(\omega_{\sigma d})$	$u_{cr,f}$	$\text{Re}(\omega_{\sigma f})$	$u_{cr,d}$	$\text{Re}(\omega_{\sigma d})$
1A	0.42	6.14	2.59	0	0.36	6.17	2.99	0
1B	0.42	6.08	2.59	0	0.36	6.11	2.99	0
1C	0.43	6.00	2.59	0	0.37	6.03	2.99	0
1D	0.43	5.93	2.59	0	0.37	5.96	2.99	0
2A	0.47	6.34	2.67	0	0.40	6.38	None	None
3A	0.78	5.35	2.38	0	0.66	5.47	2.73	0

Exp.	Theoretical flutter and buckling results			
	$f = 0.80, c_b = 0.60$			
	$u_{cr,f}$	$\text{Re}(\omega_{\sigma f})$	$u_{cr,d}$	$\text{Re}(\omega_{\sigma d})$
1A	0.42	6.13	2.38	0
1B	0.42	6.07	2.38	0
1C	0.43	5.99	2.38	0
1D	0.43	5.92	2.38	0
2A	0.47	6.33	2.45	0
3A	0.78	5.30	2.19	0

$$C_{sr} = \left[(\bar{\alpha}^* + \bar{\mu}^* / \omega) \lambda_r^4 + \frac{1}{2} \varepsilon c_N \beta^{1/2} u + \sigma \right] \delta_{sr} - 2 \chi \beta^{1/2} u b_{sr} + f \chi \beta^{1/2} u \phi_s(1) \phi_r(1) - \chi \beta^{1/2} u \phi_s(1) \phi_r(1), \quad (\text{H.15})$$

$$K_{sr} = \lambda_r^4 \delta_{sr} - \left(\frac{1}{2} \varepsilon c_T u^2 h - \gamma + \frac{1}{2} \varepsilon c_N u^2 \right) b_{sr} + \left[\frac{1}{2} c_b u^2 + \frac{1}{2} \varepsilon c_T u^2 (1 + h) - \gamma + \chi u^2 \right] c_{sr} - \left[\frac{1}{2} \varepsilon c_T u^2 (1 + h) - \gamma \right] d_{sr} - \left(\frac{1}{2} c_b u^2 + f \chi u^2 \right) \phi_s(1) \phi_r'(1) - \chi u^2 (1 - \alpha) c_{sr}. \quad (\text{H.16})$$

Now, the Argand diagrams for the three lowest modes as a function of the dimensionless flow velocity, u , are presented in Figs. H.2 to H.5 for a system with the parameters $\bar{\alpha}^* = 0.00030$, $\bar{\mu}^* = 0.03578$, $\beta = 1.14 \times 10^{-3}$, $\gamma = 17.6$, $\varepsilon = 25.3$, $h = 0.455$, $\chi = 1.22$, $\chi_e = 0.00792$, $c_N = 0.0100$, $c_T = 0.0125$, $\alpha = 0.90$, and $c_b = 1 - f$ (generally) for four different cases: (i) i.e. $f = 1.00$ and $c_b = 0$; (ii) $f = 0.80$ and $c_b = 0.20$; (iii) $f = 0.60$ and $c_b = 0.40$; and (iv) $f = 0.80$ and $c_b = 0.60$. In all instances, the system initially becomes unstable by flutter via a Hopf bifurcation in its first mode at very low flow velocities, i.e. $0.36 \leq u_{cr,f} \leq 0.51$, followed by first-mode divergence via a pitchfork bifurcation at much higher flow velocities, i.e. $2.35 \leq u_{cr,d} \leq 2.99$. It should be noted that, prior to buckling, in Figs. H.2, H.3, and H.5, the first-mode locus is shown to regain stability, since $\text{Im}(\omega)$ becomes positive, after the system undergoes flutter. Moreover, in all cases, the second and third modes remain stable for all flow velocities falling within the range $0 \leq u \leq 3$.

Furthermore, Table H.1 presents both the experimental and theoretical results for the four different combinations of f and c_b considered above. Contrary to the results presented in Section 4.3.3 of Chapter 4, all combinations of f and c_b capture qualitatively what is observed experimentally: first-mode flutter at low flow velocities and first-mode divergence at higher flow velocities, i.e. $0.270 \leq u_{cr,f} \leq 0.380$ and $1.08 \leq u_{cr,d} \leq 1.70$. The experimental results for the critical oscillation frequency also match the theoretical values agreeably: $f_{cr,f}$ is roughly equal to 1 Hz. Thus, the changes introduced in this appendix to the original model (derived in Section 4.2.1) have significantly improved the theoretical results, in the sense of bringing them closer to the experimental observations. It is worth mentioning that a theoretical model with $f = 0.80$ and $c_b = 0.60$ is perhaps the best in this regard, as compared to the other combinations of f and c_b , since $u_{cr,f}$ is kept low and $u_{cr,d}$ is not made too high.